NEUTRON TRANSPORT IN RADIOGRAPHY

by

DOUGLAS ROBERT WYMAN, B.MATH.

A Thesis

Submitted to the School of Graduate Studies

in Partial Fulfillment of the Requirements

for the Degree

Doctor of Philosophy

McMaster University

NEUTRON TRANSPORT IN RADIOGRAPHY

To Annie, mein ains

DOCTOR OF PHILOSOPHY (1984)
(Nuclear Engineering)

McMaster University
Hamilton, Ontario

TITLE: Neutron Transport in Radiography

AUTHOR: Douglas Robert Wyman
B.Math. (University of Waterloo)

SUPERVISOR: Dr. A.A. Harms

NUMBER OF PAGES: xvi, 321

ABSTRACT

A frequently important source of image degradation in diagnostic radiography arises from the scattering of radiation within the object itself. The research presented in this dissertation is directed towards the elucidation of this source of radiographic image degradation.

The physical context selected is the passage of collimated thermal neutrons through an object of radiographic interest while the mathematical context is that of neutron transport. The analytical and computational methods are selected to emphasize the macroscopic image degradation effects of object scattering. Accordingly, isotropic neutron scattering and thermal one-group neutron-nucleus macroscopic cross-sections are employed as characterizations of the relevant interaction physics. Calculations and experiments undertaken pertain primarily to homogeneous objects of planar geometry.

The conceptual basis of this dissertation is divided into two domains.

First, the transport of a collimated neutron beam through an object is modelled in isolation to the image formation domain with the goal of estimating the extent of object scattering that occurs. This is accomplished initially for a one-dimensional homogeneous infinite slab object using a one-group integral transport formulation based on the point source diffusion kernel. An original solution to this particular form of the integral neutron transport equation is developed, featuring the exact specification of a build-up factor function based on the forward partial neutron current and admitting an arbitrary degree of multiple scattering.

Additionally, an original extension to the double - P_ℓ method for solving the one-group integro-differential neutron transport equation is developed for calculating the two-dimensional transport of collimated neutrons through a rectangular object.

The second approach involves calculating the distribution of object scattered neutrons on the image formation plane thereby quantifying the incurred image degradation.

This is accomplished by incorporating both problem domains into a system transfer function framework, involving the calculation of scattering based spatially variant point and line spread functions which are applied in the response determination for a homogeneous knife-edged slab object. Applications to the location of edges and corners on blurred neutron radiographs are established. These should ultimately be useful in the accurate radiographic dimensioning of nuclear fuel pins.

One significant result of these calculations is the quantitative evaluation of scattering based distortions that have previously been noted in neutron radiographic edge responses. The existence and relative magnitude of this phenomenon has been confirmed here using an analog Monte Carlo simulation. Experimental tests using the neutron radiography facility at the McMaster Nuclear Reactor have also been undertaken. Each of these confirmation techniques suggests that this scattering based edge distortion may possess merit as a neutron beam diagnostic indicator.

In summary, image degradation attributable to object scattering has been quantitatively examined and clarified for thermal neutron radiography. Applications in the interpretation of radiographic responses are thereby enhanced.

ACKNOWLEDGEMENTS

I would like to thank my research supervisor, Dr. A.A. Harms, for his availability, flexibility, perspective, physical insight and mostly for his continual friendly encouragement.

I also thank my supervisory committee members, Dr. O.A. Trojan and Dr. D.A. Goodings, for their time and attention to this research.

Some of the groundwork and technical assistance for this research have been provided by Mike Butler, to whom I am grateful.

The objective discussions, subjective arguments, occasional verbal slugfests and general camaraderie provided by the dynamic equilibrium that is the students of SS-119 will always be warmly remembered.

Similar appreciation is expressed to the local group of squash hacks for helping maintain my mental balance during my stay at McMaster.

I wish to thank the Engineering Word Processing Center, Dave Hodgson and Helen Kennelly for their assistance with the several phases constituting the formal preparation of this dissertation.

Finally, I wish to thank my parents and family for providing a loving, stable environment conducive to learning, Joe and Bella Braun for their interest and support, and E. Anne Braun for sustaining me in those things which are more important than knowledge (103).

TABLE OF CONTENTS

TABLE OF CONTENTS (continued)

TABLE OF CONTENTS (continued)

TABLE OF CONTENTS (continued) Page

LIST OF FIGURES

LIST OF FIGURES (continued)

LIST OF FIGURES (continued)

LIST OF FIGURES (continued)

LIST OF FIGURES (continued)

LIST OF FIGURES (continued)

LIST OF TABLES

CHAPTER 1

INTRODUCTION

This introductory chapter presents brief historical and technical outlines of the nondestructive diagnostic technique that is neutron radiography. Also included is an introduction to imaging analysis presented from a radiation transport perspective. Subsequently, the scope and organization of this dissertation are discussed.

1.1 Historical and Background

While experimenting with a vacuum tube activated by a high voltage electric current from an induction coil, Wilhelm Roentgen in 1895 observed an image of the bones in his hand on a fluorescent screen even though all visible light from the tube had been excluded by black paper. This discovery of "a new form of radiation" (1) represents apparently the earliest example of radiologic examination. The subsequent availability of reliable x-ray sources increased and by the 1920's, industrial and medical x-ray radiography had become widely employed.

The central attractive feature of x-ray radiography is that it is "nondestructive" or "noninvasive". That is, two-dimensional density images of a three-dimensional object are obtainable without the physical destruction or material invasion of the object itself. This appealing characteristic, along with its demonstrated economic viability, explains its dominance as a fundamental industrial and medical diagnostic tool. The physical basis and conventional applications of industrial and medical radiology are well summarized in texts such as those of Halmshaw (2) and Herz (3).

Since the discovery and initial application of x-rays as an imaging tool, imaging technology has been employed and further developed in most fields of modern science and engineering. One reason for the continuing technological developments in imaging is the inadequacy of simple x-ray radiography in various contexts. X-ray and γ-ray radiography generates two-dimensional images of three-dimensional objects by integrating the atomic absorption of x-rays along one dimension. This integration implies the loss of detailed information about interior planes of the object, such as might for example be valuable to the medical radiologist in assessing the state of a particular human internal organ, or to the industrial radiologist in inspection of the interior of a nuclear fuel assembly. Following the perception of this need, tomographic and other three-dimensional imaging techniques were developed. Excellent review articles and feasibility studies have been presented (4-11).

Another serious limitation of x-ray radiography becomes apparent whenever it is desired to image the spatial distribution of a characteristic that is relatively insensitive to x-rays. For example, if the inspection objective is to determine the distribution of radioactive materials within an object, or if the object is highly radioactive, then x-ray radiography is generally inapplicable. Also, elements of similar atomic number are poorly differentiated through x-ray attenuation and objects deeply embedded in absorbing metals are poorly imaged by x-rays. It is for these specific application domains that the nondestructive diagnostic tool known as neutron radiography was developed (12, 13).

Central to the subject of this research, radiography with thermal neutrons is properly viewed as a technique that is complementary to x-ray and γ-ray radiography. Many metals are fairly transparent to thermal neutrons – with a few notable exceptions – and low atomic number elements such as hydrogen, lithium, and boron attenuate neutrons well. As such, the thermal neutron attenuation properties of matter are, qualitatively, almost a

reversal of those for x-rays, and permit the successful imaging of lighter objects enveloped in denser materials.

The nuclear nature of neutron absorption also often enables distinguishing between elements of similar atomic weight or isotopes of the same element. Also, intensely gamma radioactive objects which prohibit x-ray radiography can be neutron radiographed using the screen "transfer" technique, discussed in section 1.2. Excellent overviews of neutron radiography are found in Berger's text (12), in particular, the first chapter (13-15), and also in reference 16. Reference 13 includes a concise history of neutron radiography to be summarized below.

Neutron radiography was initiated by Kallman and Kuhn (17) and by Peter (18) in the late 1930's using a small accelerator-type neutron source. The first neutron radiographs taken with a reactor neutron beam were obtained at the 8 MW BEPO reactor at Harwell. After Thewlis' publications (19), Neissel (20) performed neutron radiographic experiments using a small accelerator source at the General Electric Company in Schenectady, New York. Criscuolo and Polansky (21) then investigated fast neutron radiography at the U.S. Naval Ordnance Laboratory in Maryland. Some of the first reactors to be used for neutron radiography in the U.S. were at the Armour Research Foundation in Chicago (22) and the 200 kW Juggernaut Reactor at Argonne National Laboratory (23).

In the last two decades, three main phases of neutron radiography have been identifiable. In the first phase, a large number of research centers interested in nuclear technology explored potential applications of neutron radiography. In particular, the U.S. centres such as Battelle-Columbus (24), Argonne-Idaho (25), General Electric Vallecitos (26) and Atomics International (27) were prominent in developing the nuclear fuel inspection application.

The second phase, commencing around 1968, was characterized by the creation of "service" neutron radiography centers, designed to inspect industrial users' items for a small fee. The two installations to first offer this service were the Nuclear Test Reactor at the General Electric - Vallecitos Center (28) and the TRIGA type reactor at the Aerotest Company (29). At approximately the same time, national laboratories overseas, such as Fontenay-Aux-Roses in France (30) and the Harwell Nondestructive Testing Center in England (31), set up reactor based service centers.

The third and current phase is best described as the industrial expansion and maturation of neutron radiography along the following three dimensions. Firstly, the development of standards such as the image quality indicator developed by the American Society for the Testing of Materials (ASTM) has helped to properly place neutron radiography in the company of other nondestructive testing techniques such as x-ray radiography and ultrasonic testing.

Secondly, centers with substantial neutron radiography requirements have begun to purchase their own neutron radiographic facilities, such as the TRIGA reactor at the Westinghouse-Hanford Company in Washington.

Thirdly, particular needs have seen the specific tailoring of neutron radiographic techniques, such as the high-speed neutron radiographic facility at Oregon State University, designed to examine the millisecond duration firing process of explosive items, and the development of portable neutron radiography equipment for inspection of aircraft (32).

In summary, the historical development of neutron radiography has been similar to that of x-ray radiography with approximately a 40-year time lag. Essential to further expansion of the technique are source availability, industrial knowledge and the inclusion of the method in standards.

Excellent reviews of neutron radiographic applications are found in references 12, 16, 33 and 34. These are summarized below.

Neutron radiography has important industrial aerospace applications, including the inspection of bonded metal honeycomb structures, composite metal laminates, aircraft engines, rocket nozzles, helicopter blades and corrosion detection.

A regular neutron radiographic application lies in the acceptance inspection of explosives and weapon components.

Perhaps the widest application of neutron radiography is found in the nuclear industry, particularly in the inspection of nuclear fuel elements for material integrity, burn-up and dimensional data. Miscellaneous nuclear applications include the inspection of control absorber elements, steel samples and resin filled shield plugs.

Other industrial applications are the inspection of electrical and electronic components, soil and rock samples, rubber and plastic materials, welds, castings, metals, automobile engines and two-phase flows.

The biological/medical applications of neutron radiography, limited due to the associated radiation dosage received by tissues, include histopathology, plant structural imaging and dental inspection.

Miscellaneous applications include usage as a forensic tool for the location of hidden contraband and explosives, and inspection of archaeological and museum art objects.

1.2 Neutron Radiography: A Brief Technical Outline

A brief expository outline of the processes involved in neutron radiography can be established by reference to Fig. 1.1, depicting a typical neutron radiographic imaging assembly.

Neutrons from an appropriate source traverse an object and are differentially attenuated according to the material and geometric characteristics of the object. For all cases of interest in this work, the neutron beam is assumed to be collimated and thermalized, such as is typically extracted from a nuclear reactor. The pertinent neutron interactions are therefore characterized by thermal neutron macroscopic absorption, scattering and total cross-sections, denoted by Σ_a, Σ_s and Σ_t respectively. It should be mentioned that radiography is also performed with cold, epithermal and fast neutrons (33), using sources other than a nuclear reactor.

Two other general types of neutron sources are radioactive isotopes and accelerators. Reviews of these sources are found in references 12 and 16. Generally, a practical radiography source should produce a thermal neutron flux of at least 10^9 n/cm^2/s. Because nuclear reactors are prolific thermal neutron sources, they are the most frequently used radiography neutron source. Collimation can be achieved in several ways (12, 16), with the relevant dimensionless parameter being the L/D ratio (L = collimator length, D = entrance diameter). This ratio affects both the resolution and the collimator efficiency. It is generally accepted that L/D should be at least 50 to give proper resolution of interest to most practical applications.

The information carrying nonscattered neutron beam emergent from the object comprises the "ray image". Mathematically, the ray image intensity corresponding to a uniform incident collimated neutron beam of intensity I_o is given by the familiar exponential attenuation expression:

$$I(u,v) = I_o \exp\left[-\int_{w_\ell(u,v)}^{w_u(u,v)} \Sigma_a(u,v,t)\,dt\right]. \qquad (1\text{-}1)$$

Here, w_ℓ and w_u denote the lower and upper object boundaries, and t is a dummy variable for integration along the w axis. In practice, the ray image is never ideal, because of

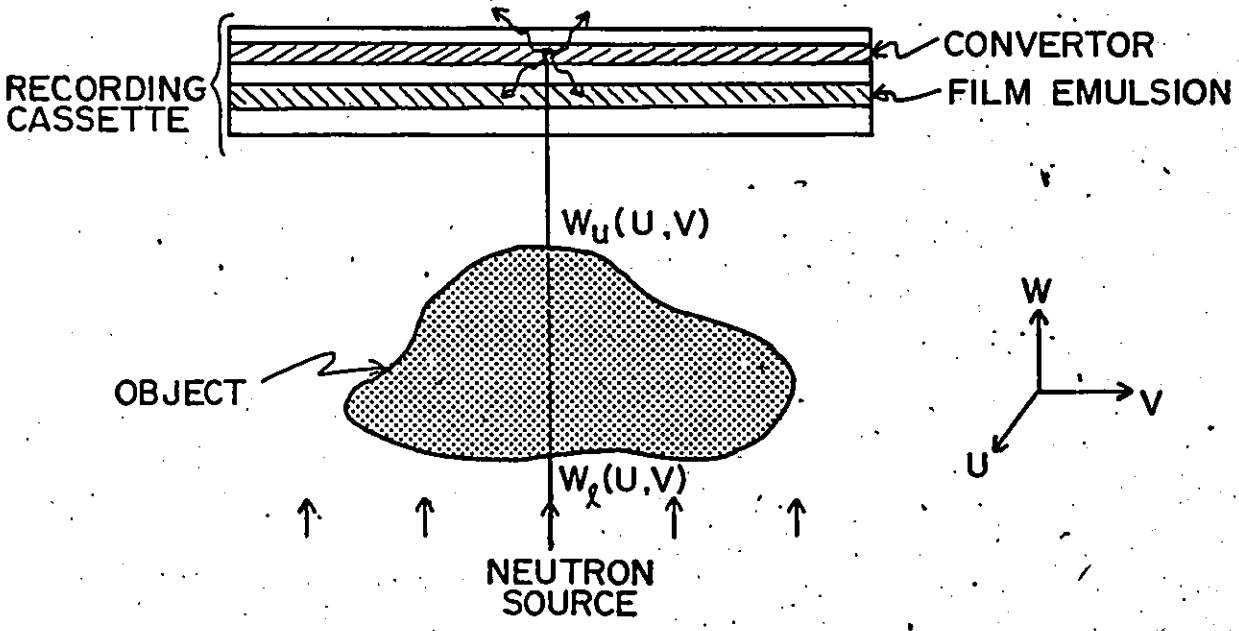

Fig. 1.1: Typical direct exposure neutron radiographic imaging assembly (not to scale).

(i) the stochastic nature and spatial variability of the incident source,

(ii) the inclusion of non-image forming object and facility scattered neutrons, and

(iii) the finite divergence of most collimated beams.

A chief advantage of collimated neutron sources over x-ray sources and other (divergent) neutron sources is the reduction in geometrical unsharpness provided by collimation. This unsharpness, illustrated in Fig. 1.2, arises because the finite area source images each point of a given plane through the object at an entire region of points on a given plane through the ray image. Source collimation also facilitates analytical transport calculations; this becomes apparent if one attempts to construct the analog to Eq. (1-1) for a finite divergent source.

The function of the recording cassette is to transform the ray image into an optical density image on a photographic film. Since these films are insensitive to neutrons, the ray image must first be converted to either electrons or photons. This is accomplished by the insertion of a convertor screen, as shown in Fig. 1.1 which absorbs the ray image neutrons and re-emits secondary image-forming radiation. Two types of conversion are distinguishable, these being "direct exposure" and the "transfer technique".

The direct exposure method features the close juxtaposition of convertor and film in the recording cassette and usually involves a gadolinium convertor. The low-energy interval conversion electrons promptly emitted from the strongly neutron absorbing gadolinium foil expose a single emulsion film triggering the formation of a latent image. Other convertor materials used are lithium, boron and cadmium.

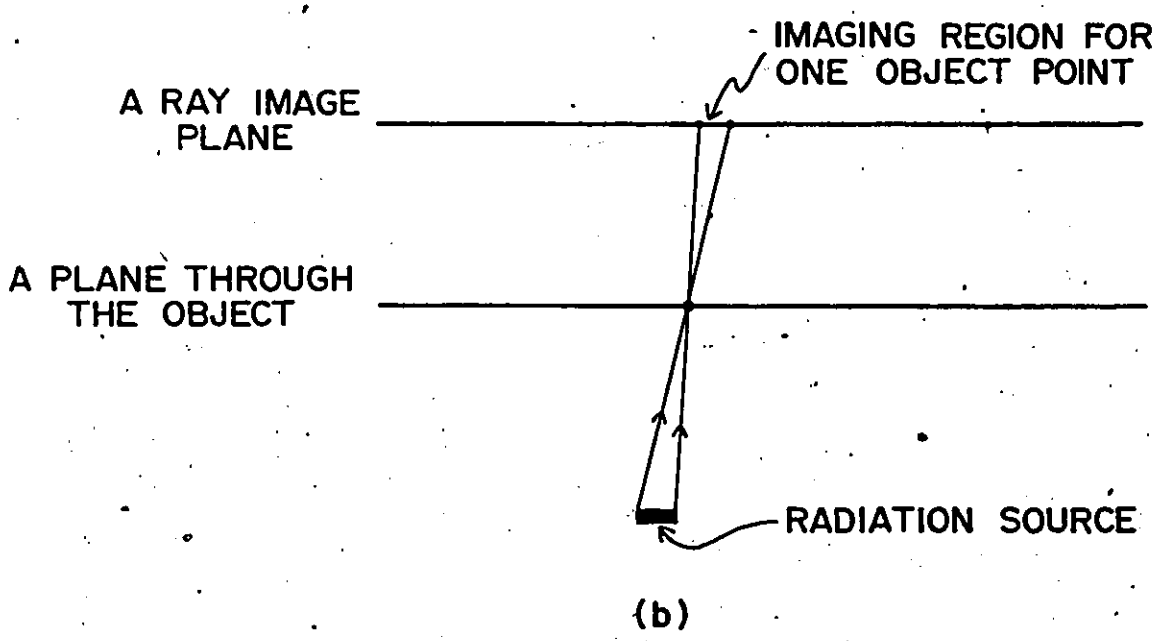

Fig. 1.2: Geometric unsharpness resulting from a divergent radiation source of finite area.

Superior spatial resolution is known to be provided by gadolinium convertors (35). The relevant neutron-nucleus conversion reactions are

$$^{155}Gd + n \rightarrow {}^{156}Gd + \gamma \xrightarrow[\text{internal conversion}]{} {}^{156}Gd + e^- \quad (1\text{-}2a)$$

$$^{157}Gd + n \rightarrow {}^{158}Gd + \gamma \xrightarrow[\text{internal conversion}]{} {}^{158}Gd + e^- \quad (1\text{-}2b)$$

$$^{6}Li + n \rightarrow {}^{3}H + \alpha \quad (1\text{-}2c)$$

$$^{10}B + n \rightarrow {}^{7}Li + \alpha. \quad (1\text{-}2d)$$

The transfer technique features the neutron exposure of only the convertor, which is subsequently removed from the beam and placed adjacent to a film in order to form an image by autoradiography. This method offers increased contrast over direct exposure radiography through the elimination of fogging radiation from the neutron beam and possibly from the object itself. For example, direct exposure radiography is completely ineffective for highly radioactive samples such as irradiated nuclear fuel elements.

Some common transfer convertor materials are dysprosium, gold and indium. The relevant neutron-nucleus conversion reactions are

$$^{164}Dy + n \rightarrow {}^{165}Dy \xrightarrow[140\,\text{min}]{} {}^{165}Ho + \beta^- \quad (1\text{-}3a)$$

$$^{115}In + n \rightarrow {}^{116}In \xrightarrow[54\,\text{min}]{} {}^{116}Sn + \beta^- \quad (1\text{-}3b)$$

$$^{197}Au + n \rightarrow {}^{198}Au \xrightarrow[2.7\,\text{days}]{} {}^{198}Hg + \beta^-. \quad (1\text{-}3c)$$

The usage of scintillator-film techniques and real-time radiographic systems based on scintillator light amplification by image intensifiers or detection by television cameras has also received much attention (15,16).

A different type of passive image detector constitutes the "track-etch" technique, in which the high-energy particles emitted by the convertor leave radiation damage tracks in a

dielectric, such as plastics, that are chemically etched to generate visibility. High resolution, linear response and gamma insensitivity are reported as being advantages of this method (16).

Several references to the above and other developing radiographic neutron detection systems are found in references 15 and 16.

A complete discussion of the photographic process is found in the text by Herz (3). In summary, the photographic emulsion is a radiation sensitive layer usually consisting of silver halide crystals or grains embedded in a gelatin. Upon absorption of incident radiation by the emulsion, individual grains are said to be rendered "developable". While the exact process underlying this developability is incompletely understood, a basic and popular descriptive model is the "Gurney- Mott" (36) mechanism.

Basically, this model features the trapping of electrons at negatively charged sites known as "sensitivity specks", to which positively charged interstitial silver ions are attracted. The subsequent formation of neutral silver defines the latent image. Since the image developing process is an important part of every film-based radiographic technique, and was thus performed repeatedly during the course of this research, it is briefly discussed below.

Development of the latent image is accomplished by immersion of the exposed film in a "developer" solution where reduction of silver metal occurs. This formation is preferentially located at previously exposed sites, where silver ions from the developer adsorb to the latent image silver nuclei, and are then reduced to atomic silver by electrons from the reducing agent of the developer. The actual physical image development is thus a catalytic reduction of silver ions.

Immersion in a "stop bath" solution then halts the development process. Finally, unexposed silver halide grains are dissolved and removed by a "fixing" solution.

The resulting negative image on the developed film is a conglomeration of regions of varying opacities, seen as blackening when viewed through a light source. Qualitatively, darker regions correspond to higher exposures and therefore to regions of lesser attenuation in the radiographed object. Quantitatively, the degree of blackening is referred to as "optical density" and is computed by

$$D = \log_{10}\left[\frac{\text{incident radiant flux}}{\text{transmitted radiant flux}}\right] \qquad (1\text{-}4)$$

when the film is subjected to a radiant light flux. The relationship between optical density and exposure is generally nonlinear and described by the characteristic, or "H and D", curve for the film emulsion (3).

1.3 Imaging Analysis and Radiation Transport

The radiographic system in Fig. 1.1 can be viewed as a combination of three components. These are the neutron source, the object being inspected, and the recording cassette containing a convertor screen and film emulsion which ultimately records a projected two-dimensional image of the object. Associated with the system are the conceptual object and image planes which, while being abstractions, have very useful physical and mathematical interpretations.

The object plane is best taken to be a plane orthogonal to the radiographic axis, defined by the direction of incident radiation and posed adjacent to the recording cassette on the same side as the object. The object plane therefore contains the ray image with intensity given by Eq. (1-1). In practice, the ray image is never as sharp as indicated in Eq. (1-1), since the finite beam divergence incurs geometrical unsharpness. Indeed, the amount of geometrical unsharpness is inversely proportional to the collimator L/D ratio (37).

Compounding this geometrical unsharpness is another source of geometrical degradation incurred by the conversion of the neutron ray image in the recording device. As

suggested in Fig. 1.1, the isotropically emitted secondary radiation spreads information from its point of origin onto the entire image plane, defined here as that plane parallel to the object plane and upon which the final image is formed. This information spreading generates a corresponding "screen-film" unsharpness in the final image. Several authors have quantified screen-film unsharpness through mathematical modelling (38-43). For high resolution neutron radiography, screen-film unsharpness (U_s) dominates geometric unsharpness (U_g). In this work, U_g has been assumed negligible, reflected in the models as collimated incident source neutrons.

A third major image degradation source is the unsharpness resulting from motion of one or more of the three system components (44), denoted by U_m. In this work all components are assumed stationary and hence U_m is eliminated.

To date there have been several analytical prescriptions for combining these unsharpness sources to generate a total unsharpness, U_t (45-50). The analysis of neutron radiographic unsharpness continues to be an area of active research (51,52).

Perhaps the most important – and often neglected – source of image degradation arises from scattered radiation in the object itself. It has been argued that object scattering is really not a source of unsharpness but rather reduces the overall image contrast (2). For the case of a large homogeneous object section of constant depth this is clearly true since at a given plane through the section, the scattered neutron component would be spatially constant near the section center. Such an idealization is in practice seldom applicable rendering the exact nature of scattering based image degradation incompletely understood.

Progress, while slow and difficult, continues to register in this area (53- 55). In principle the transport of neutrons through the object and into the convertor is completely determined by the appropriate neutron transport equation. This governing integro-differential equation forms the foundation of reactor physics analysis and has been the subject

of extensive research over the past few decades. Derivations of and specialized solutions to this equation are found in a number of texts, for example, reference 56. A heuristic derivation is given in Chapter 3. The equation is stated below without derivation or boundary conditions.

$$\frac{1}{v}\frac{\partial \Psi}{\partial t} + \Omega \cdot \nabla \Psi + \Sigma_t(r,E)\,\Psi(r,E,\Omega,t) = S(r,E,\Omega,t)$$

$$+ \int_{4\pi}\int_{0}^{\infty} \Sigma_s(E' \rightarrow E,\, \Omega' \rightarrow \Omega)\,\Psi(r,E',\Omega',t)\,dE'\,d\Omega' . \qquad (1\text{-}5)$$

Here, $\Psi(r,E,\Omega,t)$ is the angular neutron flux, a flux density that is related to $n(r,E,\Omega,t)$, the expected number density of neutrons with energy dE about E, moving in direction $d\Omega$ of Ω, at location d^3r about r and at time t, by

$$\Psi(r,E,\Omega,t) = vn(r,E,\Omega,t) \qquad (1\text{-}6)$$

where v is the neutron speed. Also, $\Sigma_s(E' \rightarrow E,\, \Omega' \rightarrow \Omega)$ and $\Sigma_t(r,E)$ are the macroscopic neutron cross-sections for scattering from (E',Ω') to (E,Ω), and for total interaction, respectively. The function $S(r,E,\Omega,t)$ represents an external source such as applies to the problem of neutron transport in a radiographic context. Radiographic neutron transport thus relates directly to modern reactor physics in that both are concerned with neutron source-driven systems. A wealth of knowledge (see, for example, reference 57) is therefore available for neutron radiographic transport analysis.

However, the general neutron transport equation involves several variables, admitting analytical solutions for only certain geometrically and materially simplified situations such as rarely apply to objects being inspected radiographically. Furthermore, the material distribution of such objects is presumably unknown rendering a transport equation solution approximate at best.

Nontrivial radiation transport underlies both screen-film unsharpness and scattering-based image degradation. The most successful characterizations of image degradation have involved transfer function theory adopted from the field of linear invariant communication systems. While initially applied to the standard unsharpness sources in the mid-1960's (38, 58-64), applications in the characterization of scattering based image degradation have recently appeared in the literature (53-55).

Transfer function analysis of a system features the overall modelling of that system by some function(s) describing its transformation of an input into an output. This "black box" logic operates by first mathematically representing the input, and then transforming it through multiplication or convolution with the system transfer function (STF) to obtain a mathematical representation of the output. Comprehensive review articles of transfer function analysis for radiographic imaging systems are found in references 65 and 66. A brief introduction is given below.

In radiographic imaging contexts, the most fundamental STF is the "point spread function" (PSF), illustrated in Fig. 1:3a. The PSF describes the spreading of an idealized point source of radiation from the object plane, by the several system unsharpness sources, onto the image plane. Defining a Cartesian coordinate system for the object and image planes, the notation PSF(x,y,u,v) describes the radiation intensity at (x,y) in the image plane due to a point source at (u,v) in the object plane.

In practice, the system input I(u,v) is the ray image intensity given by Eq. (1-1). The noise-free system output, representing the radiation intensity distribution at the image plane, is then the convolution of I(u,v) with the system PSF, and is given by

$$O(x,y) = N \int_{-\infty}^{\infty} \int_{-\infty}^{\infty} I(u,v)\, PSF(x-u, y-v)\, du\, dv. \tag{1-7}$$

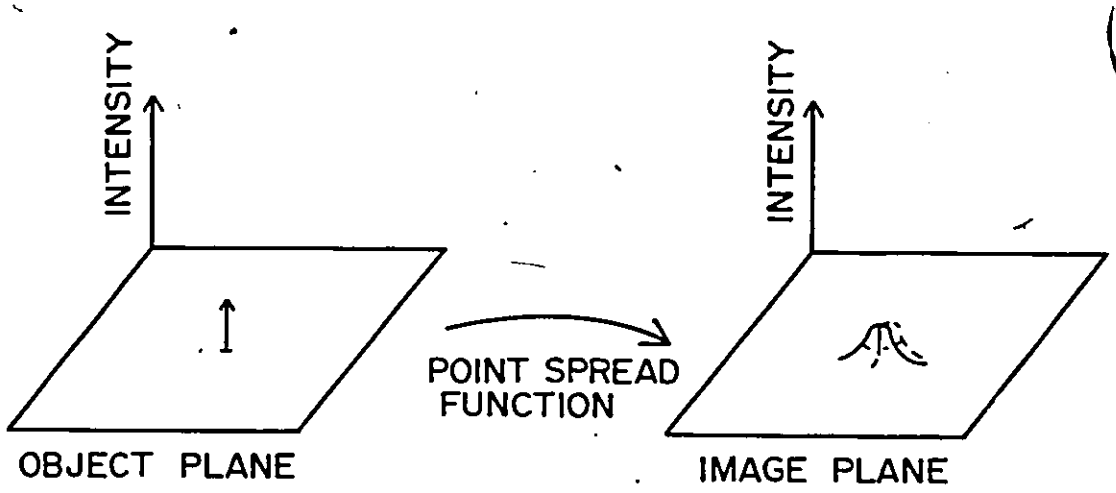

(a)

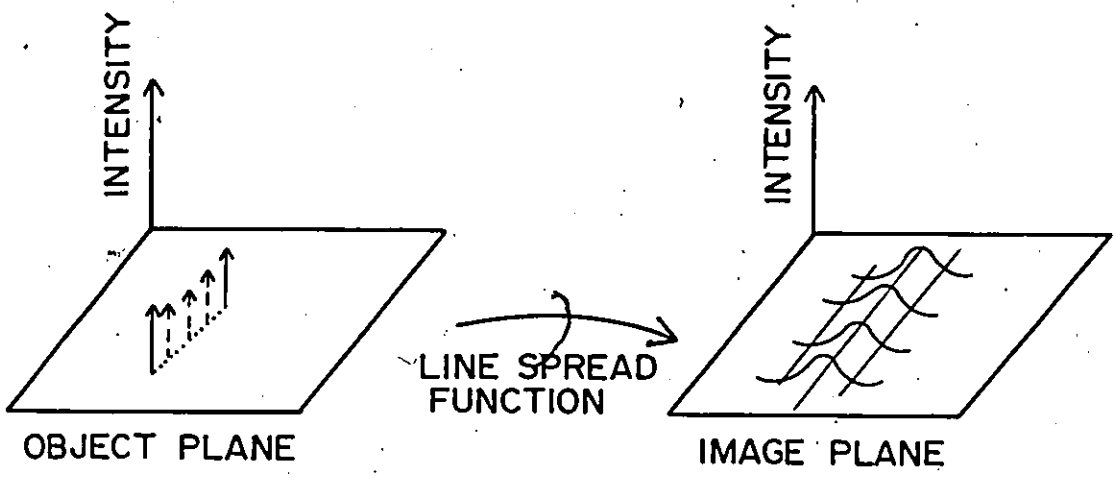

(b)

Fig. 1.3: (a) Point spread function in imaging analysis.
(b) Line spread function in imaging analysis.

Since O(x,y) is a distribution, the normalization constant N is unimportant for purposes of STF analysis. In practice, N is determined by the overall conversion of the radiation intensity at the object plane to an optical density on the developed film.

Notice in Eq. (1-7) the particular form

$$PSF(x,y,u,v) = PSF(x-u, y-v). \tag{1-8}$$

Implicit in this form is the property of "shift invariance", requiring the image of a point source to maintain a fixed shape, irrespective of the point source location in the object plane. Consequently, this property is also referred to as "isoplanatism". If the PSF can further be written in the form

$$PSF(x,y,u,v) = PSF((x-u)^2 + (y-v)^2) \tag{1-9}$$

then it possesses rotational symmetry and the system is said to be"isotropic".

The imaging system described by Eq. (1-7) also possesses the "linearity" property, requiring that the output corresponding to a linear combination of inputs equals the same linear combination of outputs corresponding to the constituent inputs.

In practice, the PSF is normalized to unity through

$$\int_{-\infty}^{\infty}\int_{-\infty}^{\infty} PSF(x-u, y-v)\,dxdy = 1, \tag{1-10}$$

so that the system only alters the distribution of intensities, and not the overall integrated intensity. The optical analogy of PSF area is the "encircled energy" (67).

Another fundamental STF is the "line spread function" (LSF) illustrated in Fig. 1.3b. Being the one-dimensional analog of the PSF, the LSF describes the spreading of an idealized line source of radiation from the object plane onto the image plane. For one dimensional inputs – that is, inputs which are constant with respect to one object plane dimension, say, v – the noise-free system output representing the radiation intensity distribution at the image plane is

$$O(x) = N \int_{-\infty}^{\infty} I(u)\, LSF(x-u)\, du \tag{1-11}$$

The LSF is less fundamental, and thus deriveable from the PSF. For an isotropic system,

$$LSF(x-u) = \int_{-\infty}^{\infty} PSF(x-u, y-v)\, dy. \tag{1-12}$$

In general, transformation between LSF and PSF is always possible although often non-trivial (68,69).

Another type of STF often encountered in imaging analysis is the "modulation transfer function" (MTF) describing the transfer through the system of sinusoidal inputs as a function of spatial frequency. Specifically, the MTF is the ratio of output amplitude to input amplitude of a sinusoidal input as a function of spatial frequency. A perfect, though unrealizable, imaging system would therefore have an MTF equal to unity for all frequencies. The MTF is calculable in two dimensions as the modulus of the two-dimensional Fourier Transform (70) of the PSF and in one dimension as the modulus of the one-dimensional Fourier Transform of the LSF.

The great advantage of the MTF over the PSF and LSF is that it facilitates imaging analysis through the replacement of the convolution in Eq. (1-7) by a simple multiplication. This is particularly valuable for analyses in which the imaging system is analyzed in terms of its components, necessitating multiple convolution to determine the overall system transfer characteristics. Fourier transformation of Eq. (1-7) from the spatial domain (x,y) to the spatial frequency domain (ν_x, ν_y) and taking moduli yields

$$|O(\nu_x, \nu_y)| = |I(\nu_x, \nu_y)| \cdot MTF(\nu_x, \nu_y). \tag{1-13}$$

Given the system MTF, inversion from output to input is now, in principle, immediate.

The descriptive equivalence of the two-dimensional MTF and the PSF is well-established (65,66,71). A few examples of the application of MTF's in neglect imaging analysis are provided in references 39 and 71-74.

1.4 Dissertation Scope, Perspective and Organization

Every radiation diagnostic system involves source, object and recording device components, denoted here symbolically by S, O and R respectively. A logical categorization of the various systems can be accomplished by assigning a state of either constancy (C) or variability (V) to each component. This state assignment is spatially and temporally based. For example, standard computerized tomographic examination of a fixed object involves the simultaneous motion of the x-ray source and the detector corresponding to a designation of (S_V, O_C, R_V) where the state subscripts the component. As another example, the stochastic nature of radiation sources precludes the exact specification of the integrated source intensity over short exposure durations implying a designation of S_V to the source component in such cases. Based on these considerations, a given radiation diagnostic system falls into precisely one of eight categories, as illustrated in Fig. 1.4.

The research constituting this dissertation is categorized as (S_C, O_C, R_C) using the above classification system. The general objective of this research is the description, comprehension and characterization of the neutron transport processes that underly standard direct exposure neutron radiography. The particular focus adopted concerns the transport of thermal neutrons through the object being diagnosed and how this degrades or impacts on a desired ideal image.

The research undertaken here does not extend in scope to image enhancement techniques but rather aims to interpret neutron radiographic images obtained prior to any enhancement.

An assertion made here is that all macroscopic phenomena can be analyzed at a variety of levels of depth. For this research topic, one could conceivably proceed from the nuclear physics consideration of the neutron as a strongly interacting fermion of spin $\frac{1}{2}$. From this level, a lifetime's work would likely fail to elucidate most particular image characteristics of general interest in neutron radiography.

By viewing the object as a medium supporting a sea of migrating neutral particles, a continuum description is appropriate (the neutron transport equation). This description begins where the previous level ends; with neutron-nuclear cross-sections. As such, however, the general neutron transport equation is far too complex to yield image interpretation results necessitating therefore approximations and simplifications. Also at this level of interest, there exists the technique of Monte Carlo analog simulation.

The most practical level for imaging analysis is the system transfer function (STF) level introduced in section 1.3 since it is directly concerned with the interpretation of images. This approach is often empirical in nature, lumping a variety of transport phenomena into a macroscopic experimentally derived function.

Direct visual qualitative inspection of a radiograph perhaps constitutes the most macroscopic level of imaging analysis. The radiologist and radiographer may indeed possess scant knowledge of the underlying levels of analysis.

This dissertation then represents an original contribution to knowledge at the boundary of the transport and STF levels, in a thermal neutron radiographic context. Attempts are made to determine STF's from neutron transport calculations, thereby connecting the two levels. Little consideration is given to the nuclear physics or visual inspection levels. For example, thermal neutron-nucleus macroscopic cross- sections are never computed, but rather are taken from existing compilations such as reference 75, or varied as input parameters. The specific organization of this dissertation is outlined below.

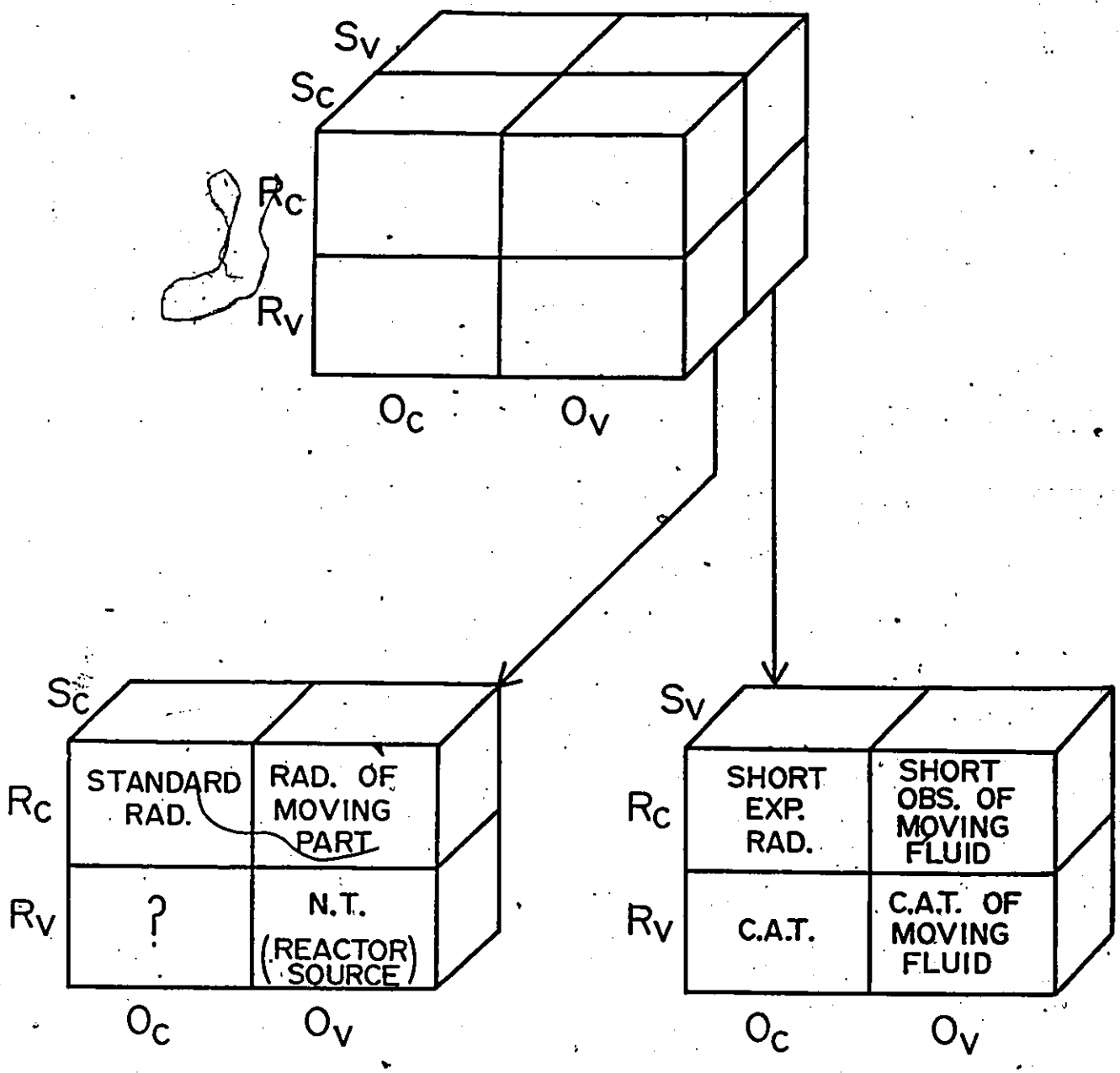

Fig. 1.4: Classification of radiation diagnostic systems according to the constancy/variability of source, object and recording device. Examples are included. Abbreviations are: EXP.-EXPOSURE, OBS.-OBSERVATION, C.A.T.-COMPUTERIZED AXIAL TOMOGRAPHY, RAD.-RADIOGRAPHY, N.T.-NEUTRON TOMOGRAPHY.

Chapter 2 presents a framework in which thermal neutron scattering by a radiographed object – hereafter referred to as "object scatter" – is properly considered as a nonlinear image degradation source. A model based on the modal solution of a derived integral transport equation is developed to describe and estimate the magnitude of such scattering.

A neutron transport equation approach to thermal neutron radiography is the subject of Chapter 3. This features an original extension of an existing solution technique, the goal being, as in Chapter 2, an estimation of the extent of scattering that can occur. The connection of neutron transport analysis to STF analysis is also established.

In Chapter 4, system transfer functions describing thermal object scattering are derived and subsequently applied in the explanation and quantification of an observed phenomenon in the image of certain knife-edged objects.

Chapter 5 presents an elaboration of the model described in Chapter 4. This is accomplished through Monte Carlo analog simulation. The feasibility of application of the knife-edged slab response, detailed in Chapter 4, as a diagnostic tool indicating the extent of thermal object scattering is discussed.

Experimental confirmation of the results calculated in Chapters 4 and 5 constitutes Chapter 6. Investigations were conducted using the neutron radiographic facility at beam port 2 of the McMaster Nuclear Reactor.

Several generalizations and possible extensions of the research conducted for this dissertation are discussed and briefly developed in Chapter 7.

The important results and original contributions embodied in this dissertation are summarized in Chapter 8.

Also included are four appendixes. Appendix A is mathematical in nature, providing a separate location for equation derivations that might otherwise interrupt the logical flow of a section or chapter. In Appendix B, the integration of information that occurs when analyzing radiographs with a scanning microdensitometer is analyzed. A relevant application of PSF's in two-dimensional radiographic imaging analysis is included in Appendix C. The collection of all original relevant computer FORTRAN programs constitutes Appendix D.

CHAPTER 2

IMAGE DEGRADATION THROUGH OBJECT SCATTERING

2.1 Nonlinearity in the System Transfer Function Formulation

As discussed in sections 1.3 and 1.4, every radiation diagnostic system can be viewed as a combination of three components these being the radiation source, the object being inspected and the recording device. Among other items, the recording device usually contains a film emulsion or screen which ultimately renders a projected two-dimensional image of the three dimensional object. Associated with each system are the conceptual object and image planes, connected by transformation of the ray image.

Many radiographic recording devices, such as those used in direct exposure neutron radiography, include a convertor screen or image intensifier in addition to the film emulsion upon which the latent image forms. The finite thicknesses and separations of these constituents, and the transport of information-carrying radiation between them, collectively effect a degradation of the original image when projected onto the image plane. This image degradation is usually referred to as screen-film unsharpness and is modelled mathematically by a system transfer function (STF) such as a point spread function (PSF), line spread function (LSF) or modulation transfer function (MTF), all introduced in section 1.3.

Image degradation arising from screen-film unsharpness is linear when modelled using STF analysis. To understand this, consider the fundamental imaging equation, Eq. (1-7), reproduced in the form

$$O(x,y) = N \int_{-\infty}^{\infty} \int_{-\infty}^{\infty} I_{obj}(u,v)\, R_{PT}(x-u, y-v)\, du dv. \qquad (2\text{-}1)$$

Here, O(x,y) is the output response at Cartesian coordinates (x,y) in the image plane, $I_{obj}(u,v)$ is the object plane radiation intensity of the input ray image, R_{PT} is the isoplanatic PSF describing the response at (x,y) to a unit point source at (u,v), and N is a normalization constant. At a given (x,y) the output response is a function of the collective input intensities, written using functional notation as

$$O^*(x,y) = O(I_{obj}(u,v)). \tag{2-2}$$

Multiplying separate sets of input intensity distributions by fixed constants α and β and then adding them yields

$$O(\alpha I_{obj1}(u,v) + \beta I_{obj2}(u,v)) = N \int_{-\infty}^{\infty}\int_{-\infty}^{\infty} [\alpha I_{obj1}(u,v) + \beta I_{obj2}(u,v)] R_{PT}(x-u, y-v)\, du\, dv$$

$$= \alpha O(I_{obj1}(u,v)) + \beta O(I_{obj2}(u,v)), \tag{2-3}$$

indicating linearity of the system. Linearity results here because of isoplanatism of R_{PT}. That is, R_{PT} exhibits no dependence on the intensity itself but rather only on the Cartesian shifts x-u and y-v.

When the imaging system is also isotropic, R_{PT} is a function only of the sum $(x-u)^2 + (y-v)^2$ as discussed in section 1.3. In this case, the rotational symmetry of R_{PT} results in some interesting and useful two-dimensional imaging properties. Since the analysis of these properties is only tangential to the subject of the dissertation, it has been included separately in Appendix C.

For an idealized system, collimated incident radiation of intensity I_0 is attenuated exponentially in a nonscattering object according to the macroscopic absorption cross-section Σ_a, so that the ideal object plane intensity is given by

$$I_{obj}(u,v) \stackrel{df}{=} I^*_{obj}(u,v)$$

$$= I_0 \exp\left[- \int_{w_\ell(u,v)}^{w_u(u,v)} \Sigma_a(u,v,w)\, dw \right]. \tag{2-4}$$

This equation is a reproduction of Eq. (1-1) in which the symbols are defined with respect to Fig. 1.1. Implicit in Eq. (2-4) is the assumption of a single energy group model, valid for the analysis of thermal neutron penetration such as is applicable here.

In practice, O(x,y) is ultimately transformed into an optical density when the recording device contains a film emulsion. In general this process is nonlinear. However, the nonlinearity is easily removed through a knowledge of the film's characteristic curve, and thus will be discussed no further.

As introduced in section 1.3, an important and difficult to remove image degradation source arises from scattering of the incident radiation within the object, according to a macroscopic scattering cross-section, Σ_s. While most researchers conducting radiographic and three-dimensional reconstructive imaging analyses acknowledge this problem, few undertake calculations to estimate the magnitude of object scattering. Perhaps this is because of the difficulty and expense of performing such calculations. In fact, object scattering represents a system nonlinearity that is particularly bothersome since it is impossible to determine which sections of the object have been traversed by the noncollimated portion of the emergent radiation. Thus, scattered radiation is non- image forming. This system nonlinearity is now examined formally.

For the general case allowing an arbitrary degree of object scattering, the total object plane input intensity at a point (u,v) is given by

$$I_{obj}(u,v) = \int_{2\pi^+} I_{obj}(u,v,\Omega)\, d\Omega \qquad (2\text{-}5)$$

where $I_{obj}(u,v,\Omega)$ is the angular intensity distribution at (u,v) in the object plane, and $2\pi^+$ denotes the forward half-plane of directions. Since the image plane output response at any point (x,y) to input radiation at (u,v) in the object plane clearly depends on the direction of the input radiation, the output response can be written as

$$O(x,y) = N \int_{-\infty}^{\infty}\int_{-\infty}^{\infty} I_{obj}(u,v)\, R_{PT}(x,y,u,v, I_{obj}(u,v,\Omega))\, du dv, \tag{2-6}$$

where the dependence of O on Ω is left understood.

The determination of $I_{obj}(u,v,\Omega)$ is in general a complex problem requiring either a direct solution of the neutron transport equation or Monte Carlo calculations, as discussed in section 1.3. Relevant and similar calculations have been performed and well-documented for several decades, usually in the context of shielding calculations (76, 77). Without endorsing any particular methodology, the above formalism is extended by noting the following functional dependencies:

$$I_{obj}(u,v,\Omega) = I_{obj}(u,v,\Sigma_s(r),\Sigma_a(r)), \tag{2-7a}$$

$$I_{obj}(u,v) = I_{obj}(u,v,\Sigma_s(r),\Sigma_a(r)). \tag{2-7b}$$

The notation in Eq. (2-7) is intended to illustrate the dependence of object plane intensities on the geometric and material characteristics ($\Sigma_a(r)$, $\Sigma_s(r)$) of the object. The scattering-induced nonlinearity of radiographic systems when viewed from the STF perspective is now clear. Both the PSF and the distribution with which it is convolved are object dependent.

In analogy to Eq. (2-3), for fixed constants α, β, and a total input intensity of

$$I_{obj,tot}(u,v) = \alpha I_{obj,1}(u,v) + \beta I_{obj,2}(u,v), \tag{2-8}$$

the output response is

$$O(I_{obj,tot}(u,v)) = N \int_{-\infty}^{\infty}\int_{-\infty}^{\infty} I_{obj,tot}(u,v)\, R_{PT,tot}(x,y,u,v, I_{obj,tot}(u,v,\Omega))\, du dv, \tag{2-9}$$

thus defining implicitly $R_{PT,tot}$ and $I_{obj,tot}$. Substitution of Eq. (2-8) into Eq. (2-9) yields

$$O(I_{obj,tot}(u,v)) = \alpha N \int_{-\infty}^{\infty}\int_{-\infty}^{\infty} I_{obj1}(u,v)\, R_{PT,tot}\, du dv + \beta N \int_{-\infty}^{\infty}\int_{-\infty}^{\infty} I_{obj2}(u,v)\, R_{PT,tot}\, du dv$$

$$\neq \alpha N \int_{-\infty}^{\infty}\int_{-\infty}^{\infty} I_{obj1}(u,v)\, R_{PT,1}\, du dv + \beta N \int_{-\infty}^{\infty}\int_{-\infty}^{\infty} I_{obj2}(u,v)\, R_{PT,2}\, du dv$$

$$= \alpha O(I_{obj,1}(u,v)) + \beta O(I_{obj,2}(u,v)), \tag{2-10}$$

where $R_{PT,1}$ and $R_{PT,2}$ are PSF's for the particular angular distributions that comprise $I_{obj,1}$ and $I_{obj,2}$. The inequality in Eq. (2-10) holds since generally,

$$R_{PT,1} = R_{PT,2} = R_{PT,tot} \tag{2-11}$$

That is, while $I_{obj,tot}$ numerically equals $\alpha I_{obj,1} + \beta I_{obj,2}$, it is not necessarily comprised of the angular distributions that comprise $I_{obj,1}$ and $I_{obj,2}$.

These angular distributions, and hence the object attenuation characteristics through which they are generated, effect the system nonlinearity. In the absence of object scattering ($\Sigma_s = 0$), all angular distributions are identical. Mathematically, this corresponds to the case in which

$$I_{obj}(u,v,\Omega) = \frac{I_{obj}(u,v)}{2\pi} \delta_D(\mu - 1), \tag{2-12}$$

where μ is the cosine of the forward scattering angle and δ_D denotes the Dirac delta distribution. Also, $I_{obj}(u,v)$ reduces to $I_{obj}^*(u,v)$ and the dependence of R_{PT} on I_{obj} is removed thereby resulting in linearity.

Two general classes of methods exist for overcoming the problem of image degradation by scattered radiation. The first of these involves reducing the formation of scattering by restricting the incident beam cross-sectional area through the application of cones, diaphragms and masks. The second class is based on the prevention of scattered radiation from reaching the film. This is accomplished primarily by the insertion of antiscatter (Potter-Bucky, Lysholm) grids (3) between the object and the recorder. Other methods involve the insertion of energy selective filters at some point between the radiation source and the film, and increasing the object-to-film distance. Discussions of the above methods for scattering suppression in industrial and medical radiography are found in reference 3.

In neutron radiography, antiscatter grids are often used to suppress object scatter (78, 79). Unfortunately, these grids also degrade the ideal ray image; this is manifested by a superimposition of the grid pattern onto the resulting image. This problem can be overcome through motion of the grids with the commensurate increase in complexity of apparatus. Alternatively, high strip density (HSD) grids leave very little grid pattern due to the low value of the modulation transfer function at high spatial frequencies. These grids are often expensive, and furthermore, the use of antiscatter grids necessitates increased exposures.

Because of the drawbacks associated with antiscatter grids in neutron radiography, they have failed to achieve universal application. For this reason, it is useful to estimate the magnitude of object scattering whenever applicable. Such estimation might also be useful for situations in which antiscatter grids are employed, since it can be used to suggest a priori the approximate exposure required.

2.2 Model for Neutron Radiographic Object Scattering

As indicated in section 2.1, considerable research has been directed towards the study of neutral particle attenuation (76, 77, 80). A comprehensive compendium of existing methodologies is found in reference 76. In this section, a geometrically simplified one-group model of scattered radiation transport is presented which is specifically tailored to the problem of neutron transport in thermal neutron radiography. Given the collectively large effort that has centred on neutron penetration problems, it seems surprising that meaningful new descriptions can still be found. It appears that the following Neumann series solution of a governing integral transport equation and the subsequent developments, specialized to the particular material, geometrical and radiation combination under consideration, are original. The integral equation itself, however, is a specialization of the more general integral form of the Boltzmann transport equation (81, 82).

The model consists geometrically of a half-plane source of thermalized neutrons normally incident on an infinite homogeneous slab characterized by the one-group macroscopic absorption, scattering and total cross-sections Σ_a, Σ_s, Σ_t. The results will thus be applicable to the inspection of the central portion of a relatively spatially constant object by thermal neutron radiography.

In the terminology of section 2.1, this assumption of spatial constancy corresponds to linearizing the imaging system through the assumption of isoplanation. Specifically, a shift invariant PSF can be constructed to model the various image degradation sources, including object scatter.

The object is delineated by the object plane Cartesian coordinates (u,v) and by an orthogonal coordinate w, parallel to the radiographic axis, such that the slab lies in $w\in[0,w^*]$ with an incident neutron intensity of I_0 at $w=0$. The object geometry and other spatial parameters are illustrated in Fig. 2.1.

At any point P = (u,v,w) inside or outside the object, the intensity can be written as the sum of a collimated (or uncollided) term and a scattering term, as follows:

$$I(P) = I^*(P) + \int_{\text{all } P'} I(P')\Sigma_s(P')K(P',P)\,dP' . \tag{2-13}$$

Here, $I^*(P)$ is the collimated term, given generally by

$$I^*(P) = \begin{cases} I_0, & w \le 0 \\ I_0 \exp\left[-\int_0^w \Sigma_t(u,v,t)dt\right], & w\in[0,w^*] \\ I_0 \exp\left[-\int_0^{w^*} \Sigma_t(u,v,t)dt\right], & w \ge w^*. \end{cases} \tag{2-14}$$

The second term in Eq. (2-13) describes the intensity contribution from scattered neutrons at all other slab points P' = (r,s,t). The scattering point source diffusion kernel K(P' P) describes the fraction of neutrons scattered at P' that travel directly to P, that is,

without any further interaction. Note that scattering of all orders is accounted for here. For instance, neutrons that scatter at P′ and then proceed to reach P indirectly through possibly multiple other scatterings are accounted for as being neutrons that arrive directly at P from the last centre at which they scattered. This subtlety is elucidated later in section 2.3.

Equation (2-13) is a Fredholm integral equation of the second kind (83), written in a usual form for integral transport equations (84). It is essentially a specialization of the general integral form of the Boltzmann transport equation to slab geometry with the planar surface source distributed to give a source term of $I^*(P)$. Equation (2-13) is also similar in form to "Peierl's Equation" (82) from the field of electromagnetic radiation hydrodynamics, see section 7.1.

For isotropic scatter, such as is typically valid for the scattering of thermal neutrons in nonhydrogenous media, $K(P',P)$ is the following combination of exponential material attenuation and geometric "$1/r^2$" (spherical divergence) attenuation:

$$K(P',P) = \frac{\exp[-\Sigma_t(P')\alpha(P',P)|P'-P|]}{4\pi|P'-P|^2}. \tag{2-15}$$

Here, $\alpha(P',P)$ is an additional geometric variable representing the distance from P′ to the slab boundary B that possibly separates P′ and P, and is given by

$$\alpha(P',P) = \frac{|B-t|}{|w-t|}, \tag{2-16}$$

where
$$B = \begin{cases} 0, & w \le 0 \\ w, & w \in [0,w^*] \\ w^*, & w \ge w^*. \end{cases} \tag{2-17}$$

Also, the scattering cross-section Σ_s vanishes outside of the slab. Equation (2-15) is frequently referred to as the "ray approximation" (76) since, in some contexts, it involves an approximation to account for multiple scattering. In these calculations, however, multiple scatterings will be treated precisely.

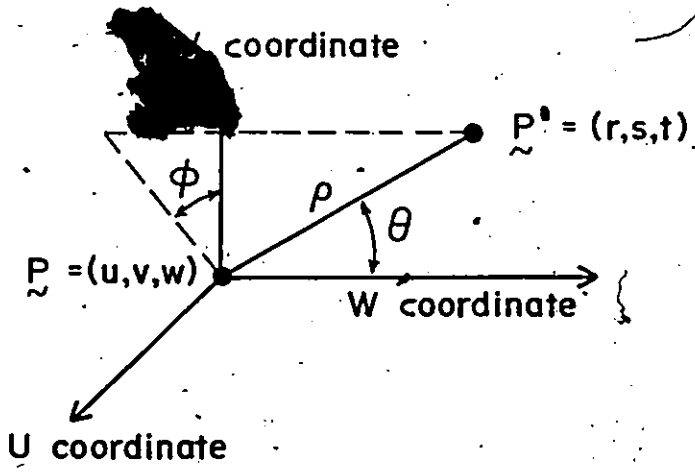

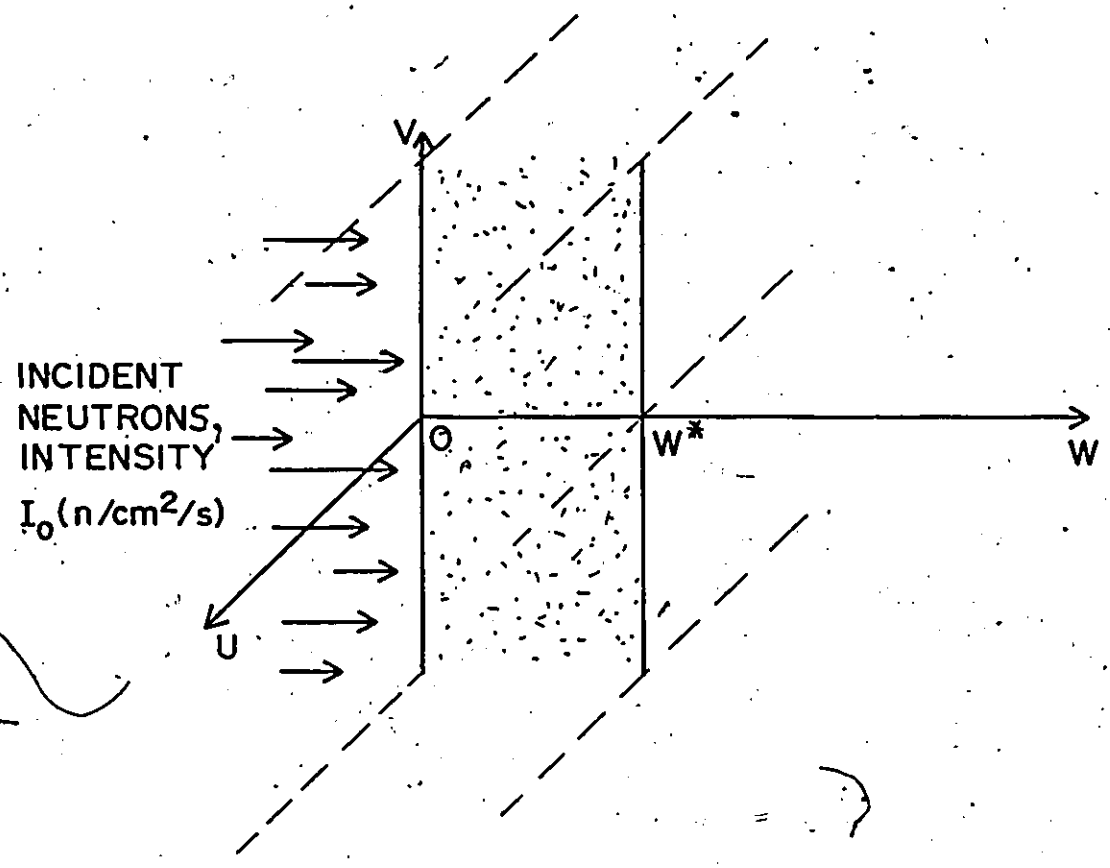

Fig. 2.1: Object slab geometry, coordinate systems and spatial parameters for the model of section 2.2.

For a homogeneous slab, one expects a solution in the form

$$I(P) = I(w) \tag{2-18}$$

so that the governing equation of transport, Eq. (2-13), becomes

$$I(w) = I^*(w) + \Sigma_s \int_0^{w^*} I(t)\, f(t,w)\, dt \tag{2-19}$$

where

$$f(t,w) = \int_{-\infty}^{+\infty} \int_{-\infty}^{+\infty} K(r-u, s-v, t-w, \alpha(t,w))\, d(r-u)\, d(s-v). \tag{2-20}$$

It is quite cumbersome and difficult to make any useful analytical progress on Eq. (2-19) due to the nature of the scattering kernel. Rather, a solution is facilitated by switching to spherical polar coordinates, defined here implicitly by connecting P and P′ as follows:

$$\begin{aligned} r &= u + \rho \sin\phi \sin\theta, \\ s &= v + \rho \cos\phi \sin\theta, \\ t &= w + \rho \cos\theta. \end{aligned} \tag{2-21}$$

These coordinates are also illustrated in Fig. 2.1. For w inside the slab, Eq. (2-19) transforms (see section A.8) to

$$I_{in}(w) = I_o \exp[-\Sigma_t w] + \frac{\Sigma_s}{2} \left\{ \int_0^1 \int_0^{(w^*-w)/\mu} I_{in}(w+\rho\mu) \exp[-\Sigma_t \rho] d\rho d\mu + \right.$$

$$\left. \int_{-1}^0 \int_0^{-w/\mu} I_{in}(w+\rho\mu) \exp[-\Sigma_t \rho] d\rho d\mu \right\} \tag{2-22}$$

where $\mu = \cos(\theta)$. The emergent neutron intensity, for $w > w^*$, is likewise (see section A.8)

$$I_{out}(w) = I_o \exp[-\Sigma_t w^*] + \frac{\Sigma_s}{2} \int_{-1}^0 \int_{\frac{w^*-w}{\mu}}^{-w/\mu} I_{in}(w+\rho\mu) \exp\left[\frac{\Sigma_t}{\mu} (w^* - w - \rho\mu) \right] d\rho d\mu. \tag{2-23}$$

Equation (2-22) is similar, although far from identical, in form to the planar integral transport expression given by Eq. (3-136) in reference 81. The dimensionless attenuation product $\Sigma_t \rho$ is referred to as the "optical distance" between the points that it separates. Upon transformation from ρ to γ, where

$$\gamma = \rho - \left(\frac{w^* - w}{\mu} \right), \tag{2-24}$$

Eq. (2-23) reduces to $I_{in}(w^*)$. In short,

$$I_{out}(w) = I_{in}(w^*), \quad w \geq w^*$$

$$= \text{constant}, \quad w \geq w^*. \tag{2-25}$$

This is expected on physical grounds since there are no neutron removal processes outside the object. Similarly,

$$I_{out}(w) = I_{in}(0), \quad w \leq 0. \tag{2-26}$$

Thus, the neutron intensity at any w in the system is determined strictly by the solution to Eq. (2-22). The approach adopted here to solve Eq. (2-22) is seminumerical, with the indicated point kernel integration accomplished through the development of an iterative series solution in which the complexity of the modes necessitates numerical evaluations for all but the first two modes.

The application of Neumann series (83) in the solution of integral transport equations similar to Eq. (2-13) is well known. The modal expansion described here is a Neumann series with the appealing property that each mode has a direct physical interpretation. One initiates the iterative solution by substituting the initial estimate

$$I_{in}^{(0)}(w) = I_o \exp[-\Sigma_t w] \tag{2-27}$$

into the RHS of Eq. (2-22), which then solves directly to yield $I_{in}^{(1)}(w)$. This estimate is then similarly used to generate $I_{in}^{(2)}(w)$, and so on. Only the first two modes can be expressed in a reasonably compact analytical form; these are $I_{in}^{(0)}(w)$ as in Eq. (2-27) and

$$I_{in}^{(1)}(w) = I_{in}^{(0)}(w) \left\{ 1 + \left(\frac{\Sigma_s}{2} \right) f_1(w; \Sigma_t, w^*) \right\}, \tag{2-28}$$

where

$$f_1(w; \Sigma_t, w^*) = \frac{1}{\Sigma_t} \left\{ \begin{array}{l} \ell n\,|2\Sigma_t w| - Ei[-2\Sigma_t(w^* - w)] - \exp[\Sigma_t w] Ei[-\Sigma_t w] \\ + C + \exp[-\Sigma_t(w^* - w)] Ei[-\Sigma_t(w^* - w)] \end{array} \right\}. \tag{2-29}$$

Here, Ei and C denote the exponential integral (85) and Euler's constant (85) respectively. The complete solution is

$$I_{in}(w) = I_o \exp[-\Sigma_t w] \sum_{i=0}^{\infty} \lambda^i f_i(w; \Sigma_t, w^*) \tag{2-30}$$

where the f_i obey the recurrence relation

$$f_i(w; \Sigma_t, w^*) = \begin{cases} \int_{-1}^{0} \int_{0}^{-w/\mu} \exp[-\rho\Sigma_t(1+\mu)] f_{i-1}(w+\rho\mu; \Sigma_t, w^*) d\rho d\mu \\ + \int_{0}^{1} \int_{0}^{(w^*-w)/\mu} \exp[-\rho\Sigma_t(1+\mu)] f_{i-1}(w+\rho\mu; \Sigma_t, w^*) d\rho d\mu . \end{cases} \tag{2-31}$$

Also, $\lambda = \Sigma_s/2$ and

$$f_o(w; \Sigma_t, w^*) = 1 : \tag{2-32}$$

Unlike similar slab source point kernel integrations used in shielding calculations (76), the point diffusion kernel being integrated here is multiplied by a changing source intensity distribution prior to integration at each iteration.

It is instructive at this point to recognize that "neutron intensity" corresponds to the "neutron scalar flux" to be introduced formally in Chapter 3. Basically, the neutron scalar flux represents, at a point, the total rate at which neutrons pass through a unit-area centered on that point regardless of the orientation of the area. In this sense, a total rate implies summation over all such unit areas.

Another useful neutron population indicator is the neutron current, a vector quantity describing the net rate at which neutrons pass through a particular surface oriented in a specific direction. For the one-dimensional neutron population studied in this section, the neutron current will always be directed through a unit surface dS in the u-v, or object, plane. In this case, the useful current based intensity to calculate is the forward partial neutron current, defined as the total rate at which neutrons pass through dS from left to right. A formal definition of the partial current is also given in Chapter 3. Since the integrated scattering neutron contributions that constitute the integral in Eq. (2-13) must ultimately

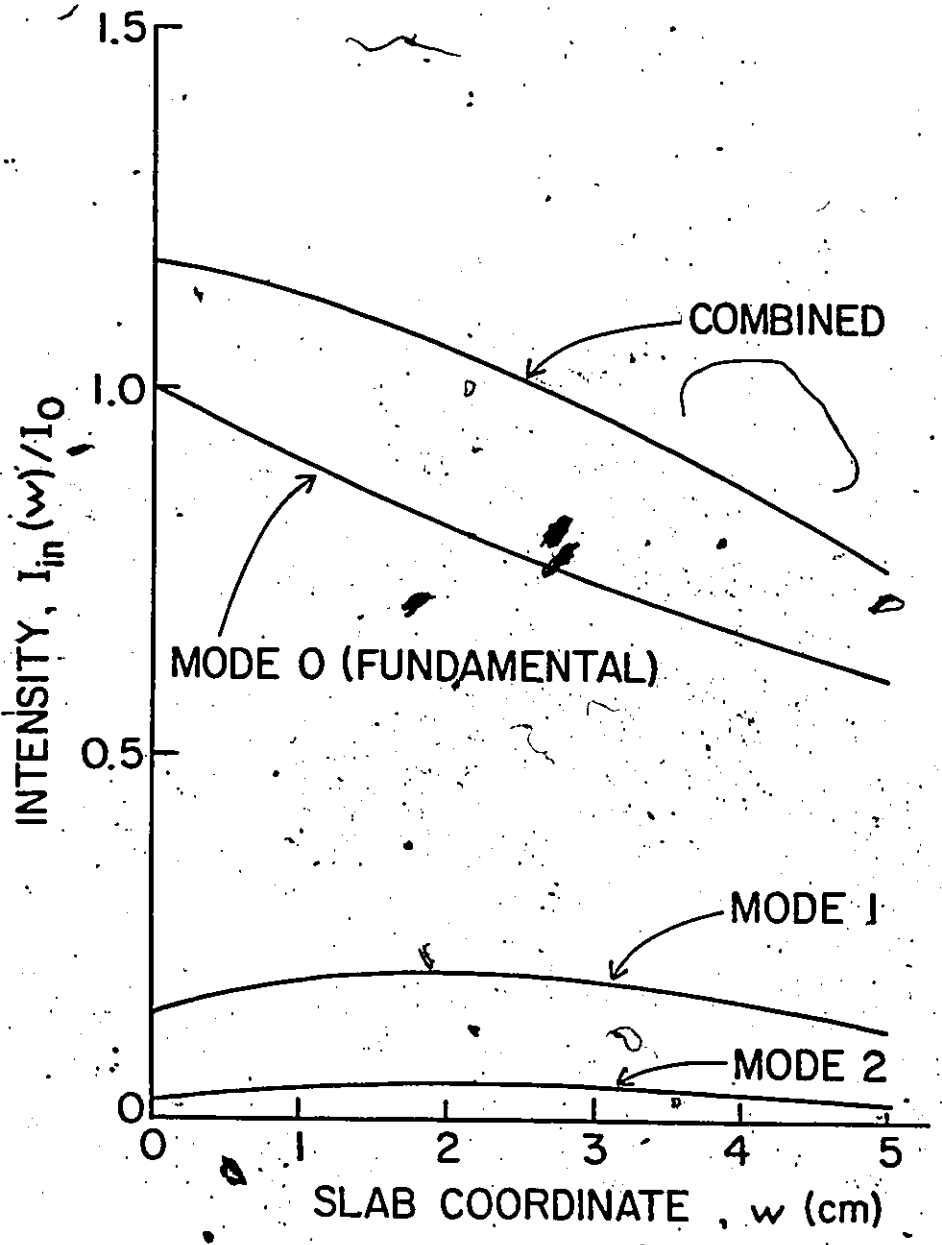

Fig. 2.2: Neutron scalar flux calculation for a slab with $\Sigma_t = 0.1\ cm^{-1}$, $\Sigma_s = 0.05\ cm^{-1}$ and $w^* = 5.0$ cm.

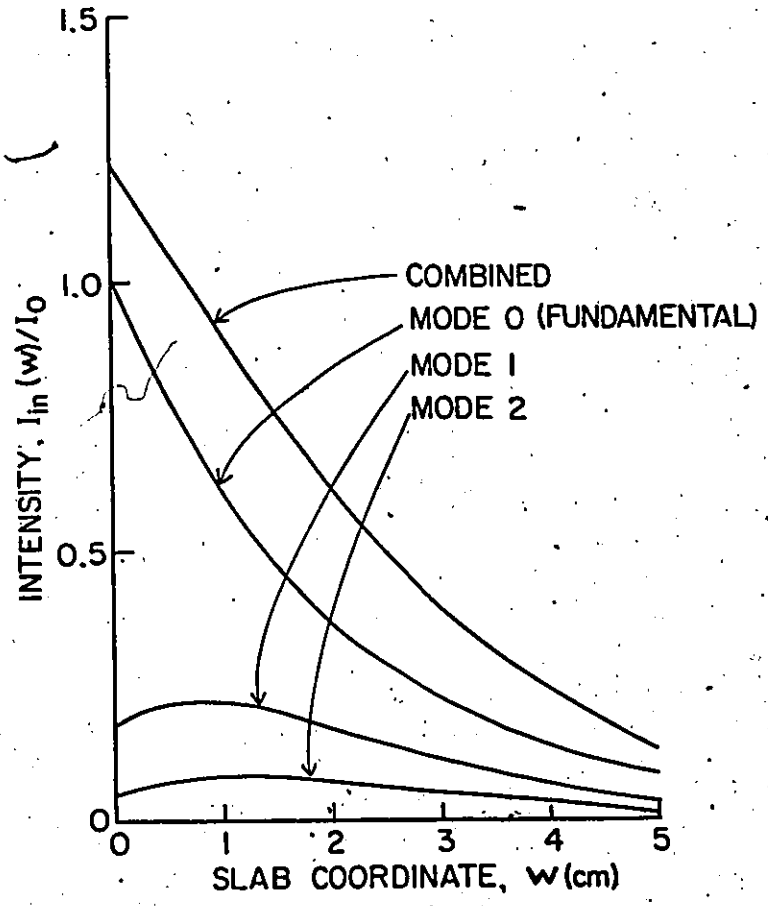

Fig. 2.3: Neutron scalar flux calculation for a slab with $\Sigma_t = 0.5\ cm^{-1}$, $\Sigma_s = 0.25\ cm^{-1}$ and $w^* = 5.0$ cm.

pass through dS at P to be counted in the population at P, only the fraction $|\mu| = |\cos(\theta)|$ of scattered neutrons normally incident on a given unit area at P, with incident direction cosine μ, would pass through dS. This factor accounts for the geometric configuration of dS and the various elemental areas whose normal vectors are in the incidence direction.

Mathematically, the point source diffusion kernel must be multiplied by a factor of μ for such a calculation. The resulting solution, similar in form to the scalar flux solution in Eq. (2-30), is

$$I_{in}\text{current}(w) = I_o \exp[-\Sigma_t w] \sum_{i=0}^{\infty} \lambda^i \, g_i(w; \Sigma_t, w^*), \tag{2-33}$$

where the g_i obey the recurrence relation

$$g_i(w; \Sigma_t, w^*) = \begin{cases} \displaystyle\int_{-1}^{0} \int_{0}^{-w/\mu} \exp[-\rho\Sigma_t(1+\mu)]\, g_{i-1}(w+\rho\mu)(-\mu)\, d\rho d\mu \\ \displaystyle + \int_{0}^{1} \int_{0}^{(w^*-w)/\mu} \exp[-\rho\Sigma_t(1+\mu)]\, g_{i-1}(w+\rho\mu)\, \mu\, d\rho d\mu, \end{cases} \tag{2-34}$$

and

$$g_o(w; \Sigma_t, w^*) = 1. \tag{2-35}$$

While the scalar flux, Eq. (2-30), will be used as the intensity indicator for calculations in this chapter, the forward partial current, Eq. (2-34) will be useful for checking calculations in subsequent chapters.

2.3 Solution Properties

This particular Neumann series, Eq. (2-30), is useful in illustrating the role and inclusion of multiple scatterings in the formulation. Referring to $I_{in}^{(0)}(w)$ as the "exponential solution", it is seen that $I_{in}^{(1)}(w)$ is the sum of the exponential solution and that portion of the exponential solution which scatters and passes through w directly with no other interaction. That is, $I_{in}^{(1)}(w)$ includes zeroth and first order scattering. Likewise, $I_{in}^{(2)}(w)$ is the sum of

$I_{in}^{(1)}(w)$ and all direct uncollided scatter from $I_{in}^{(1)}(w)$, thereby representing zeroth, first and second order scattering. By induction, $I_{in}^{(n)}(w)$ includes scattering up to n orders.

The series solutions in Eqs. (2-13) and (2-33) therefore alleviate the need for multiplication of the point kernel by an artifical or empirical "build-up" factor, to be defined later in this section. Such alteration of the kernel is common to ray approximation calculations in which the effects of multiple scatterings are being estimated.

Normalized solution calculations are given in Figs. 2.2 and 2.3. Since each mode requires the evaluation of a double iterated integral, computation has been limited to the first three modes, enabling restriction of the relative error in each mode to 10^{-5}. A listing of the FORTRAN program CALKERN, written to perform the above modal calculations, is included in Appendix D.

In general, the magnitude of the modes decreases rapidly with the order suggesting convergence of the series solution for these parameters. In each case the fundamental mode, that is the "exponential solution", is bolstered by unimodal secondary modes consistent with the expectation that the scattered population should peak internally. Note also that in Fig. 2.3, the scattering population peaks closer to the incidence boundary than in Fig. 2.1, consistent with the larger total cross-section used in the computations.

Results of radiation scattering studies are conventionally reported in the form of "build-up" factors (2), defined at any point as the ratio of total radiation to collimated radiation. For the problem at hand, the solution in Eq. (2-30) can be written as

$$I_{in}(w) = I_o B(w) \exp[-\Sigma_t w] \tag{2-36}$$

where the build-up factor, B(w), is

$$B(w) = \sum_{i=0}^{\infty} \lambda^i f_i(w; \Sigma_t, w^*). \tag{2-37}$$

Clearly, B(w) is constant outside the object. The build-up factor has been plotted in Fig. 2.4 for several macroscopic cross-sections; note that B(w) is unimodal and peaks inside the slab. This is consistent with the observation that the scattering contribution is reduced at the slab boundaries relative to its magnitude in the slab center, since at the boundaries, scattered neutrons arrive from only a half-plane of directions. From Eq. (2-29) and Eq. (2-37), an approximation to B(0) including first order scattering is given simply by

$$B(0) \approx 1 + \frac{\Sigma_s}{2\Sigma_t} \tag{2-38}$$

In light of Eq. (2-22) B(w) can also be written as

$$B(w,\Sigma_t,w^*) = 1 + \left(\frac{\exp[\Sigma_t w]}{I_0}\right)\left(\frac{\Sigma_s}{2}\right)\left\{\int_0^1\int_0^{(w^*-w)/\mu} I_{in}(w+\rho\mu)\exp[-\Sigma_t\rho]d\rho d\mu \right.$$

$$\left. + \int_{-1}^{0}\int_{0}^{-w/\mu} I_{in}(w+\rho\mu)\exp[-\Sigma_t\rho]d\rho d\mu\right\} \tag{2-39}$$

where the intensity dependence on the parameters Σ_t, w^* is now explicitly functionally included by expanding B(w) to $B(w,\Sigma_t,w^*)$. Upon partial differentiation of Eq. (2-39) through application of Leibnitz' Rule one obtains

$$\frac{\partial B}{\partial w^*} = \left(\frac{\Sigma_s}{2}\right)\exp[\Sigma_t w^*]\left(\frac{I(w^*)}{I_0}\right)\{\Sigma_t(w^*-w)\,Ei[-\Sigma_t(w^*-w)] + \exp[-\Sigma_t(w^*-w)]\}$$

$$\geq 0, \tag{2-40}$$

equality holding when $\Sigma_s = \Sigma_t = 0$, designated here as the trivial case. The important implication of Eq. (2-40) is that increasing the slab thickness always increases the build-up factor. Since B(w) decreases as $w \rightarrow w^*$ from inside the slab, it may be thought that the appendage of some additional absorbing layer onto the right side of the slab could serve to decrease B(w) still further thereby enhancing the radiographic contrast. Eq. (2-40) implies, however, that this procedure will be ineffective if the additional layer is of the same composition as the slab itself. An interesting extension here arises from the possibility that

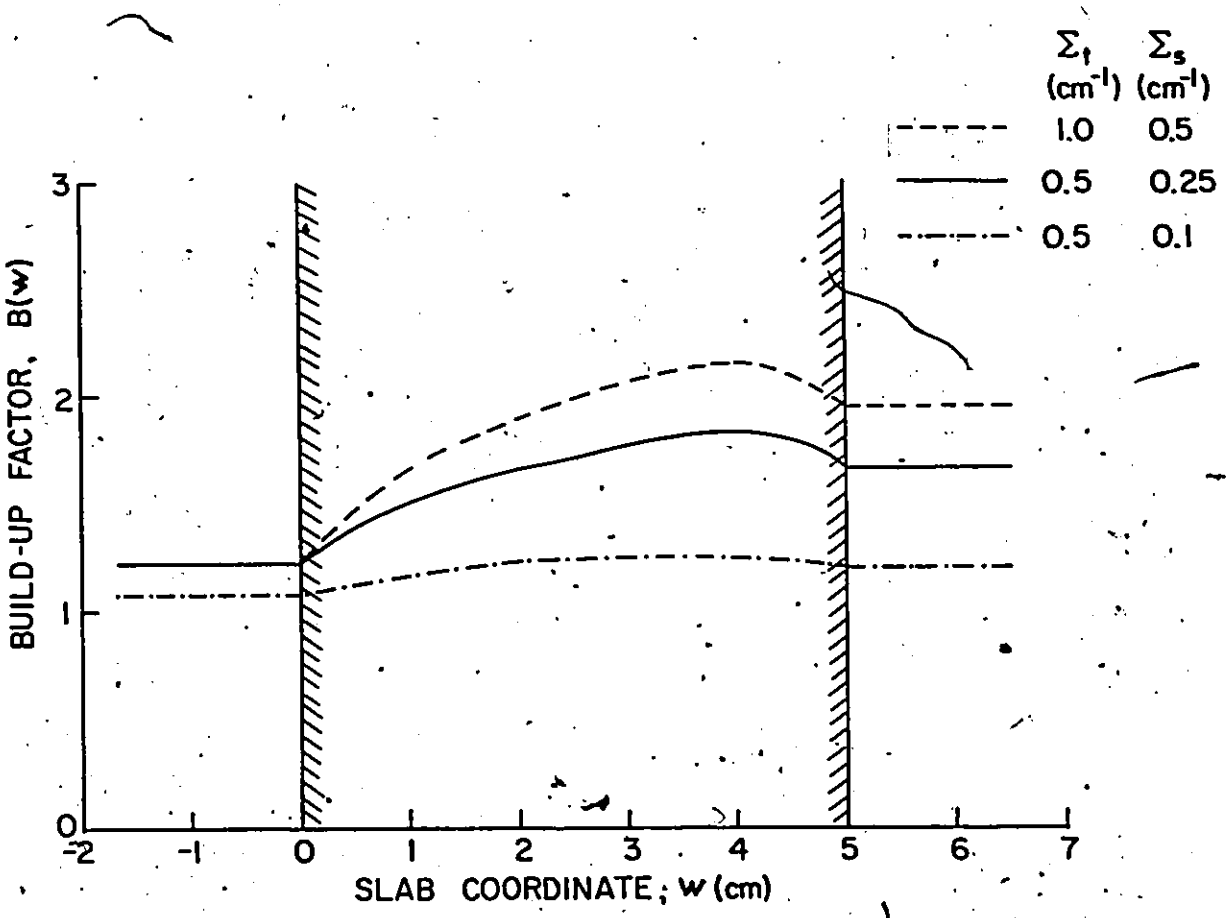

Fig. 2.4: Neutron scalar flux-based build-up factor for a slab with $w^* = 5.0$ cm and several cross-section combinations.

the appendage layer may reduce the emergent build-up factor if it is nonscattering and uniformly absorbing since the oblique angles at which scattered neutrons impinge on the appendage imply increased absorption relative to the normally incident neutrons. In effect, this describes an antiscatter device that leaves no grid markings. A similar preferential absorption principle is frequently employed in industrial x-ray radiography through the absorption of scattered radiation by lead filters (3). For this application, the preferential absorption is energy based.

For each computation, it has been found that

$$B(w^*) \geq B(0), \tag{2-41}$$

with the equality holding only for the trivial case. This intuitive result corresponds to the inequality

$$I_{in}(w^*) \geq I_{in}(0) \exp[-\Sigma_t w^*]. \tag{2-42}$$

Equality in Eq. (2-42) holds when $\Sigma_s = 0$ and the inequality is evident from the physics of the situation when $\Sigma_s > 0$. Also, for any $\Sigma_s > 0$, the intensity initially rises with distance into the slab if only for a small but finite distance. This is seen by first noting from Eq. (2-22) that for first order scattering

$$\left.\frac{dI_{in}}{dw}\right|_{w=0} = -\Sigma_t I_0\left(1+\left(\frac{\Sigma_s}{2}\right)\int_0^1\int_0^{w^*/\mu} \exp[-\Sigma_t\rho(1+\mu)]\,d\rho d\mu\right)$$

$$-\left(\frac{\Sigma_s}{2}\right) I_{in}(w^*)\int_0^1 \frac{\exp[-\Sigma_t w^*/\mu]}{\mu}\,d\mu - \left(\frac{\Sigma_s}{2}\right) I_{in}(0)\int_{-1}^{0}\frac{d\mu}{\mu} \tag{2-43}$$

Each term in Eq. (2-43) is finite except the last term, which is infinitely large and positive. Thus,

$$\lim_{w\to 0}\frac{dI_{in}}{dw} = +\infty - \tag{2-44}$$

explaining the initial intensity increase. Note that this increase can be nontrivial. For instance, when $\Sigma_s = \Sigma_t = 0.1\ cm^{-1}$, I(w) rises for the first 1.0 cm of a 5.0 cm thick slab. The

increase in I(w) is, however, limited to the first half of the slab. This is recognized by noting that for $\delta \in (0, w^*/2]$ we have $I_{in}(w^*/2 - \delta) > I_{in}(w^*/2 + \delta)$. To prove this from Eq. (2-22), we proceed as follows:

$$I_{in}\left(\frac{w^*}{2}-\delta\right)-I_{in}\left(\frac{w^*}{2}+\delta\right)=\left(I_o\exp\left[-\Sigma_t\left(\frac{w^*}{2}-\delta\right)\right]+\left(\frac{\Sigma_s}{2}\right)\int_0^1\int_0^{\left(\frac{w^*}{2}+\delta\right)/\mu}\right.$$

$$I\left(\frac{w^*}{2}-\delta+\rho\mu\right)\exp[-\Sigma_t\rho]\,d\rho d\mu+\left(\frac{\Sigma_s}{2}\right)\int_{-1}^0\int_0^{-\left(\frac{w^*}{2}+\delta\right)/\mu}$$

$$\left.I\left(\frac{w^*}{2}-\delta+\rho\mu\right)\exp[-\Sigma_t\rho]\,d\rho d\mu\right)-\left(I_o\exp\left[-\Sigma_t\left(\frac{w^*}{2}+\delta\right)\right]\right.$$

$$\left.+\left(\frac{\Sigma_s}{2}\right)\int_0^1\int_0^{\left(\frac{w^*}{2}-\delta\right)/\mu}I\left(\frac{w^*}{2}+\delta+\rho\mu\right)\exp[-\Sigma_t\rho]\,d\rho d\mu\right.$$

$$\left.+\left(\frac{\Sigma_s}{2}\right)\int_0^1\int_0^{-\left(\frac{w^*}{2}+\delta\right)/\mu}I\left(\frac{w^*}{2}+\delta+\rho\mu\right)\exp[-\Sigma_t\rho]\,d\rho d\mu\right)$$

$$=(A+B+C)-(D+E+F),\ \text{say.} \tag{2-45}$$

Clearly, A > D. Transforming the integration variable u to s = -u in terms B and C, and to s = u in terms E and F, one obtains

$$B-F=\int_{-1}^0\int_0^{-\left(\frac{w^*}{2}+\delta\right)/s}\left[I\left(\frac{w^*}{2}-\delta-\rho s\right)-I\left(\frac{w^*}{2}+\delta+\rho s\right)\right]\exp[-\Sigma_t\rho]\,d\rho ds \tag{2-46}$$

and

$$C-E=\int_0^1\int_0^{\left(\frac{w^*}{2}-\delta\right)/s}\left[I\left(\frac{w^*}{2}-\delta-\rho s\right)-I\left(\frac{w^*}{2}+\delta+\rho s\right)\right]\exp[-\Sigma_t\rho]\,d\rho ds. \tag{2-47}$$

Substituting the exponential zeroth order solution, $I_{in}^{(0)}(w)$, from Eq. (2-27) into Eqs. (2-46) and (2-47), the integrands are seen to be positive over the entire integration range in each case. As a result, B > F and C > E, which proves that the intensities including scattering up

to the first order obey the relationship

$$I_{in}^{(1)}\left(\frac{w^*}{2}-\delta\right) > I_{in}^{(1)}\left(\frac{w^*}{2}+\delta\right). \tag{2-48}$$

This property of $I_{in}^{(1)}(w)$ is sufficient to generate positive integrands in Eqs. (2-46) and (2-47) upon substitution, so that Eq. (2-48) also holds for $I_{in}^{(2)}(w)$. By mathematical induction, it follows that

$$I_{in}\left(\frac{w^*}{2}-\delta\right) > I_{in}\left(\frac{w^*}{2}+\delta\right), \tag{2-49}$$

proving that the initial intensity increase is limited to the first half of the slab. A secondary result arising from Eq. (2-49) is that $I(0) > I(w^*)$ for all Σ_s, Σ_t. Note that the above proof assumes convergence of the $I^{(n)}(w)$, which will be discussed in the next section. Combining this result with Eq. (2-41), the build-up factors at the slab faces are related by the following inequality:

$$B(w^*)\exp[-\Sigma_t w^*] < B(0) \leq B(w^*). \tag{2-50}$$

Finally, the forward partial current calculation given in Eq. (2-33) has also been performed for a particular slab object. The results, including a comparison with the corresponding scalar flux calculation, are presented in Figs. 2.5 and 2.6.

As expected, the forward partial current scattered neutron modes are smaller than those for the scalar flux. Except in regions where the angular neutron intensity distribution, section 2.1, corresponding to the angular neutron flux to be defined in Chapter 3, is highly anisotropic, such as near the slab boundaries, the n^{th} $(n>1)$ forward partial current mode can be expected to be smaller than half the corresponding scalar flux mode.

In Fig. 2.6, the build-up factor evaluation is shown to possess strong dependence on the particular intensity being calculated. This reaffirms the need for clarification of the word "intensity" when various build-up factor values are being compared. Note that both build-up factor curves possess the property of unimodality.

2.4 Solution Convergence

In light of the intrinsic subcriticality of this physical model in which neutrons scatter and are absorbed in a nonmultiplying medium, a given incident neutron will undergo at most a finite number of scatterings in the slab object, reference 84, pp. 85-96;. thus, the series solution can be expected to converge. In search of a proof, however, the most general convergence criterion here established is a guarantee of convergence when

$$f_1 < \frac{1}{\lambda}. \tag{2-51}$$

In this case, it can be shown by mathematical induction that

$$\frac{\lambda f_{n+1}}{f_n} < 1 \tag{2-52}$$

for all orders n. By the ratio test, the series solution, Eq. (2-30), converges. Through differentiation, it can also be shown that for a given Σ_t and w*, $f_1(w; \Sigma_t, w^*)$ peaks for w such that

$$\mathrm{Ei}[-\Sigma_t w] = \exp[-\Sigma_t w^*]\,\mathrm{Ei}[-\Sigma_t(w^* - w)]. \tag{2-53}$$

Denoting this maximum value by $f_{1,max}$, Eq. (2-51) reduces to the requirement:

$$f_{1,max} < \frac{1}{\lambda}. \tag{2-54}$$

Fig. 2.7 suggests the convergence of the series solution developed in this chapter to the fairly accurate neutron transport theory DP_1 solution, Chapter 3.

The correctness of the calculation presented in section 2.2 can be partially verified through a comparison of solutions with the standard analytical shielding calculation given by Goussev, Kovalev and Foderaro, reference 76, section 6.6.5.2. Their calculations give the radiation flux at a point P outside of and due to an infinite slab source of thickness h with attenuation constant μ_s, as shown in Fig. 2.8. The intensity distribution of their slab source is

$$S_V(x) = S_{V_0} \exp[\alpha x], \tag{2-55}$$

identifying their variables and source parameter with the first order scattering source used in this text as follows:

$$S_{V_0} \exp[\alpha x] \equiv \Sigma_s I_o \exp[-\Sigma_t w]. \tag{2-56}$$

Also, their parameters μ_s and h correspond to Σ_t and w^* used in this text.

For the case in which P is located on the planar slab boundary, the parameters b_1 and a vanish. Through cylindrical coordinate integration of a point diffusion kernel, they arrive at the following final expression, involving the exponential integral, for the radiation flux at point P:

$$\phi(P) = \frac{S_{V_0}}{2\mu_s} \int_0^{\mu_s h} E_1(z) \exp[-z]\, dz, \tag{2-57}$$

where

$$E_1(z) = -Ei(-z). \tag{2-58}$$

From a comparison of the geometries in Figs. 2.1 and 2.8, it is clear that the flux in Eq. (2-57) should correspond to $I_{in}^{(1)}(0) - I_{in}^{(0)}(0)$, representing the total intensity of first order scattered neutrons reaching any point on the planar boundary at w=0. From Eqs. (2-27), (2-28) and (2-29), one obtains

$$I_{in}^{(1)}(0) - I_{in}^{(0)}(0) = I_{in}^{(0)}(0)\left(\frac{\Sigma_s}{2}\right) f_1(0; \Sigma_t, w^*)$$

$$= I_o\left(\frac{\Sigma_s}{2\Sigma_t}\right)\left\{\begin{array}{l} \ell n(2) - Ei[-2\Sigma_t w^*] \\ + \exp[-\Sigma_t w^*]\, Ei[-\Sigma_t w^*] \end{array}\right\}. \tag{2-59}$$

Evaluation of Eq. (2-57) using a table of integrals (85) followed by a replacement of its symbols with the corresponding symbols from this text yields identification of Eq. (2-57) with Eq. (2-59). The first mode of the neutron scalar flux solution in Eq. (2-30) is therefore correct.

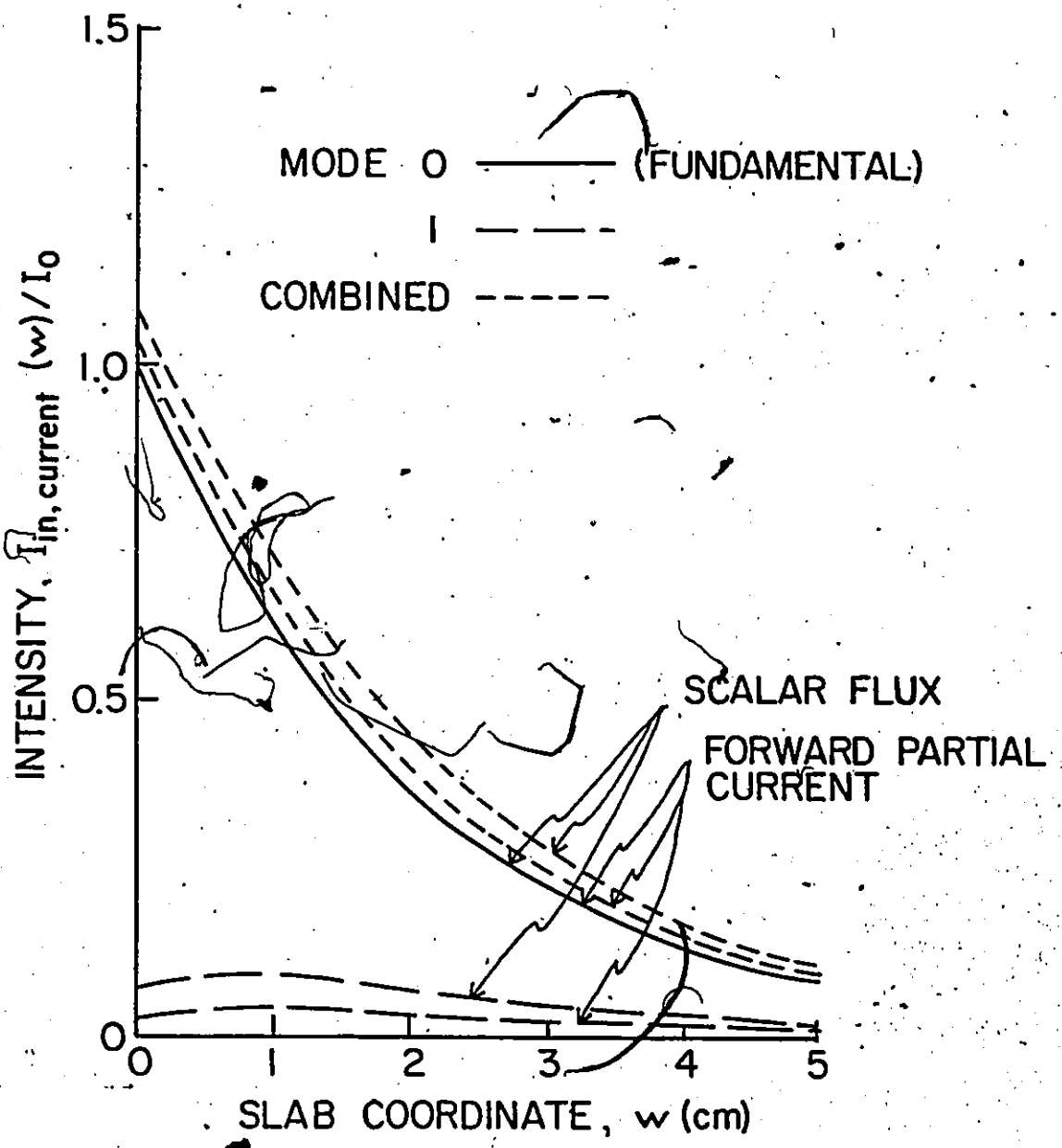

Fig. 2.5: Comparison of intensity calculations for a slab with $\Sigma_t = 0.5\ cm^{-1}$, $\Sigma_s = 0.1\ cm^{-1}$ and $w^* = 5.0$ cm.

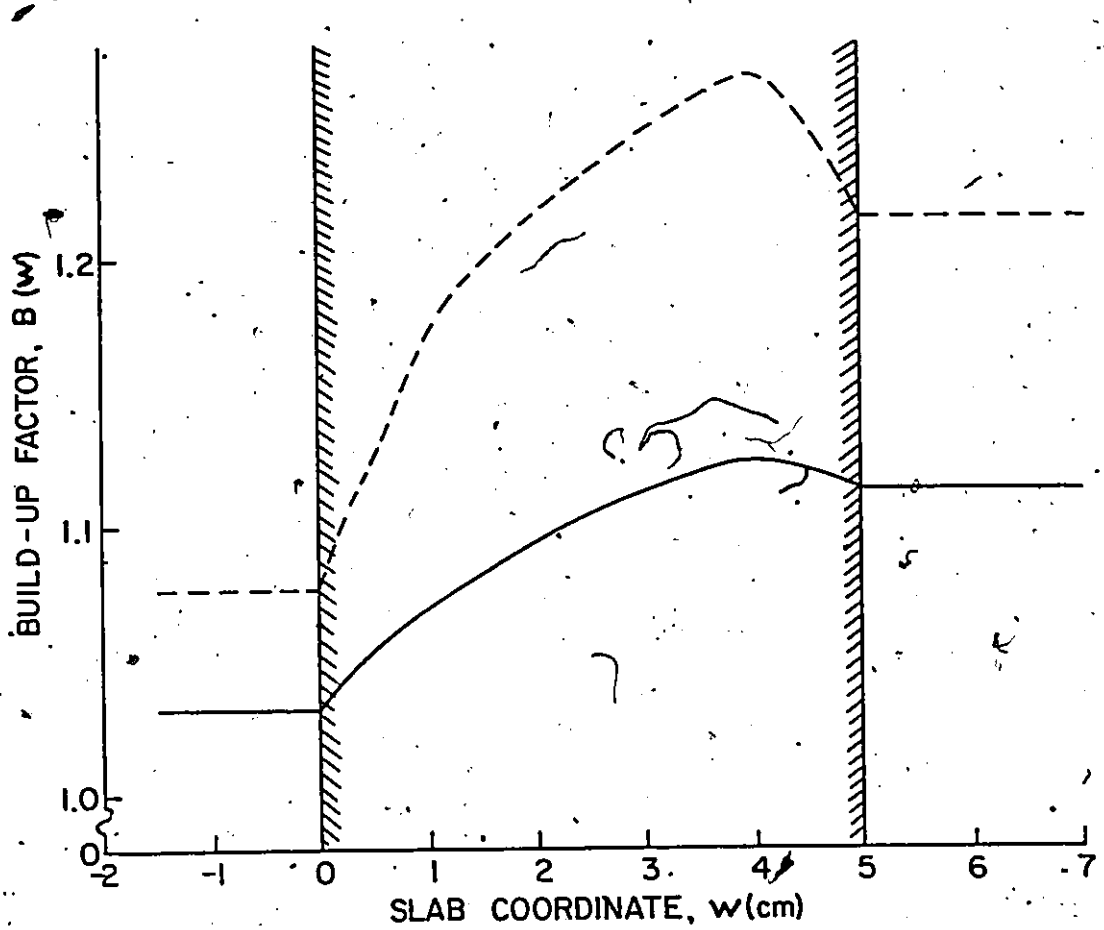

Fig. 2.6: Comparison of neutron scalar flux (---) and forward partial current (——) build-up factors for a slab with $\Sigma_t = 0.5\ cm^{-1}$, $\Sigma_s = 0.1\ cm^{-1}$ and $w^* = 5.0$ cm.

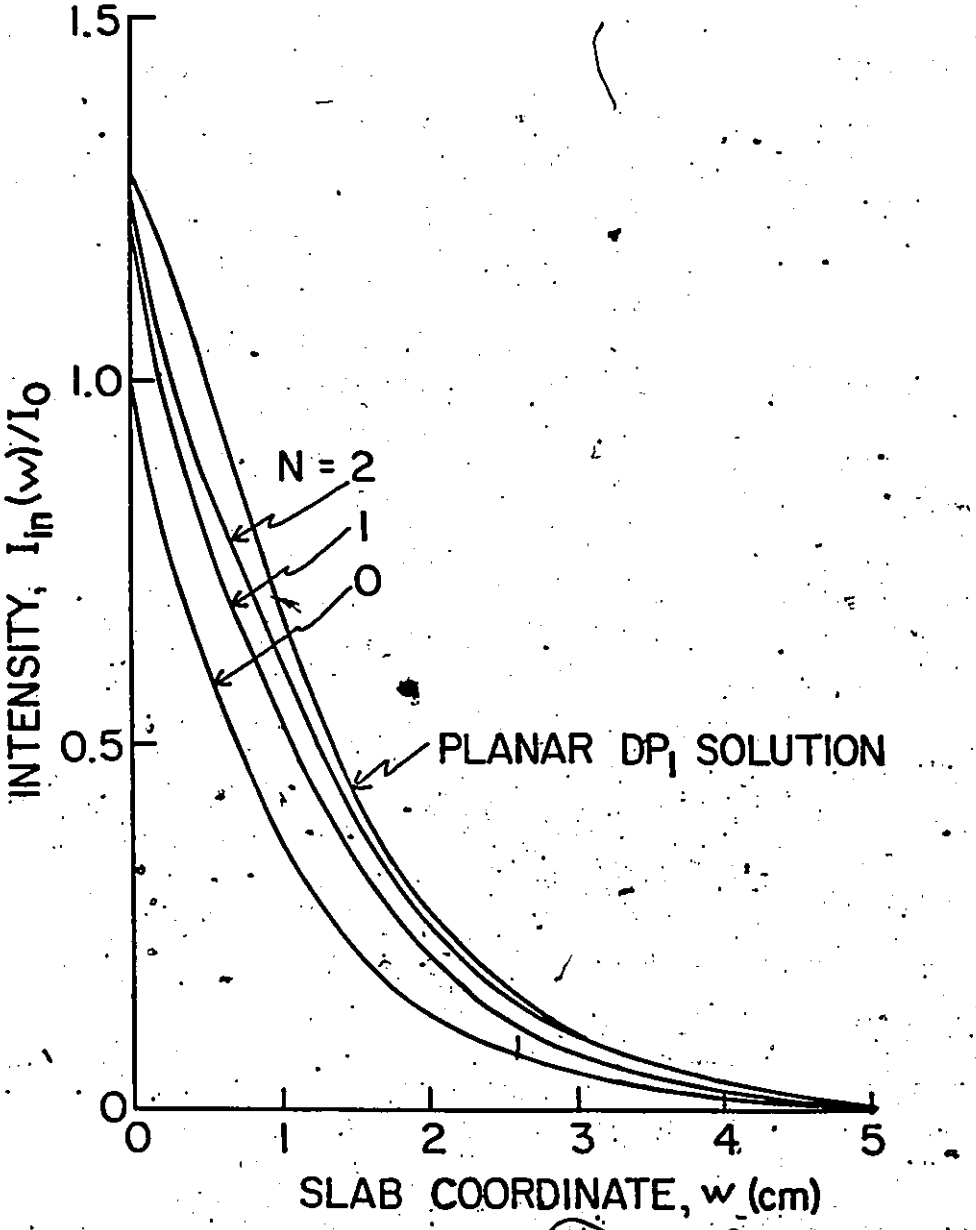

Fig. 2.7: Comparison of neutron scalar flux calculations for a slab with $\Sigma_t = 1.0\ cm^{-1}$, $\Sigma_s = 0.5\ cm^{-1}$ and $w^* = 5.0$ cm.

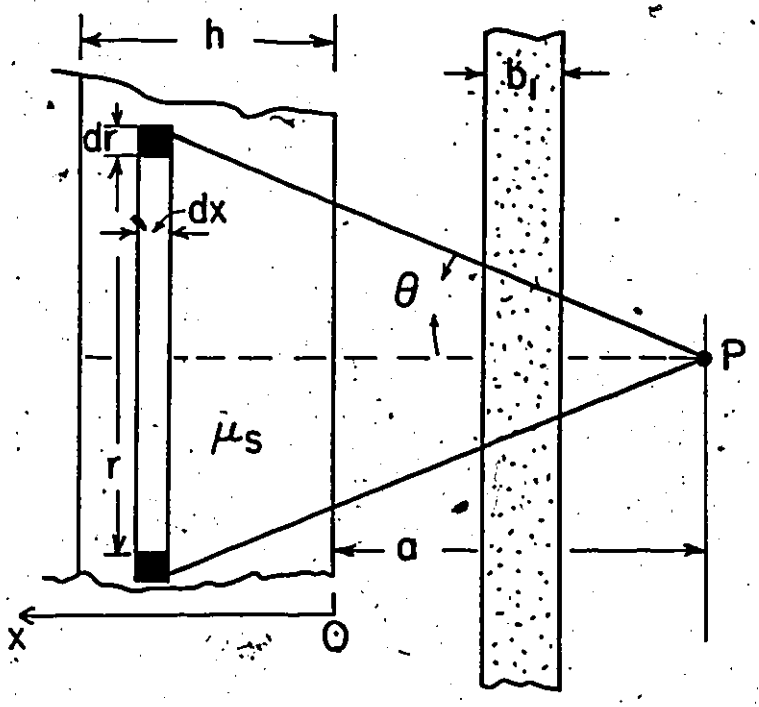

Fig. 2.8: Slab source geometry for the shielding calculation of Goussev et.al. (76). Source intensity distribution is $S_V(x) = S_{V_o} \exp[\alpha x]$.

CHAPTER 3

NEUTRON TRANSPORT ANALYSIS

3.1 Two-Dimensional Neutron Transport Formulation

A major shortcoming of the integral transport equation presented in Chapter 2 is its limited applicability to radiographed objects that are well describable by a one-dimensional analysis. In practice, such an object is likely to be the actual central portion of a larger, relatively spatially constant object, as discussed in section 2.2.

In general, not all inspected objects fit the above description, necessitating multi-dimensional analyses describing the neutron intensity at any point in or around the object. Indeed, if the infinite uniform slab in Chapter 2 has just one object plane dimension reduced to some finite value, then a two- dimensional analysis is required near those two boundaries and possibly near the slab center as well.

For all but the one-dimensional case analyzed in Chapter 2, the integral transport formulation of Eqs. (2-13) and (2-14) is of limited value in generating analytically specified solutions. This limitation arises because for a multidimensional analysis, each of the integrations generating successive Neumann series terms must be performed over three variables as opposed to two variables for the one-dimensional analysis. Furthermore, the integration limits become non-trivial, and each integration must be performed numerically.

The subject of this chapter then is the investigation of thermal neutron scattering in a radiographic context with the objective being the determination of the two-dimensional neutron intensity for purposes of estimation of the extent of scattering that can occur. Like Chapter 2, the approach here adopted involves the solution of a transport equation. However, the governing integro-differential equation for this analysis is Eulerian based and derived

from an accounting of sources and sinks in a general control volume of the object. The object boundaries therefore form no part of the governing equation as was the case for the integral equation in Chapter 2. This serves to render the governing equation more computationally tractable for multidimensional analyses than that of Chapter 2.

The inspected object to be analyzed in this chapter is illustrated in Fig. 3.1. Initially the object is homogeneous with rectangular geometry in the x-y plane and possessing negligible property variation in the transverse (z) direction. Such an object, while not the most general two-dimensional object imaginable, represents a starting point for multi-dimensional radiographic neutron transport analyses. Increased generality is accorded by monitoring the transport of neutrons through some narrow "band" of the object as depicted in Fig. 3.1. This partitioning of the object is based on the premise that any two-dimensional object can be approximated as a collection of such bands adjacently placed and of different lengths.

The validity of this partitioning is, from a neutron transport perspective, ensured by linearity of the neutron transport equation. Specifically, the transport of source neutrons incident on the face of a particular band is independent of the existence of all other source neutrons and their ultimate spatial distribution.

A brief derivation of the relevant governing neutron transport equation is now presented based on that given by Duderstadt and Hamilton (56). Define $n(\mathbf{r},E,\Omega,t)$ as the angular neutron population density describing the expected number of neutrons within the volume element d^3r of $\mathbf{r}$, possessing energies within dE of E, travelling in a direction $d\Omega$ about the unit vector Ω, at time t. The time rate of change of the total neutron population occupying an arbitrary control volume dV at any time t is then symbolically given by

$$\frac{\partial}{\partial t}\left[\int_V n(\mathbf{r},E,\Omega,t)\,d^3r\right] dE d\Omega = \text{gains in } V - \text{losses from } V. \qquad (3\text{-}1)$$

Now the gain mechanisms for the phase space element $d^3r dE d\Omega$ are

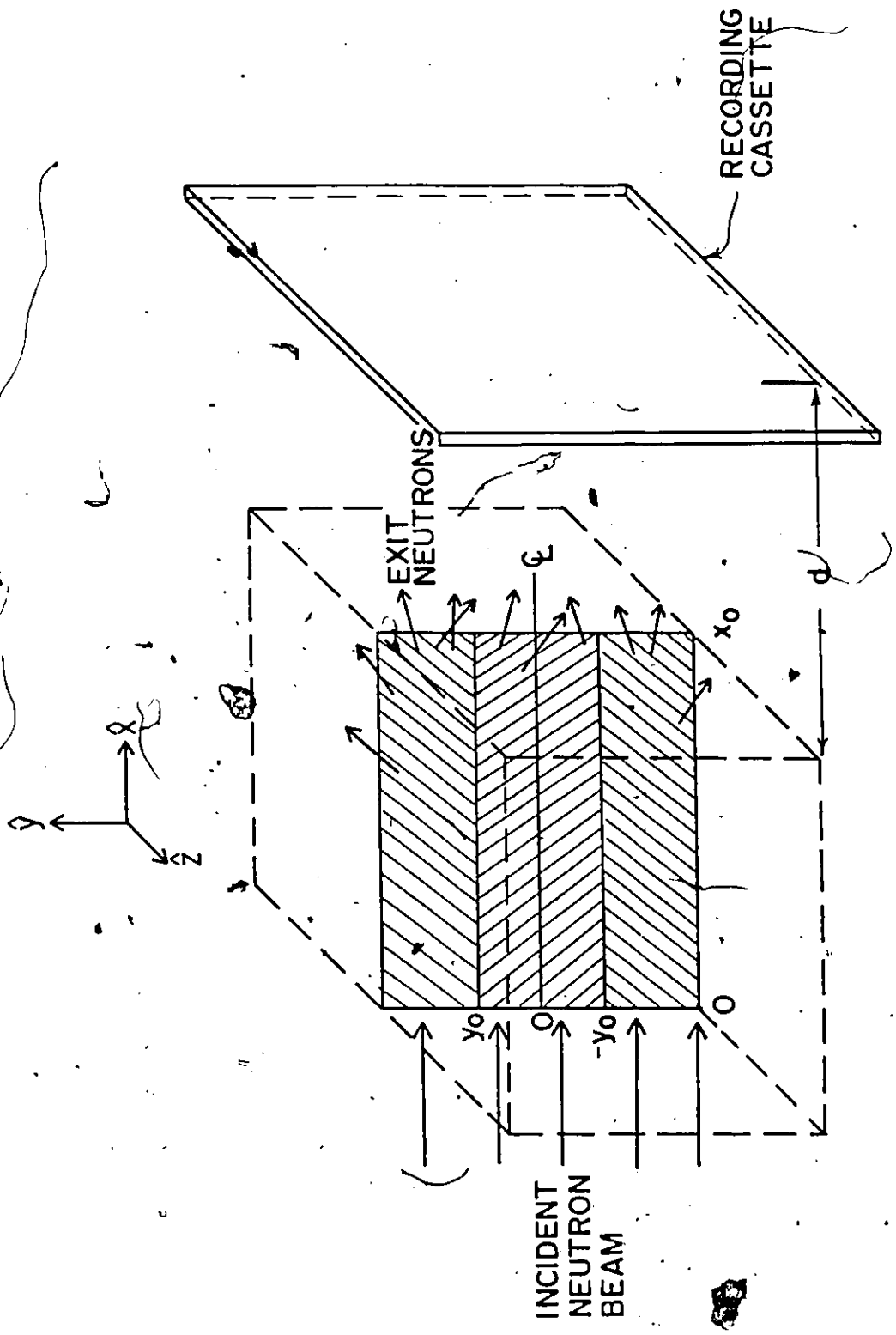

Fig. 3.1: Schematic of neutron radiographic system including the rectangular (x,y) object. The transport of neutrons initially impingent on the sub-band is to be determined.

(1) neutrons streaming into V through its surface S,

(2) neutrons scattering within V from other energies and directions to dE about E and $d\Omega$ about Ω,

(3) neutron sources in V, such as fission.

Likewise, the loss mechanisms for $d^3r dE d\Omega$ are

(4) neutrons leaking out of V through the surface S,

(5) neutrons undergoing any collision whatsoever.

At this point is is useful to introduce two other phase space quantities. Firstly, the angular neutron flux, initially discussed in section 1.3, is defined as the product of the angular neutron density and the neutron speed v:

$$\Psi(r,E,\Omega,t) = vn(r,E,\Omega,t). \tag{3-2}$$

Secondly, the angular current density is the vector whose magnitude is $\Psi(r,E,\Omega,t)$, defined by

$$j(r,E,\Omega,t) = \Omega\Psi(r,E,\Omega,t). \tag{3-3}$$

The physical interpretation of $j(r,E,\Omega,t)dA\ dE\ d\Omega$ is that of being the expected number of neutrons passing through an area dA per unit time with energy E in dE, in direction $d\Omega$ of Ω, at time t. This interpretation renders the angular current density useful for calculating leakage-based mechanisms such as (1) and (4) above. Specifically, the total leakage contribution over the entire surface area S of the volume V is, for neutrons of energy E and direction Ω,

$$(4) - (1) = \left[\int\int_S j(r,E,\Omega,t) \cdot dS \right] dE d\Omega$$

$$= \left[\int\int_V \nabla \cdot j(r,E,\Omega,t)\, d^3r \right] dE d\Omega, \tag{3-4}$$

where the latter equality follows from Gauss' divergence theorem. Substitution of Eq. (3-3) into Eq. (3-4) followed by expansion of the divergence operation then yields

$$(4) - (1) = \left[\int_V \Omega \cdot \nabla \Psi d^3r \right] dE d\Omega . \tag{3-5}$$

For the inscattering gain mechanism, the rate at which neutrons in V scatter from (E',Ω') to (E,Ω) is given by

$$\text{inscatter rate}\,(E',\Omega') = \left[\int_V v' \Sigma_s (r,E' \rightarrow E, \Omega' \rightarrow \Omega) n(r,E',\Omega',t)\, d^3r \right] dE d\Omega . \tag{3-6}$$

where $\Sigma_s(r,E' \rightarrow E, \Omega' \rightarrow \Omega)$ is the "double-differential" scattering cross-section (56) describing the probability that a neutron scatters from (E',Ω') to (E,Ω). Using the angular neutron flux definition, Eq. (3-2), and considering contributions from all E',Ω', the total inscattering contribution is

$$(2) = \left[\int_V \int_{4\pi} \int_0^\infty \Sigma_s (r,E' \rightarrow E, \Omega' \rightarrow \Omega)\, \Psi(r,E',\Omega',t)\, dE' d\Omega'\, d^3r \right] dE d\Omega . \tag{3-7}$$

Defining $s(r,E,\Omega,t)\, d^3r\, dE\, d\Omega$ as the rate at which neutrons are produced by sources in the phase space element, the total control volume source production of neutrons with energy E and direction Ω is

$$(3) = \left[\int_V s(r,E,\Omega,t)\, d^3r \right] dE d\Omega . \tag{3-8}$$

Finally, the removal rate of neutrons in V through collisions is

$$(5) = \left[\int_V v \Sigma_t (r,E)\, n(r,E,\Omega,t)\, d^3r \right] dE d\Omega , \tag{3-9}$$

where $\Sigma_t(r,E)$ is the total macroscopic cross-section (56).

Upon substitution of Eqs. (3-5), (3-7), (3-8) and (3-9) into Eq. (3-1), the following balance relation results:

$$\left[\int_V \left\{ \frac{1}{v} \frac{\partial \Psi}{\partial t} + \Omega \cdot \nabla \Psi + \Sigma_t (r,E)\, \Psi - \int_0^\infty \int_{4\pi} \Sigma_s (r,E' \rightarrow E, \Omega' \rightarrow \Omega)\, \Psi(r,E',\Omega',t)\, d\Omega' dE' \right. \right.$$

$$\left. \left. - s(r,E,\Omega,t) \right] d^3r \right] dE d\Omega = 0 . \tag{3-10}$$

Here, the application of Eq. (3-2) has followed the carrying of the time differentiation across an integral whose boundaries are temporally fixed. Since the control

volume V was arbitrarily chosen, the integrand in Eq. (3-10) vanishes, leaving the general neutron transport equation

$$\frac{1}{v}\frac{\partial\Psi}{\partial t} + \Omega\cdot\nabla\Psi + \Sigma_t(r,E)\,\Psi(r,E,\Omega,t) = \int_{4\pi}\int_0^\infty \Sigma_s(r,E'\rightarrow E,\,\Omega'\rightarrow\Omega)\,\Psi(r,E',\Omega',t)\,dE'd\Omega' + s(r,E,\Omega,t)\,. \tag{3-11}$$

For this study of time-independent thermal neutron transport, the time derivative in this equation vanishes and all explicit energy dependence is removed through weighted energy averaging of the cross-sections. Furthermore, the two- dimensional geometry of Fig. 3.1 implies the expansion of $\Omega\cdot\nabla\Psi$ to (86)

$$\Omega\cdot\nabla\Psi = \mu\,\frac{\partial\Psi}{\partial x} + \cos(\phi)\sqrt{1-\mu^2}\,\frac{\partial\Psi}{\partial y}\,, \tag{3-12}$$

where the direction cosines μ and $\cos(\phi)\sqrt{1-\mu^2}$ are, respectively, the x and y components of the unit direction vector Ω. That is, $\mu = \cos(\theta)$ where

$$\Omega = (\Omega_x, \Omega_y, \Omega_z) = (\cos(\theta), \sin(\theta)\cos(\phi), \sin(\theta)\sin(\phi))\,. \tag{3-13}$$

In x-y Cartesian geometry, the relevant one-group neutron transport equation for the angular neutron flux $\Psi(x,y,\Omega) \equiv \Psi(x,y,\mu,\phi)$ is therefore

$$\mu\,\frac{\partial\Psi}{\partial x} + \cos(\phi)\sqrt{1-\mu^2}\,\frac{\partial\Psi}{\partial y} + \Sigma_t(x,y)\,\Psi(x,y,\Omega) = \Sigma_s(x,y)\int_{4\pi}\Psi(x,y,\Omega')\,K(\Omega'\rightarrow\Omega)d\Omega' + s(x,y,\Omega)\,, \tag{3-14}$$

where the directional transport kernel $K(\Omega'\rightarrow\Omega)$ is defined implicitly by

$$\Sigma_s(x,y,\Omega'\rightarrow\Omega) = \Sigma_s(x,y)\,K(\Omega'\rightarrow\Omega)\,. \tag{3-15}$$

3.2 Development of the Transport Equations

At this point it is useful to ascertain precisely which quantities should correspond to the neutron "intensity" discussed in Chapter 2. As in most reactor physics calculations, one

indicator of the neutron spatial intensity resulting from the calculations in this chapter will be the "neutron scalar flux", defined by

$$\Phi(x,y) = \int_{4\pi} \Psi(x,y,\Omega)\, d\Omega \,. \tag{3-16}$$

Physically, $\Phi(x,y)dA$ represents the total number of neutrons passing through all orientations of an area element dA located at (x,y) per unit of time and $\Phi(x,y)$ has units of $n/cm^2/s$. Another useful intensity indicator for this radiographic context is the forward neutron scalar flux defined by

$$\Phi^+(x,y) = \int_0^{2\pi} \int_0^1 \Psi(x,y,\mu,\phi)\, d\mu\, d\phi \,, \tag{3-17}$$

and representing that portion of $\Phi(x,y)$ with forward (towards the recording device) directions. In fact, $\Phi^+(x,y)$ will be the neutron population indicator calculated in this analysis. The neutron scalar flux will also be directly obtainable, however.

Yet another useful intensity indicator for this analysis is the forward partial neutron current, briefly introduced in section 2.2. The forward partial neutron current, denoted here by $J_+(x,y)$, is the x-component of the total neutron current vector and is defined by

$$J_+ = \left(\int_{2\pi^+} j(x,y,\Omega)\, d\Omega \right)_x , \tag{3-18}$$

where $2\pi^+$ denotes the forward direction.

Upon conversion from angular neutron current to angular neutron flux using Eq. (3-3), Eq. (3-18) becomes

$$J_+ = \left(\int_{2\pi^+} \Omega\, \Psi(x,y,\Omega)\, d\Omega \right)_x$$

$$= \int_{2\pi^+} \Omega_x\, \Psi(x,y,\Omega)\, d\Omega$$

$$= \int_{2\pi^+} \mu \, \Psi(x,y,\mu,\phi)\, d\Omega \,. \qquad (3\text{-}19)$$

Equation (3-19) connects the formal definition of the forward partial neutron current in Eq. (3-18) to the physical interpretation presented in section 2.2. Specifically, the role of μ as a configurational factor distinguishing neutron current and flux is reconciled with the vectorial nature of the neutron current.

For the geometry of Fig. 3.1, the z-component of the total neutron current vector vanishes. It is clear from Eq. (3-18) that the total neutron current, defined by

$$\mathbf{J}(x,y) = \int_{4\pi} \mathbf{j}(x,y,\Omega)\, d\Omega \,, \qquad (3\text{-}20)$$

is related to the partial neutron currents by

$$\mathbf{x} \cdot \mathbf{J} = J_+ - J_- , \qquad (3\text{-}21)$$

where $\mathbf{x}$ is the unit x direction vector and J_- is the reverse partial neutron current.

It should be noted that the inaccuracy of diffusion based descriptions within a few mean free paths of material boundaries necessitates a more precise treatment of the angular variables Ω than is afforded by the approximation that is Fick's law (56).

Solution methods involving angular variable expansions exist for this version of the neutron transport equation (87), but the solution to be given here offers greater computational expediency. This new solution is properly classified as an original extension to an existing class of eigenfunction expansion techniques.

The existing expansion technique begins with an arbitrary level of directional generality, accorded by the following segmentation of the x-component (μ) of the direction vector (88):

$$U_N = \{-1, \mu_1, \ldots, 0, \ldots, \mu_{N-1}, 1\} . \qquad (3\text{-}22)$$

The angular flux is then expanded as

$$\Psi(x,y,\mu,\phi) = \sum_{\ell=0}^{n} \sum_{n=0}^{N} \left(\frac{2\ell+1}{\mu_n - \mu_{n-1}} \right) \Psi_\ell^n(x,y,\phi)\, P_\ell^n\!\left(\frac{2\mu - \mu_n - \mu_{n-1}}{\mu_n - \mu_{n-1}} \right) . \qquad (3\text{-}23)$$

Here, P_ℓ^n are the Legendre partial-range polynomials which reduce to full- range or half-range polynomials by the imposition of the appropriate segmentation U_N (88, 89) and $\Psi_\ell^n(x,y,\phi)$ are expansion coefficients. The angular flux $\Psi(x,y,\mu)$ is simply the angular flux $\Psi(x,y,\mu,\phi)$ averaged over ϕ, and is correspondingly written as

$$\Psi(x,y,\mu) = \sum_{\ell=0}^{\infty} \sum_{n=0}^{N} \left(\frac{2\ell+1}{\mu_n - \mu_{n-1}} \right) \Psi_\ell^n(x,y)\, P_\ell^n\left(\frac{2\mu - \mu_n - \mu_{n-1}}{\mu_n - \mu_{n-1}} \right). \tag{3-24}$$

This latter expansion has associated with it a wealth of spherical harmonics based analysis so that it is advantageous to relate these two expansions. With no loss in generality, this can be accomplished by writing

$$\Psi_\ell^n(x,y,\phi) = \Psi_\ell^n(x,y)\, f^n(x,y,\phi) \tag{3-25}$$

where the distribution $f^n(x,y,\phi)$ carries the ϕ-angular dependence and is therefore also a function of x and y since this dependence varies spatially. Stated otherwise, the $\Psi_\ell^n(x,y)$ carry the main parts of the neutron population spatial dependence. Indeed, the integral relationship between $\Psi(x,y,\mu)$ and $\Psi(x,y,\mu,\phi)$ implies that at every point (x,y), the following normalization exists:

$$\int_0^{2\pi} f^n(x,y,\phi)\, d\phi = 2\pi . \tag{3-26}$$

The lack of transverse property variation implies that the $f^n(x,y,\phi)$ are even in ϕ, so that $f^n(x,y,\phi)$ can be expanded in the following complete set of eigenfunctions:

$$f^n(x,y,\phi) = \sum_{i=0}^{\infty} b_i^n(x,y) \cos(i\phi). \tag{3-27}$$

The normalization in Eq. (3-26) then fixes b_0^n at

$$b_0^n(x,y) = 1 . \tag{3-28}$$

The introduction of the angular distribution functions $f^n(x,y,\phi)$ with the eigenfunction expansion in Eq. (3-23) embodies the originality of the approach adopted here. Since the ultimate goal of neutron transport analysis is usually a determination of the neutron scalar flux $\Phi(x,y)$, the angular flux $\Psi(x,y,\mu,\phi)$ must first be integrated over ϕ. It will

be seen that such integration isolates, at different points in the transport equation, the first two coefficients of the expansion in Eq. (3-27); all other terms vanish, explaining the motivation for the representation of the ϕ-angular dependence employed in Eq. (3-27).

While this new solution procedure can be pursued independently of other existing formalisms, it is developed here in conjunction with the Double-P_L (DP_L) method (90, 91) which is particularly well-suited to rectangular geometries with external sources. In this case, the scattering and source terms are expanded as

$$\Sigma_s(x,y)K(\Omega'\rightarrow\Omega') = \sum_{j=0}^{\infty}\left(\frac{2j+1}{4\pi}\right)\Sigma_{sj}(x,y)P_j(\mu_o), \tag{3-29}$$

$$s(x,y,\Omega) = \sum_{\ell=0}^{\infty}(2\ell+1)\{s_\ell^+(x,y,\phi)P_\ell^+(2\mu-1)+ s_\ell^-(x,y,\phi)P_\ell^-(2\mu+1)\}, \tag{3-30}$$

where $\mu_o = \Omega\cdot\Omega'$ and the symbols "+" and "−" denote forward ($\mu\in(0,1)$) and reverse ($\mu\in(-1,0)$), respectively. The particular version of the expansion Eq. (3-23) used here is therefore

$$\Psi(x,y,\mu,\phi) = \sum_{\ell=0}^{\infty}(2\ell+1)\{\Psi_\ell^+(x,y)f^+(x,y,\phi)P_\ell^+(2\mu-1) +$$

$$+ \Psi_\ell^-(x,y)f^-(x,y,\phi)P_\ell^-(2\mu+1)\}. \tag{3-31}$$

Substitution of Eqs. (3-29)-(3-31) into the governing equation, Eq. (3-14), results in

$$\sum_{\ell=0}^{\infty}(2\ell+1)\left\{\mu P_\ell^+\frac{\partial}{\partial x}[\Psi_\ell^+ f^+]+\mu P_\ell^-\frac{\partial}{\partial x}[\Psi_\ell^- f^-]+\cos(\phi)\sqrt{1-\mu^2}\right.$$

$$\left.\left\{P_\ell^+\frac{\partial}{\partial y}[\Psi_\ell^+ f^+]+P_\ell^-\frac{\partial}{\partial y}[\Psi_\ell^- f^-]\right\}+\Sigma_t(P_\ell^+\Psi_\ell^+ f^+ + P_\ell^-\Psi_\ell^- f^-)-(s_\ell^+P_\ell^+ + s_\ell^-P_\ell^-)\right\}$$

$$= \sum_{\ell=0}^{n}\sum_{j=0}^{\infty}\int_0^{2\pi}\int_{-1}^{+1}(2\ell+1)\left(\frac{2j+1}{4\pi}\right)\Sigma_{sj}(P_\ell^+\Psi_\ell^+ f^+ + P_\ell^-\Psi_\ell^- f^-)$$

$$\{P_j(\mu)\,P_j(\mu') + 2\sum_{k=1}^{j}\frac{(j-k)!}{(j+k)!}\,P_j^k(\mu)\,P_j^k(\mu')\cos[k(\phi-\phi')]\}\,d\mu'\,d\phi' \qquad (3\text{-}32)$$

where the spherical harmonics addition theorem (83) has been used to expand $P_j(\mu_o)$ in terms of the associated Legendre functions $P_j^k(\mu)$, and the superscript "'" denotes dependence on μ' or ϕ' rather than μ or ϕ.

For the DP_L formulation, a set of $2(L+1)$ coupled partial differential equations are ultimately obtained which, for all but the most trivial applications, must be solved numerically. Half of these equations focus on neutrons travelling in forward directions (Ψ_ℓ^+); the other half on those with reverse directions (Ψ_ℓ^-). Each half-set is obtained by utilizing the orthogonality and geometrical properties of the half-range Legendre polynomials, illustrated in Fig. 3.2 and tabulated in Table 3.1. The first half-set is obtained by multiplying Eq. (3-32) by a general factor $P_m^+(2\mu\text{-}1)$ and then integrating with respect to μ over the entire range $\mu \in (-1,+1)$. By application of the Legendre recurrence relation

$$\mu P_\ell(\mu) = (\ell+1)\,P_{\ell+1}(\mu) + \ell\,P_{\ell-1}(\mu) \qquad (3\text{-}33)$$

with the above-mentioned properties of P_ℓ^+ and P_ℓ^-, Eq. (3-32) becomes

$$\frac{1}{2}\left\{\frac{\partial}{\partial x}\left[\Psi_m^+ f^+\right] + \left(\frac{m}{2m+1}\right)\frac{\partial}{\partial x}\left[\Psi_{m-1}^+ f^+\right] + \left(\frac{m+1}{2m+1}\right)\frac{\partial}{\partial x}\left[\Psi_{m+1}^+ f^+\right]\right.$$

$$\left. + \cos(\phi)\sum_{\ell=0}^{\infty}(2\ell+1)\,q_{\ell m}^+\frac{\partial}{\partial y}\left[\Psi_\ell^+ f^+\right]\right\} + \Sigma_t\,\Psi_m^+ f^+ - s_m^+$$

$$= \sum_{\ell=0}^{\infty}\sum_{j=0}^{\infty}\int_0^{2\pi}\int_{-1}^{+1}\int_{-1}^{+1}(2\ell+1)\left(\frac{2j+1}{4\pi}\right)\Sigma_{sj}P_m^+\{\Psi_\ell^+ P_\ell^+ + \Psi_\ell^- P_\ell^-\}$$

$$\left\{P_j(\mu)\,P_j(\mu')f^+ + 2\sum_{k=1}^{j}\left\{\frac{(j-k)!}{(j+k)!}\,P_j^k(\mu)\,P_j^k(\mu')\cos[k(\phi-\phi')]\sum_{i=0}^{\infty}b_i^+\cos(i\phi')\right\}\right\}d\mu\,d\mu'\,d\phi'$$

$$= \text{RHS, say.} \qquad (3\text{-}34)$$

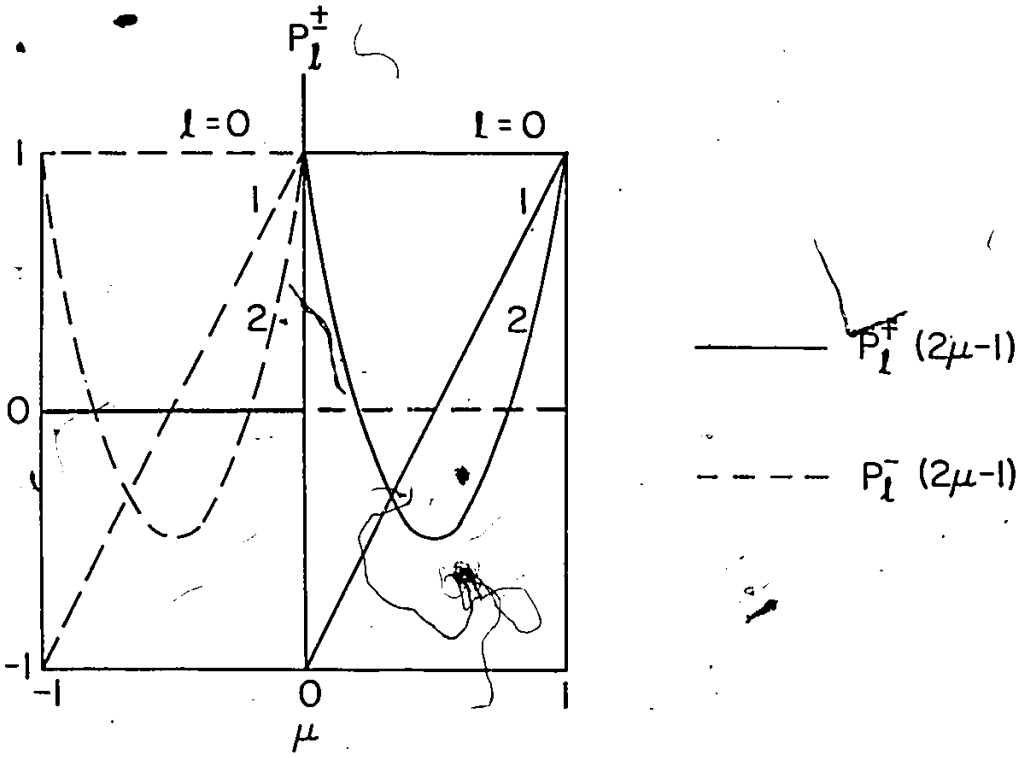

Fig. 3.2: Geometrical and orthogonality properties of the half-range Legendre polynomials, $P_\ell^{\pm}(2\mu\mp1)$, useful in DP_L transport theory.

Here the constants $q_{\ell m}^{\pm}$ are defined by

$$q_{\ell m}^{\pm} = \int_{-1}^{+1} \sqrt{1-\mu^2}\, P_{\ell}^{\pm}(2\mu \mp 1) P_{m}^{\pm}(2\mu \mp 1)\, d\mu \tag{3-35}$$

and are listed in Table 3.2. Noting that for positive integer values of i,

$$\int_{0}^{2\pi} \cos[k(\phi - \phi')] \cos[i\phi']\, d\phi' = \pi \cos(k\phi)\, \delta_{ki}, \tag{3-36}$$

Table 3.1: Half-range and full-range Legendre polynomials.

	HALF RANGE	FULL RANGE
DEFINITION	$P_{\ell}^{+}(2\mu-1) = \begin{cases} P_{\ell}(2\mu-1), \mu \geq 0 \\ 0, \mu < 0 \end{cases}$	$P_{\ell}(\mu) = \frac{1}{2^{\ell}\ell!}\left(\frac{d}{d\mu}\right)^{\ell}(\mu^2-1)^{\ell}$
	$P_{\ell}^{-}(2\mu+1) = \begin{cases} 0, \mu > 0 \\ P_{\ell}(2\mu+1), \mu \leq 0 \end{cases}$	
ORTHOGONALITY PROPERTIES	$\int_{-1}^{+1} P_{\ell}^{\pm} P_{m}^{\pm}\, d\mu = \frac{\delta_{\ell m}}{2m+1}$	$\int_{-1}^{+1} P_{\ell} P_{m}\, d\mu = \frac{2\delta_{\ell m}}{2m+1}$
	$\int_{-1}^{+1} P_{\ell}^{+} P_{m}^{-}\, d\mu = 0$	

where δ_{ki} is the Kronecker delta, the final term in the RHS of Eq. (3-34) simplifies as follows:

$$\int_0^{2\pi} 2 \sum_{k=1}^{j} \left\{ \frac{(j-k)!}{(j+k)!} P_j^k(\mu) P_j^k(\mu') \cos[k(\phi-\phi')] \sum_{i=0}^{\infty} b_i^+ \cos(i\phi') \right\} d\phi'$$

$$= 2\pi \sum_{k=1}^{j} \left\{ \frac{(j-k)!}{(j+k)!} P_j^k(\mu) P_j^k(\mu') b_k^+ \cos(k\phi) \right\} . \tag{3-37}$$

The RHS of Eq. (3-34) can thus be simplified to

$$\text{RHS} = \sum_{j=0}^{\infty} \left(\frac{2j+1}{2} \right) \Sigma_{sj} \sum_{\ell=0}^{\infty} (2\ell+1) \sum_{k=0}^{j} \frac{(j-k)!}{(j+k)!} p_{jm}^{k+} b_k^+ \cos(k\phi) \left\{ \Psi_\ell^+ P_{j\ell}^{k+} + \Psi_\ell^- P_{j\ell}^{k-} \right\} \tag{3-38}$$

where the constants $p_{jm}^{k\pm}$ are defined by

$$p_{jm}^{k\pm} = \int_{-1}^{+1} P_j^k(\mu) P_m^{\pm}(2\mu \mp 1) d\mu \tag{3-39}$$

and are tabulated in Table 3.2.

Since the neutron scalar flux is ultimately to be determined, Eq. (3-34) must be further integrated over ϕ. The following unique integral properties of the angular distribution eigenfunctions readily permit simplification of the first half set of DP_L equations:

$$\int_0^{2\pi} \cos(k\phi) d\phi = 2\pi \delta_{k0} \tag{3-40a}$$

$$\int_0^{2\pi} \cos(\phi) \cos(k\phi) d\phi = \pi \delta_{k1} . \tag{3-40b}$$

The first half set of equations can thus be written as

$$\frac{\partial \Psi_m^+}{\partial x} + \left(\frac{m}{2m+1} \right) \frac{\partial \Psi_{m-1}^+}{\partial x} + \left(\frac{m+1}{2m+1} \right) \frac{\partial \Psi_{m+1}^+}{\partial x} + \sum_{\ell=0}^{\infty} (2\ell+1)$$

$$q_{\ell m}^+ \frac{\partial}{\partial y} \left[\Psi_\ell^+ b_i^+ \right] + 2\Sigma_t \Psi_m^+ - 2 s_m^+$$

$$= \sum_{j=0}^{\infty} (2j+1) \Sigma_{sj} \sum_{\ell=0}^{\infty} (2\ell+1) p_{jm}^{0+} \left\{ \Psi_\ell^+ p_{j\ell}^{0+} + \Psi_\ell^- p_{j\ell}^{0-} \right\} . \tag{3-41}$$

Table 3.2: Tabulation of constants $p_{ij}^{0\pm}$, $q_{ij}^{\pm}$, $r_{ij}^{\pm}$ for $0 \le j \le 2$.

	p_{ij}^{0+}			q_{ij}^{+}			r_{ij}^{+}		
j =	0	1	2	0	1	2	0	1	2
i = 0	1	0	0	$\pi/4$	$-\alpha$	$-\beta$	π	0	0
i = 1	1/2	1/6	0	$-\alpha$	2α	$-\gamma$	$-\pi$	π	0
i = 2	0	1/4	1/20	$-\beta$	$-\gamma$	δ	4π	-3π	$3\pi/2$

	p_{ij}^{0-}			q_{ij}^{-}			r_{ij}^{-}		
j =	0	1	2	0	1	2	0	1	2
i = 0	1	0	0	$\pi/4$	α	$-\beta$	π	0	0
i = 1	$-1/2$	1/6	0	α	2α	γ	π	π	0
i = 2	0	$-1/4$	1/20	$-\beta$	γ	δ	4π	3π	$3\pi/2$

Decimal values are accurate to 5 places and

$\alpha = 0.11873, \beta = 0.03651, \gamma = 0.02651, \delta = 0.14447.$

Consequently, only the first two terms in the expansion Eq. (3-27) remain in these DP_L equations thereby illustrating the utility of the expansion.

Similarly, the multiplication of Eq. (3-32) by the general term $P_m^- (2\mu+1)$ and subsequent integration over μ results in the other half-set of equations. Collectively, the two half-sets are written as

$$\pm \frac{\partial \Psi_m^{\pm}}{\partial x} + \left(\frac{m}{2m+1}\right)\frac{\partial \Psi_{m-1}^{\pm}}{\partial x} + \left(\frac{m+1}{2m+1}\right)\frac{\partial \Psi_{m+1}^{\pm}}{\partial x} + 2\Sigma_t(x,y)\,\Psi_m^{\pm}$$

$$+ \sum_{\ell=0}^{\infty}(2\ell+1)\,q_{\ell m}^{\pm}\,\frac{\partial}{\partial y}\left[\Psi_\ell^{\pm}\, b_1^{\pm}(x,y)\right]$$

$$= 2s_m^{\pm}(x,y) + \sum_{j=0}^{\infty}(2j+1)\,\Sigma_{sj}(x,y)\,p_{jm}^{0\pm} \sum_{\ell=0}^{\infty}(2\ell+1)\left\{\Psi_\ell^{+}(x,y)\,p_{\ell}^{0+} + \Psi_\ell^{-}(x,y)\,p_{\ell}^{0-}\right\}. \tag{3-42}$$

The DP_L approximation involves a truncation of the ℓ series in Eq. (3-42) at $\ell = L$, leaving $2(L+1)$ coupled partial differential equations in the $2(L+1)$ unknowns $\Psi_\ell^{\pm}(x,y)$, $0 \le \ell \le L$. Equation (3-42) is similar to the corresponding planar DP_L equation with the important distinction of the inclusion of a series term containing the y and ϕ dependence. The accuracy of this description is bounded only by the magnitude of L and the accuracy to which $b_1^{\pm}(x,y)$ can be determined. For planar DP_L analysis it is generally accepted that a DP_L description is at least as accurate as a corresponding P_{2L+1} description; where the familiar P_L formulation (86) uses a single interval of segmentation ($N=1$ in Eq. (3-22)) and P_1 is equivalent to diffusion theory. On this basis, a DP_1 description suffices here as it strikes the proper balance between computational complexity and adequacy of description. However, higher order calculations are possible with the commensurate increase in coding complexity and execution time.

Using Eq. (3-31), the neutron scalar flux is found to be given by

$$\Phi(x,y) = 2n\left[\Psi_0^{+}(x,y) + \Psi_0^{-}(x,y)\right]. \tag{3-43}$$

Because of the radiographic context of this transport analysis, a better neutron population indicator here is the forward neutron scalar flux, defined by $\Psi_0^+(x,y)$ to within a normalization constant (see Eqs. (3-17) and (3-31)).

3.3 Calculation of $b_1^{\pm}(x,y)$

Upon first inspection this method appears to suffer from the drawback that calculation of the unknown scalar flux $\Phi(x,y)$ requires pre-calculation of a quantity ($b_1^{\pm}(x,y)$ with the same variable dependence as the unknown itself. The important difference between these two quantities is that $\Phi(x,y)$ is basically a neutron population indicator whereas $b_1^{\pm}(x,y)$ is a distribution indicator and retains no population connection. Rather, $b_1^{\pm}(x,y)$ is the key coefficient in $f^{\pm}(x,y,\phi)$, which at any (x,y) represents that fraction of the forward and reverse neutrons, respectively, with their second direction angle within $d\phi$ of ϕ.

If $\Omega = (\mu,\phi)$ is the general direction vector and **x**, **y**, **z** are the unit Cartesian direction vectors, Fig. 3.1, then ϕ is the angle between the planes formed by the **x** and **y** vectors and by the Ω and **x** vectors. The angle ϕ is thus measured in a y-z plane and is completely independent of the x-related μ component so that for this rectangular geometry, $f^{\pm}$ and $b_k^{\pm}$ have no +/− dependence, that is, $f^{\pm} = f$ and $b_k^{\pm} = b_k$.

Let $b_1(x_p,y)$ denote the y dependent b_1 at a particular x coordinate x_p. Under the assumption that no neutrons enter the band $y\epsilon(-y_0+y_0)$ from outside the band, $b_1(x_p,y)$ will be overestimated in magnitude. This follows since b_1 is the coefficient of $\cos(\phi)$ in the expansion Eq. (3-27) and thus at the top and bottom of the band ($y = \pm y_0$), b_1 is positive and negative, respectively, with magnitude inversely proportional to the fraction of neutrons entering the band at these locations.

Now underestimating the reentrant neutron fraction implies overestimating the emergent (at $y = \pm y_0$) fraction thereby providing an upper bound on the lateral scattering of

neutrons in this problem. That is, if at every x_p, the y dependence of b_l is taken as being the extreme case characterized by no reentrant neutrons at the band edges, then the calculated scalar flux will include an overestimated leakage in the y direction. This overestimation decreases with proximity to the plane of incidence ($x = 0$). In subsequent calculations, $b_l(x,y)$ has additionally been approximated by $b_l(x_0/2,y)$.

For the radiographic application being considered, such overestimation is desireable since it corresponds to extreme beam spreading. If, for a given object, this calculated spreading is deemed to be acceptably low, there will actually be even less spreading.

Proceeding as outlined, the b_l are now only y dependent and $f^n(x,y,\phi)$ in Eq. (3-27) reduces to $f(y,\phi)$. The coefficients $b_l(y)$ can be calculated using a laterally planar (y direction) DP_L transport formulation, with boundary conditions as indicated in Fig. 3.3. If $\Phi_{lat}(y)$ is the resulting scalar flux, the above calculation is accomplished by setting

$$f(y,\phi) = C(y)\Psi_{lat}(y,\phi) \tag{3-44}$$

where $C(y)$ is a constant chosen to make $b_0 = 1$, as previously shown to be required by normalization, and $\Psi_{lat}(y,\phi)$ is the lateral angular flux with the following DP_L expansion:

$$\Psi_{lat}(y,\phi) = \sum_{n=0}^{\infty} (2n+1)\left\{ \Psi^{+}_{lat,n}(y)\, P^{+}_{n}(2\cos(\phi) - 1) + \Psi^{-}_{lat,n}(y)\, P^{-}_{n}(2\cos(\phi) + 1)\right\}. \tag{3-45}$$

It should be mentioned that invoking the above approximations for b_l is equivalent to assuming separability of the ϕ dependence from the x,y and μ expansion in Eq. (3-31). That is, the factor $f(y,\phi)$ is common to all terms in the original expansion.

We note here that this separability approximation is superior to the weakest possible approximation in which isotropy of the angular neutron flux with respect to ϕ is assumed at all points. For the assumption of isotropy, it follows from Eq. (3-27) that b_l

vanishes everywhere thereby completely removing any y dependence in the resulting DP_L equations and thus reducing the problem to one dimension.

Furthermore, the DP_L system in Eq. (3-42) is receptive to enhancement through more accurate calculation of b_1.

Substituting $f(y,\phi)$ and $\Psi_{lat}(y,\phi)$ into Eq. (3-44), multiplication by the general term $\cos(m\phi)$ and subsequent integration over ϕ produces

$$b_m(y) = C(y) \sum_{n=0}^{\infty} \frac{(2n+1)(m+1)}{2\pi} \left\{ \Psi^+_{lat,n}(y)\, r^+_{nm} + \Psi^-_{lat,n}(y)\, r^-_{nm} \right\}, \quad m = 0,1 \tag{3-46}$$

where the constants $r_{nm}^{\pm}$ are defined by

$$r^{\pm}_{nm} = \int_{-\pi}^{+\pi} P^{\pm}_n (2\cos(\phi) \mp 1) \cos(m\phi)\, d\phi \tag{3-47}$$

and are tabulated in Table 3.2.

Imposing the condition that $b_0 = 1$ results in

$$b_1(y) = 2 \frac{\sum_{n=0}^{\infty} (2n+1)\{\Psi^+_{lat,n}(y)\, r^+_{n1} + \Psi^-_{lat,n}(y)\, r^-_{n1}\}}{\sum_{n=0}^{\infty} (2n+1)\{\Psi^+_{lat,n}(y)\, r^+_{n0} + \Psi^-_{lat,n}(y)\, r^-_{n0}\}} \tag{3-48}$$

This equation involves a ratio of weighted fluxes and is consistent with the definition of b_1 as a distribution rather than a population.

For values of y outside the band, b_1 has, in subsequent calculations, been taken to be the corresponding boundary value, serving to partially reduce the overestimation inherent in this method.

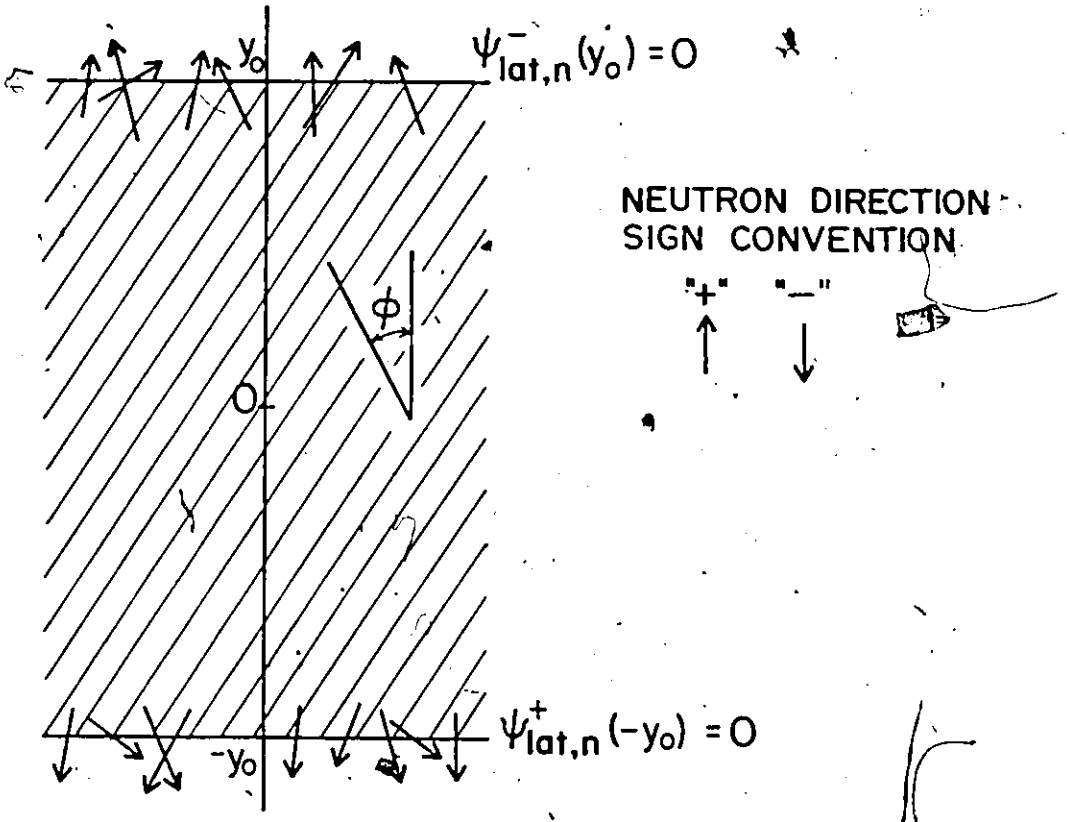

Fig. 3.3: Geometry for laterally planar (y direction) DP_L formulation illustrating boundary conditions and notational features, applied to determine $b_l(y)$. $\psi^{\pm}_{lat,n}(y)$ are the angular flux($\psi_{lat}(y,\phi)$) expansion coefficients.

3.4 Numerical Solution

In light of the complexity of Eq. (3-42) it is meaningless to attempt an analytical solution; rather, a numerical solution is necessitated. A stable numerical differencing and iterative solution scheme has been developed to solve Eq. (3-42) at the DP_1 level of description. While rapid convergence of the iterations has been attained over a wide range of input parameters, this provides no guarantee of numerical convergence to the correct solution to the equations. It can only be reported that all obtained solutions are reconcilable with the transport physics of the situation, given the assumptions made in the mathematical model. From Eq. (3-42) the DP_1 equations are

$$\pm \frac{\partial \Psi_0^{\pm}}{\partial x} + \frac{\partial \Psi_1^{\pm}}{\partial x} + 2\Sigma_t \Psi_0^{\pm} + q_{00}^{\pm} \frac{\partial}{\partial y}\left[\Psi_0^{\pm} b_1\right] + 3\, q_{10}^{\pm} \frac{\partial}{\partial y}\left[\Psi_1^{\pm} b_1\right] \tag{3-49}$$

$$= \Sigma_{s0} p_{00}^{0\pm} [\Psi_0^{+} p_{00}^{0+} + \Psi_0^{-} p_{00}^{0-}] + 3\Sigma_{s1} p_{10}^{0+} [\Psi_0^{+} p_{10}^{0+} + \Psi_0^{-} p_{10}^{0-} + 3\Psi_1^{+} p_{11}^{0+} + 3\Psi_1^{-} p_{11}^{0-}],$$

$$\pm \frac{\partial \Psi_1^{\pm}}{\partial x} + \frac{1}{3}\frac{\partial \Psi_0^{\pm}}{\partial x} + 2\Sigma_t \Psi_1^{\pm} + q_{01}^{\pm} \frac{\partial}{\partial y}\left[\Psi_0^{\pm} b_1\right] + 3\, q_{11}^{\pm} \frac{\partial}{\partial y}\left[\Psi_1^{\pm} b_1\right] \tag{3-50}$$

$$= 3\Sigma_{s1} p_{11}^{0\pm} [\Psi_0^{+} p_{10}^{0+} + \Psi_0^{-} p_{10}^{0-} + 3\Psi_1^{+} p_{11}^{0+} + 3\Psi_1^{-} p_{11}^{0-}],$$

where it has been noted that $p_{01}^{0\pm} = 0$ and $s_m^{\pm} = 0$ since there is no fission source and the externally impingent source is to be accommodated by boundary conditions. Also, linearly anisotropic scattering has been assumed implying that Σ_{sj} is negligibly small for $j \geq 2$.

A chief advantage offered by DP_L methods in planar geometries is the simple specification of boundary conditions. For collimated incident neutrons, the external source boundary condition is

$$\Psi(0,y,\mu) = \begin{cases} S_o\, \delta_D(\mu - 1), & |y| \leq y_o \\ 0, & |y| > y_o \end{cases} \tag{3-51}$$

where δ_D is the Dirac delta and S_o is the source strength with units of n /(cm^2-s-μ-ϕ). Multiplication of Eq. (3-51) by the general term $P_m^+(2\mu-1)$ followed by substitution for $\Psi(0,y,\mu)$ from Eq. (3-24) with $N=1$ and integration over μ produces the boundary condition

$$\Psi_m^+(0,y) = \begin{cases} S_o, & |y| \le y_0 \\ 0, & |y| > y_o \end{cases} \tag{3-52}$$

At the $x = x_o$ boundary, no neutrons enter from $x > x_o$ so that

$$\Psi(x_o, y, \mu) = 0, \mu < 0. \tag{3-53}$$

Repeating the integration procedure described above with $P_m^-(2\mu+1)$, the $x = x_o$ boundary condition is

$$\Psi_m^-(x_o,y) = 0. \tag{3-54}$$

As regards the y boundaries, the only specifiable conditions are

$$\Psi_m^{\pm}(x, \pm\infty) = 0 \tag{3-55}$$

since no neutrons from the band scatter out to $y = \pm\infty$.

In order to properly solve Eqs. (3-49) and (3-50), a transformation is required to compress the y axis into some finite length. This is easily accomplished with the familiar transformation

$$v = \tan^{-1}(y), v\in(-\pi/2, \pi/2) \tag{3-56}$$

where the dimensions of y are suppressed until later inversion. The symbol v is not to be confused with the neutron speed in Eq. (3-2), which will see no further application in this chapter. Equation (3-56) implies

$$\frac{\partial\phi}{\partial y} = \cos^2(v)\frac{\partial\phi}{\partial v} \tag{3-57}$$

so that the DP_1 equations, Eqs. (3-49) and (3-50), become

$$\pm\frac{\partial\Psi_0^{\pm}}{\partial x} + \frac{\partial\Psi_1^{\pm}}{\partial x} + 2\Sigma_t\Psi_0^{\pm} + \frac{\pi}{4}\cos^2(v)\frac{\partial}{\partial v}\left[\Psi_0^{\pm} b_1\right] \mp 3\alpha\cos^2(v)\frac{\partial}{\partial v}\left[\Psi_1^{\pm} b_1\right]$$

$$= \Sigma_{s0}[\Psi_0^+ + \Psi_0^-] \pm \frac{3\Sigma_{s1}}{4}[\Psi_0^+ - \Psi_0^- + \Psi_1^+ + \Psi_1^-], \tag{3-58}$$

$$\pm \frac{\partial \Psi_1^\pm}{\partial x} + \frac{1}{3}\frac{\partial \Psi_0^\pm}{\partial x} + 2\Sigma_t \Psi_1^\pm \mp a\cos^2(v)\frac{\partial}{\partial v}\left[\Psi_0^\pm b_1\right] + 6a\cos^2(v)\frac{\partial}{\partial v}\left[\Psi_1^\pm b_1\right]$$

$$= \frac{\Sigma_{s1}}{4}[\Psi_0^+ - \Psi_0^- + \Psi_1^+ + \Psi_1^-]. \tag{3-59}$$

Here, values for $p_{ij}^{0\pm}$, $q_{ij}^{\pm}$ and a have been substituted from Table 3.2.

The unknowns $\Psi_0^\pm$ and $\Psi_1^\pm$ are now replaced symbolically by $\phi^\pm$ and $\Psi^\pm$, respectively, in order to simplify future numerical subscripting, with the understanding that no confusion arises between $\phi^\pm$ and the angle ϕ or the neutron scalar flux Φ.

The rationale underlying the adopted differencing scheme is next presented and is an adaptation of the original logic presented by Knickle and Daitch (92)-for time-dependent, planar DP_L analysis. Since ϕ^+ represents neutrons travelling from left to right, we use the backward difference

$$\left.\frac{\partial \phi^+}{\partial x}\right|_{(i,j)} = \frac{\phi_{i,j}^+ - \phi_{i-1,j}^+}{\Delta x} \tag{3-60}$$

for evaluation at the (i,j)th grid point. Here, i and j denote the x and v directions, respectively. Similarly, with ϕ^-, information is passed from right to left suggesting the forward difference

$$\left.\frac{\partial \phi^-}{\partial x}\right|_{(i,j)} = \frac{\phi_{i+1,j}^- - \phi_{i,j}^-}{\Delta x}. \tag{3-61}$$

The backward differences

$$\left.\frac{\partial \phi^\pm}{\partial v}\right|_{(i,j)} = \frac{\phi_{i,j}^\pm - \phi_{i,j-1}^\pm}{\Delta v}, \tag{3-62}$$

$$\left.\frac{db_1}{dv}\right|_j = \frac{b_{1j} - b_{1j-1}}{\Delta v}, \tag{3-63}$$

were used so that information could be passed from bottom to top while solving iteratively from top to bottom (see Fig. 3.4). This differencing logic was likewise applied to $\Psi_{i,j}^{\pm}$. Substitution of these differencing formulae into the four DP_1 equations, Eqs. (3-58) and (3-59), and subsequent isolation of ϕ^+, ϕ^-, Ψ^+, Ψ^-, from the first, second, third and fourth equations, respectively, results in

$$\phi_{i,j}^{+(k+1)} = \frac{1}{D10}\left\{ \begin{array}{l} \phi_{i-1,j}^{+(k+1)} + \Psi_{i-1,j}^{+(k+1)} - \Psi_{i,j}^{+(k)} + D11^{*}\phi_{i,j}^{-(k^{*})} + D2^{*}[\Psi_{i,j}^{+(k)} + \Psi_{i,j}^{-(k^{*})}] \\ + D14^{*}\phi_{i,j-1}^{+(k+1)} + D12^{*}(\Psi_{i,j}^{+(k)} - \Psi_{i,j-1}^{+(k+1)}) + D13^{*}\Psi_{i,j}^{+(k)} \end{array} \right\} \tag{3-64a}$$

$$\Psi_{i,j}^{+(k+1)} = \frac{1}{D16}\left\{ \begin{array}{l} \Psi_{i-1,j}^{+(k+1)} + \frac{1}{3}(\phi_{i-1,j}^{+(k+1)} - \phi_{i,j}^{+(k+1)}) + D1^{*}[\phi_{i,j}^{+(k+1)} - \phi_{i,j}^{-(k^{*})} + \Psi_{i,j}^{-(k^{*})}] \\ + D7^{*}(\phi_{i,j}^{+(k+1)} - \phi_{i,j-1}^{+(k+1)} + 6\Psi_{i,j-1}^{+(k+1)}) + D8^{*}\phi_{i,j}^{+(k+1)} \end{array} \right\} \tag{3-64b}$$

$$\phi_{i,j}^{-(k+1)} = \frac{1}{D10}\left\{ \begin{array}{l} \phi_{i+1,j}^{-(k+1)} - \Psi_{i+1,j}^{-(k+1)} + \Psi_{i,j}^{-(k)} + D11^{*}\phi_{i,j}^{+(k^{*})} - D2^{*}[\Psi_{i,j}^{+(k^{*})} + \Psi_{i,j}^{-(k)}] \\ + D14^{*}\phi_{i,j-1}^{-(k+1)} - D12^{*}(\Psi_{i,j}^{-(k)} - \Psi_{i,j-1}^{-(k+1)}) - D13^{*}\Psi_{i,j}^{-(k)} \end{array} \right\} \tag{3-65a}$$

$$\Psi_{i,j}^{-(k+1)} = \frac{1}{D16}\left\{ \begin{array}{l} \Psi_{i+1,j}^{-(k+1)} + \frac{1}{3}(\phi_{i,j}^{-(k+1)} - \phi_{i+1,j}^{-(k+1)}) + D1^{*}[\phi_{i,j}^{+(k^{*})} - \phi_{i,j}^{-(k+1)} + \Psi_{i,j}^{+(k^{*})}] \\ + D7^{*}(\phi_{i,j-1}^{-(k+1)} - \phi_{i,j}^{-(k+1)} + 6\Psi_{i,j-1}^{-(k+1)}) - D8^{*}\phi_{i,j}^{-(k+1)} \end{array} \right\}, \tag{3-65b}$$

where, for reasons of programming convenience, the following constants have been defined:

$$D0 = \frac{\Delta x}{\Delta v};\ D1 = \frac{\Sigma_{s1}\Delta x}{4};\ D2 = 3^{*}D1;\ D3 = \Sigma_{s0}\Delta x + D2;\ D4 = \Sigma_{s0}\Delta x - D2$$

$$D5 = D0^{*}\cos^{2}(v_j)b_{1,j};\ D6 = D0^{*}\cos^{2}(v_j)(b_{1,j} - b_{1,j-1});\ D7 = \alpha^{*}D5;\ D8 = \alpha^{*}D6;$$

$$D9 = 1 + (2\Sigma_t - \nu\Sigma_f)\Delta x - D3;\ D10 = D9 + \frac{\pi}{4}(D5 + D6);\ D11 = D4 + \nu\Sigma_f\Delta x;\ D12 = 3^{*}D7$$

$$D13 = 3^{*}D8;\ D14 = \frac{\pi}{4}{}^{*}D5;\ D15 = 1 - 2\Sigma_t\Delta x - D1;\ D16 = D15 + 6^{*}(D7 + D8). \tag{3-66}$$

While vanishing in this radiographic context, the fission cross-section, Σ_f has been retained to illustrate the more general applicability of this formulation. Also, the superscript "(k)" denotes the value at the kth iteration and k^* assumes values of k or k + 1, depending on whether or not, at a given row, the calculation has proceeded to the midpoint of the row. Following the neutron direction, ϕ^+ and Ψ^+ are calculated from left to right, ϕ^- and Ψ^- from right to left at each row, Fig. 3.4. This directional procedure also arises naturally from the boundary conditions, Eqs. (3-52) and (3-54). Calculation proceeds downwards from the top row to the centerline where a reflection boundary condition is afforded by the symmetry of the problem. This constitutes one complete iteration. In short, at any stage of the calculation, the most recently obtained values of $\phi^{\pm}$ and $\Psi^{\pm}$ at each grid point were used in calculating the unknown. As a result of the bidirectionality in the solution procedure, k^* is thus sometimes k and sometimes k + 1, as outlined above.

The FORTRAN program SCATTER was written to solve Eqs. (3-49) and (3- 50), using the differencing equations Eqs. (3-64) and (3-65) with allowance for over/under relaxation, which was used as necessary. The FORTRAN program PLANAR generates the coefficients $b_1(y)$ from Eq. (3-48) using the planar DP_1 formulation outlined in section 3.3. Listings of these programs are included in Appendix D.

3.5 Application to Scattering Quantification

The analytical and numerical machinery developed in this chapter applies to the simplified model in Fig. 3.1 and is therefore of limited utility in practical situations as a precise neutron flux calculator. It can, however, be used to estimate the maximum extent of scattering and thus beam spreading when an object is diagnosed using a collimated neutron beam.

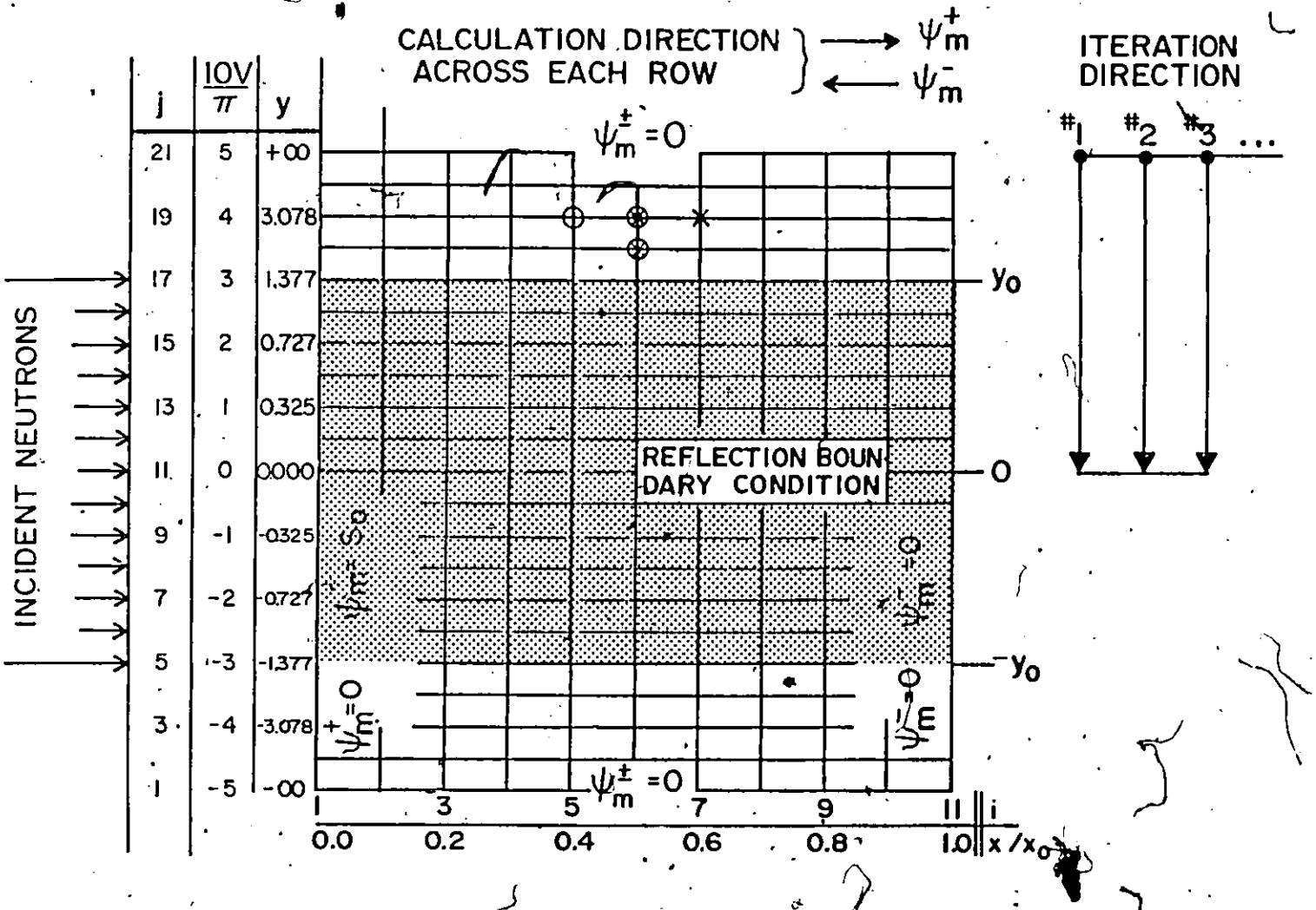

Fig. 3.4: Sample differing grid ($\Delta v \neq \pi/20$, $y_0 \approx 1.377$ cm) illustrating nonlinear compression of the y-axis, boundary conditions, calculation directions and computational molecules. Calculation of ψ_m^+ and ψ_m^- at the grid point '•' uses information from points 'O' and 'X' respectively.

This would involve performing the above DP_L calculations for the rectangular object, Fig. 3.1, whose dimensions most closely approximate those of the given object. Of course, estimates of Σ_a and Σ_s are required for the calculations. Although Σ_a is the unknown property here, these calculations are designed to estimate the magnitude of beam spreading and can be performed over a range of Σ_a estimates. Note that increasing Σ_a tends to decrease beam spreading so that the procedure of determining extreme case scattering can be adhered to by estimating a lower bound for Σ_a.

If, based on calculations, the beam spreading is judged to be excessive, the resulting radiograph will be too blurred to interpret properly. The application of an antiscatter grid or other methods of scattering suppression, see section 2.1, are suggested in this case. At the other extreme, if the amount of beam spreading is calculated to be negligible, then the radiographer is assured that measured optical density differences are, after accounting for other system transfer functions, manifestations of the actual property variation within the object. For radiography with neutrons, the property of interest is $\Sigma_a(x,y)$; the ideal object has a negligibly small $\Sigma_s(x,y)$.

It is important to understand the fundamental difference between neutron scattering and beam spreading in the context of a rectangular band section of an object. Specifically, not all scattered neutrons contribute to beam spreading. If neutrons scattered in the band ultimately impinge on the image plane in a region bounded by the extrapolated upper and lower planar band boundaries, then these neutrons contribute to the imaging of the band. This leads to an enhancement of imaging quality relative to that predicted by conventional object scattering analyses in which all scattered neutrons are assumed to be non-image forming.

Applications of this analysis need not be restricted to radiography since beam spreading through scattering also serves to blur detail in neutron tomography, which features the use of detectors (see, for example, reference 93).

Further, the boundary condition Eq. (3-52) is easily generalized to accommodate an arbitrary incident neutron angular distribution. For instance, when the incident neutrons are isotropic over the half plane $\mu \geq 0$, the boundary condition corresponding to Eq. (3-52) is

$$\Psi_m^+(0,y) = \begin{cases} S_o\, \delta_{m0}, & |y| \leq y_0 \\ 0, & |y| > y_0 \end{cases} \tag{3-67}$$

where δ_{m0} is the Kronecker delta.

An illustrative example of the application of this theory is now presented in which the objective is to estimate the amount of beam spreading in a water- saturated object whose rectangular approximation has depth x_o = 5 cm, and an arbitrarily large height. The thermal macroscopic cross-sections for water were taken from reference 75. The object additionally contains some unknown distribution of a neutron absorber with a negligible macroscopic scattering cross-section. This distribution is to be determined non-destructively using neutron radiography, but it is first desired to estimate the maximum extent of spreading of the collimated neutron beam arising from neutron scattering.

This can be accomplished by performing the DP_L calculation for various sections of the incident beam. While this beam will almost certainly span a lateral range wider than the 2.75 cm band in Fig. 3.4, linearity of neutron transport ensures the validity of determining the spreading of a band of neutrons, as discussed in section 3.1. In adherence to extreme spreading estimation, an upper bound for beam spreading has been determined by using the thermal cross-sections for water. The results from program SCATTER are displayed in Fig. 3.5.

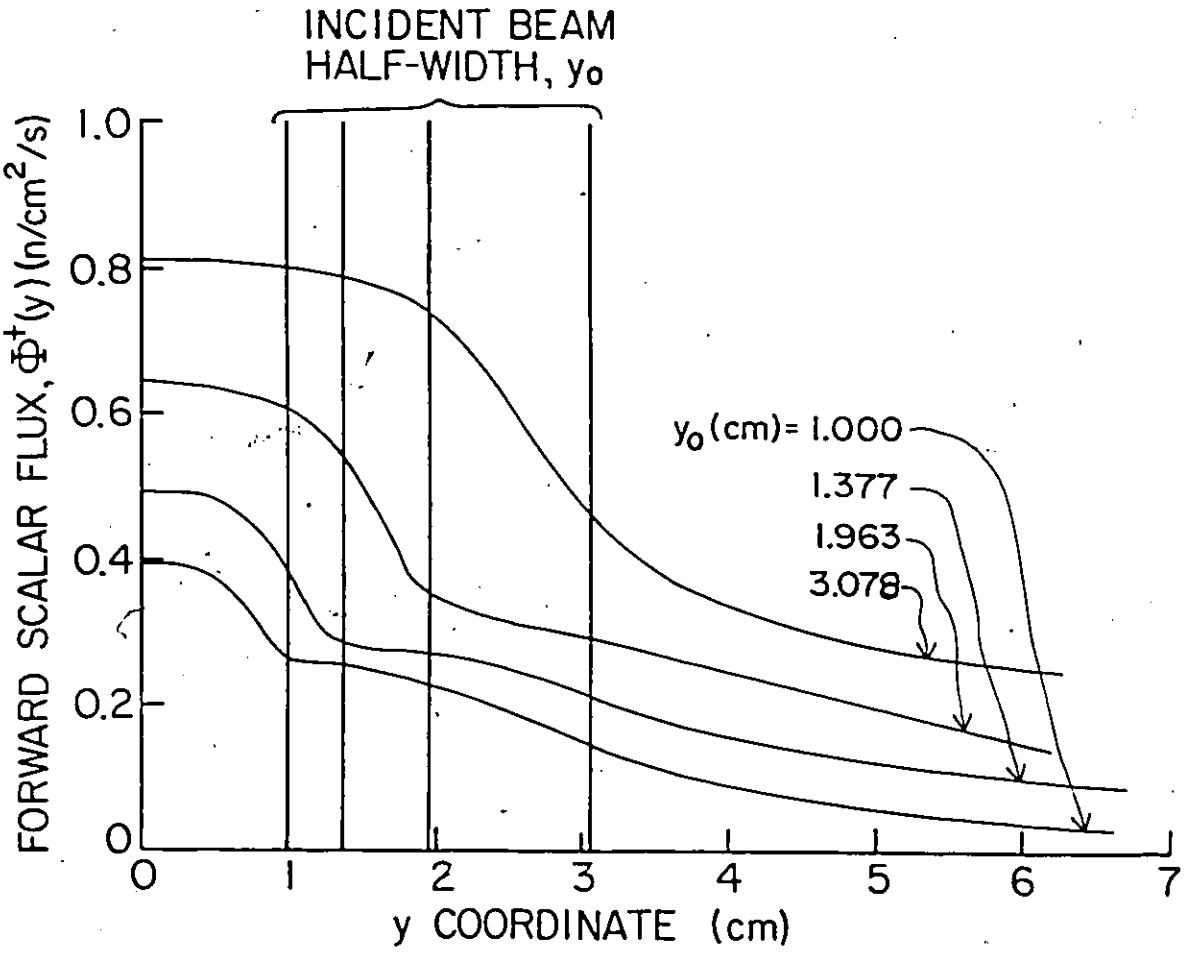

Fig. 3.5: Forward direction neutron scalar flux, normalized to an incident collimated flux of $\phi_o^+ = 1$ n/cm^2/sec, and measured at x = 2cm for various y_o. Other parameters are $x_o = 5$ cm, $\Sigma_s = 3.45$ cm^{-1}, $\Sigma_a = 0.022$ cm^{-1}, $\Sigma_f = 0.0$ cm^{-1}.

As expected, both the forward neutron flux $\phi^+(x,y)$ and the amount of beam spreading increase with the band width. The overestimation of outward- scattered neutrons at the band boundaries is manifested quite clearly in each of the four curves at the respective boundaries, denoted in Fig. 3.5 by the vertical lines. Just outside each boundary, the corresponding flux locally changes curvature representing the overestimated neutron population outside the band. More accurate calculations for $b_1(y)$ should remove this phenomenon. As expected, the magnitude of the inflection decreases with proximity to the plane of incidence, $x=0$.

Interestingly, a form of line spreading function emerges here. As y_0 is decreased, the incident band of collimated radiation approaches a line source and thus the subsequent beam spreading, by definition, approaches a line spreading function. However, the accuracy of the calculations decreases as y_0 is decreased and thereby limits the utility of this methodology as a line spread function calculator. Rather, the transfer function emerging here is a "band spread function", less fundamental and of less general applicability than the line spread function. A more macroscopic approach to system transfer function calculations for thermal neutron scattering is the subject of Chapter 4.

3.6 Convergence of Numerical Solution

While the prescribed iterative numerical solution to Eqs. (3-49) and (3-50) has been found stable over a wide range of input parameters, there is no guarantee of convergence to the correct solution even though the obtained solution is physically plausible. With an overrelaxation parameter ω applied to Eqs. (3-64) and (3-65), acceleration of iteration convergence was obtained so that the fastest convergence for the 11 x 21 grid in Fig. 3.4 required, depending on the input parameters, approximately 20 iterations and occurred for ω in the range from 1.1 to 1.2.

The complexity of Eqs. (3-49) and (3-50) renders an analytical determination of convergence unfeasible. The only indication of convergence of this method has been that the rectangular (x,y) DP_1 solution converges to the separately calculated planar (x) DP_1 solution as $y_o \rightarrow \infty$, as indicated in Fig. 3.6. For comparison purposes, the corresponding planar diffusion theory scalar flux is also shown. The calculations were performed for a half-plane, $\mu \geq 0$, isotropic incident neutron beam since diffusion theory deals poorly with highly directional fluxes such as obtains from collimated incident neutrons. Also, a fission cross-section was included to illustrate the more general applicability of this work.

Briefly, the planar diffusion theory flux was obtained using the following analysis. For an infinite slab with an extrapolated boundary at $x=\tilde{a}$ and a boundary net current strength of S_o^{DIFF} n/cm^2/s, the familiar diffusion theory one- group neutron scalar flux is given (57) by

$$\phi(x) = \frac{S_o^{DIFF} L}{D} \left\{ \sinh\left(\frac{\tilde{a}-x}{L}\right) / \cosh\left(\frac{\tilde{a}}{L}\right) \right\}, \tag{3-68}$$

where L,D are the diffusion length and coefficient, respectively, and are used as conventionally defined (56). Now S_o^{DIFF} is simply $|J(0)|$ where $J(x)$ is the net current density, related to the angular neutron flux by

$$J(x) = \int_{4\pi} \Omega\, \Psi(x,\Omega)\, d\Omega. \tag{3-69}$$

In order to meaningfully compare the diffusion theory scalar flux and the DP_1 calculated flux, the boundary conditions at $x=0$ must be unified. From the planar DP_1 expansion for $\Psi(x,\mu)$, being of the form in Eq. (3-41), and using Eq. (3-69), this implies setting S_o^{DIFF} to

$$S_o^{DIFF} = \int_0^{2\pi} \int_{-1}^{+1} \mu \sum_{\ell=0}^{1} (2\ell+1) \{ \Psi_\ell^+(0) P_\ell^+(2\mu-1) + \Psi_\ell^-(0) P_\ell^-(2\mu+1) \} d\mu d\phi$$

$$= \pi [\, \Psi_0^+(0) - \Psi_0^-(0) + \Psi_1^+(0) + \Psi_1^-(0) \,]. \tag{3-70}$$

For the unit half-plane ($\mu \geq 0$) isotropic neutron source, Eq. (3-67) implies

$$\Psi_0^+(0) = 1, \tag{3-71a}$$

$$\Psi_1^+(0) = 0. \tag{3-71b}$$

so that the relation

$$S_0^{DIFF} = \pi[1 - (\Psi_0^-(0) - \Psi_1^-(0))] \tag{3-72}$$

connects the diffusion theory and DP_1 formulations.

From Fig. 3.6 the convergence of the rectangular DP_1 flux to the planar DP_1 flux as $y_0 \to \infty$ is evident. Also the DP_1 flux is slightly larger than the diffusion theory flux. All calculations were performed for a 41 x 21 grid. It was noticed that doubling the mesh density from 21 x 21 to 41 x 21 diminished the calculated flux by approximately 1.4%.

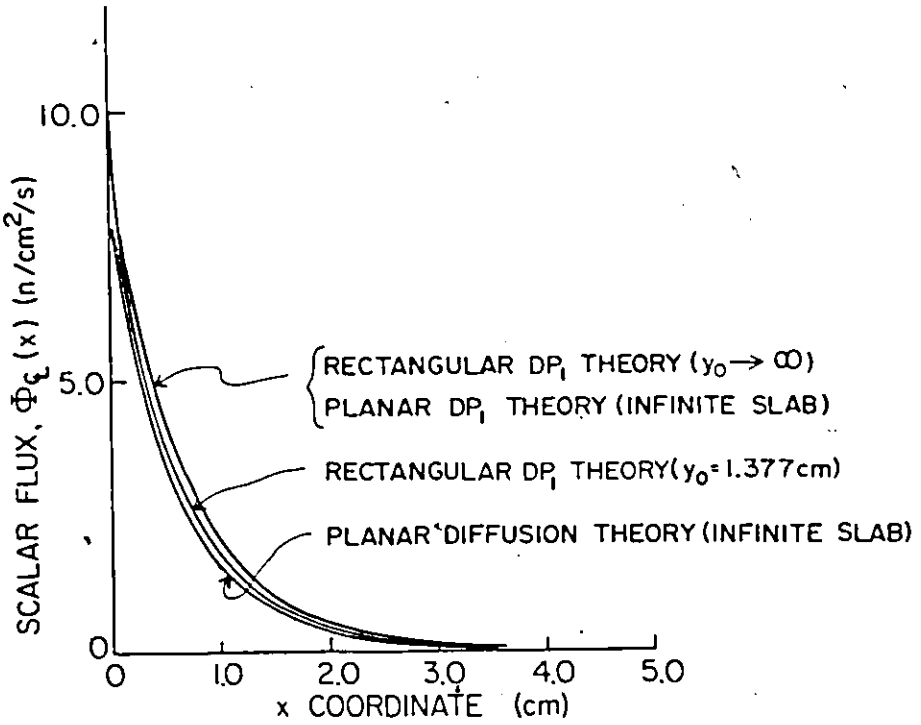

Fig. 3.6: Convergence of rectangular DP_1-calculated neutron scalar flux $\Phi(x,0)$ to planar DP_1 flux as $y_o \rightarrow \infty$. For comparison purposes, the corresponding diffusion theory flux is presented. Results are for a $y_o \times 5$ cm^2 homogeneous slab with linearly anisotropic scattering, $\Sigma_s = 3.45$ cm^{-1}, $\Sigma_a = 0.022$ cm^{-1}, $\nu\Sigma_f = 0.48$ cm^{-1}.

CHAPTER 4

SYSTEM TRANSFER FUNCTION FORMULATION FOR OBJECT SCATTERING

4.1 Scattering Line Function (SLF)

As discussed in Chapters 1 and 2, a system transfer function (STF) is a mathematical tool describing the traversal of some simple input through the system under consideration. In an imaging context, the imaging system serves to degrade while transforming an idealized input so that the STF models degradation sources.

The system response to more complex inputs is obtainable as the convolution or multiplication of the input function with the STF with the exact operation depending on whether or not the STF is constructed as a function on the spatial frequency space. Two previously encountered examples of STF's are line and point spread functions, describing the spreading of idealized line and point sources of radiation in the object plane onto the image plane. In each case conservation of integrated intensity is maintained so that for an idealized input of unit integrated intensity, the spatial output is given in general by STF(r), where

$$\int_{\text{all } r} \text{STF}(r)\,dr = 1\,. \tag{4-1}$$

As discussed in section (2.1), a general transfer function formulation of radiographic scattering is nonlinear since the derived STF is, in general, object dependent. However, such a formulation can still be of practical utility particularly if the object being inspected is such that a good approximation to the STF is possible without a detailed knowledge of the object's material distribution. This would, for example, apply to objects known to possess a nearly spatially uniform scattering cross-section even in the presence of

an unknown (and to be determined) nonuniform absorption cross-section. Absorbing, non-scattering materials embedded in an otherwise uniformly hydrogenous medium, such as water, fit this description.

In section 3.5, it was suggested that the emergent distribution of a collimated band of neutrons normally incident on a plane-face section of a slab could serve to generate a scattering based LSF under conditions of a sufficiently narrow band. Unfortunately, the complexity of the transport calculations described in Chapter 3, in addition to their inaccuracy for the limiting case of a narrow band, suggests the need for a more macroscopic approach to the development of an STF describing radiographic neutron scattering. That is precisely the goal of this chapter.

To demonstrate the analytical transfer function formulation of thermal neutron scattering in a radiographic context, consider initially the traversal of a single unit intensity line source of thermalized neutrons through an infinitesimally narrow slab of width Δx as illustrated in Fig. 4.1a. If the slab is nonscattering with a one-group thermal macroscopic absorption cross-section Σ_a, then to the Dirac delta input intensity distribution

$$I(y) = \delta_D(y - y_o) \tag{4-2}$$

there corresponds an output intensity distribution

$$I^*_{\Delta x}(y, y_o) = (1 - \Sigma_a \Delta x)\,\delta_D(y - y_o), \tag{4-3}$$

where y_o is included in the function notation as a reference to the source location and the asterisk denotes the idealization inherent in the assumption of no scattering.

To understand the effects of scattering within the slab, one may view the simple idealized output in Eq. (4-3) as an input to a system, i.e. object scattering, which acts to degrade this input. Adding the scattering cross-section Σ_s to Σ_a to give a total cross-section of

$$\Sigma_t = \Sigma_a + \Sigma_s, \tag{4-4}$$

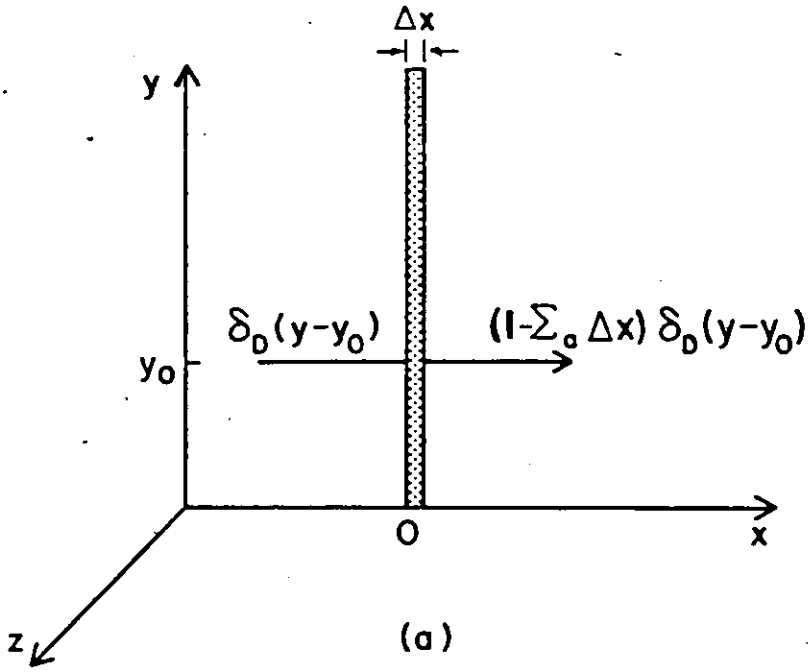

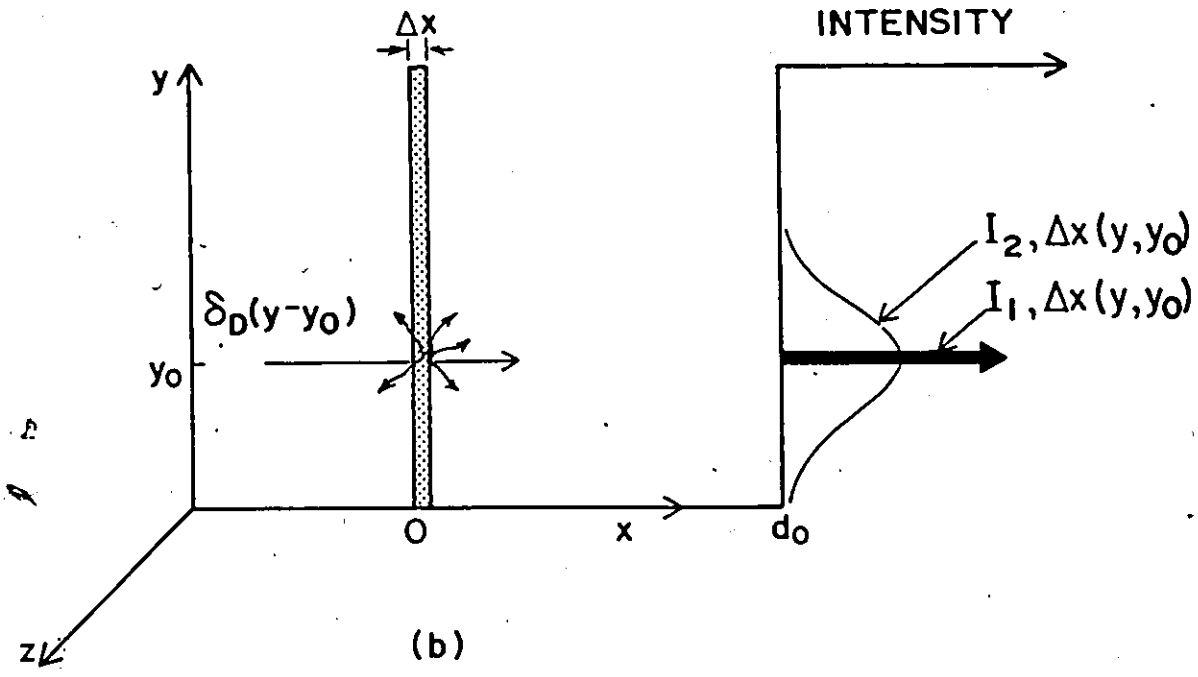

Fig. 4.1: (a) Line source of thermal neutrons traversing an elemental slab.

(b) Two-component intensity distribution at the plane $x = d_0$, resulting from uncollided and once-scattered neutrons.

the emergent neutron beam is seen to consist of two components - the original noninteracted, or "uncollided", portion of the beam and the scattering contribution. Note that the infinitesimal slab width precludes the occurrence of multiple interactions. The uncollided beam component has the intensity distribution

$$I_{1,\Delta x}(y, y_o) = (1 - \Sigma_t \Delta x)\, \delta_D(y - y_o). \tag{4-5}$$

For isotropic scattering, the scattering component intensity distribution, see section A.1, when taken at the plane $x = d_o$, is given by

$$I_{2,\Delta x}(y, y_o) = \frac{\Sigma_s \Delta x}{2\pi d_o} \left[1 + \left(\frac{y - y_o}{d_o} \right)^2 \right]^{-1}. \tag{4-6}$$

The emergent neutron intensity distribution at the line y on the plane $x = d_o$ due to an incident unit intensity line source at y_o undergoing absorption and isotropic scattering in the slab, Fig. 4.1b, is therefore

$$I_{\Delta x}(y, y_o) = (1 - \Sigma_t \Delta x)\delta_D(y - y_o) + \frac{\Sigma_s \Delta x}{2\pi d_o} \left[1 + \left(\frac{y - y_o}{d_o} \right)^2 \right]^{-1}. \tag{4-7}$$

It is important to understand that since both the uncollided and scattered components are derived by considering the populations of neutrons passing through a plane at $x = d_o$, the resulting neutron intensities are actually forward partial neutron currents, as discussed in section 2.2.

In the context of object scattering, Eq. (4-3) can be viewed as representing an idealized "input" which, when operated upon by the physical process that is object scattering, yields the "output" given by Eq. (4-7). Normalizing to an input of unit integrated intensity, the output is then the desired STF here named the "scattering line function" (SLF) and given by

$$SLF^{(0)}(y, y_o) = \frac{1}{(1 - \Sigma_a \Delta x)} \left\{ (1 - \Sigma_t \Delta x)\delta_D(y - y_o) + \frac{\Sigma_s \Delta x}{2\pi d_o} \left[1 + \left(\frac{y - y_o}{d_o} \right)^2 \right]^{-1} \right\}. \tag{4-8}$$

The superscript "0" indicates that the model is geometrically designated here as being of "zeroth order" since it assumes an infinitesimal slab as an object.

The transfer function analysis of neutron scattering in radiography through the splitting of an STF into two components has recently been studied by Segal et al (53-55). In that work, the STF was calculated by Monte Carlo simulation for uniform slabs of various materials. The approach taken in this chapter is to analytically initiate a framework for a scattering based STF and to advance the resulting models through selected applications.

We observe that $SLF^{(0)}$ violates conservation of integrated intensity, since

$$\int_{-\infty}^{\infty} SLF^{(0)}(y,y_o)\,dy = 1 - \frac{\Sigma_s \Delta x}{2(1-\Sigma_a \Delta x)} < 1. \qquad (4\text{-}9)$$

This is expected, however, given that the transfer from input to output involves a loss of neutrons due to backscatter. Removal of the STF unity normalization indicated in Eq. (4-1) poses no problems here since it is ultimately only the distribution of the output which is sought after.

Furthermore the input used to generate $SLF^{(0)}$ must always differ in magnitude from the actual slab incident neutron line source input by the attenuation factor of $f = 1 - \Sigma_a \Delta x$. As a result, the product, $f \cdot SLF^{(0)}(y, y_o)$ is also the output response at the line y to a normally incident unit intensity line source of thermal neutrons at y_o that undergoes absorption and scattering in the slab.

The above model can be enhanced at the expense of simplicity. For example, by expanding the slab from infinitesimal width Δx to finite width x^*, while retaining single scattering as an approximation, the resulting "first order" SLF is given by (see section A.2)

$$SLF^{(1)}(y, y_o) = \exp[-\Sigma_s x^*]\,\delta_D(y - y_o) + \left(\frac{\Sigma_s}{2\pi}\right)\exp[\Sigma_a x^*]\int_0^{x^*}\left|[d_o - x]\left[1 + \left(\frac{y - y_o}{d_o - x}\right)^2\right]\right|^{-1}\exp[-\Sigma_t x]\,dx. \qquad (4\text{-}10)$$

4.2 Isotropic Scattering Point Function (SPF)

Corresponding to the one-dimensional SLF is a two-dimensional "scattering point function" (SPF) which describes the spreading of a normally incident point source of neutrons onto an image plane, due to internal object scattering. For the isotropic system described in Fig. 4.1, the zeroth order SPF, consisting of a collimated uncollided component and a scattering component, see section A.3, is given by

$$SPF^{(0)}(R) = \frac{1}{(1-\Sigma_a \Delta x)}\left\{(1-\Sigma_t \Delta x)\,\delta_D(R) + \frac{\Sigma_s \Delta x}{4\pi d_o^2}\left[1+\left(\frac{R}{d_o}\right)^2\right]^{-3/2}\right\}, \tag{4-11}$$

where R denotes distance from the origin of emission.

This rotationally symmetric, or isotropic, SPF also possesses shift invariance; the response at (y, z) to an input at (y_o, z_o) is geometrically a function only of the Euclidean distance, R, between the two points. Similarly, the corresponding first order SPF, see section A.3, is given by

$$SPF^{(1)}(R) = \exp[-\Sigma_s x^*]\,\delta_D(R)$$

$$+\left(\frac{\Sigma_s}{4\pi}\right)\exp[\Sigma_a x^*]\int_0^{x^*}(d_o-x)^{-2}\left[1+\left(\frac{R}{d_o-x}\right)^2\right]^{-3/2}\exp[-\Sigma_t x]\,dx\,. \tag{4-12}$$

4.3 Infinite Knife-Edged Slab Object

One interesting and potentially useful application of scattering transfer function analysis through the SLF lies in the determination of the system response to an infinite knife-edged slab as illustrated in Fig. 4.2. This analysis closely parallels previous work involving the generation of "edge spread functions" (51,52,105) from the relevant STF, the line spread function and applicable to screen-film and general radiographic unsharpness analysis. As will be shown, the effects of object scattering in the output response are distinctive – to the extent that they suggest the development of a diagnostic tool based on this response.

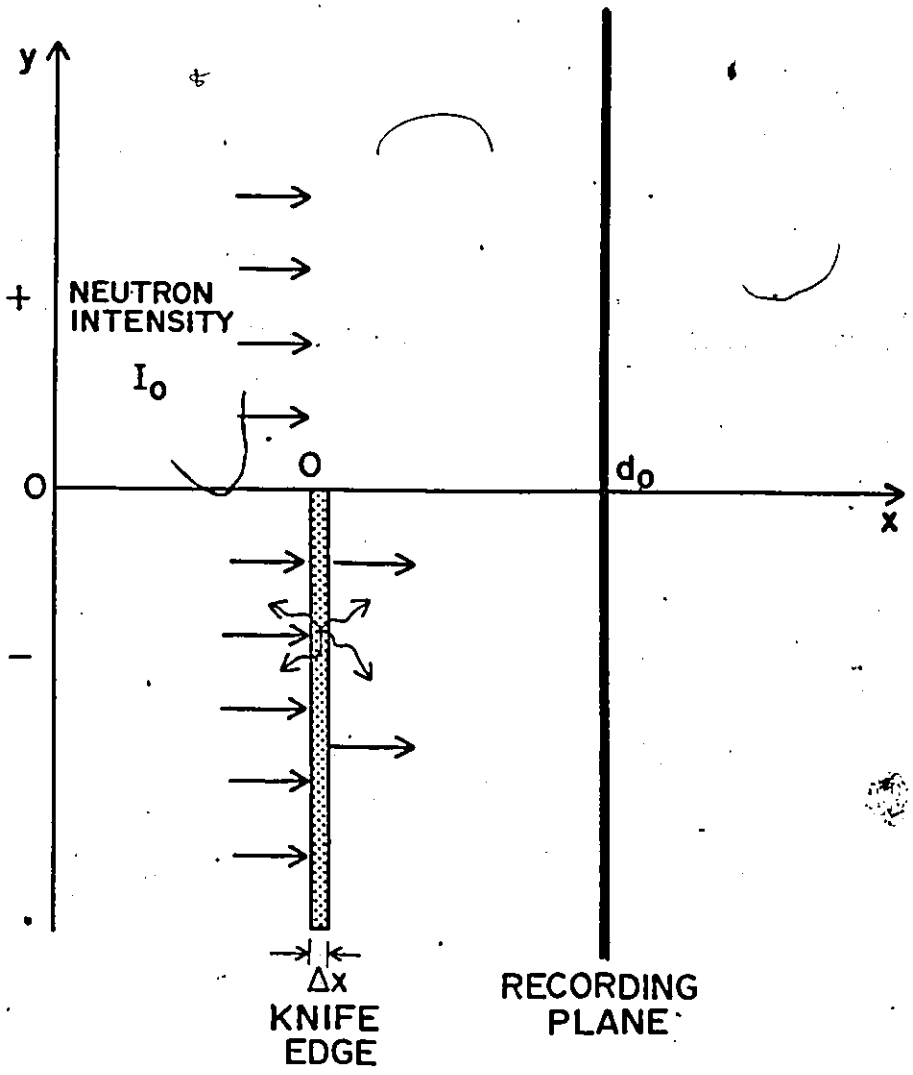

Fig. 4.2: Scattering (Σ_s) or absorption (Σ_a) of collimated neutrons impingent on an "infinite" knife-edged slab.

Referring to Fig. 4.2, the emergent beam intensity corresponding to an incident collimated beam of intensity I_o would, in the absence of object scattering and taken at the plane $x = d_o$, be given by

$$I_d = I_o(1 - \Sigma_a \Delta x). \tag{4-13}$$

For simplicity, the geometrically zeroth order model is initially used here as applicable to knife edges for which Δx is sufficiently small that the attenuation product obeys $\Sigma_t \Delta x << 1$. Consistent with the definition of SLF in Eq. (4-8), the system input is

$$\text{INPUT}(y) = \begin{cases} I_d, & y<0 \\ I_o, & y>0 \end{cases} \tag{4-14}$$

The edge response function accounting for the effects of scattering is then the convolution of the system input with the SLF, section A.4, and is given by

$$\text{SEF}^{(0)}(y) = \int_{-\infty}^{\infty} \text{INPUT}(v)\,\text{SLF}^{(0)}(y-v)\,dv$$

$$= I_o\left[H(y) + (1-\Sigma_t\Delta x)\,H(-y) + \left(\frac{\Sigma_s \Delta x}{2}\right) \text{ftan}(y/d_o)\right], \tag{4-15}$$

where H(y) is the Heaviside step function (83), and

$$\text{ftan}(y) = \frac{1}{2} - \left(\frac{1}{\pi}\right)\tan^{-1}(y). \tag{4-16}$$

The corresponding first order edge response function is also derived in section A.4. This response is here named the "scattering edge function" (SEF) by analogy with its generating transfer function, the SLF, and is shown in Fig. 4.3. The outstanding features are the two inverted but otherwise identical hump-shaped distortions on either side of the knife edge location, centred on and diminishing in magnitude with distance from the edge location. Note that the scaled abscissa in Fig. 4.3 implies that these distortions elongate with increasing separation of the distribution plane from the knife-edged slab.

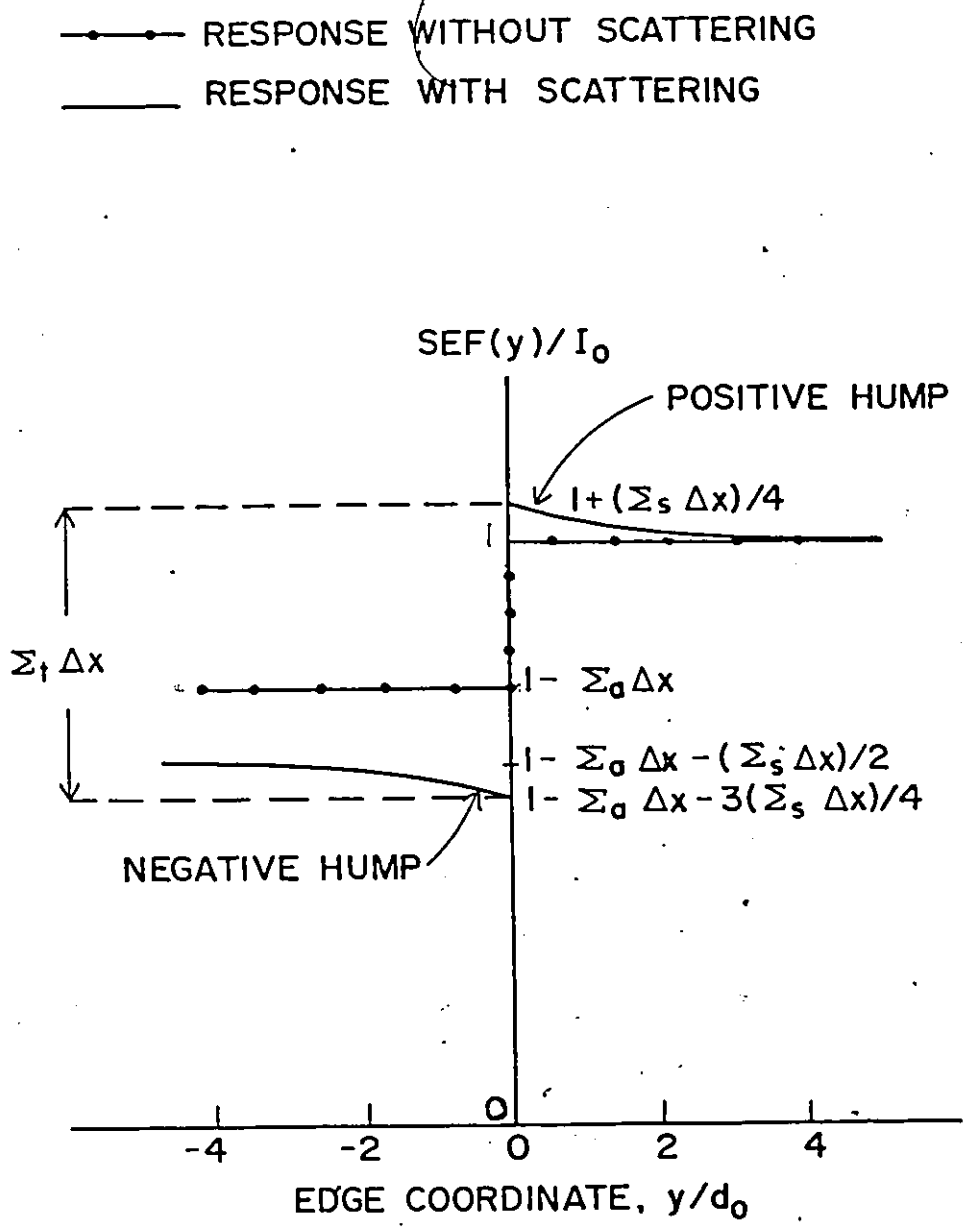

Fig. 4.3: Normalized SEF illustrating scattering based edge distortions, for slab attenuation values of $\Sigma_t \Delta x = 1/2$, $\Sigma_s \Delta x = 1/4$.

As suggested by the included response curve for the case of no scattering, these hump distortions are strictly a manifestation of object scattering. Quite simply, neutrons scattering at $y < 0$ will fractionally enter the $y > 0$ region but the reverse doesn't occur. This results in a net outward current from the solid portion of the slab in the y direction so that relative to the nonscattering response there is an increase in intensity for $y > 0$ and a decrease for $y < 0$. The relative decrease also has a constant component due to backscattered neutrons. This explains the existence of the humps. To explain the shape of these scattering based edge distortions (SBED's), it is true that localized edge effects must vanish at large distances from the edge so that the SBED's should diminish with distance from the edge. A geometric elucidation is offered by the shape of the scattering distribution in Fig. 4.1b; the intensity of the isotropic scattered distribution taken along a plane at $x = d_0$ diminishes with the distance along the y axis from the line source.

The effect of scattered radiation at a thick edge appears to have first been studied by Wideroe (95), who neither predicted nor found SBED's in the edge responses. Halmshaw (2) asserts that the edge scattering effect only reduces local contrast. From Fig. 4.3, the edge scattering effect evidently increases contrast nonuniformly; the SBED's are not of constant height.

The existence of positive and negative SBED's in a neutron radiographic edge response appears to have first been documented by Matfield (96) while qualitatively explaining the shape of a cylindrical object edge optical density trace. This phenomenon was also predicted by Butler and Harms (97) from the results of a Monte Carlo simulation. However, no analyses have appeared in the literature quantitatively describing or analyzing this phenomenon. Such an analysis is clearly necessary to estimate the magnitude of the effect and also the impact it may have on existing edge response analytical methods. The need for this and related mathematical models still exists, particularly in dimensional neutron radiography (98), where the goal is to determine an edge location.

Note that these SBED's differ significantly from those of the Eberhard effect (128). The ratio of the total SBED height to the SEF amplitude, defined as SEF(∞) − SEF($-\infty$), for the zeroth order model is given by the following relative SBED height:

$$R_{SBED}^{(0)} = \frac{\Sigma_s}{\Sigma_s + 2\Sigma_a} \qquad (4\text{-}17)$$

Because there are no multiple interactions, $R_{SBED}^{(0)}$ is the maximum attainable ratio over all such edges. In the limiting case of no absorption, $R_{SBED}^{(0)} \rightarrow 1.0$, which is indeed significantly large.

Of course, other image unsharpness sources will tend to smooth over the SBED's as each source represents a convolution of $SEF^{(0)}(y)$ with another STF. For high resolution neutron radiography in which the dominant unsharpness source is screen-film unsharpness, it will be shown in section 4.5 that such smoothing is not so great as to remove these SBED's.

This suggests the application of the SEF as a diagnostic tool for the determination of the build-up factor, section 2.3, in the neutron radiation emergent from an inspected object and impingent on a recording device. By placing a small "infinite" knife edge between the object and the recording device, the degree of deviation of R_{SBED} from the ideal value obtained for collimated neutrons impingent on the knife edge is indicative of the build-up factor in the neutron beam emergent from the object. Rather than using absolutes, such as either the total SBED height or the maximum SEF amplitude, R_{SBED} is an appealing indicator since, as a ratio, it allows for the isolation of scattering effects from other system parameters such as characteristic curve and absolute intensity of the incident neutron beam. For example, inspection of Fig. 4.3 reveals that the SBED height itself depends on I_o, whereas $R_{SBED}^{(0)}$ does not. It will be verified in Chapters 5 and 6 that R_{SBED} indeed possesses merit as an object scattering indicator.

In practice, an infinitesimally narrow slab represents an idealization if only because it precludes the possibility of multiple interactions. Indeed, multiple interactions will cause the SLF to be positively skewed since neutrons emergent from the $y = 0$ face can undergo no further collisions. Moreover, this skewing attains a maximum as $y_0 \rightarrow 0^-$ and reduces to complete symmetry as $y_0 \rightarrow -\infty$. A better model should thus account for the property that the SLF changes shape across the slab and is therefore shift variant. Toward this end, the SLF model is hereby extended to exhibit a degree of asymmetry, although constant and thus assumed averaged over $y \in (-\infty, 0)$. Retaining the notational simplicity of the zeroth order model, which is justified on the grounds that exponential attenuation is approximated for the general cross-section Σ by

$$\exp[-\Sigma x] \approx 1 - \Sigma x, \tag{4-18}$$

the improved model features the following SLF:

$$SLF^{(0)}(y,y_0) = \frac{1}{(1-\Sigma_a \Delta x)} \{(1-\Sigma_t \Delta x)\,\delta_D(y-y_0) + \Sigma_s \Delta x\, F(y-y_0)\}, \tag{4-19}$$

where

$$F(y-y_0) = [2\pi d]^{-1} \begin{cases} \left[1+\left(\frac{y-y_0}{d_1}\right)^2\right]^{-1}, & y \geq y_0 \\ \left[1+\left(\frac{y-y_0}{d_2}\right)^2\right]^{-1}, & y \leq y_0 \end{cases} \tag{4-20}$$

Here, the spreading coefficients d_1 and d_2 are analogs of the previous spreading coefficient, d_0, which had a direct and simple physical interpretation as a distance under conditions of single isotropic scattering. These new coefficients are left further unspecified, except to note that they must account for multiple scattering, that $d_1 > d_2$, and that their average value is defined as $\bar{d}$. The SEF is determined, as before, by convolution and is found to be

$$SEF(y) = I_0 \left| H(y) + (1-\Sigma_t \Delta x) H(-y) + \frac{\Sigma_s \Delta x}{4}\left(\frac{d_1}{\bar{d}}\right) - \left(\frac{\Sigma_s \Delta x}{2\pi \bar{d}}\right) g(y) \right|, \tag{4-21}$$

where

$$g(y)=\begin{cases} d_2 \tan^{-1}(y/d_2), & y \le 0 \\ d_1 \tan^{-1}(y/d_1), & y \ge 0 \end{cases} \tag{4-22}$$

Equation (4-21) reduces to Eq. (4-15) when $d_o = d_1 = d_2$. The function SEF(y) is shown in Fig. 4.4. Notice that the asymmetric SLF has resulted in asymmetric SBED's. The contribution of neutrons from $y < 0$ to $y > 0$ is more uniform than the corresponding accumulation in $y > 0$ so that the positive SBED is more pronounced than its negative counterpart.

4.4 Comparison with Monte Carlo Calculations

The validity of the above transfer function modelling is suggested by a comparison of the SEF with Monte Carlo simulation results, Chapter 5, for the case of a slab sufficiently narrow that the single scattering assumption is valid. The situation is as shown in Fig. 4.2, with $\Sigma_s = 5.0\ cm^{-1}$, $\Sigma_a = 0.0\ cm^{-1}$ and $\Delta x = d_o = 0.01$ cm. For increased accuracy, $SLF^{(1)}$ in Eq. (4-10) was used to generate a theoretical SEF, section A.4, given approximately by

$$SEF^{(1)}(y)= I_o\Bigg\{ H(y)+ \exp(-\Sigma_t \Delta x)H(-y)+\left(\frac{\Sigma_s \Delta x}{2}\right) \exp\left[\frac{-\Sigma_t \Delta x}{2}\right] \text{ftan}\left[\frac{y}{\left(d_o-\frac{\Delta x}{2}\right)}\right]\Bigg\}. \tag{4-23}$$

A comparison between the theoretical and Monte Carlo SEF is given in Fig. 4.5. The agreement is evidently of high order. Discrepancies arise from

(i) the assignment of Monte Carlo "bin" totals to the location corresponding to the bin centre, representing an averaging error,

(ii) multiple interactions during the simulation; despite the relatively narrow slab ($\Sigma_t \Delta x = 0.05 << 1.0$), as many as 7 interactions occurred for a single neutron over 500,000 histories, and

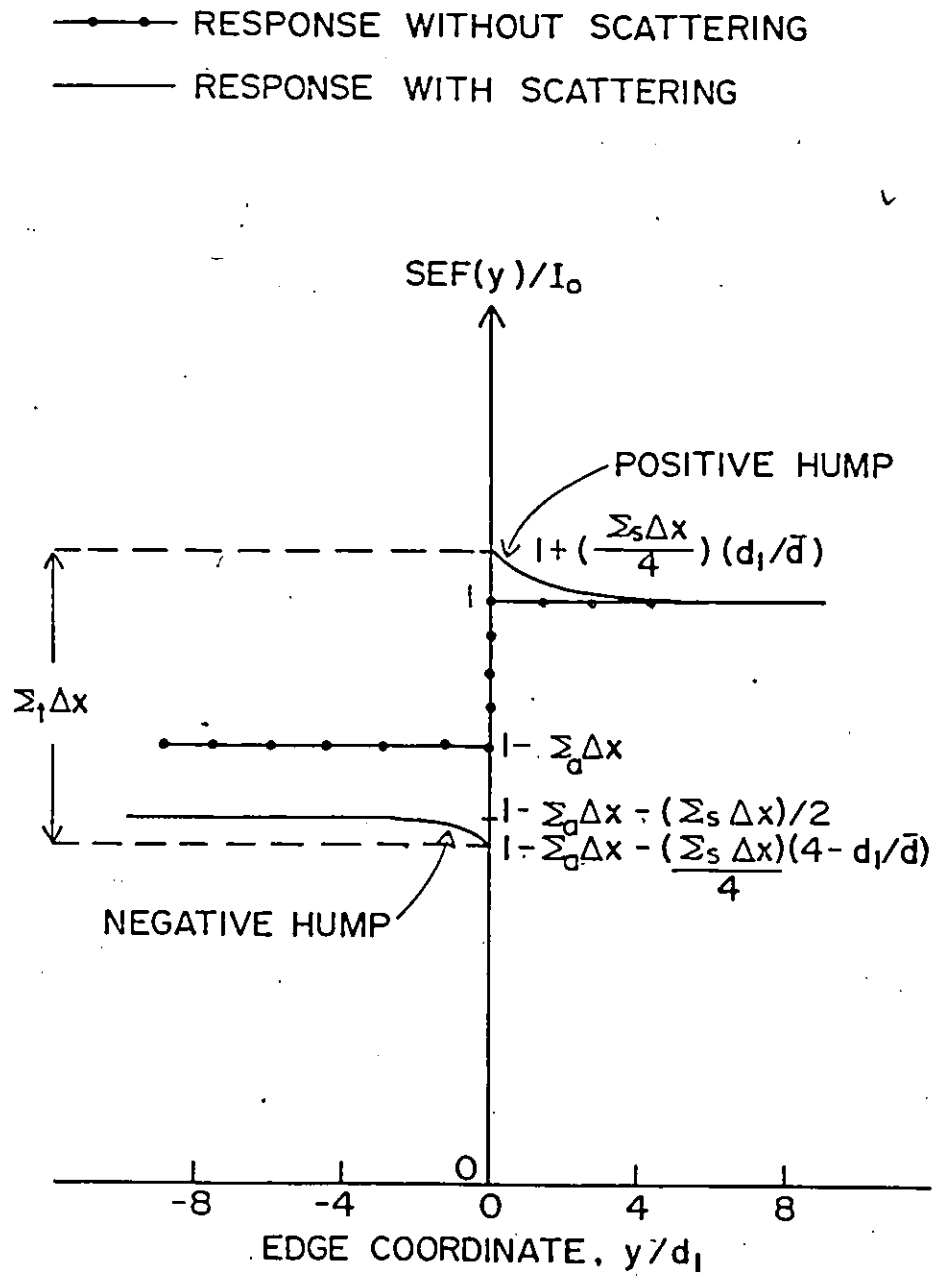

Fig. 4.4: Normalized SEF illustrating scattering based edge distortions, for slab attenuation values of $\Sigma_t\Delta x = 1/2$, $\Sigma_s\Delta_x = 1/4$. Improved calculational model features asymmetric SLF, with $d_1/d_2 = 2.0$.

(iii) the unification of the two solution scales as this involved estimating the Monte Carlo edge response at $y = \pm \infty$.

4.5 Screen-Film Unsharpness Effect – Multiple Convolution

A general system output function $O^{(n)}(y)$, obtained as the convolution of the system input $I^{(n)}(y)$ with the general system scattering transfer function $SLF^{(n)}_{gen}(y)$, is written using the following unambiguous notation:

$$O^{(n)}(y) = I^{(n)}(y) * SLF^{(n)}_{gen}(y)$$

$$\stackrel{df}{=} \int_{-\infty}^{\infty} I^{(n)}(v)\, SLF^{(n)}_{gen}(y-v)\, dv. \qquad (4\text{-}24)$$

The superscript n refers to geometric order, discussed in section 4.1. This output response, for all forms of radiography, is further degraded by screen-film unsharpness which mathematically is represented here by a general line spread function, LSF_{gen}. The resulting total output response, $O'^{(n)}(y)$, combines the effects of screen-film unsharpness and scattering degradation. Mathematically, $O'^{(n)}(y)$ is given by the following convolution:

$$O'^{(n)}(y) = O^{(n)}(y) * LSF_{gen}(y). \qquad (4\text{-}25)$$

Substituting Eq. (4-24) into Eq. (4-25) yields

$$O'^{(n)}(y) = (I^{(n)}(y) * SLF^{(n)}_{gen}(y)) * LSF_{gen}(y)$$

$$= I^{(n)}(y) * (SLF^{(n)}_{gen}(y) * LSF_{gen}(y))$$

$$\stackrel{df}{=} I^{(n)}(y) * TSLF^{(n)}_{gen}(y), \qquad (4\text{-}26)$$

defining the "total scattering line function" ($TSLF_{gen}{}^{(n)}(y)$) as the convolution of STF's representing screen-film unsharpness and scattering degradation.

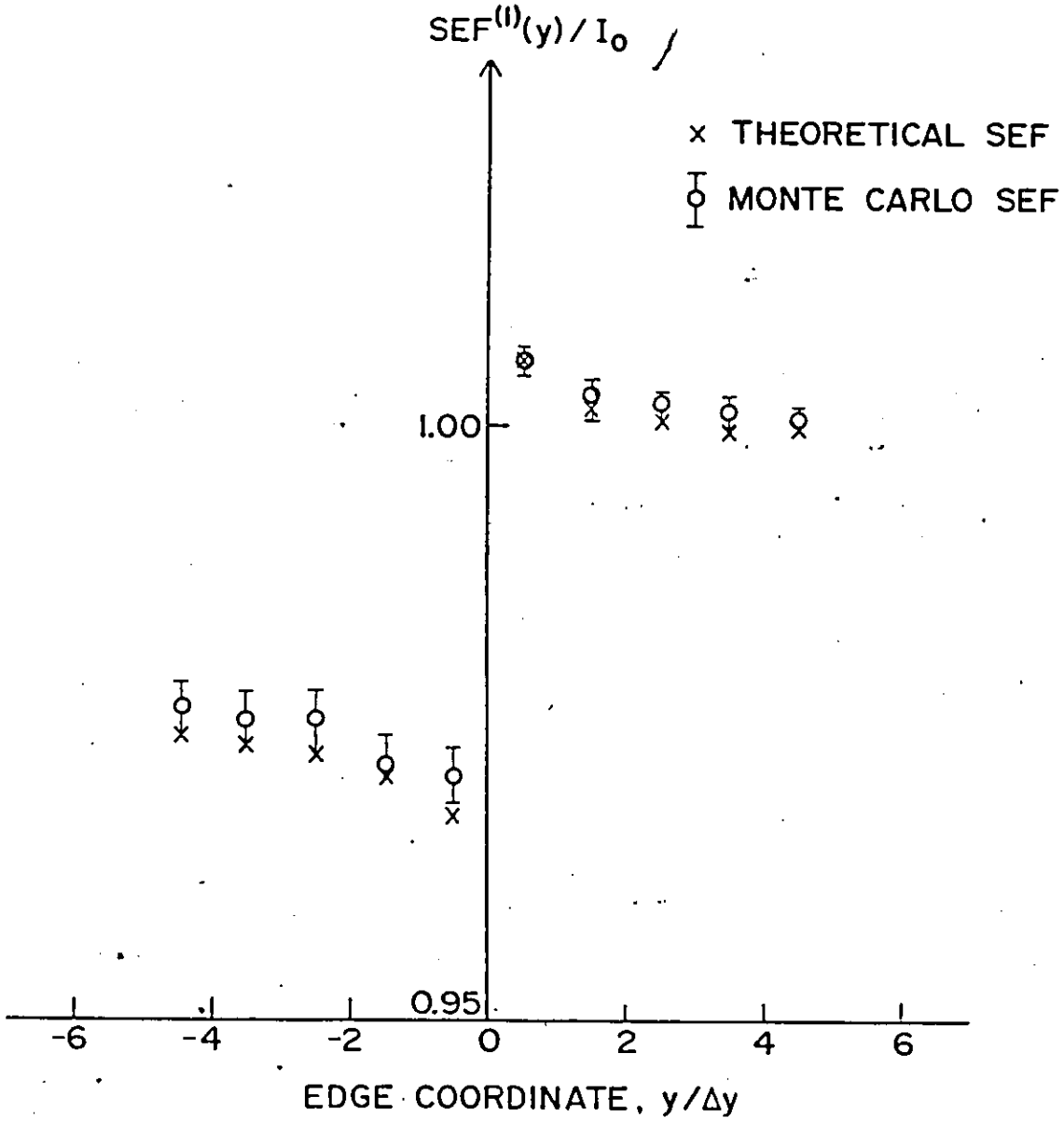

Fig. 4.5: Comparison of Monte Carlo and theoretical SEF calculations for a slab with $\Sigma_s = 5.0\ cm^{-1}$, $\Sigma_a = 0.0\ cm^{-1}$, $d_0 = \Delta x = 0.01$ cm. For the Monte Carlo calculation, the results of 500,000 histories were scored in bins of width $\Delta y = 2/300$ cm.

For high resolution neutron radiography, these two are the only significant image degradation effects, so that $TSLF_{gen}^{(n)}(y)$ is the overall system transfer function. The system is assumed to be represented here by a shift invariant SLF_{gen} and LSF. This assumption is usually valid for the LSF, at least over any given isoplanatic patch (99). The image plane can be partitioned into regions over each of which shift invariance of the LSF holds. These regions are referred to as "isoplanatic patches". For more general geometries in which SLF_{gen} is shift variant, the convolution notation in Eq. (4-24) is extended to mean

$$I^{(n)}(y) * SLF_{gen}^{(n)}(y) \stackrel{df}{=} \int_{-\infty}^{\infty} I(v) SLF_{gen}^{(n)}(y,v)\, dv. \tag{4-27}$$

The function $SLF_{gen}^{(n)}$ is interpreted as the response at y to a collimated incident line source at v and does not necessarily have the form $SLF_{gen}^{(n)}(y - v)$. We add that although the general system transfer function STF(y, v) describes an output at y due to an input at v, the v-dependence is often suppressed, as in the convolution notation in Eq. (4-27).

Applying the above formalism to the knife-edge geometry of Fig. 4.2, it follows that for a collimated incident neutron beam of uniform intensity I_o, the input, output and system transfer functions become:

$$I^{(n)}(y) \rightarrow \begin{cases} I_o(1-\Sigma_a \Delta x) \stackrel{df}{=} I_-^{(0)}(y), & y < 0,\ n=0 \\ I_o \exp(-\Sigma_a \Delta x) \stackrel{df}{=} I_-^{(1)}(y), & y < 0,\ n=1, \\ I_o \stackrel{df}{=} I_+(y), & y > 0,\ n=0,1 \end{cases} \tag{4-28}$$

$$SLF_{gen}^{(n)}(y) \rightarrow \begin{cases} SLF^{(n)}(y,v) \stackrel{df}{=} SLF_-^{(n)}(y,v), & v < 0 \\ \delta_D(y-v) \stackrel{df}{=} SLF_+^{(n)}(y,v), & v \geq 0 \end{cases} \tag{4-29}$$

$$LSF_{gen}(y,v) \rightarrow \frac{1}{n\bar{d}_f}\left[1+\left(\frac{y-v}{\bar{d}_f}\right)^2\right]^{-1} \stackrel{df}{=} LSF(y,v), \tag{4-30}$$

$$TSLF_{gen}^{(n)}(y) \rightarrow \begin{cases} SLF_{-}^{(n)}(y) \ * \ LSF(y) \overset{df}{=} TSLF_{-}^{(n)}(y), & y<0 \\ SLF_{+}^{(n)}(y) \ * \ LSF(y) \overset{df}{=} TSLF_{+}^{(n)}(y), & y>0 \end{cases} \quad (4\text{-}31)$$

$$O^{(n)}(y) \rightarrow SEF^{(n)}(y), \quad (4\text{-}32)$$

$$O'^{(n)}(y) \rightarrow TSEF^{(n)}(y). \quad (4\text{-}33)$$

Here, $SLF^{(n)}(y, v)$ is the nth order SLF, given by Eqs. (4-8) and (4-10), and $SEF^{(n)}(y)$ is the corresponding SEF, given by Eqs. (4-15) and (4-23). The overall edge output response has been defined above as $TSEF^{(n)}(y)$, the "total scattering edge function", and is computed using

$$TSEF^{(n)}(y) = [\, I_{-}^{(n)}(y) \ * \ SLF_{-}^{(n)}(y) \ + \ I_{+}^{(n)}(y) \ * \ SLF_{+}^{(n)}(y)] \ * \ LSF(y)$$

$$= I_{-}^{(n)}(y) \ * \ TSLF_{-}^{(n)}(y) \ + \ I_{+}^{(n)}(y) \ * \ TSLF_{+}^{(n)}(y). \quad (4\text{-}34)$$

A derivation of the line spread function, LSF(y, v), used in Eq. (4-30) is given in section A.1. It suffices here to understand that the parameter $\overline{d}_f$ is indicative of the magnitude of screen-film unsharpness in the system.

The calculation of the various STF's is now direct, analytical and performed in section A.5. The results are written compactly as:

$$TSLF_{+}^{(n)}(y,v) = LSF(y,v), \quad (4\text{-}35)$$

$$TSLF_{-}^{(n)}(y,v) = A^{(n)}\left\{ K^{(n)} LSF(y-v) + \frac{1}{nd_n}\left(\frac{s_n \Sigma_s \Delta x}{2} \right) F_{-}^{(n)}(y-v) \right\}, \quad (4\text{-}36)$$

$$TSEF^{(n)}(y) = I_o\left\{ \frac{G_{+}^{(n)}}{2} + \frac{G_{-}^{(n)}}{\pi} \tan^{-1}\left(\frac{y}{\overline{d}_f} \right) + \left(\frac{s_n \Sigma_s \Delta x}{2} \right) \text{ñân}\left(\frac{y}{\beta_n d_n} \right) \right\}. \quad (4\text{-}37)$$

The following constituent functions and additional terms are defined for usage in the above equations:

$$G_{\pm}^{(n)} = 1 \pm K^{(n)}, \quad (4\text{-}38)$$

$$K^{(n)} = \begin{cases} 1-\Sigma_t\Delta x & , n=0 \\ \exp[-\Sigma_t\Delta x], & n=1 \end{cases} \quad , \tag{4-39}$$

$$d_n = \begin{cases} d_o & , n=0 \\ d_o - \frac{\Delta x}{2}, & n=1 \end{cases} \quad , \tag{4-40}$$

$$s_n = \exp[-n\,\Sigma_t\,\Delta x/2],\ n = 0, 1 \quad , \tag{4-41}$$

$$A^{(n)} = \begin{cases} (1-\Sigma_a\Delta x)^{-1} & , n=0 \\ \exp[\Sigma_a\Delta x] & , n=1 \end{cases} \quad , \tag{4-42}$$

$$F_{\pm}^{(n)}(y) = \left(\frac{1}{\beta_n}\right)\left[1+\left(\frac{y-v}{\beta_n d_n}\right)^2\right]^{-1} \quad , \tag{4-43}$$

$$\beta_n = 1 + (\bar{d}_f/d_n) \quad . \tag{4-44}$$

Since neutrons incident on $y > 0$ emerge uncollided, $TSLF_+^{(n)}(y, v)$ reduces to $LSF(y, v)$ as stated in Eq. (4-35). Note that $TSLF_-^{(n)}(y, v)$ in Eq. (4-36) is split into two terms. The first term represents neutrons that traverse the solid slab, $y < 0$, without interaction, and thus lead to image degradation only through the screen-film unsharpness symbolized by $LSF(y, v)$. The second term represents the distribution of scattered neutrons being further smoothed by convolution with $LSF(y)$ and reduces to $SLF^{(n)}$ in Eqs. (4-8) and (4-10) when $\bar{d}_f \to 0$. Finally, $TSEF^{(n)}(y)$ reduces to $SEF^{(n)}(y)$ in Eqs. (4-15) and (4-23) when $\bar{d}_f \to 0$.

The system transfer functions $TSLF_{\pm}^{(n)}$ and $TSEF^{(n)}$, given in Eqs. (4-35) to (4-37), have been plotted in Figs. 4.6 and 4.7 for representative geometric and material parameters, and over a range of applicable LSF functions. The FORTRAN program STFS was written to perform these calculations and is listed in Appendix D.

Since $\bar{d}_f$ is interpreted geometrically, section A.1, as being approximately the convertor to film emulsion separation, it should typically lie in the range $\bar{d}_f \in [10\ \mu m, 100\ \mu m]$

for high resolution neutron radiography. The relevant attenuation product used to generate Figs. 4.6 and 4.7 was

$$\Sigma_s \Delta x = 0.3, \tag{4-45}$$

so that approximately only 26% of the neutrons incident on the solid slab portion would initially scatter. Since only a fraction of these would undergo multiple scattering, the single scattering approximation should be applicable to these calculations.

The smoothing of the Dirac delta component of SLF_ through convolution with an LSF is evident in Figs. 4.6. Although not identical, the shapes of LSF and TSLF_ are similar, consistent with the observation (50) that the Lorentzian form is well suited as an overall system line spread function. Indeed, evidence of a two-component SLF has been virtually removed through convolution in Fig. 4.6b, even though the LSF spreading parameter, $\bar{d}_p$ is only one-twentieth the magnitude of the scattering spreading parameter, d_o. It should be noted that LSF is normalized to unit area whereas TSLF_ is normalized to an area, section A.5, given by

$$\int_{-\infty}^{\infty} \mathrm{TSLF}_{-}^{(n)}(y-v)\,dy = A^{(n)}\left[K^{(n)} + \frac{s_n \Sigma_s \Delta x}{2}\right], \tag{4-46}$$

reducing to unity when $\Sigma_s = 0.0\ \mathrm{cm}^{-1}$. As explained in section 4.1, this nonstandard normalization arises because of backscattering losses.

The TSEF shown in Figs. 4.7 is a convolution of SEF with LSF as indicated in Eq. (4-34). While smoothing the discontinuity and sharp SBED's of SEF, this convolution by itself will not remove these SBED's as initially suggested in section 4.3. However, for recorders characterized by an unsharpness parameter of $\bar{d}_f \geq 50\ \mu\mathrm{m}$, the SBED's have been flattened so as to render them unnoticeable. If these SBED's are to form the basis of a scattering diagnostic tool, a high resolution recorder, such as includes a gadolinium convertor, is desirable. This convolution also partially explains why the SBED's phenomenon has been previously overlooked.

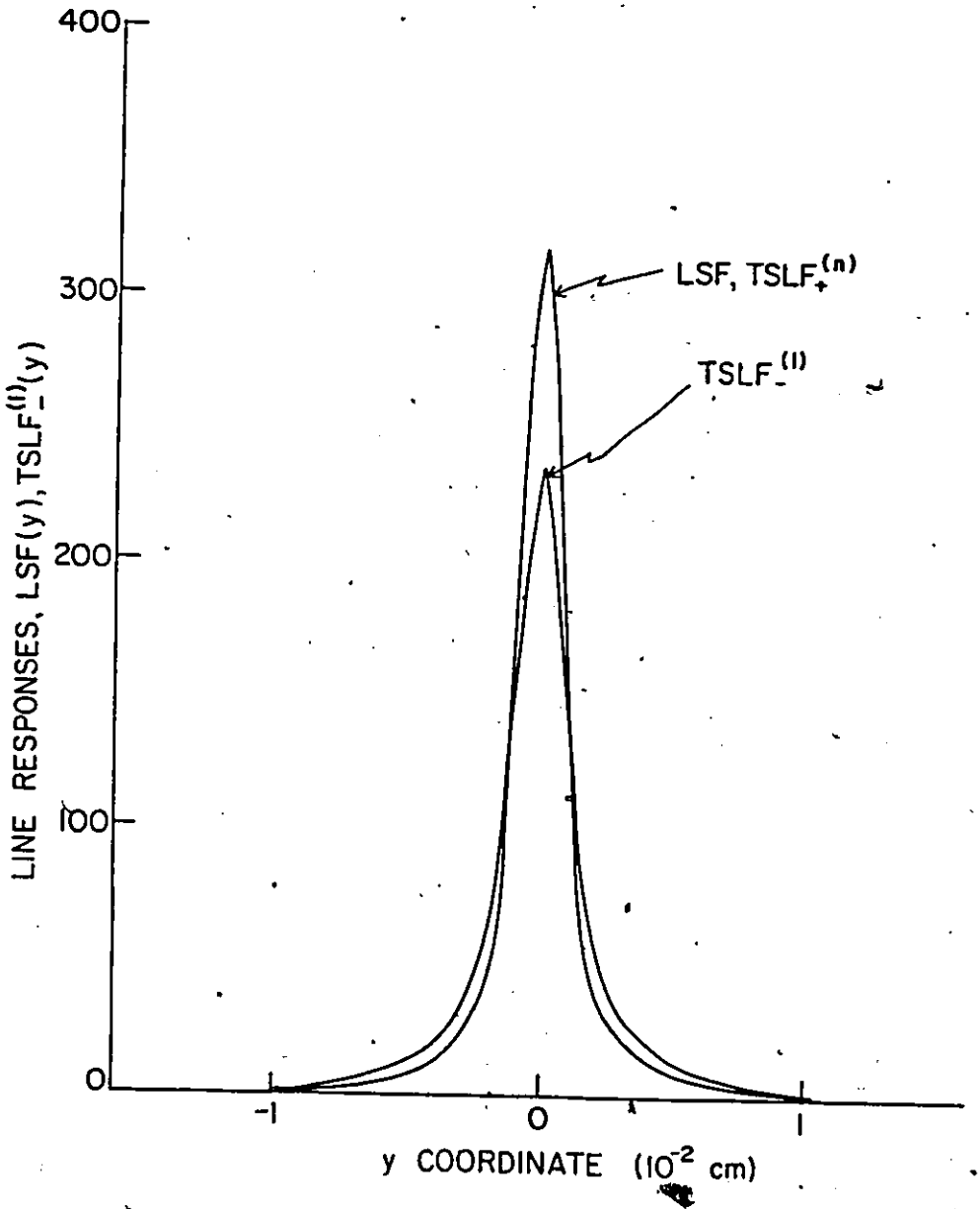

Fig. 4.6a: LSF and TSLF_ for $\Sigma_s = 6.0\ cm^{-1}$, $\Sigma_a = 0.0\ cm^{-1}$, $\Delta x = 0.05$ cm, $d = 0.1$ cm and $\bar{d}_f = 10.0$ μm.

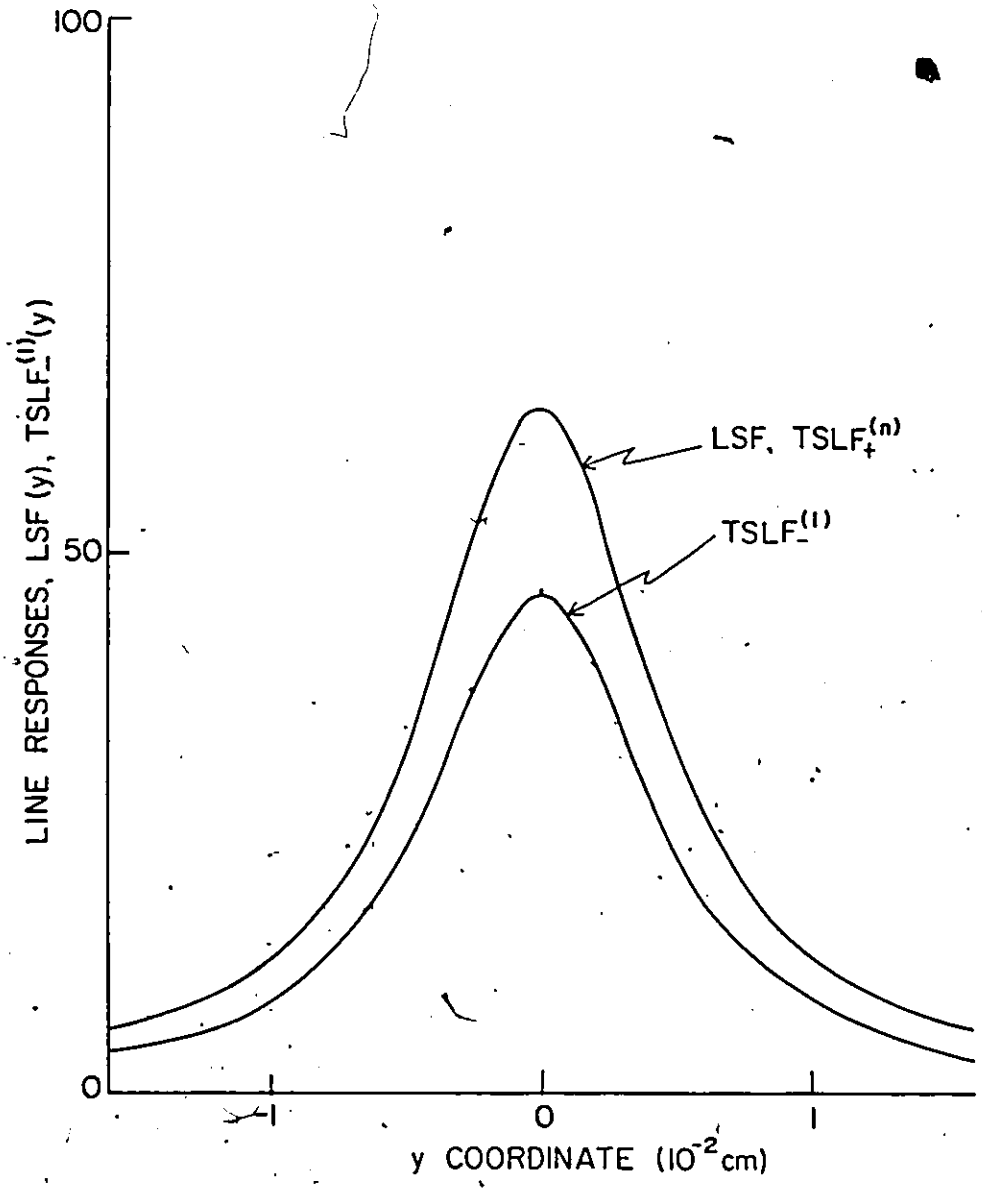

Fig. 4.6b: LSF and TSLF$_-$ for $\Sigma_s = 6.0$ cm^{-1}, $\Sigma_a = 0.0$ cm^{-1} $\Delta x = 0.05$ cm, $d = 0.1$ cm and $\bar{d}_f = 50.0$ μm.

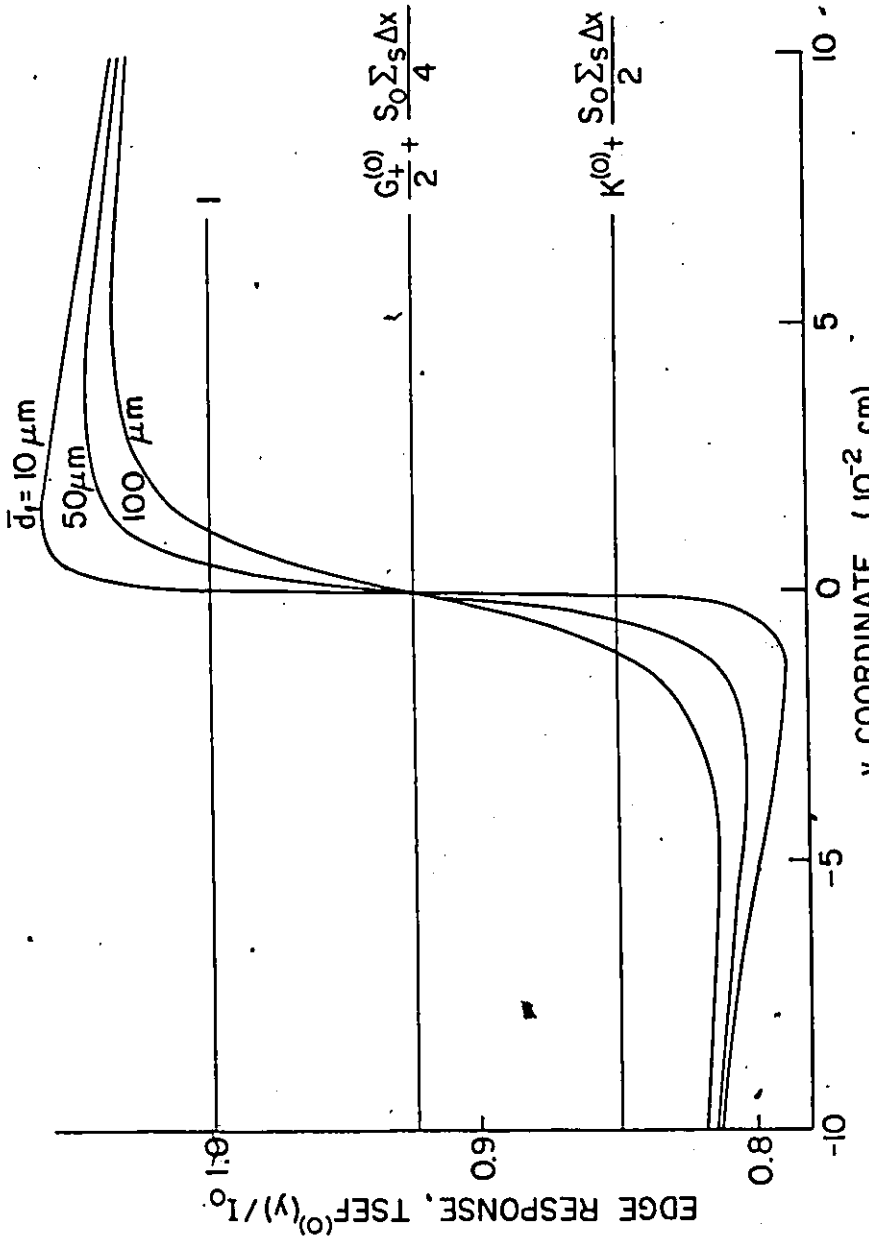

Fig. 4.7a: $TSEF^{(0)}(y)$ for a slab with $\Sigma_s = 6.0\ cm^{-1}$, $\Sigma_a = 0.0\ cm^{-1}$, $\Delta x = 0.05$ cm, $d = 0.1$ cm and various $\bar{d}_f$.

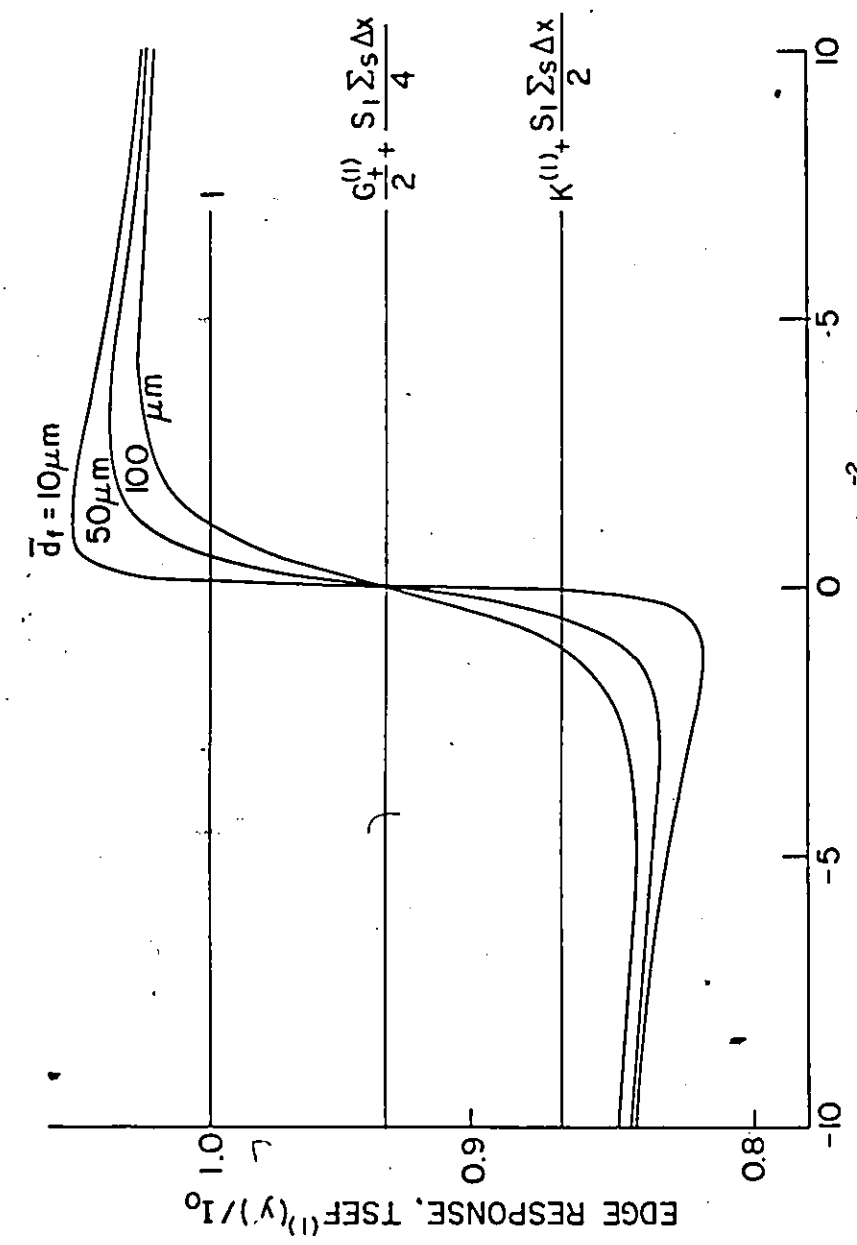

Fig. 4.7b: TSEF$^{(1)}$(y) for a slab with $\Sigma_s = 6.0$ cm^{-1}, $\Sigma_a = 0.0$ cm^{-1}, $\Delta x = 0.05$ cm, d = 0.1 cm and various $\bar{d}_f$.

It is relevant to note the TSEF response corresponding to the actual knife edge since this determination has been the subject of previous research (100-102). From Eq. (4-37), the edge location corresponds to the output response

$$TSEF^{(n)}(0) = I_o\left\{ \frac{G_+^{(n)}}{2} + \frac{s_n \Sigma_s \Delta x}{4} \right\}, \tag{4-47}$$

exhibiting dependence on several fundamental geometric and material parameters whenever scattering occurs. The incorporation of scattering effects into an edge location prescription is thus an important consideration. It has not previously been quantitatively assessed. Since additional processing of the TSEF response through the film's characteristic curve must precede actual image interpretation, the goal of an objective edge location through identification with a certain optical density appears elusive at this stage due to the multi-parameter dependence of $TSEF^{(n)}(0)$.

It is significant, however, that $TSEF^{(n)}(0)$ exhibits no dependence on the image degradation parameters d and $\bar{d}_f$ consistent with the common intersection of all the curves in Figs.4.7 at the edge location, y = 0.0 cm. This lack of dependence on the system transfer functions is remarkable, fortunate, generalizable and the subject of Appendix C.

It is also relevant to note the TSEF response at $y = \pm\infty$, since these values determine the actual SBED height. From Eq. (4-37), these output responses are

$$TSEF^{(n)}(\infty) = I_o, \tag{4-48}$$

$$TSEF^{(n)}(-\infty) = I_o\left\{ K^{(n)} + \frac{s_n \Sigma_s \Delta x}{2} \right\}. \tag{4-49}$$

These responses are also independent of d and $\bar{d}_f$; this is expected in light of the knife edge's spatial uniformity at $y = \pm\infty$. Also, and for the same reason, the $TSEF^{(n)}(-\infty)$ response is precisely the area under the $TSLF_-^{(n)}$ curve multiplied by a factor accounting for the total incident neutron fluence.

4.6 Modulation Transfer Functions

In the general case, as discussed in sections 1.3 and 2.1, an imaging system is represented mathematically by the transformation of an input function i(u,v) to an output response function o(x, y), given by

$$o(x,y) = \int_{-\infty}^{\infty}\int_{-\infty}^{\infty} i(u,v)\,h(x,y,u,v)\,du\,dv + n(x,y)\,. \tag{4-50}$$

Here, (u, v) and (x, y) are identical Cartesian coordinate systems defined on the object and image planes, respectively. The PSF h(x, y, u, v) is the relevant STF and n(x, y) denotes the system noise contribution. Recall from section 1.3 that for a linear shift invariant system

$$h(x, y, u, v) = h(x - u, y - v)\,. \tag{4-51}$$

In this case, Eq. (4-50) is the following convolution

$$o(x, y) = i(x, y) \;*\; h(x, y) + n(x, y)\,. \tag{4-52}$$

Equation (4-52) can in principle be solved for i(x, y) given the image o(x, y) through the use of Fourier transform methods. Fourier transformation of Eq. (4-52) yields, by the convolution theorem (70),

$$O(\nu_x, \nu_y) = I(\nu_x, \nu_y)\,H(\nu_x, \nu_y) + N(\nu_x, \nu_y). \tag{4-53}$$

Here, ν_x and ν_y are spatial frequencies in the x and y directions, O and I are the complex spatial frequency spectra of o and i, N is the noise spectrum, and H is the "optical transfer function" (OTF) (65,66) of the system.

In the absence of noise, Eq. (4-53) admits the following direct solution for $I(\nu_x, \nu_y)$:

$$I(\nu_x, \nu_y) = O(\nu_x, \nu_y)/H(\nu_x, \nu_y)\,. \tag{4-54}$$

The original input, i, is then obtained by inverse Fourier transforming I. The deconvolution of Eq. (4-50) has thus been performed in this simple illustrative case through Fourier transformation, effectively replacing a double integral by a multiplication. For

isotropic imaging systems (65), $H(\nu_x, \nu_y)$ is real and reduces to the "modulation transfer function" (MTF), defined in the general case by

$$MTF(\nu_x, \nu_y) = |H(\nu_x, \nu_y)|. \tag{4-55}$$

Also, for isotropic systems, MTF is calculable as the Hankel Transform (66) of h(r), and is given by

$$MTF(\nu_r) = 2\pi \int_0^\infty h(r)\, Jo(2\pi\nu_r r)\, r dr, \tag{4-56}$$

where Jo is the zeroth order Bessel function (83), and

$$r = [(x-u)^2 + (y-v)^2]^{\frac{1}{2}}, \tag{4-57}$$

$$\nu_r = [\nu_x^2 + \nu_y^2]^{\frac{1}{2}}. \tag{4-58}$$

Physically, $MTF(\nu_x, \nu_y)$ is interpreted as being the ratio of the output amplitude to input amplitude of a sinusoidal pattern with rectangular spatial frequencies ν_x and ν_y being passed through the imaging system.

For the case of one-dimensional imaging, in which the input varies with only one spatial coordinate, the relevant imaging equation is

$$o(y) = \int_{-\infty}^{\infty} i(v)\, h(y-v)\, dv + n(y) \tag{4-59}$$

where n(y) is the noise contribution and h(y - v) is the shift invariant LSF corresponding to the one-dimensional MTF

$$MTF(\nu_y) = \int_{-\infty}^{\infty} h(y-v) \exp[-2\pi i \nu_y (y-v)]\, d(y-v). \tag{4-60}$$

In practice, the noise spectrum must be accounted for and the image restoration problem is ill-conditioned (103). That is, trivial perturbations in the output o(x, y) can produce non-trivial perturbations in the input i(x, y). The general image restoration problem currently constitutes a major field of research, but is not the specific concern of this research. Rather, this work is focussed on the accurate determination and interpretation of responses to fixed, usually geometrically and materially simple inputs. For purposes of completion,

however, the one- and two-dimensional MTF's corresponding to the STF's developed in this chapter are now given. Since each STF was developed for a linear, shift invariant system, each calculated OTF will also be its corresponding MTF (65). From section A.6, the MTF's corresponding to LSF, $TSLF_+^{(n)}$, $SLF_-^{(n)}$, $SPF^{(n)}$ and $TSLF_-^{(n)}$ are:

$$\text{LSF, } TSLF_+^{(n)}\text{: } MTF^{(n)}(\nu_y) = \exp[-2\pi \nu_y \bar{d}_f], \tag{4-61}$$

$$SLF_-^{(n)}: MTF^{(n)}(\nu_y) = A^{(n)}\left[K^{(n)} + \left(\frac{s_n \Sigma_s \Delta x}{2}\right) \exp[-2\pi\nu_y d_n]\right], \tag{4-62}$$

$$SPF^{(n)}: MTF^{(n)}(\nu_r) = A^{(n)}\left[K^{(n)} + \left(\frac{s_n \Sigma_s \Delta x}{2}\right) \exp[-2\pi\nu_r d_n]\right], \tag{4-63}$$

$$TSLF_-^{(n)}: MTF^{(n)}(\nu_y) = A^{(n)}\left[K^{(n)} \exp[-2\pi\nu_y \bar{d}_f] + \left(\frac{s_n \Sigma_s \Delta x}{2}\right) \exp[-2\pi\nu_y \beta_n d_n]\right]. \tag{4-64}$$

Since the MTF describes the transfer through the system of spatial frequencies, the identical form of Eqs. (4-62) and (4-63) is expected.

Note that the MTF in Eq. (4-64) is the product of the MTF's in Eqs. (4-61) and (4-62), illustrating the advantage of this Fourier analytical approach over direct convolution for cascaded systems. That is, each step of a multiple convolution of STF's requires only a multiplication of MTF's.

The MTF's in Eqs. (4-61) to (4-64) were calculated using the FORTRAN program STFS and are plotted in Figs. 4.8. For small $\bar{d}_f$ such as in Figs. 4.8a and 4.8b, the screen-film unsharpness system transfers all but the ultra-high frequencies better than the scattering system; this is referred to as a difference in fidelity.

For larger $\bar{d}_f$ such as in Figs. 4.8c and 4.8d, the fidelity superiority switches to the scattering system even though its degradation parameter d_n may be an order of magnitude greater than $\bar{d}_f$. Qualitatively, the scattering system has high fidelity when the attenuation

product $\Sigma_t \Delta x$ is small since in this case, most of the incident neutron radiation remains uncollided and hence undegraded.

Quantitatively, the scattering system has fidelity superior to that of the screen-film unsharpness system for frequencies higher than ν_y^*, where ν_y^* solves the transcendental equation

$$A^{(n)}[K^{(n)} + \left(\frac{s_n \Sigma_s \Delta x}{2}\right) \exp[-2\pi\nu_y^* d_n]] = \exp[-2\pi\nu_y^* \bar{d}_f]. \tag{4-65}$$

Note that the MTF's for $SLF_-^{(n)}$ and $TSLF_-^{(n)}$ are less than unity for $\nu_y = 0$. The interpretation here is that even ultra-low frequencies are modulated by the scattering system, a manifestation of backscattering losses.

As expected, the MTF for $TSLF_-^{(n)}(y)$ is always smaller than that for either $SLF_-^{(n)}(y)$ or LSF(y) for all ν_y since compounding individual image degradation sources can never enhance the resultant image quality.

Finally, as shown in section A.5, the convolution of two Lorentzian functions is also Lorentzian. One interesting implication of this result occurs in the analysis of multiple image degradation sources. If the i^{th} of a total of n such sources is modelled to some degree of approximation by the Lorentzian LSF

$$LSF_i(y,\nu) = \frac{1}{nd_i}\left[1 + \left(\frac{y-\nu}{d_i}\right)^2\right]^{-1}, \tag{4-66}$$

then to an input I(y) there will correspond an output

$$\begin{aligned} O(y) &= I(y) * LSF_1(y) * \ldots * LSF_n(y) \\ &= I(y) * LSF_{tot}(y), \end{aligned} \tag{4-67}$$

defining

$$LSF_{tot}(y) = LSF_1(y) * \ldots * LSF_n(y) \tag{4-68}$$

as the overall system LSF. Fourier transformation of Eq. (4-68) yields

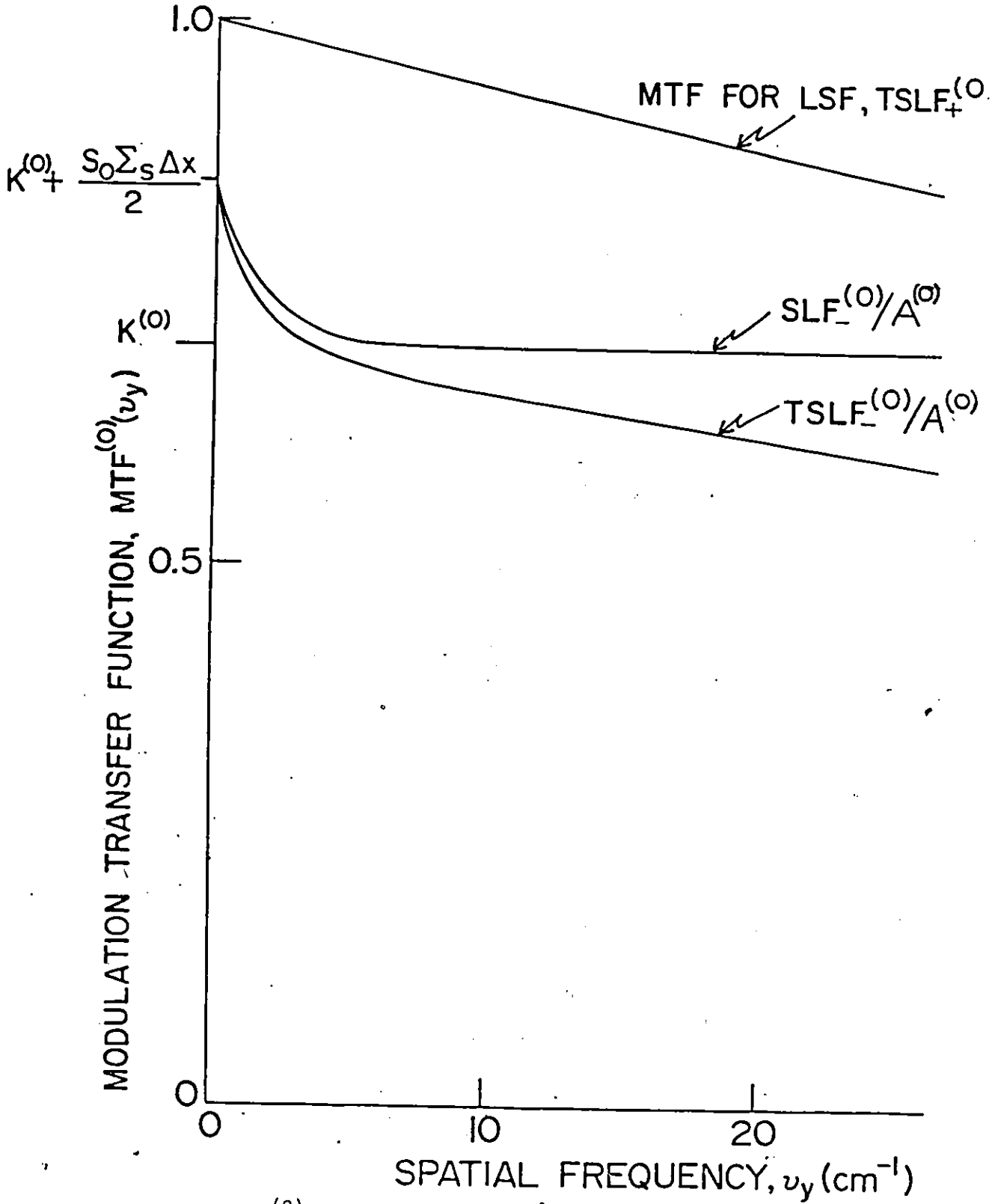

Fig. 4.8a: $MTF^{(0)}(\nu_y)$ for $\Sigma_s = 6.0\ cm^{-1}$, $\Sigma_a = 0.0\ cm^{-1}$, $\Delta x = 0.05$ cm, $d_n = 0.1$ cm and $\bar{d}_f = 10.0$ μm.

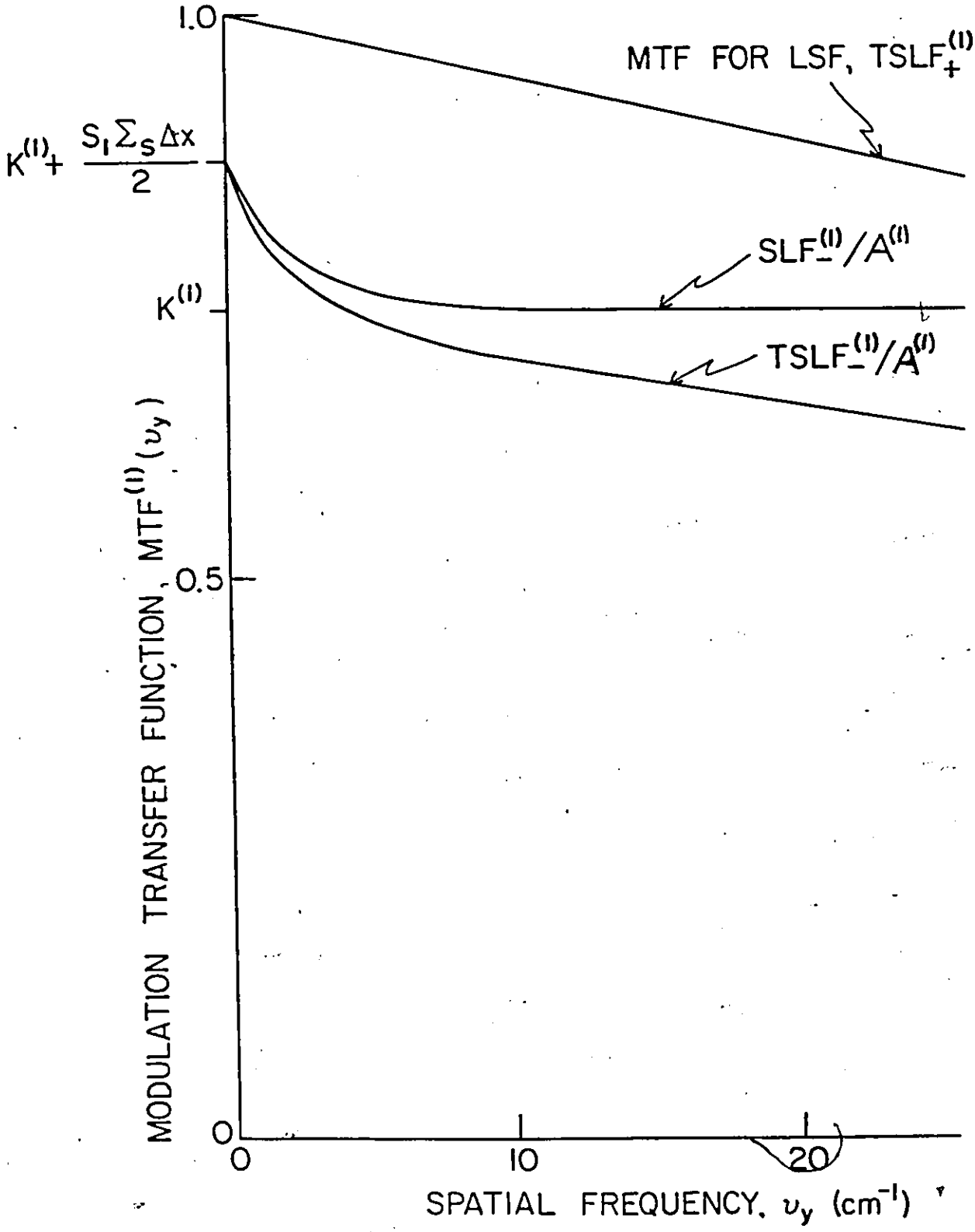

Fig. 4.8b: $MTF^{(1)}(\upsilon_y)$ for Σ_s = 6.0 cm^{-1}, Σ_a = 0.0 cm^{-1}, Δx = 0.05 cm, d_n = 0.1 cm and $\bar{d}_f$ = 10.0 μm.

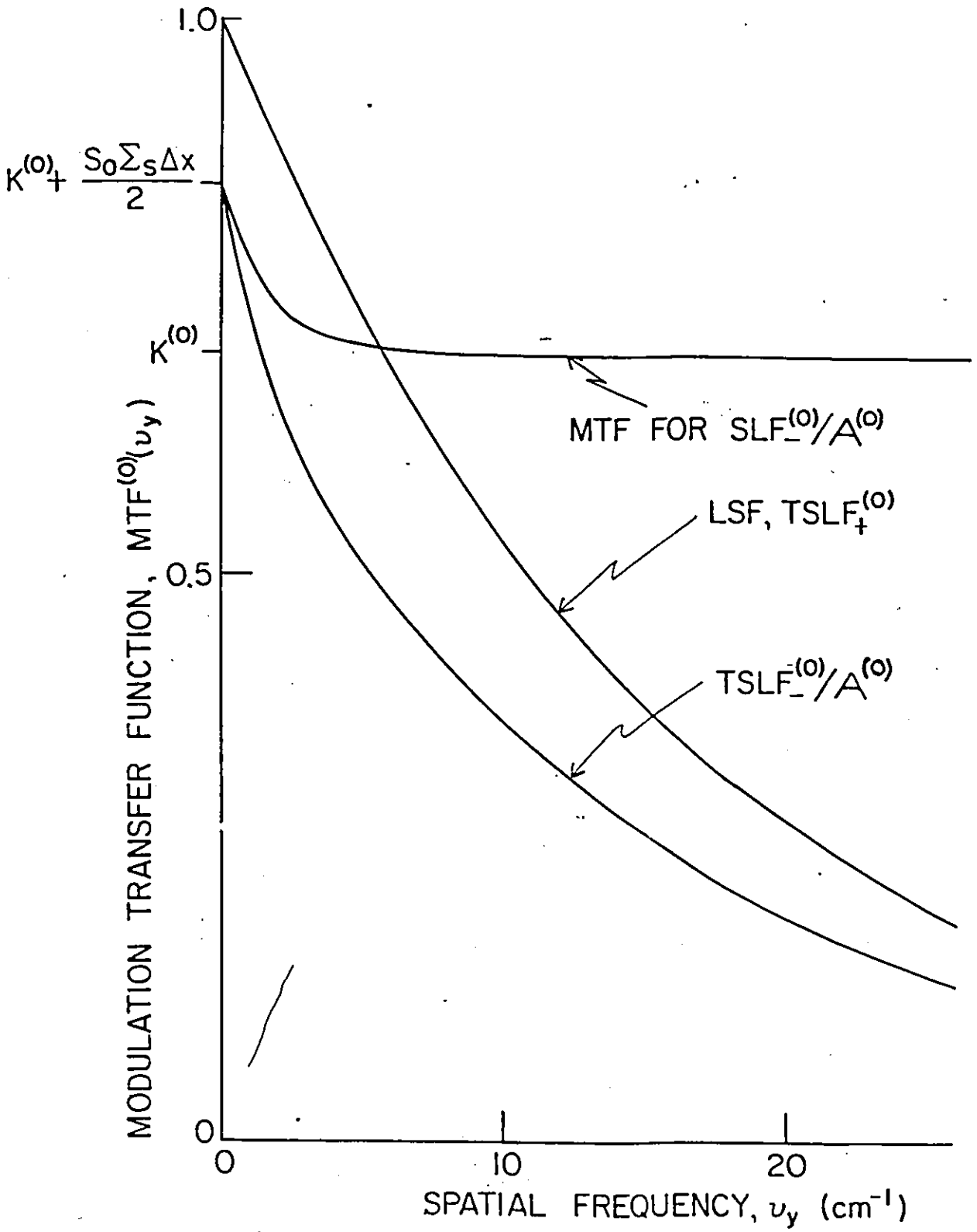

Fig. 4.8c: $MTF^{(0)}(\nu_y)$ for Σ_s = 6.0 cm^{-1}, Σ_a = 0.0 cm^{-1}, Δx = 0.05 cm, d_n = 0.1 cm and $\bar{d}_f$ = 100.0 μm.

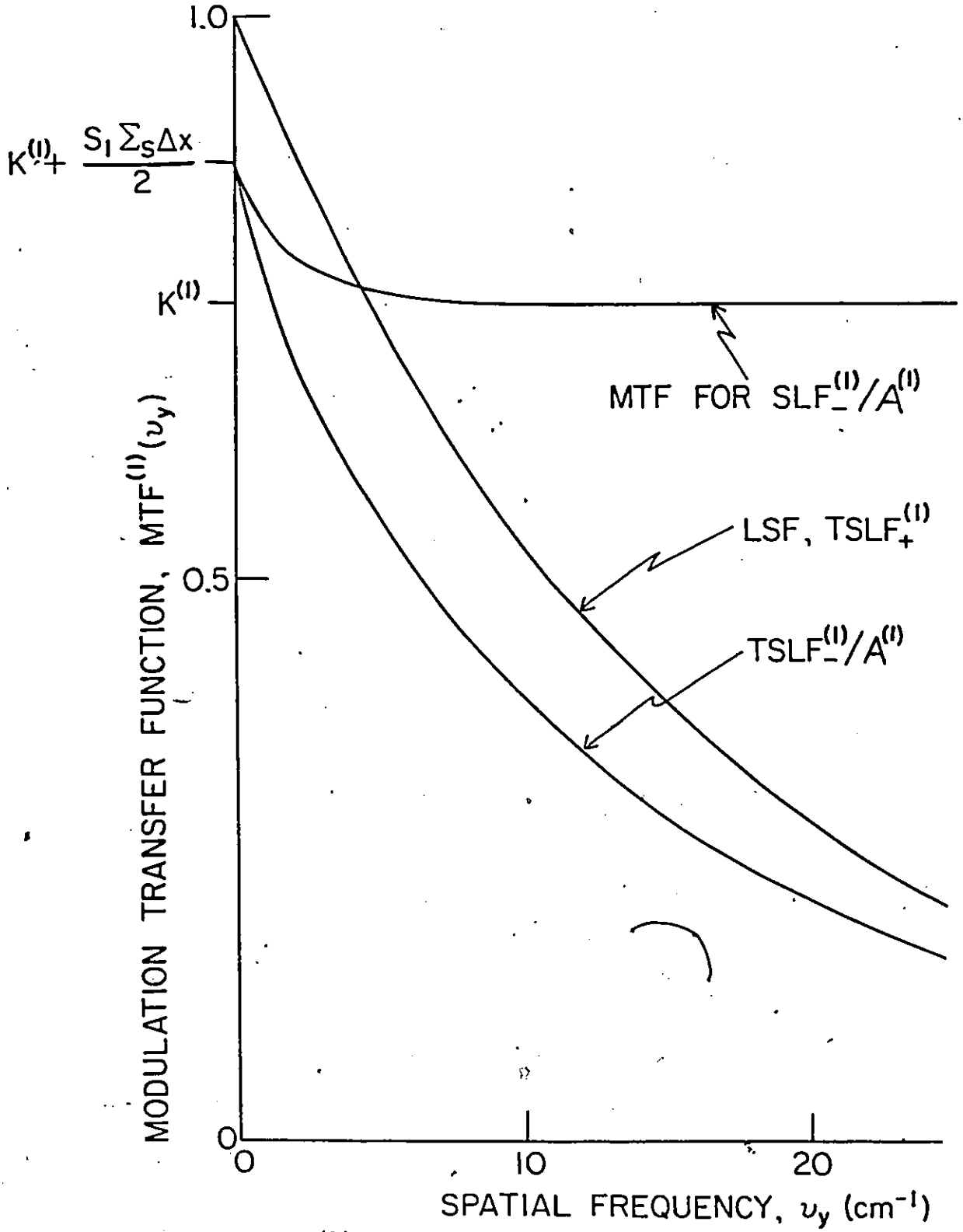

Fig. 4.8d: $MTF^{(1)}(\nu_y)$ for $\Sigma_s = 6.0$ cm^{-1}, $\Sigma_a = 0.0$ cm^{-1}, $\Delta x = 0.05$ cm, $d_n = 0.1$ cm and $\bar{d}_f = 100.0$ μm.

$$\overline{LSF}_{tot}(\nu_y) = \prod_{i=1}^{n} \overline{LSF}_i(\nu_y)$$

$$= \prod_{i=1}^{n} \exp[-2\pi \nu_y d_i] \text{ (see section A.5)}$$

$$= \exp[-2\pi \nu_y \sum_{i=1}^{n} d_i]. \tag{4-69}$$

The inverse Fourier transform of $\overline{LSF}_{tot}(\nu_y)$ follows immediately:

$$LSF_{tot}(y,v) = \frac{1}{\pi \sum_{i=1}^{n} d_i} \left[1 + \left(\frac{y - v}{\sum_{i=1}^{n} d_i} \right)^2 \right]^{-1} \tag{4-70}$$

This modelling framework provides a useful additive property for image degradation analysis. Specifically, image degradation is additive in the sense that each of n degradation parameters d_i add to give the total parameter when used in a Lorentzian functional form.

4.7 Connection to Integral Transport Formulation

A connection between the STF scattering formulation of this chapter and the point kernel integral transport solution developed in Chapter 2 is best established through a comparison of the system output response to a collimated thermal neutron beam normally incident on an object that is well approximated by an infinite slab of thickness Δx and total macroscopic cross-section Σ_t.

This response is here defined as the "scattering slab function" (SSF) in analogy to SEF knife-edge response defined in section 4.3. It is evaluated by convolving a uniform input with the system SLF, section A.4. The result, dependent only on the integrated magnitude of

the SLF and not its actual distribution, is

$$SSF(y) = I_o\{\exp[-\Sigma_t \Delta x] + \frac{1}{2}\left(\frac{\Sigma_s}{\Sigma_t}\right)(1-\exp[-\Sigma_t \Delta x])\}$$

$$= \text{constant}. \qquad (4\text{-}71)$$

Equation (4-71) is interpreted physically as follows. At every point P on or beyond the emergent slab plane, the total intensity is the sum of the intensity of uncollided normally incident neutrons travelling along a line through P (the first term), and the integrated intensity of all neutrons that scatter forward from points on that line (the second term). Because of the configurational uniformity, all outscatter from a line is precisely balanced by inscatter from other points.

Before comparing Eq. (4-71) with results from Chapter 2, we emphasize that Eq. (4-71) assumes only single interactions and is thus most applicable to narrow slabs ($\Sigma_t \Delta x << 1$). For the slab of width w* analyzed in section 2.2, the calculated intensity $I_{in}(w^*)$ should therefore include only the first two modes and the point kernel (Eq. (2-15)) should exclude exponential attenuation ($\Sigma_t \to 0$), since the once-scattered neutrons are to be assumed further uncollided. Also, the intensity functions analyzed in this chapter are forward partial neutron currents, section 4.1, rather than fluxes. This necessitates the inclusion of a factor of $-\mu = -\cos(\theta)$ in the scattering point kernel of section 2.2 to account for geometrical considerations discussed in that section. The resulting $I_{in}(w^*)$ is then calculated similarly to Eq. (2-22) and from the general form in Eq. (2-19) as follows:

$$I_{in}^{(1)}(w^*) = I_o \exp[-\Sigma_t w^*] - \frac{\Sigma_s}{2}\int_{-1}^{0}\int_{0}^{-w^*/\mu} I_{in}^{(0)}(w^* + \rho\mu)\,\mu\, d\rho\, d\mu. \qquad (4\text{-}72)$$

Here, $I_{in}^{(0)}(w)$ is the fundamental exponential mode, given in Eq. (2-27). Substitution for $I_{in}^{(0)}(w)$ followed by analytical evaluation of the double integral in Eq. (4-72) and identification of the parameter w* with Δx in this section then identifies Eq. (4-72) with Eq. (4-71).

The STF formulation of this chapter is therefore consistent with the transport calculations performed in Chapter 2.

CHAPTER 5

MONTE CARLO ANALYSIS OF THE KNIFE-EDGED SLAB RESPONSE

5.1 Monte Carlo Analysis

The transfer function analysis of Chapter 4 established a useful mathematical framework in which the scattering of thermalized neutrons in a radiographic context can be analyzed. While expository in nature, the analysis was essentially exact for the geometrically zeroth order object, a narrow infinite slab, described in section 4.1. The SLF model also applies to similar objects, such as the knife edge of section 4.2, or an aligned sequence of separated slab sections. For such objects, the collection of mathematical tools referred to as linear systems analysis can be utilized ultimately enabling the determination of a realistic output distribution.

In the general case, however, the radiographed object is a heterogeneous conglomeration of regions of different interaction cross-sections and geometry in which multiple interactions will differentially occur. As described in section 2.1, this results in a nonlinear system since the PSF depends on the local object properties.

All analyses in previous chapters have assumed perfectly collimated incident radiation for the purpose of facilitating transport calculations. For the feasibility determination of the knife edge response as a build-up factor indicator, it is necessary to expand the calculational model to include obliquity of incidence. This consideration, as well as that of differential multiple scattering, could analytically be incorporated into the transfer function model of Chapter 3, admitting some degree of approximation. The resulting upgraded model would certainly be analytically cumbersome and still of limited practical value due to the imposed geometrical constraints on the object.

Two approaches remain whereby the applicability of the knife edge response as a diagnostic indicator can be assessed. Firstly, the transport of thermalized neutrons in the object can be calculated through a deterministic solution of the neutron transport equation, Chapter 3. Unfortunately, only an approximate solution is realistically possible for the situation of neutrons obliquely incident on a knife-edged slab. As seen in Chapter 3, a great amount of computational effort can be expended in obtaining even an approximate solution for this two-dimensional problem.

Secondly, the particle transport can be directly simulated using the probabilistic based technique of Monte Carlo analysis, featuring the simulation of particle histories and conducted with the aid of pseudo-random numbers. The simulation can either directly solve the neutron transport equation or be analog, properly treating the transport of neutrons through a medium as a Markov process. The latter approach is the subject of this chapter. Each of the simulation techniques and characteristics described in subsequent sections are incorporated into the FORTRAN program PSFSCAT, listed in Appendix D. All results displayed in this chapter were obtained from PSFSCAT.

Analog Monte Carlo simulation of the neutron radiographic knife edge response appears to first have been performed by Butler and Harms (51, 97). Under the assumption that single scattering and absorption are the only interactions suffered by normally incident neutrons, it was noticed that "blips" repeatedly appeared in the calculated image response, near and on either side of the edge location. These blips were correctly but qualitatively identified as a scattering based phenomenon with the suggestion that further research be conducted to experimentally confirm their existence and to quantify their magnitude. The blips are potentially of great importance in the determination of the edge location on a neutron radiograph. Several previous studies focussing on this determination have either not specifically accounted for this edge outscattering phenomenon or have assumed that the

object is nonscattering (52, 94, 100, 101). Interestingly, for the edge of a cylindrical scattering object, Basham et al (102) found no observable scattering based effect, although such an effect has been documented by Matfield (96). The radiographic response calculations for an object of cylindrical geometry performed in section 7.2 also suggest the existence of "blips" in the cylindrical edge response.

The purpose of this chapter is to quantitatively evaluate the relative magnitude of the scattering based edge distortions (SBED's) in the knife edge response, using analog Monte Carlo simulation. The results are compared to analytical predictions from Chapters 2 and 3. Unlike the study conducted by Butler (51), an arbitrary degree of multiple scattering is incorporated into this simulation with an allowance for obliquity of neutron incidence and including the application of variance reduction techniques. Within the estimated statistical errors and scattering kernel accuracy, the results should therefore be exact. The calculations are ultimately aimed at a semiquantitative preliminary feasibility study of these SBED's as a diagnostic indicator of the build-up factor in an emergent neutron beam.

5.2 Sampling Methods

The sampling techniques described below are well-known and succinctly described by Carter and Cashwell (104).

The probability that a thermal neutron undergoes a first collision between s and ds along its line of flight is given by

$$p(s)ds = \Sigma_t \exp[-\Sigma_t s]ds \qquad (5\text{-}1)$$

where Σ_t is the thermal one-group macroscopic total cross-section for the medium properly interpreted as the probability per unit path length of a collision. The cumulative distribution function corresponding to the probability density function p(s) is P(s), given by

$$P(s) = \int_0^s p(t)\,dt. \qquad (5\text{-}2)$$

Now P(s) lies between zero and one so that the event defined by a first collision at s can be determined through the selection of a uniform [0,1] random number, ξ, by equating

$$\begin{aligned} \xi &= P(s) \\ &= \int_0^s \Sigma_t \exp[-\Sigma_t t]\, dt \\ &= 1 - \exp[-\Sigma_t s]. \end{aligned} \tag{5-3}$$

Inverting Eq. (5-3), the distance to collision, when viewed as a stochastic process, is determined by selecting a random number ξ from the uniform [0,1] distribution, and choosing

$$s = -\frac{1}{\Sigma_t} \ell n(1-\xi). \tag{5-4}$$

Since $1-\xi$ and ξ are identically distributed, it is computationally more efficient to choose

$$s_c = -\frac{1}{\Sigma_t} \ell n(\xi) \tag{5-5}$$

as the distance to collision. If s_c results in a position outside the medium, then the neutron has escaped without absorption. The intended application for the simulation is the determination of the emergent neutron distribution along the plane at $x = d_o$, as shown in Fig. 4.2, after traversal through an "infinite" knife-edged slab. For escape through the right hand side of the geometry, here termed "right escape", the line of flight leading to escape must be extrapolated to the desired scoring plane at $x = d_o$. For "left escape", the neutron is lost to backscatter and the history is terminated.

If s_c should otherwise locate inside the medium, the resulting collision point must be calculated using the direction vector of the neutron. Defining this direction vector $\Omega = (\theta,\phi)$ implicitly in the usual spherical polar coordinates (r,θ,ϕ) by

$$\begin{aligned} x &= r\cos(\theta) \\ y &= r\sin(\theta)\cos(\phi) \\ z &= r\sin(\theta)\sin(\phi) \end{aligned}, \tag{5-6}$$

the Cartesian collision coordinates (x_f, y_f, z_f) are related to the original position coordinates (x_i, y_i, z_i) by

$$x_f = x_i + s_c \cos(\theta)$$
$$y_f = y_i + s_c \sin(\theta) \cos(\phi) \qquad (5\text{-}7)$$
$$z_f = z_i + s_c \sin(\theta) \sin(\phi).$$

Given the position of a collision, the nature of the collision must next be played for. For the general case of n interaction types, each having an associated macroscopic cross-section Σ_i, the real line segment [0,1] is partitioned into n segments, where the length of the i^{th} segment is Σ_i/Σ_t. The type of collision is then determined by the segment into which a selected random uniform [0,1] number falls. For this calculation n=2 and the three cross-sections of interest are Σ_a, Σ_s and Σ_t, corresponding to absorption, scattering and total interaction.

If the collision being played for is an absorption, the history is simply terminated with the optional counting of the absorbed neutron. If the collision is a scatter then the altered energy and direction of the neutron must be determined, given the scattering kernel. There are a variety of methods in existence for treating thermal scattering, which can potentially include chemical binding and diffraction as effects.

In Monte Carlo codes, favored methods involve a multigroup treatment of the thermal energy range and the free gas kernel model. The former model utilizes the near isotropy of scattering induced by thermal target motion using a low order Legendre expansion of the frequency distribution for the scattering angle. The latter model assumes that neutrons are being transported in a monatomic gas with an isotropic Maxwellian distribution of velocities.

Since the purpose of the Monte Carlo code being developed is to verify and describe a thermal neutron radiographic scattering effect by calculating an output distribution, the

very simplest of scattering kernels – isotropic scattering – is used here. Since the probing neutrons are thermalized, all energy dependence is incorporated into the one-group cross-sections. It is felt that the computational savings accorded by these assumptions are well worth any inaccuracies thereby incurred in the output distributions. That is, the simple isotropic scattering model should be sufficient as an indicator of the existence of the predicted effect as well as its approximate magnitude. In practice, neutron scattering is usually isotropic in the centre-of-mass system and nearly isotropic in the laboratory system except for low mass scatterers such as hydrogen.

For isotropic scattering, each element $d\Omega$ of solid angle receives the same scattering contribution, where $d\Omega$ is given by

$$d\Omega = \sin(\theta)d\theta\, d\phi$$

$$= -d\mu d\phi\,, \tag{5-8}$$

defining $\mu = \cos(\theta)$.

Isotropic scattering is therefore simulated by randomly uniformly selecting μ between -1 and +1, and ϕ between 0 and 2π. Thus, given random numbers ξ and ρ, choose

$$\mu = 2\xi - 1\,, \tag{5-9}$$

$$\phi = 2\pi\rho\,. \tag{5-10}$$

From Eq. (5-7), however, it is evident that the angle ϕ is used exclusively in the evaluation of $\cos(\phi)$ and $\sin(\phi)$ so that direct sampling for $\cos(\phi)$ and $\sin(\phi)$ may be computationally more efficient. The following widely used sampling procedure, belonging to a more general class of methods known as the "rejection technique", is used here.

Referring to Fig. 5.1 in which a unit circle is inscribed in a square of side length 2, it is clear that random number pairs (ξ_1, ξ_2) selected from the uniform [0,1] distribution will uniformly populate the square with points (x_1, x_2), where

$$x_i = 2\xi_i - 1, \quad i = 1,2\,. \tag{5-11}$$

$$x_1 = 2\xi_1 - 1$$
$$x_2 = 2\xi_2 - 1$$

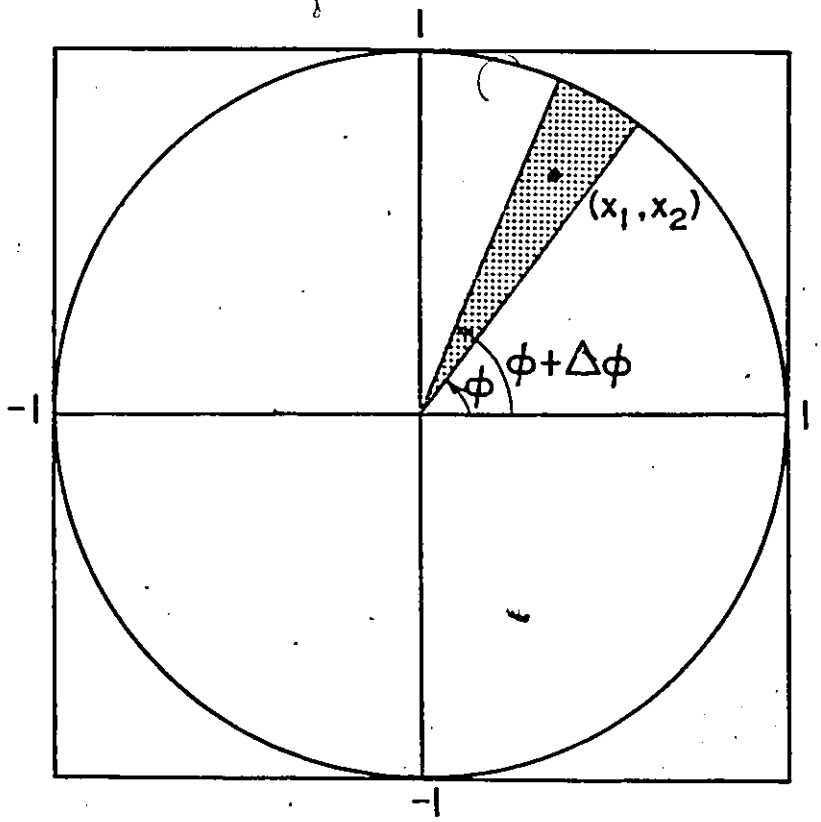

Fig. 5.1: The rejection technique for direct sampling for $\sin(\phi)$ and $\cos(\phi)$.

If points falling inside the circle are retained while those falling outside are rejected, then each angle element $\Delta\phi$ will receive the same number of retained points. Thus, if each (x_1, x_2) retained point determines a ϕ value, then ϕ will be sampled uniformly between 0 and 2π. Also, the functions $\cos(\phi)$ and $\sin(\phi)$ are directly computed as

$$\cos(\phi) = x_1 (x_1^2 + x_2^2)^{-1/2}$$
$$\sin(\phi) = x_2 (x_1^2 + x_2^2)^{-1/2}. \tag{5-12}$$

Now sampling ϕ uniformly between 0 and 2π is, for purposes of evaluating $\sin(\phi)$ and $\cos(\phi)$, equivalent to sampling ϕ uniformly between 0 and 4π, which implies sampling 2ϕ uniformly between 0 and 2π. The standard trigonometric double angle formulae then lead to

$$\cos(\phi) = (x_1^2 - x_2^2) / (x_1^2 + x_2^2)$$
$$\sin(\phi) = 2 x_1 x_2 / (x_1^2 + x_2^2). \tag{5-13}$$

The result is that $\sin(\phi)$ and $\cos(\phi)$ are directly and easily sampled for avoiding trigonometric or square root computer evaluation. The efficiency of this process, defined as the fraction of selected random numbers that are retained, is simply the ratio of the circle to square areas and hence is $\pi/4$. This acceptable efficiency also contributes to the acceptability of the sampling process.

5.3 Importance Sampling and Variance Reduction

The universal bane of Monte Carlo codes is the requirement that a large number of histories be simulated in order to achieve an acceptably small variance in the quantity being scored. For penetration problems such as that being studied here, it is frequently the case that only a small fraction of the incident neutrons survive to be counted - in this case at the plane $x = d_o$. Thus, a great number of histories must be simulated in order to achieve a statistically acceptably large number of emergent counts. This inefficiency is manifested as a high computational cost. As a result, techniques have been devised to reduce the variance, or

statistical error, in the output data by assigning increased "importance" to regions where particles would be more likely to contribute to a desired scoring and decreased importance to regions where histories would be more likely to culminate in simple termination. While several variance reduction schemes exist, the techniques used here fall under the "importance sampling" category alluded to above; specifically, the "splitting" and "Russian rouletting" of particles are used. The knife-edged slab of Fig. 4.2 has been distributed from 0 to x_{max} and reproduced in Fig. 5.2.

For $i>j$, particles in region R_i are more likely to exit right — and thus contribute to the scoring at $x = d_o$ — than particles in region R_j so that the regional importances are such that $I_i > I_j$. Denoting the boundary between R_i and R_{i+1} by B_i, a particle in region R_i and of weight w is "split" into v particles each of weight w/v upon crossing B_i into R_{i+1}. The result is to improve statistical confidence while retaining a constant total weight. Each particle travelling in a favorable direction is split into subparticles that help map out the object.

Likewise, a particle crossing B_i from R_{i+1} into R_i is entering a region of lesser importance or, equivalently, is less likely to contribute to the scoring at $x = d_o$ than its counterpart travelling in the reverse direction. Since it is computationally desireable to decrease the number of such particles followed, a game of Russian roulette is played in which the particle survives with probability v^{-1} and dies with probability $1 - v^{-1}$. To maintain global weight conservation, each roulette surviving particle has its original weight multiplied by v.

Note that Russian roulette and splitting are inverse processes. That is, the inverse of having a particle of unit weight split into v particles of weight v^{-1} is to have the unit particle collapse into "v^{-1}" th of a particle of weight v, which in turn is equivalent to having every v unit particles collapse into a single particle of weight v. This is achieved by Russian roulette. Also, if $v = I_i/I_j$ for particles entering R_i from R_j, then all the particles in a given region will have identical weights, facilitating scoring and reducing computational costs since

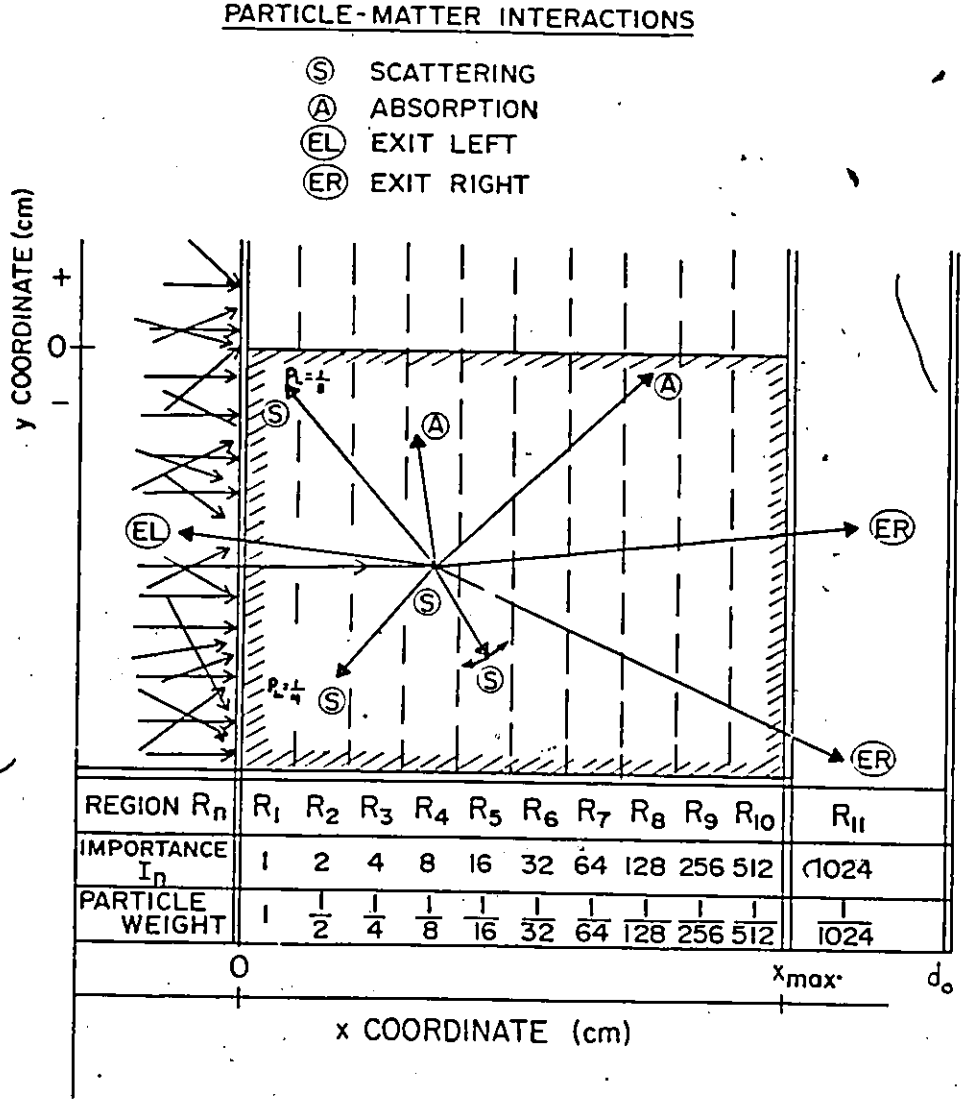

Fig. 5.2: Schematic diagram illustrating the logical basis of the Monte Carlo scheme including Russian roulette and splitting as importance sampling techniques. P_L is the probability of survival at the relevant scattering location.

in this case, weights need not be accounted for. This procedure has been followed here with a constant importance ratio of

$$I_{i+1}/I_i = 2, \qquad (5\text{-}14)$$

as indicated in Fig. 5.2.

When only one region is used, splitting and roulette are eliminated. Even for narrow slabs, variance reduction was achieved by using a few regions. This is discussed in section 5.5.

5.4 Results at the Scoring Plane

The output distributions calculated were the scattering point function (SPF), scattering line function (SLF) and the scattering edge function (SEF). The neutron intensities generating these functions are forward partial currents, section 4.1. In the conventional imaging analysis of isoplanatic and isotropic systems, point and line spread functions (PSF, LSF) are, through the mathematical procedure of convolution, the building blocks of edge spread functions (ESF). Only a single determination of either the PSF or LSF is required to generate the ESF. Although the SPF and SLF are shift invariant with respect to the z axis here, they are each shift variant with respect to the y axis so that a single evaluation of an SLF is insufficient to generate an SEF.

The notation SPF (y,z,y_o, z_o) is used for the SPF, describing the output response distribution at (y,z) on the image plane, $x = d_o$, to a thermal neutron point source normally incident at $(y_o\ z_o)$ on the plane $x=0$. This computationally convenient definition of SPF, and also the subsequent definition of SLF, are slightly different from those of Chapter 4, where the input function was actually the ideal nonscattering output distribution. These different definitions result in equivalent SEF distributions, however, because the inputs of Chapter 4 were always multiplied back into the SPF, SLF for SEF calculations. Recalling that the knife

edge geometry is that of Fig. 4.2, define (r,θ) as any set of polar coordinates for all x = constant planes, centred on (y_0, z_0). The SPF is then written as $SPF(r,\theta)$, describing the response at (r,θ) on the plane $x=d_0$ to a point source at $r=0$ on the plane $x=0$.

In order to decrease computational costs, the output response distribution

$$\overline{SPF}(r) = \int_0^{2\pi} SPF(r,\theta)\, d\theta \tag{5-15}$$

was calculated. This was accomplished by segmenting the $x=d_0$ plane into annular bins of width Δr centred on $r=0$ and counting the emergent subparticles that fell into each bin. Typical resulting histograms, indicative of the shape of $SPF(r)$ and normalized to unit area, are presented in Fig. 5.3 for $y_0 = -0.01$ cm and $y_0 = -10.0$ cm. The value of the incidence coordinate z_0 is irrelevant here.

Calculation of errors is discussed in section 5.5. As expected, the SPF for $y_0 = -0.01$ cm is flatter than that for $y_0 = -10.0$ cm since neutrons emergent from the $y=0$ plane are further uncollided. Note that for $y_0 = -10.0$ cm, to an excellent approximation,

$$SPF(r,\theta) \approx \overline{SPF}(r)\,. \tag{5-16}$$

The SLF describes the response to a line source as being the line integration of responses to point sources as follows:

$$SLF(y, y_0) = \int_{-\infty}^{+\infty} SPF(y, z, y_0, z_0)\, dz_0$$

$$= \int_{-\infty}^{+\infty} SPF(y, y_0, z - z_0)\, dz_0 \tag{5-17}$$

where z shift invariance has been used. The situation involving the evaluation of SLF at $y = y_f$ is depicted in Fig. 5.4a. It would appear that an entire infinite line source must be simulated in the Monte Carlo calculation of $SLF(y_f, y_0)$. However, Eq. (5-17) can be written through variable changes as

$$SLF(y, y_0) = \int_{-\infty}^{+\infty} SPF(y, y_0, z - z_0)\, dz \tag{5-18}$$

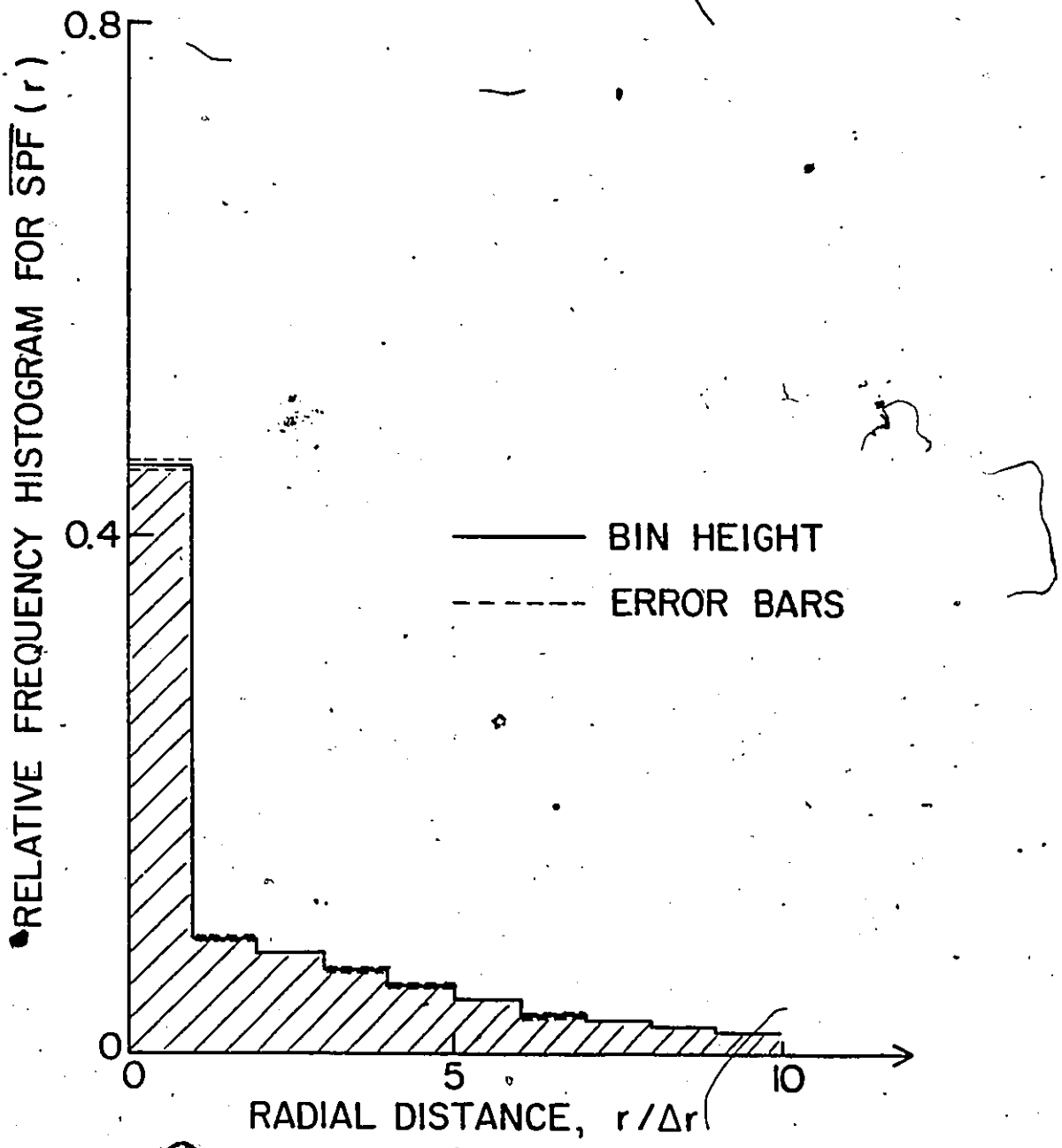

Fig. 5.3a: Histogram approximately $\overline{SPF}(r)$ for any point source normally incident at $y_0 = -0.01$ cm, on a knife-edged slab with cross-sections $\Sigma_a = 1.0\ cm^{-1}$, $\Sigma_s = 3.0\ cm^{-1}$, and width $x_{max} = d_o = 0.5$ cm. The bin width is $\Delta r = 0.1$ cm.

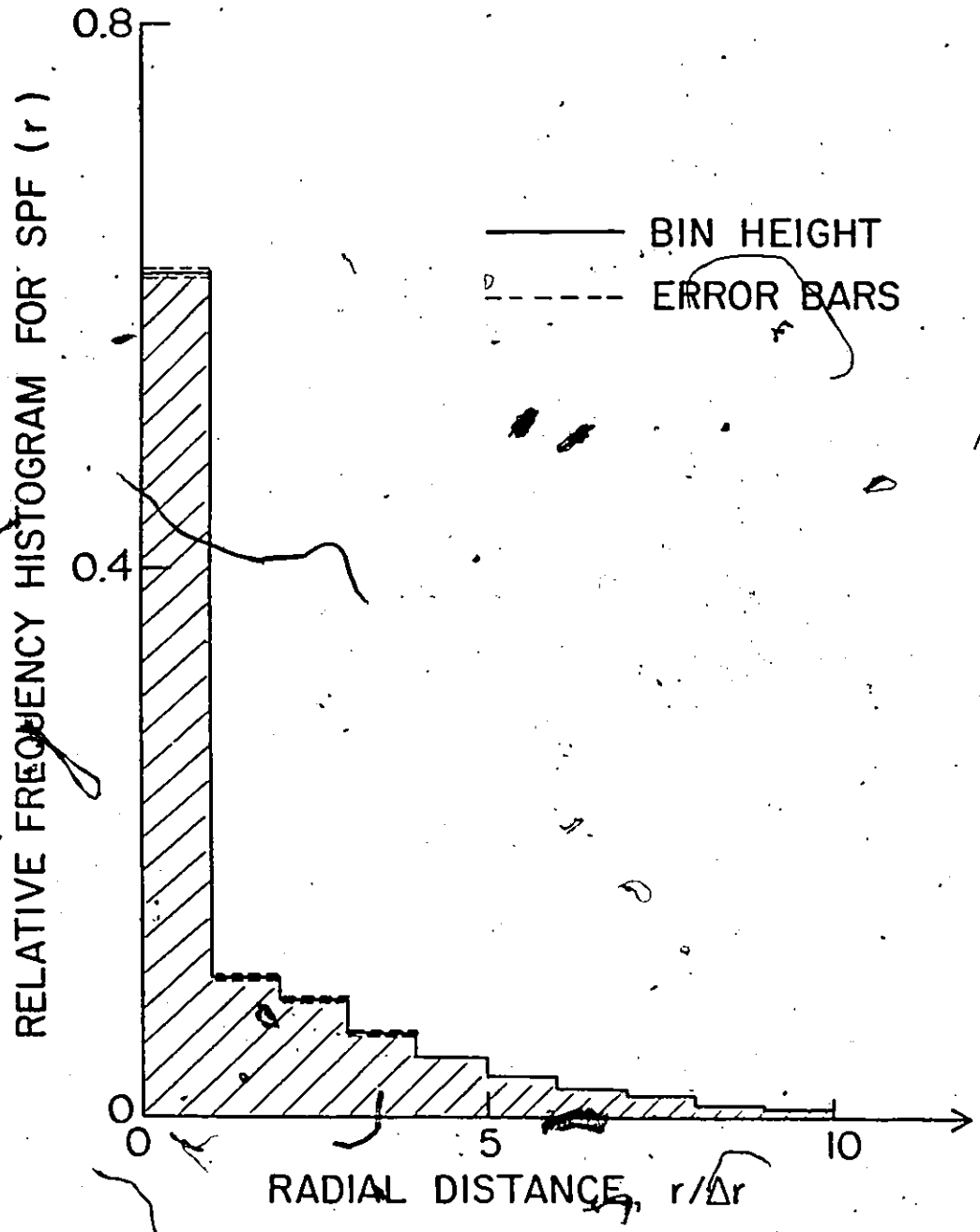

Fig. 5.3b: Histogram approximating SPF(r) for any point source normally incident at $y_o = -10.0$ cm, on a knife-edged slab with cross-sections $\Sigma_a = 1.0\ cm^{-1}$ & $\Sigma_s = 3.0\ cm^{-1}$ and width $x_{max} = d_o = 0.5$ cm. The bin width is $\Delta r = 0.1$ cm.

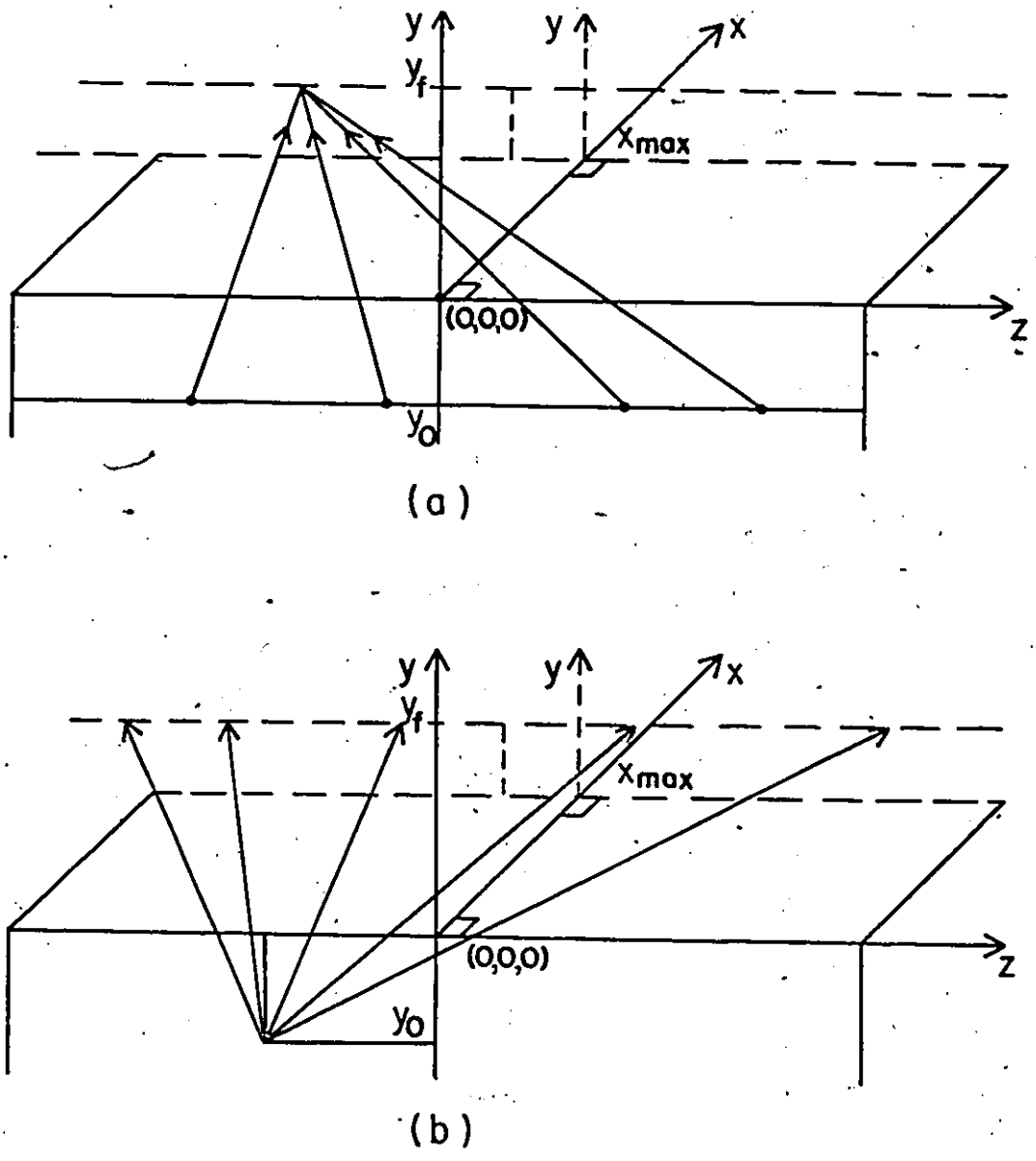

Fig. 5.4: Figure illustrating the equivalence of the response at a point to a line source and the line response to a point source. Arrows indicate radiation contributions in the (y-z) plane.

The geometrical interpretation of this variable change is that the response at any point on the line at y_f to a line source at y_0 equals the integrated response from all points along the line at y_f to any single point source on the line at y_0, as indicated in Fig. 5.4b. This greatly reduces the necessary computational effort since only a point source is required to calculate a line response.

The output distribution $SLF(y,y_0)$ was thus calculated by segmenting the $x = d_0$ plane into rectangular, parallel bins of width Δy, each bin spanning the entire z axis, and by then counting the number of subparticles that fell into each bin. Typical resulting histograms, indicative of $SLF(y,y_0)$ and normalized to unit area are presented in Figs. 5.5 for $y_0 = -0.01$ cm and $y_0 = -10.0$ cm. As for the SPF calculation, the incidence z coordinate is irrelevant here.

The exit of neutrons from the $y=0$ plane, of great importance for the case of $y_0 = -0.01$ cm above but negligible for the other case, is manifested in two distinct features of Figs. 5.5. Firstly, the histogram in Fig. 5.5a is flatter than that in Fig. 5.5b. Secondly, Fig. 5.5b is, within the included error bars, symmetric about $y=0$, whereas Fig. 5.5a is strongly positively skewed. This asymmetry validates the prescription that $d_1 > d_2$ in the SLF model described in section 4.3.

The SEF is obtained, in principle, as a convolution of the SLF with the appropriate intensity function which in this case is uniform. As indicated in Figs. 5.5, however, SLF is strongly shift variant so that given this Monte Carlo calculational tool, the most expedient way to calculate SEF(y) is to use an incident source distributed uniformly across the entire y axis. For the same reason that an SLF calculation requires only a point source, the SEF calculation requires a distributed source taken only at a fixed z coordinate as opposed to an entire planar source. This is of considerable aid in reducing computational effort.

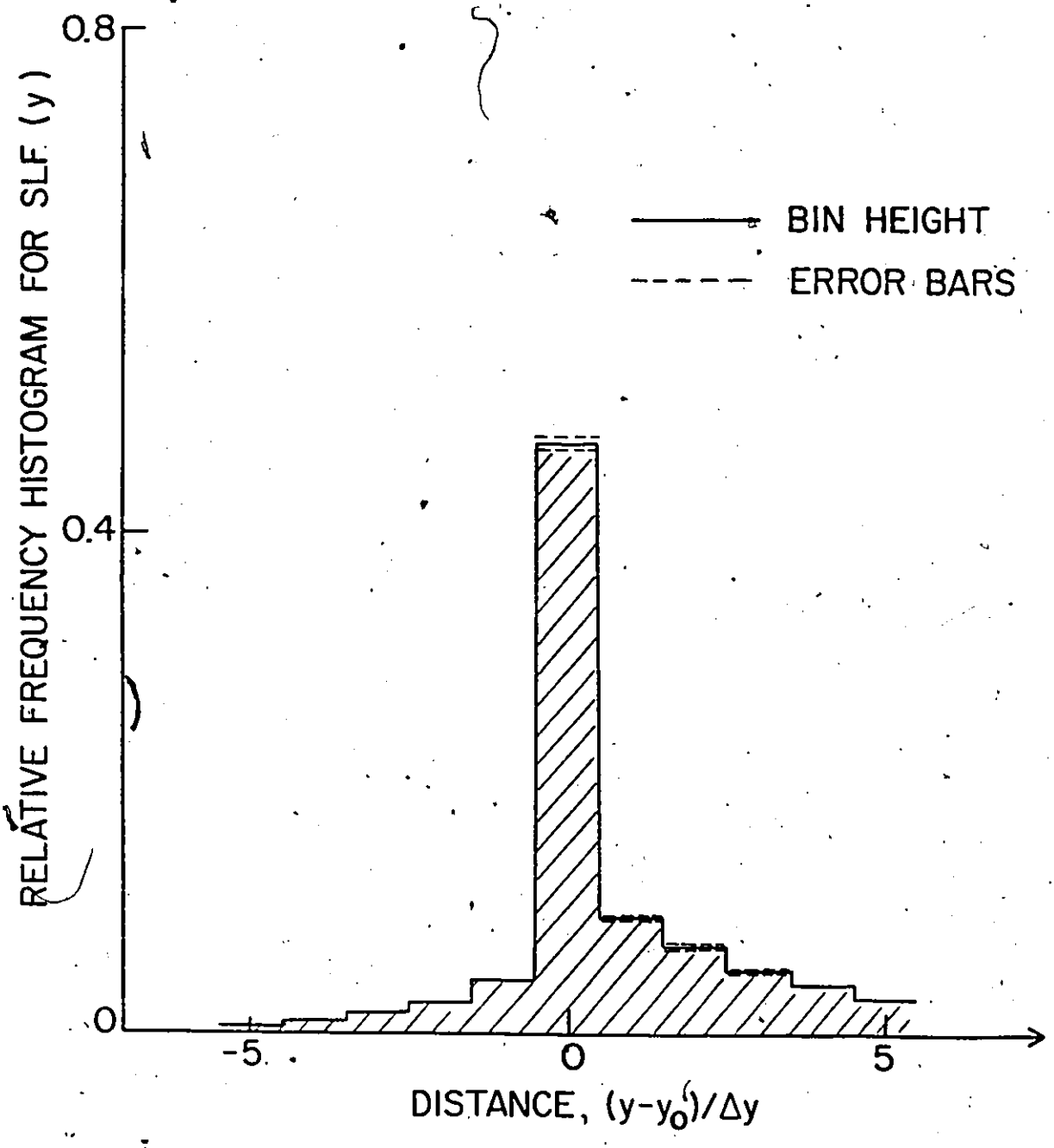

Fig. 5.5a: Histogram approximating $SLF(y,y_0)$ for a line source normally incident at $y_0 = -0.01$ cm on the knife-edged slab used for Fig. 5.3. The bin width is $\Delta y = 0.1$ cm.

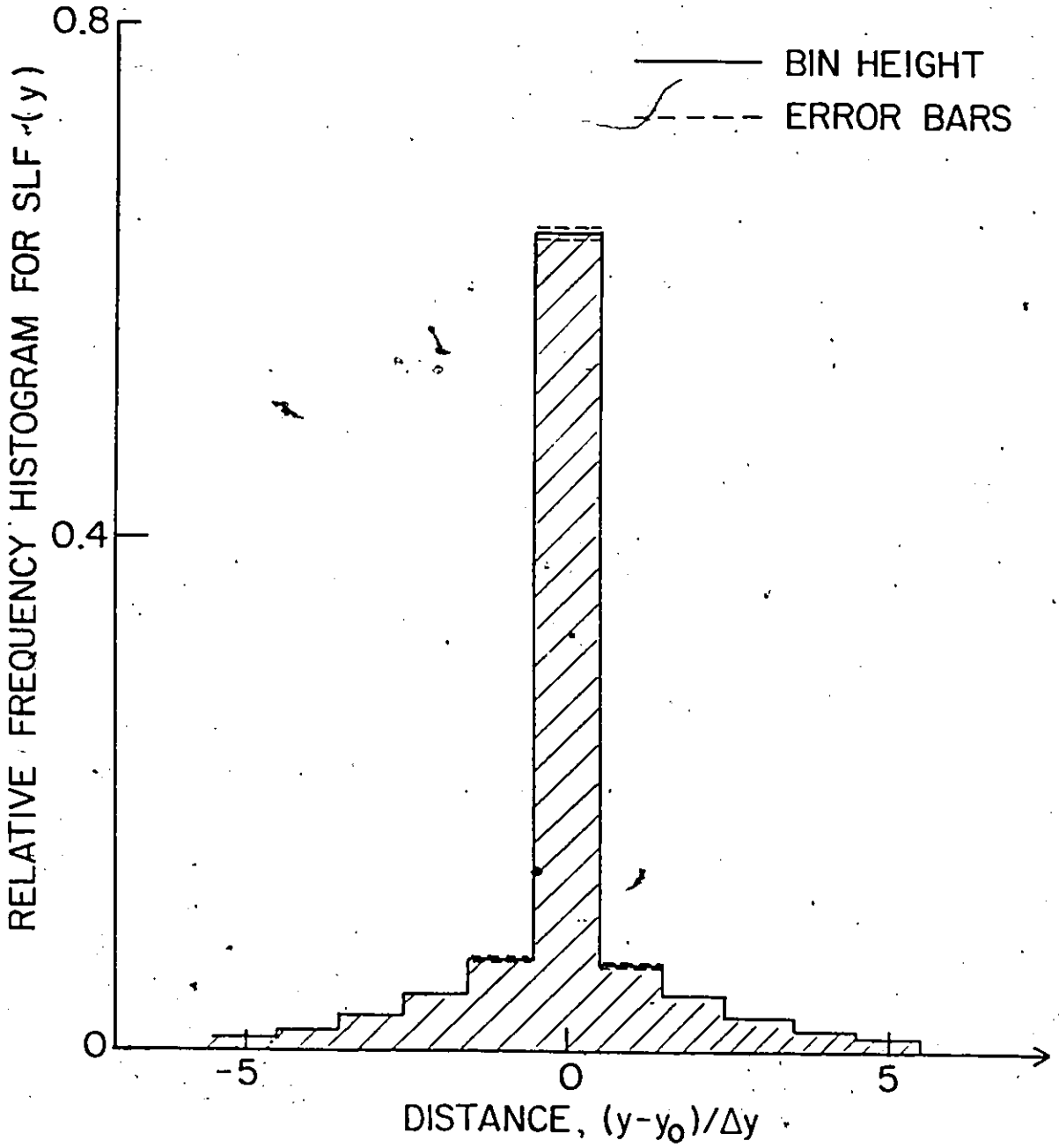

Fig. 5.5b: Histogram approximating $SLF(y,y_0)$ for a line source normally incident at y_0 = -10.0 cm on the knife-edged slab used for Fig. 5.3. The bin width is Δy = 0.1 cm.

In passing, we note that the "entire" y axis translates into choosing a sufficiently large segment of the y axis that information from y outside this segment will contribute negligibly to obtained results. For the range of material and geometrical properties present in this analysis, it was found that the entire y axis was well represented by the segment Y_{out} = [- 5.0 cm, 5.0 cm].

All incident neutrons, regardless of their total number, were distributed uniformly along Y_{out} at a fixed z coordinate. For large numbers of incident neutrons, this is equivalent to uniform random placement.

As for SLF calculations, SEF(y) was calculated by counting the number of subparticles falling into rectangular parallel bins of width Δy, each bin spanning the entire z axis. The results, such as are displayed in Figs. 5.6, have involved the replacement of a bin total by the total applied to the centre of the bin in order to facilitate plotting the distribution. This approximation is only permissable when all bins have equal width and is justified here since each curve portion in Figs. 5.6 is monotonic and slowly-varying.

The bin errors were calculated as described in section 5.5. The errors for $y>0$ have been excluded since they are estimated as being negligibly small. However, the errors for $y<0$ are substantial to the extent that best-fit lines are meaningless in this range. This difference in error magnitude is explained by the observation that more processes affect neutrons in $y<0$ than neutrons in $y>0$.

The primary feature in Figs. 5.6 is the existence of SBED's around $y=0$, as predicted analytically by the models in Chapter 4. Each of the three figures was constructed for a slab with a total macroscopic cross-section of $\Sigma_t = 2.0\ cm^{-1}$ and of width $x_{max} = 0.5$ cm; only the ratio of Σ_s to Σ_t varies between the figures. As predicted earlier, the SBED magnitude grows in proportion to this ratio. In Fig. 5.6a, $\Sigma_s/\Sigma_t = 0.5$ and the SBED's are

small though noticeable. In Fig. 5.6c, $\Sigma_s/\Sigma_t = 0.95$ and the SBED's are substantial, even in relation to the SEF amplitude defined as

$$\text{SEF amplitude} = [\text{SEF}(\infty) - \text{SEF}(-\infty)]. \tag{5-19}$$

Since the "negative" SBED has a large error associated with it, a useful indicator of the relative magnitude of this outscattering phenomenon is the ratio of the positive SBED height, at $y = 0^+$, to the SEF amplitude. This ratio is shown in Fig. 5.7 for each of the SEF curves in Figs. 5.6. Clearly, it is the magnitude of this ratio which ultimately determines the feasibility of this SEF feature as a diagnostic tool.

Because of the large possible errors associated with the $y < 0$ data in Fig. 5.6, it is difficult to ascertain the degree of asymmetry in these SEF curves rendering a direct comparison with the analytical model of section 4.3 difficult. A comparison of Monte Carlo and analytical SEF curves has, however, been performed as outlined in section 4.4.

It should be understood that in practice, convolution of the SEF curves in Figs. 5.6 with other system transfer functions, such as the screen-film unsharpness SEF, will smooth the sharp peaks of Figs. 5.6. For a knife edge with a sufficiently large Σ_s/Σ_t ratio, however, this smoothing should not be so great as to completely remove the SBED phenomenon. This expectation was analytically predicted in section 4.5. Indeed, for high resolution neutron radiography, screen-film edge unsharpness is usually less than 150 microns, well confined within the SBED as indicated in Fig. 5.6c.

Finally the SBED area may prove to be a more useful diagnostic tool than the relative SBED height, since it is relatively less sensitive to convolution with other STF's than is the SBED height. On the other hand, it may be difficult to accurately measure SBED area due to uncertainty in the determination of the point at which the SBED effectively terminates.

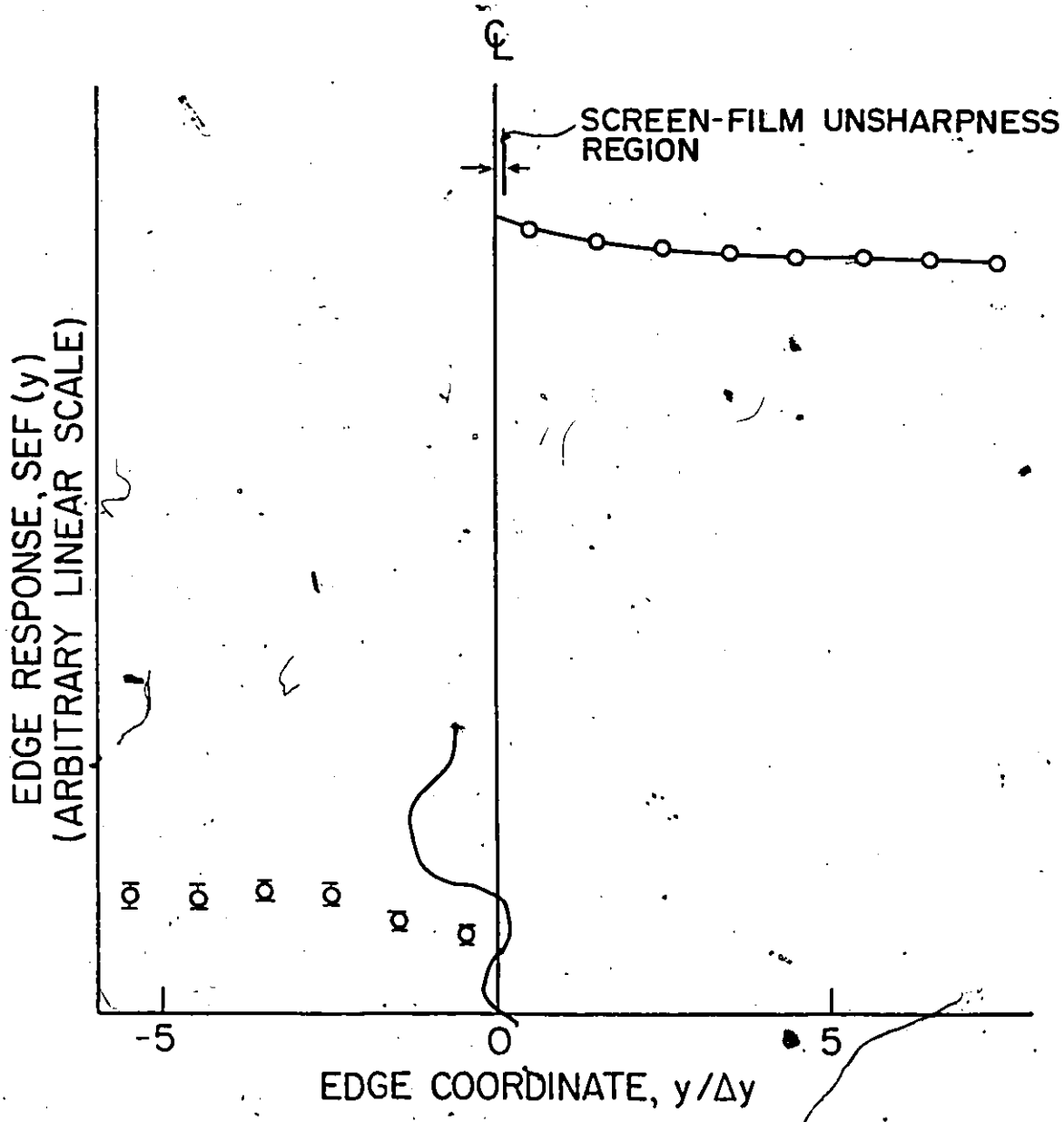

Fig. 5.6a: SEF(y) for a distributed source normally incident on a knife-edged slab with $\Sigma_t = 2.0\ cm^{-1}$, $\Sigma_s = 1.0\ cm^{-1}$ and $x_{max} = d_o = 0.5$ cm. Points are estimated from histogram bins of width $\Delta y = 0.15$ cm.

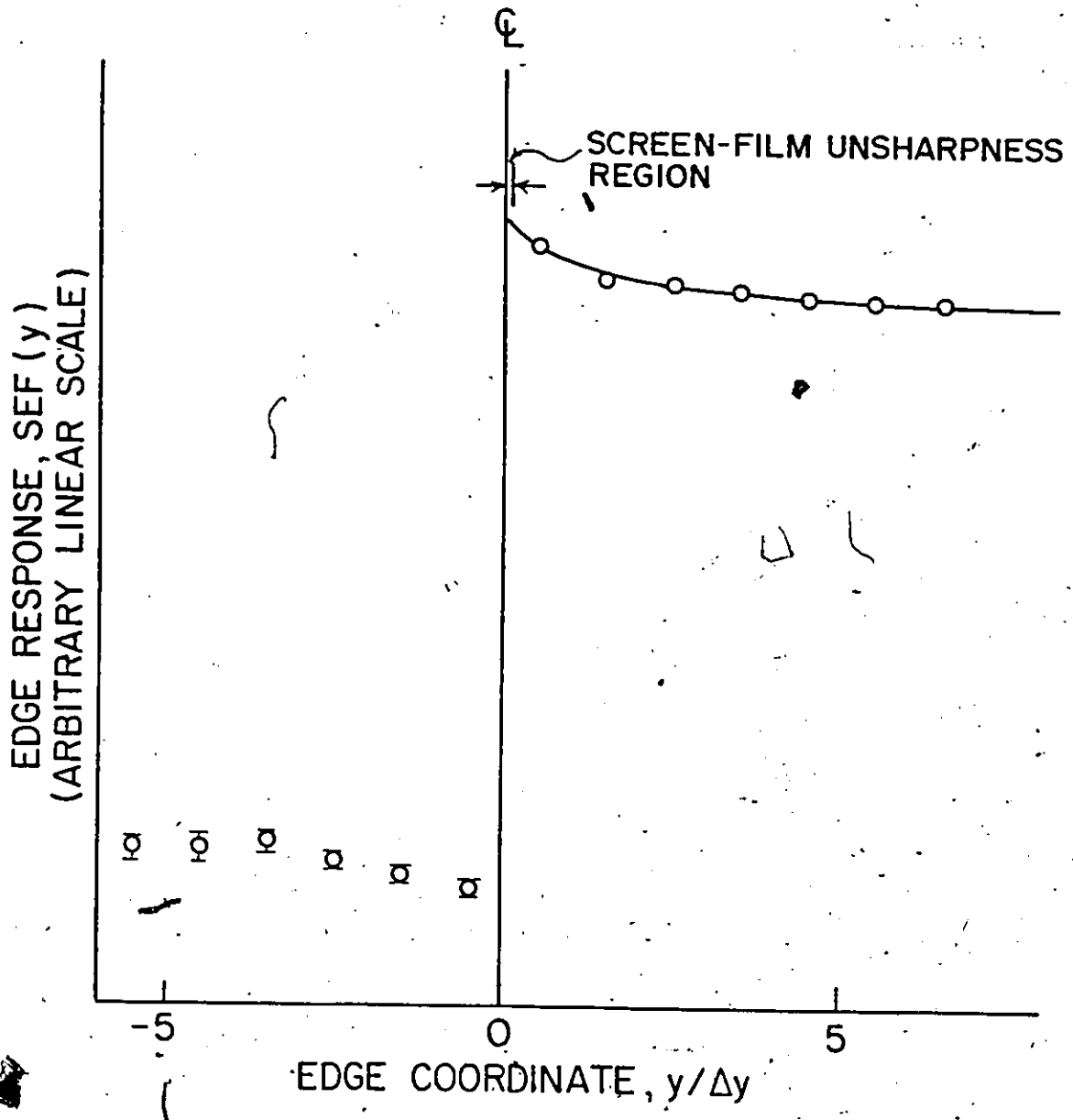

Fig. 5.6b: SEF(y) for a distributed source normally incident on a knife-edged slab with $\Sigma_t = 2.0\ cm^{-1}$, $\Sigma_s = 1.5\ cm^{-1}$ and $x_{max} = d_o = 0.5$ cm. Points are estimated from histogram bins of width $\Delta y = 0.15$ cm.

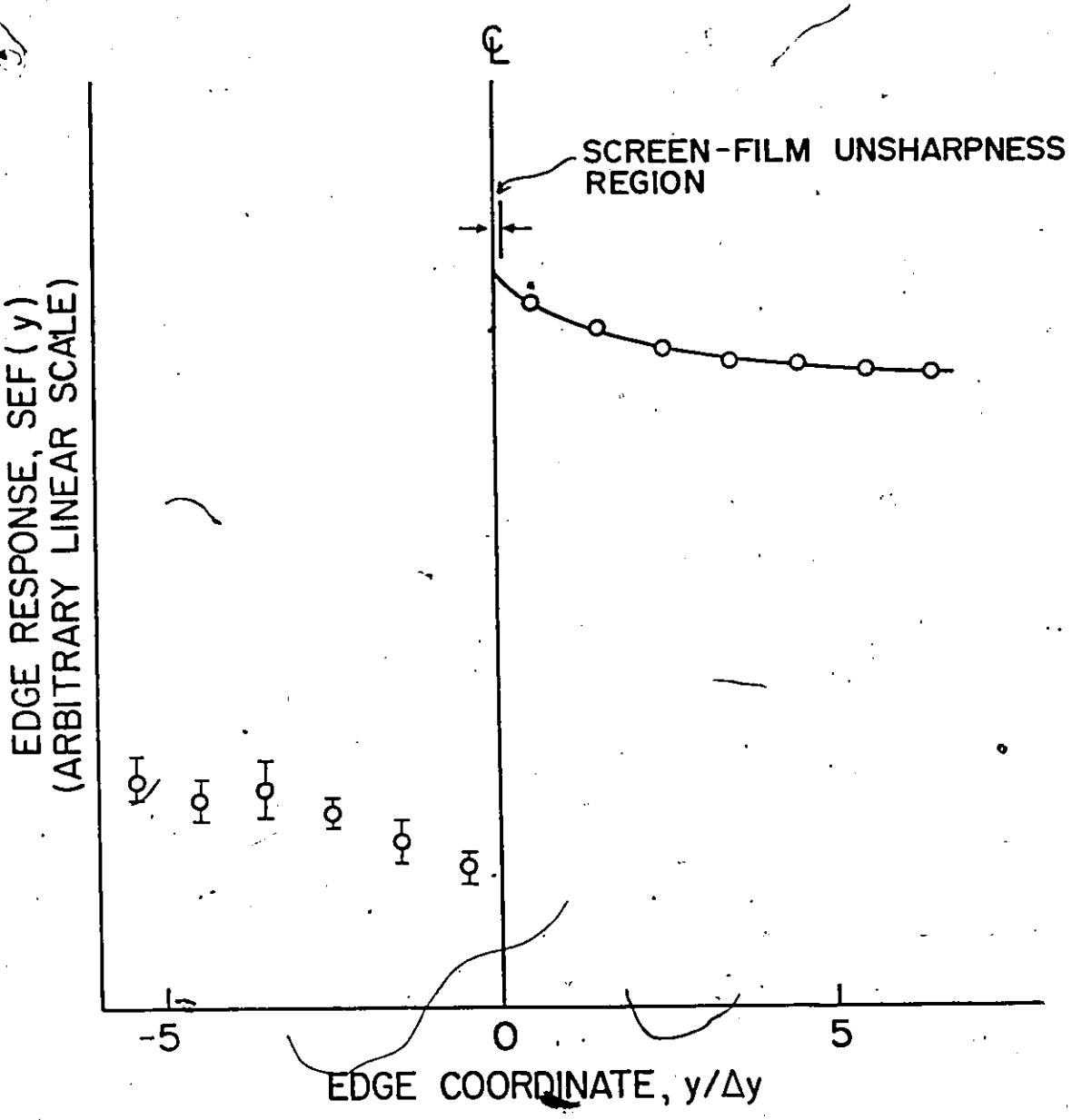

Fig. 5.6c: SEF(y) for a distributed source normally incident on a knife-edged slab with Σ_t = 2.0 cm^{-1}, Σ_s = 1.9 cm^{-1} and $x_{max} = d_o = 0.5$ cm. Points are estimated from histogram bins of width Δy = 0.15 cm.

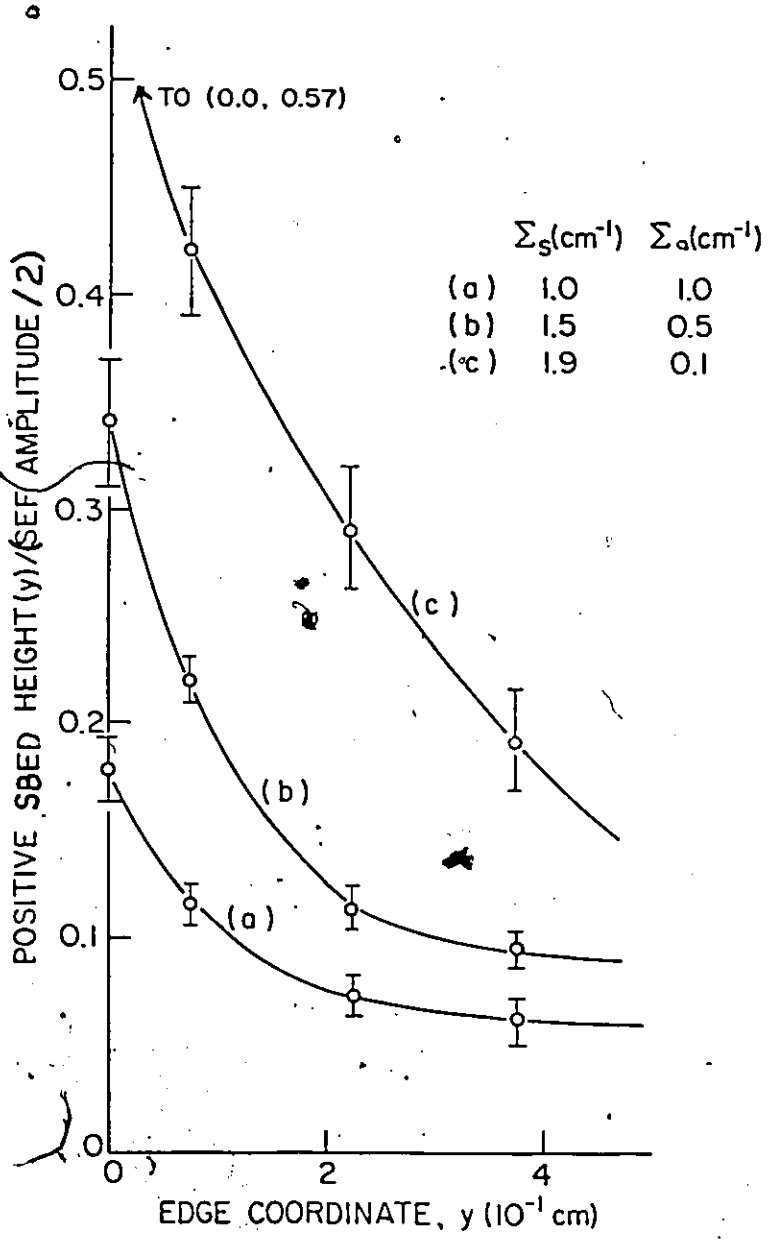

Fig. 5.7: Relative heights of the scattering based edge distortions (SBED's) for the three SEF curves in Fig. 5.6. The relative significance of the phenomenon is suggested for materials with a large Σ_s/Σ_t ratio. The ordinate at y = 0.0 cm was calculated using an extrapolated SBED height value, incurring a large error.

5.5 Error Analysis

The scoring plane at which emergent subparticles were counted, placed at $x = d_o$, was divided into either 40 or 50 of the relative frequency histogram bins described in section 5.4, with the number of bins depending on the distribution being calculated. Counting was facilitated since all emergent subparticles had identical weights of 2^{-r}, where r is the number of regions into which the object is divided. Define RFH_i as the fraction of the total number of emergent particles (T) that fell into the i^{th} relative frequency histogram bin (T_i), so that

$$RFH_i = T_i/T. \tag{5-20}$$

Further, we define additionally the quantities

N: the total number of "trials" into which the total number of simulated histories has been divided, for purposes of error estimation,

S_j: the total number of j^{th} trial subparticles counted at $x = d_o$,

D_{ij}: the total number of j^{th} trial subparticles counted at $x = d_o$ that fell into the i^{th} bin,

X_{ij}: the fraction of S_j that D_{ij} represents,

M_i: the mean value of X_{ij} over all N trials,

$\bar{S}$: the mean value of S_j over all N trials,

D_i: the standard deviation in the X_{ij}, j = 1 to N.

The following relationships result from the above definitions:

$$X_{ij} = D_{ij}/S_j \tag{5-21a}$$

$$T_i = \sum_{j=1}^{N} D_{ij} \tag{5-21b}$$

$$T = \sum_{j=1}^{N} S_j \tag{5-21c}$$

$$\bar{S} = \frac{1}{N} \sum_{j=1}^{N} S_j \tag{5-21d}$$

$$M_i = \frac{1}{N} \sum_{j=1}^{N} X_{ij} \tag{5-21e}$$

$$D_i^2 = \frac{1}{N-1} \sum_{j=1}^{N} (X_{ij} - M_i)^2 \tag{5-21f}$$

Assume initially that for each of the j trials, the number of subparticles falling into the i^{th} bin is Poisson distributed with mean μ_i and variance $\sigma_i^2 = \mu_i$. Note that since μ_i is typically large ($\mu_i \geq O(10^3)$), this distribution is well approximated by the continuous normal distribution. If m_i and s_i are the observed mean and standard deviation for the i^{th} bin count over n trials, the trend

$$\frac{s_i}{m_i} \alpha \frac{1}{\sqrt{m_i}} \tag{5-22}$$

is expected for sufficiently large n. Equation (5-22) states that the estimated bin count relative error varies inversely approximately with the square root of the bin count itself. Therefore, the relative error in bin counts is decreased by decreasing the total number of bins into which a fixed number of emergent particles fall.

Now the approximation

$$X_{ij} \approx D_{ij}/\bar{S} \tag{5-23}$$

will, from Eq. (5-21a), incur a relative error of

$$\Delta X_{ij}/X_{ij} = |S_j - \bar{S}|/\bar{S}$$
$$= \Delta S_j/\bar{S} \; . \tag{5-24}$$

This is small in comparison to the relative deviations D_i/M_i since the D_i/M_i are taken when the scoring plane is segmented into 40 or 50 bins whereas $\Delta S_j/\bar{S}$ is the relative deviation when the scoring plane is segmented into only one bin.

It now follows from Eq. (5-20), (5-21) and (5-23), to a good approximation, that

$$M_i \approx T_i/T$$

$$= RFH_i . \qquad (5\text{-}25)$$

The error in RFH_i has therefore been estimated as the error in M_i,

$$\Delta(RHF_i) \approx \Delta M_i$$

$$= \sqrt{\frac{D_i^2}{N}} \qquad (5\text{-}26)$$

since the estimated variance of the sample mean M_i is D_i^2/N. Note that $\Delta(RFH_i)$ is taken here strictly as a measure of deviation and subscribes to no assumptions regarding normality or the Central Limit Theorem. Also, errors estimated on this basis are in conjunction with observed deviations and hence carry more information than the generic Poisson based prescription:

$$\frac{\Delta(RFH_i)}{RFH_i} \approx \frac{1}{\sqrt{T_i}} . \qquad (5\text{-}27)$$

In passing, we emphasize that Eq. (5-26) estimates the probable error and not the maximum incurred error.

For computational purposes, Eq. (5-26) is expanded to

$$\Delta(RFH_i) = \left\{ \frac{1}{N(N-1)} \left[\sum_{j=1}^{N} \left(\frac{D_{ij}}{S_j} \right)^2 - N M_i^2 \right] \right\}^{1/2} . \qquad (5\text{-}28)$$

All errors were estimated using Eq. (5-28) with $N = 5$, although in retrospect, a larger value of N could have been used. In addition, the code computed percentages rather than fractions so that RFH_i and $\Delta(RFH_i)$ as presented above were multiplied by 100.

The effect of variance reduction using splitting and Russian roulette through the introduction of importance regions is illustrated in Fig. 5.8. Each data point was generated by calculating SPF histograms for a knife edge of width $x_{max} = 1.0$ cm, cross sections $\Sigma_s = 1.0$ cm^{-1}, $\Sigma_a = 2.0$ cm^{-1} and with a point source normally incident at $y_o = -10.0$ cm. The

estimated percent relative error in the inner histogram is plotted as a function of CP time required to obtain that error so that proximity to the origin is the measure of the efficiency of an importance scheme. In each case, a meaningful comparison was effected by working in the "linear" range. That is, CP time varied directly with the number of particle interactions implying that initialization, counting and i/o time were negligible.

The usage of only one region, corresponding to the complete absence of splitting and roulette, was clearly the most inefficient scheme tested. It appears that for this assembly, three or four regions are most efficient. Qualitatively, the interpolated curve shapes in Fig. 5.8 appear consistent with the Poisson based relationship

$$[\text{Relative error}] \propto [\text{Number of histories}]^{-\frac{1}{2}}, \tag{5-29}$$

since the curves are consistent with the relationship

$$[\text{Relative error}] \propto [\text{Execution time}]^{-\frac{1}{2}} \tag{5-30}$$

and, in the linear range,

$$[\text{Execution time}] \propto [\text{Number of histories}]. \tag{5-31}$$

For the range of assemblies studied in this chapter, the use of three or four regions was invariably more efficient than either one or ten regions.

5.6 Program Testing

5.6.1 Boundary Conditions

The code was tested by performing a series of "boundary condition" tests for some of which familiar and simple analytical solutions exist. The most important of these tests are briefly described below:

(i) When $\Sigma_s = 0\ \text{cm}^{-1}$, check for simple exponential attenuation of intensity, given by

$$I^*(x_{max}) = I_o \exp[-\Sigma_a x_{max}], \tag{5-32}$$

over a wide range of the attenuation product $\Sigma_a x_{max}$.

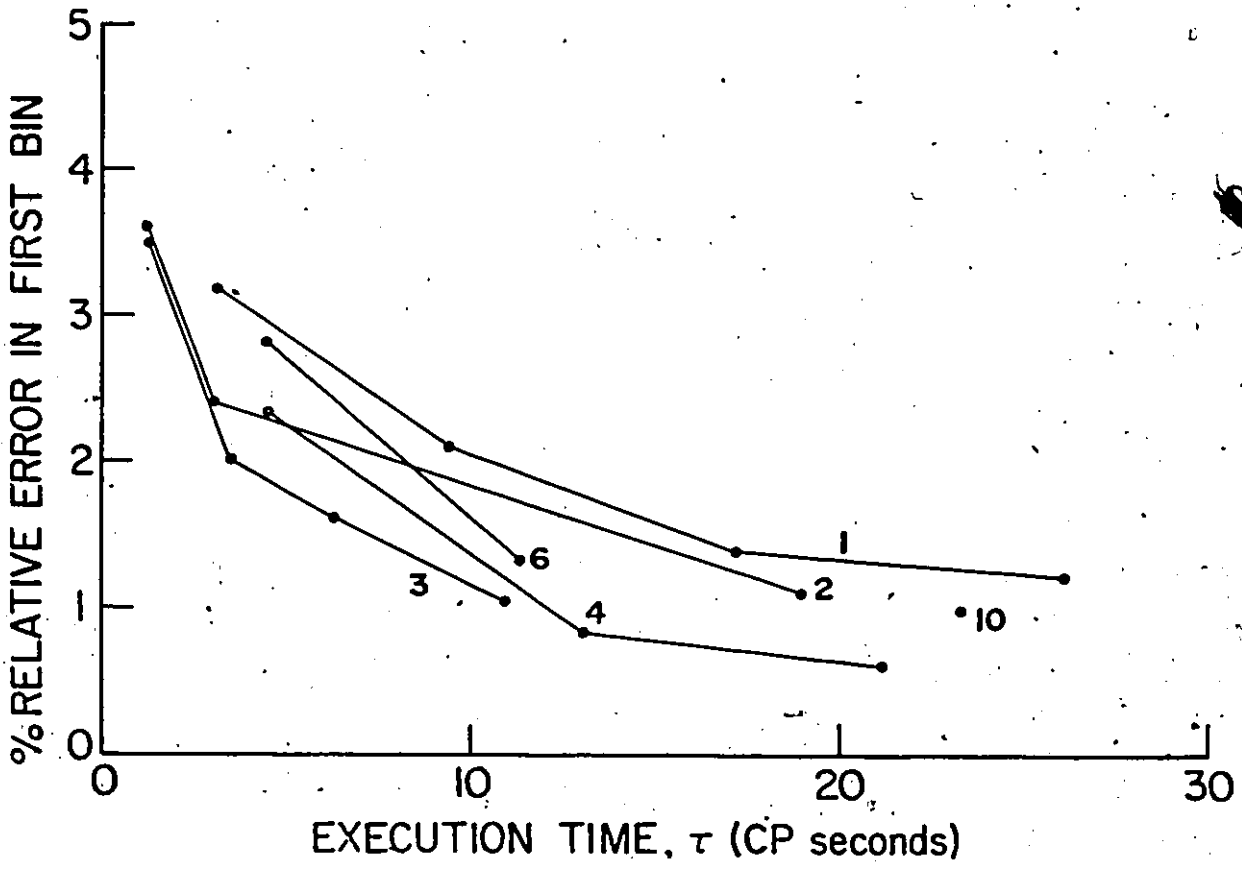

Fig. 5.8: Efficiency of importance regions in variance reduction for an SPF Monte Carlo calculation on a knife-edged slab with $\Sigma_t = 3.0\ cm^{-1}$, $\Sigma_s = 1.0\ cm^{-1}$ and $x_{max} = 1.0$ cm. The point source was normally incident at $y_o = -10.0$ cm. The curve labels are the number of regions used.

(ii) Upon adding Σ_s to test (i), check that the resulting intensity $I(x_{max})$ is smaller than $I^*(x_{max})$, and that beam spreading occurs for SPF, SLF calculations.

(iii) Check that SPF, SLF solutions for large negative y are independent of the planar boundary at y = 0.0 cm (Fig. 4.2).

(iv) Check that neither splitting nor roulette occur when there is precisely one region.

(v) Check that for large numbers of histories, the total right emergent weight is independent of the amount of splitting and roulette.

(vi) Check for conservation of weight, i.e., that the sum of left emergent , right emergent and absorbed weight equals the total number of simulated histories.

(vii) For $y_0 > 0.0$ cm, check that all particles fall into a single bin for SPF and SLF calculations.

(viii) For an SEF calculation with $\Sigma_s = 0.0$ cm^{-1} and normally incident neutrons, check for uniformity of both the positive and negative bins.

(ix) For oblique incidence with $\Sigma_a = \Sigma_s = 0.0$ cm^{-1}, check that right emergent neutrons fall into the proper bins, for a range of incidence directions.

5.6.2 Comparison with Other Solutions

An opportune way to test the code is to compare its solution, where applicable, to other solutions independently developed in this research. Convergence of several solutions suggests the correctness of each method although by no means constituting a proof.

Firstly, the convergence of the Monte Carlo SEF calculation to the model generating $SEF^{(1)}(y)$ in Eq. (4-23) has been illustrated in Fig.4.5 and discussed in section 4.4.

Secondly, the convergence of the Monte Carlo SEF calculation to the Neumann series intensity calculation of Chapter 2 is demonstrated in Table 5.1, through the comparison of right boundary intensities and build-up factors for an infinite slab object with

representative attenuation characteristics. Each pair of values is consistent within the estimated errors. Note that since the Monte Carlo intensities calculated in this chapter are forward partial currents, the intensity given in Eq. (2-33) was employed in the comparison.

Table 5.1: Comparison of slab right boundary forward partial currents (intensities) and build-up factors for an infinite slab with $\Sigma_t = 0.5\ cm^{-1}$, $\Sigma_s = 0.1\ cm^{-1}$ and $x_{max} = 5.0$ cm.

	(i) MONTE CARLO	(ii) NEUMANN SERIES	|(i) − (ii)| DEVIATION
$I(x_{max})/I_o$	0.095 ± 0.010 *1	0.092 ± 0.001 *2	0.003
$BUF(x_{max})$	1.16 ± 0.11	1.11 ± 0.01	0.05

*1 : See section 5.5 for estimation of Monte Carlo errors.

*2: Neumann series errors have been estimated as half the third, and smallest, mode evaluated at $x = x_{max}$.

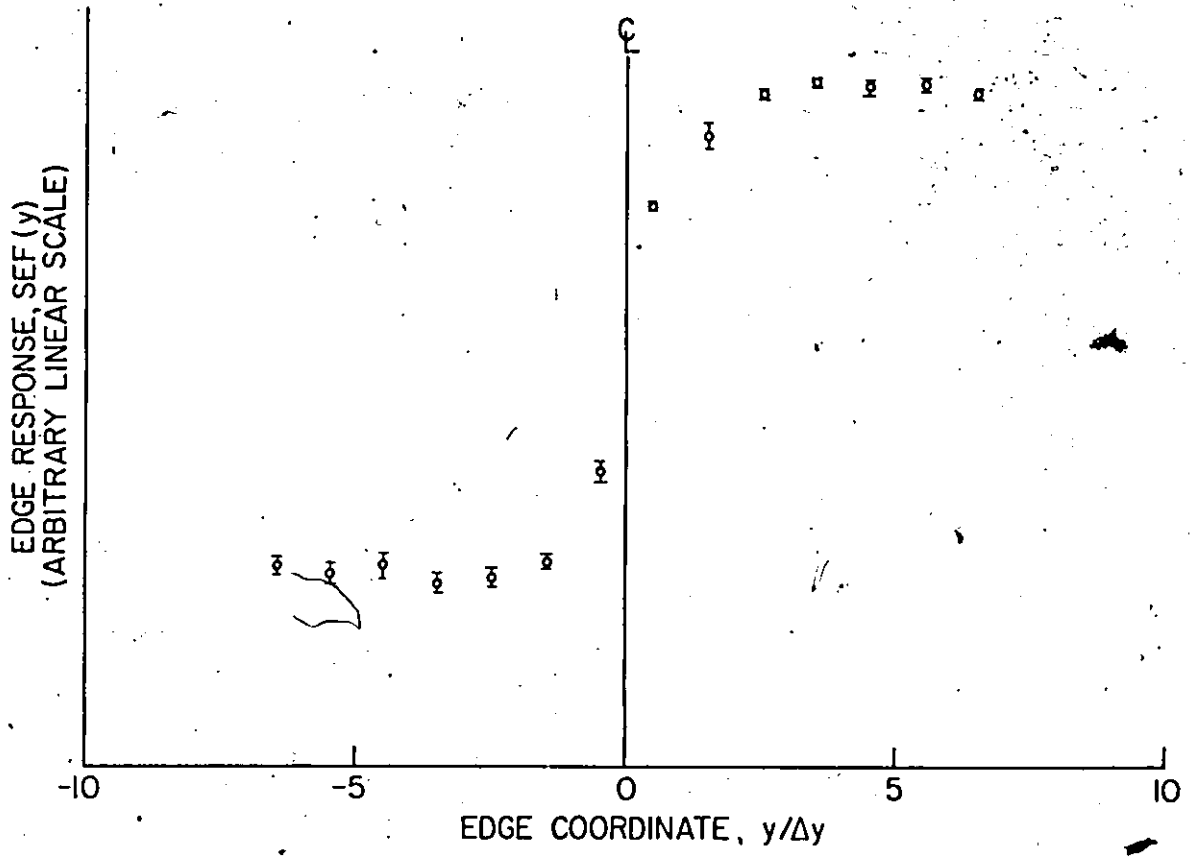

Fig. 5.9a: SEF for a totally and uniformly diffuse neutron source with $\theta_{max} = \pi/4$, incident on a knife-edged slab with $\Sigma_t = 2.0\ cm^{-1}$, $\Sigma_s = 1.0\ cm^{-1}$ and $x_{max} = d_o = 0.5$ cm. The bin width is $\Delta y = 0.15$ cm.

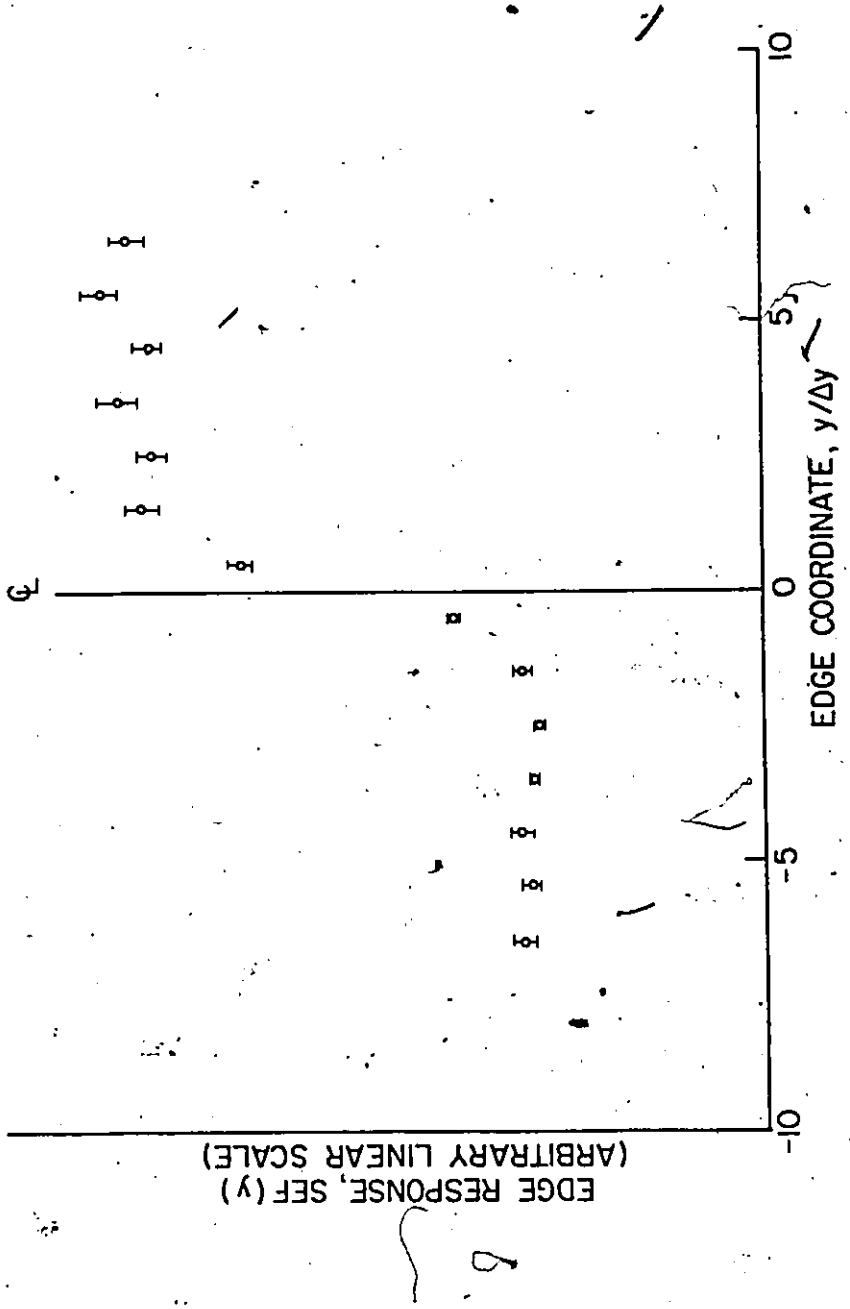

Fig. 5.9b: SEF for a totally and uniformly diffuse neutron source with $\theta_{max} = \pi/4$, incident on a knife-edged slab with $\Sigma_t = 2.0\ cm^{-1}$, $\Sigma_s = 1.5\ cm^{-1}$ and $x_{max} = d_o = 0.5$ cm. The bin width is $\Delta y = 0.15$ cm.

5.7 The SEF as a Diagnostic Tool: A Preliminary Assessment

The SEF curves with the characteristic positive and negative SBED's, as illustrated in Fig. 5.6, represent the knife-edged slab output response to collimated uniformly incident thermal neutrons. For a diffusely incident source, considerable blurring of the SEF in Fig.5.6 is expected. Even uncollided neutrons registering at a point on the scoring plane at $x = d_o$ will contribute information from sections of the object other than the line passing through the object orthogonal to the scoring plane at that point. The SEF for a uniformly diffuse source is illustrated in Figs. 5.9 for two different edges. The Monte Carlo calculation was performed by uniformly randomly selecting, for each incident neutron, an initial direction in the forward cone

$$\Omega_{cone} = \{(\theta,\phi) \mid \theta \in [0,\theta_{max}], \phi \in [0,2\pi]\}, \qquad (5\text{-}33)$$

where θ_{max} is a pre-specified upper bound on θ, and smaller than $\pi/2$. The data points in Figs. 5.9 are actually histogram bin values.

Figs. 5.9 show that the SBED's have all but disappeared, particularly near the planar boundary at $y = 0.0$ cm. This SEF resembles the conventional edge spread function (ESF), found for example, in reference 105. The existence of a degree of diffuse incident radiation partially explains why the SEF shape in Figs. 5.6 has been almost completely unnoticed in practice. The chief explanation is that in usual applications involving some type of edge response measurement, nonscattering materials have been preferred.

As expected, the SEF curve in Fig. 5.9b exhibits a slightly greater spreading of the ideal edge response than that in Fig. 5.9a, due to the cross- section differences. The diffuse obliquity of the incident source tends to minimize such differences, however.

The effect of the SBED dampening by diffuse incidence suggests the application of a knife edge with a high Σ_s/Σ_t ratio as a diagnostic tool for determining the ratio of diffuse (D)

to collimated (C) incident radiation. This latter ratio has an obvious radiographic application it is related to the build-up factor (BUF), by

$$BUF = 1 + \frac{D}{C}, \tag{5-34}$$

describing the extent to which scattering in a radiographed object will degrade the collimated, information-carrying ray image, section 2.3. This prospective diagnostic tool is outlined schematically in Fig. 5.10. Its application is based on the idea that the extent of dampening of the SBED's is an indication of the D/C ratio of neutrons impingent on the knife edge. This ratio in turn indicates the BUF of object emergent neutrons.

It is difficult to attempt to quantify this relationship other than empirically, since other image degradation and interpretation effects, such as screen-film unsharpness, the edge-scanning techniques and characteristic curve, will ultimately determine the feasibility of this diagnostic tool.

It is encouraging, from the modelling standpoint of section 4.3, that the SBED height to SEF amplitude ratio approaches unity when $\Sigma_a \rightarrow 0.0\ cm^{-1}$. This ratio has previously been defined as the "relative SBED height", in section 4.3.

As a preliminary feasibility test, the SEF was calculated for a knife-edged slab with various D/C incidence ratios between zero and one. The results are illustrated in Fig. 5.11. Since errors were sufficiently small and to avoid cluttering, best-fit curves were drawn for three of the four sets of points. As expected, increasing D/C corresponds to decreasing the SBED height from a maximum at D/C = 0.0 to non-existence at D/C = 1.0. Figure 5.11 suggests that the SBED height, as an indicator of D/C, will be most effective for D/C values smaller than approximately 0.4, corresponding to a BUF of 1.4. The relative SBED height should actually be the important indicator, as discussed in section 4.3.

There are several problems associated with the usage of the SEF relative SBED height as an indicator of the D/C incidence ratio. These are:

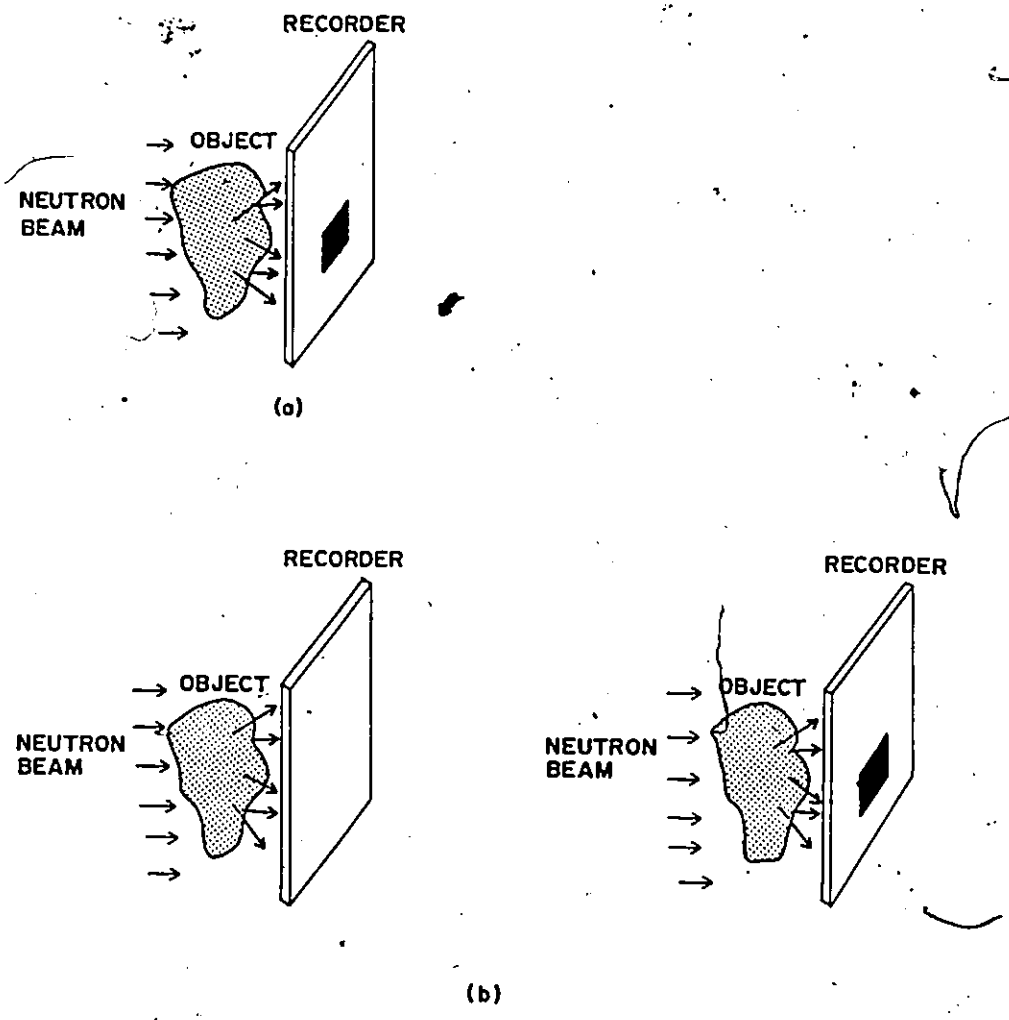

Fig. 5.10: Illustration of prospective application of the SEF as a diagnostic tool. Rectangular sections of a highly scattering material comprise "infinite" knife edges which are placed adjacent to the recorder (a) during the exposure, or b) during a separate exposure to avoid unacceptable interference with the radiograph.

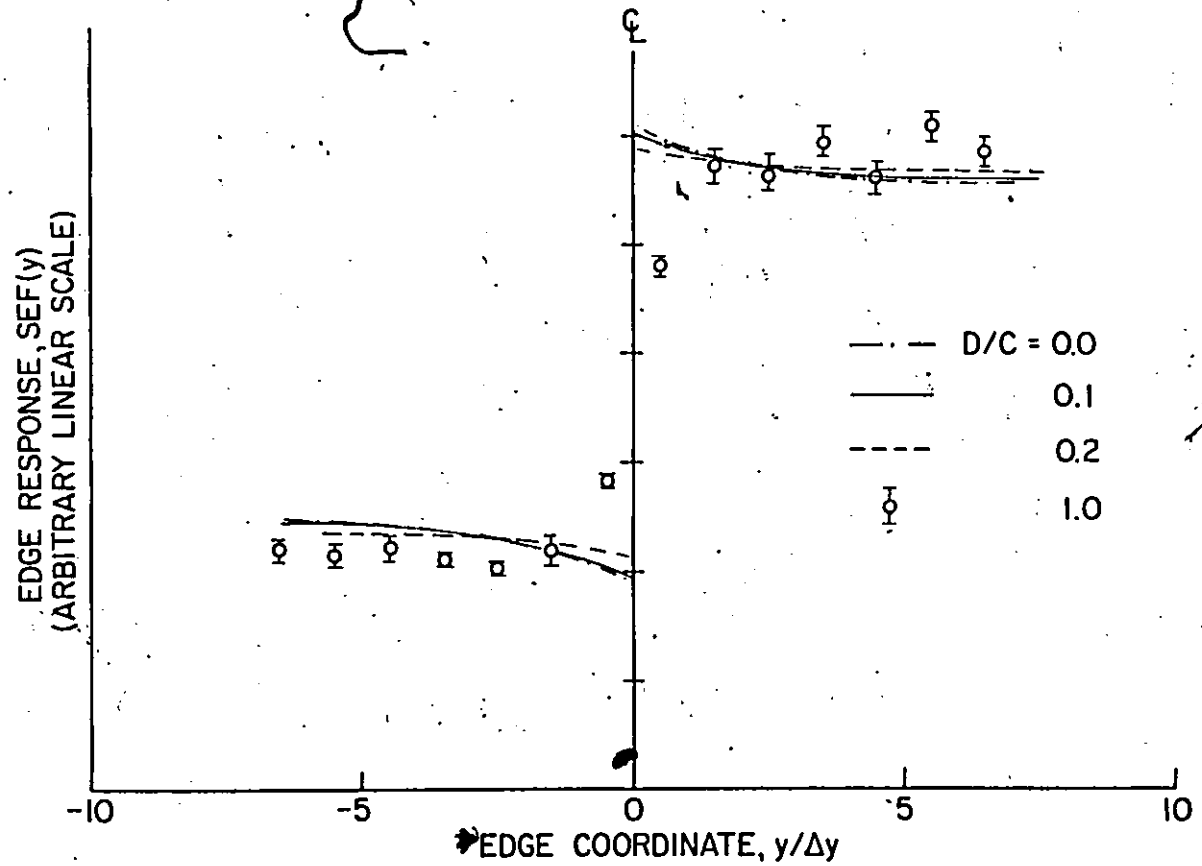

Fig. 5.11: SEF for various diffuse-to-collimated (D/C) ratios of neutrons incident on the same knife-edged slab as in Fig. 5.9b. Here, $\theta_{max} = \pi/4$ and the bin width is $\Delta y = 0.15$ cm.

(i) The uniformity of the incident beam affects the SEF; thus the knife-edged slab should be aligned with a section of the radiographed object that has nearly constant attenuation characteristics.

(ii) The proximity of the knife-edged slab to the object determines θ_{max}, which in turn affects the SEF.

(iii) The proximity of the knife-edged slab to the recording film plane affects the SEF.

These latter two problems are now discussed.

Firstly, as the distance between the object and knife-edged slab increases, the forward cone of incident directions decreases in scope; indeed, this variation is used to some extent in the suppression of scattered radiation in medical radiology (3). In practice, the knife-edged slab should then be placed at a fixed distance from objects being radiographed. While the uniformity of incident directions within the forward cone should not be a problem, some diagnostic tool to determine θ_{max} would be helpful. In Fig. 5.12, the SEF variation with θ_{max} is illustrated for completely and uniformly diffuse incident neutrons. As expected, the SEF for $\theta_{max} = \pi/4$ appears to be sharper than that for $\theta_{max} = 3\pi/8$, although the difference in the two curves is not great. This suggests stability of the proposed method with respect to errors in the estimation of θ_{max}.

Secondly, increasing the separation of the knife edge and recording film serves to stretch the SEF by increasing the spread of scattered neutrons. In practice, this separation, defined here as Δ_{film}, should then be maintained constant. In Fig. 5.13, the SEF variation with Δ_{film} is illustrated for collimated incident neutrons. The proximity of the two SEF curves over Δ_{film} differences as large as 0.4 cm strongly suggests stability with respect to the small differences in Δ_{film} that might typically occur over various exposures. Indeed the SEF curves for $\Delta_{film} = 0.0$ cm and $\Delta_{film} = 0.1$ cm are indistinguishable.

The above results are not intended to suggest the scattering edge response as a BUF indicator that is superior to existing calculational and experimental techniques, such as described in references 2 and 16; further research is required before any such assertion is possible. Qualitatively, however, it is interesting to note that the calculational BUF indicator described by Halmshaw (reference 2, p. 146) for x-ray radiography is based on the extent to which emergent scattered radiation degrades a defined "contrast sensitivity" parameter. The indicator is valid for large, constant-depth, homogeneous objects and is accordingly restricted in application. Barton (79) has previously verified this proportionality between the BUF and contrast sensitivity for the neutron radiographic inspection of objects of similarly constant geometry. A discussion of image quality indicators, sensitivity and beam purity can be found in reference 16. The similarity between the image-quality indicator developed in this chapter and that described in Halmshaw's text (2) is clear – both are based on the degradation of some response parameter by emergent scattered radiation. Also, proper usage of each of these indicators is subject to the chief restriction given by (i) above.

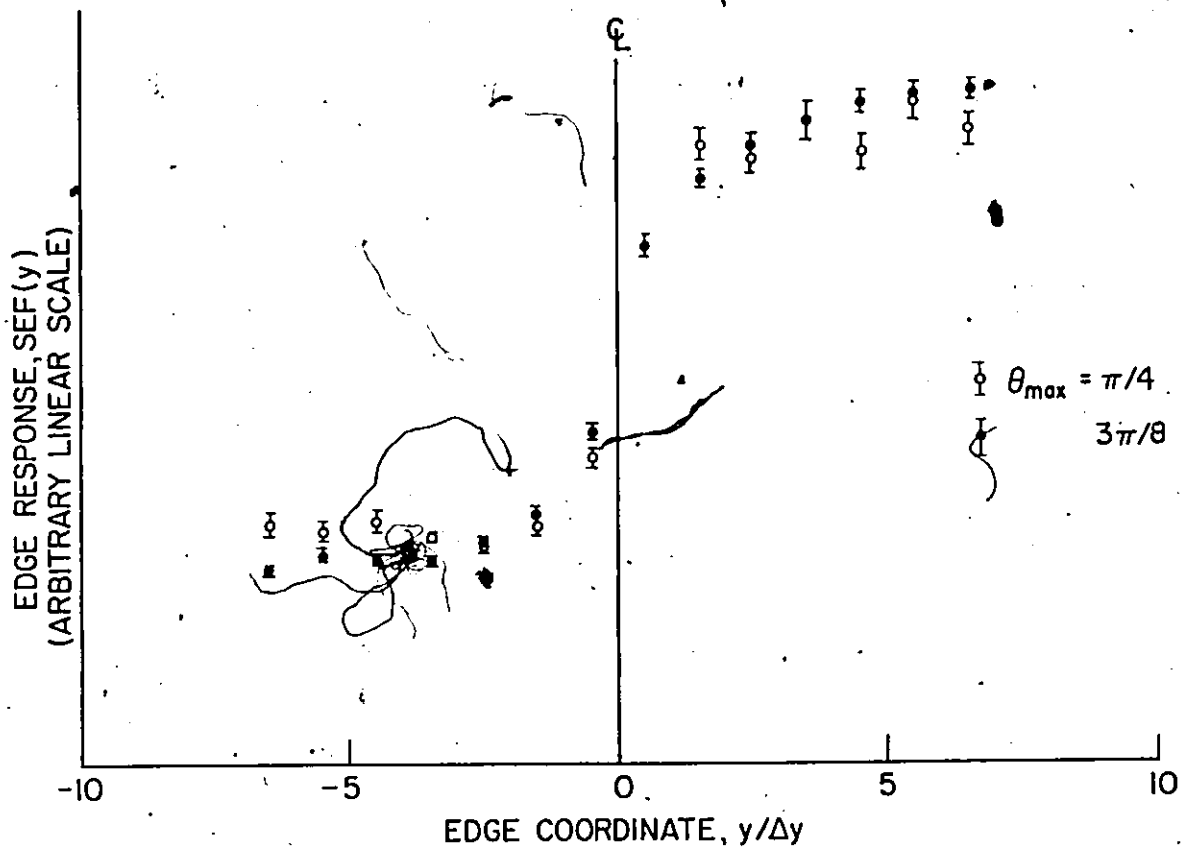

Fig. 5.12: SEF for different incident direction cone magnitudes, for completely diffuse ($D/C \to \infty$) neutrons incident on the same knife-edged slab as in Fig. 5.9b. The bin width is $\Delta y = 0.15$ cm.

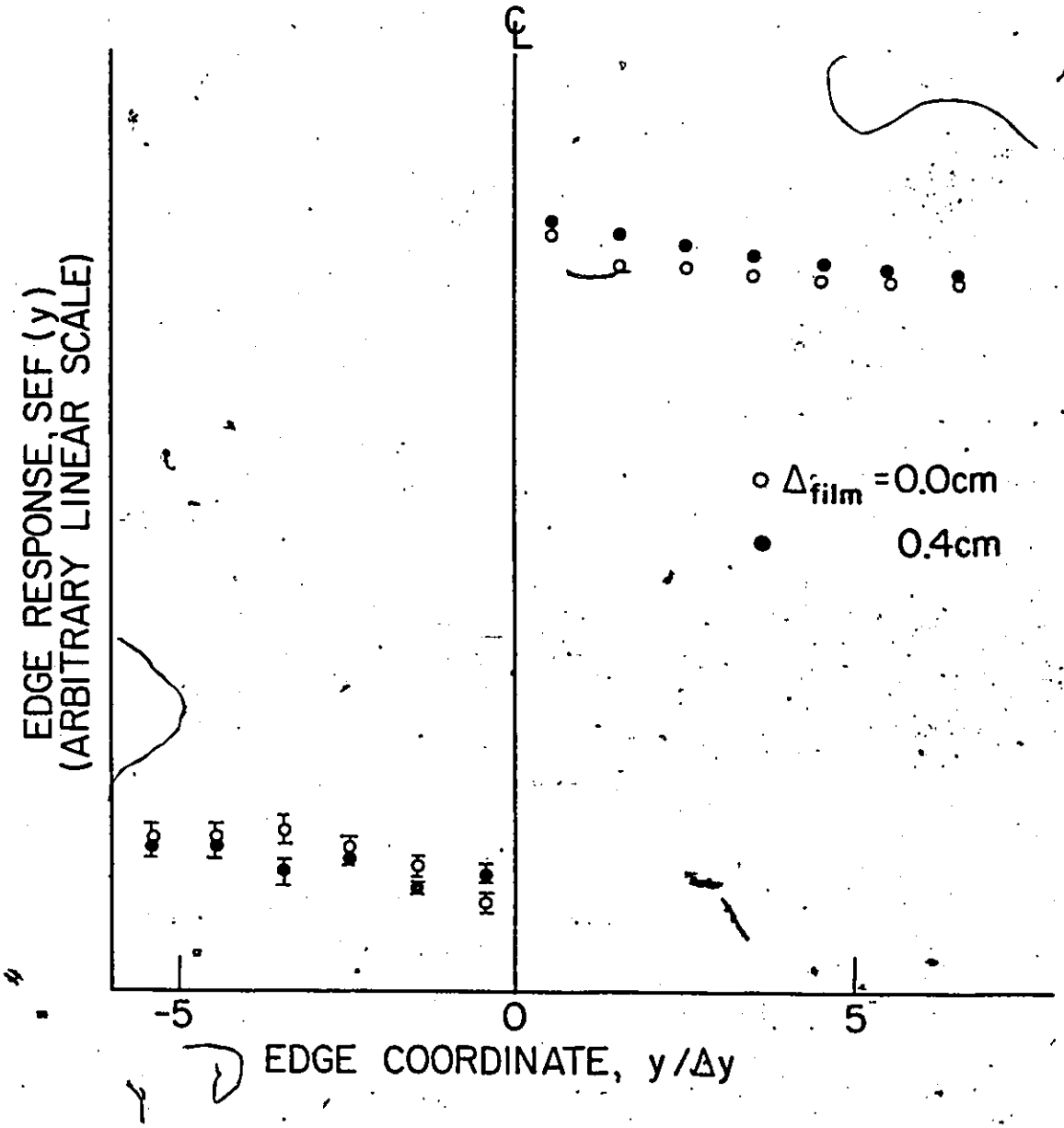

Fig. 5.13: SEF for different knife edge-to-film separations (Δ_{film}) for collimated neutrons incident on the same knife-edged slab as in Fig. 5.9b. The bin width is $\Delta y = 0.15$ cm.

CHAPTER 6

EXPERIMENTAL CONFIRMATION OF THE EDGE SCATTERING PHENOMENON

6.1 Equipment

Experimental investigations were conducted at the McMaster Nuclear Reactor (MNR) to study the edge scattering output response distortion phenomenon analyzed in Chapters 4 and 5. Specifically, it is desirable to detect these scattering based edge distortions (SBED's) and to experimentally estimate their relative magnitude under the various degradation conditions discussed in section 5.7. In that section, it was suggested that the SBED height measurement might find application as an indicator of the build-up factor (BUF) in the neutron radiation emergent from a radiographed object, particularly for smaller BUF values.

With respect to this suggested diagnostic application, the purpose of these investigations was not to develop a reliable image quality indicator but rather to judge whether or not such a diagnostic tool could be developed. The need for experimental confirmation and analysis of this phenomenon has previously been recognized (51).

The investigations were conducted at the thermal neutron radiographic facility constructed around beam port 2 at the MNR, and shown in Fig. 6.1. Type T (fine grain emulsion) Kodak x-ray film placed adjacent to a gadolinium foil of uniform thickness 25 μm comprised the direct exposure image recorder. This combination, enclosed in a pressure cassette, was exposed to the neutron beam by manual control of a shutter over the beam, Fig. 6.2. The neutron scalar flux, approximately equal to the neutron current incident on the objects being inspected, was approximately $2 * 10^6$ n/cm^2/s. The beam was well thermalized with the most probable energy of its Maxwellian spectrum being 0.025 eV. This permits the usage of standard 2200 m/s cross-section data in calculations. The beam gamma content

Fig. 6.1: McMaster Nuclear Reactor neutron radiography facility.

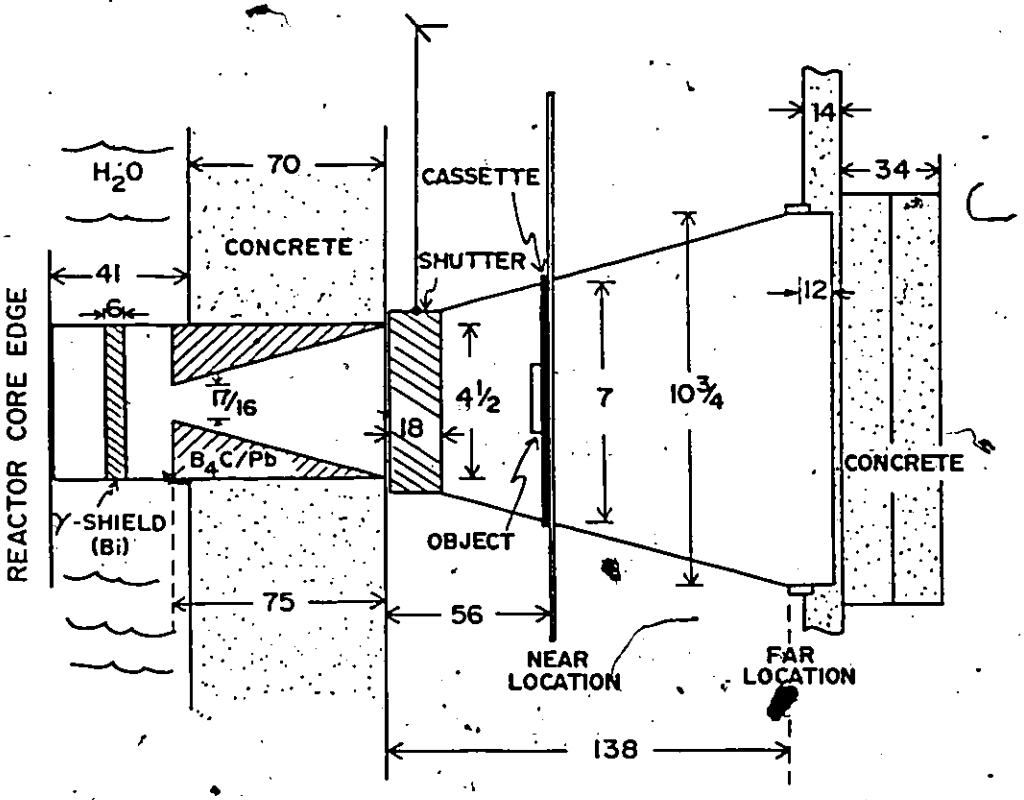

Fig. 6.2: Side view schematic illustration of relevant beam and geometrical characteristics for the neutron radiography facility in Fig. 6.1. All dimensions have units of 2.54 cm.

Beam divergence: $L/D \approx 70.6$.

Gamma content: $\gamma \approx 5.0*10^6$ n/cm^2/mrem.

Neutron scalar flux:

(a) Near location: $\phi \approx 2.0*10^6$ n/cm^2/s

(b) Far location: $\phi \approx 1.0*10^6$ n/cm^2/s.

value has been measured (106) and found to be approximately $5 * 10^6$ n/cm^2/mrem. This is easily within the acceptable limits of beam contamination (12). The L/D ratio of the beam collimator is approximately 70.6, so that the resulting beam divergence is also well within commonly acceptable limits (12).

Typical exposure times were 2.5 m to 4 m. The resulting developed negatives, commonly referred to as "radiographs", were analyzed using a Leitz Wetzlar MPV scanning microdensitometer, shown in Fig. 6.3. Using this equipment, strip chart records of straight-line transmission optical density scans were obtained. Since these scans were taken perpendicular to a knife edge image, a rectangular geometry was selected for the scanning window. Tests suggested that useful window dimensions were height - 200 μm and width - 30 μm; the relatively large window height reduces the effects of emulsion granular noise while the small width increases the accuracy of the scan by reducing the magnitude of smoothing of the actual optical density variation being scanned. This is discussed further in Appendix B.

A photograph of the pressure cassette and radiographed samples is displayed in Fig. 6.4.

6.2 Film Emulsion Characteristics

Although the standard emulsion properties are supplied by the manufacturer of the film, it is common practice in careful densitometric work to obtain a density vs. exposure curve for the film being used. This is necessary because of variations arising from the particular spectral composition of the image carrying radiation and also from the local developing conditions (107).

For the x-ray film used in these experiments, the density vs. exposure curve was generated by scanning a sensitometric strip consisting of a series of adjacent radiographic negative regions differing in exposure by thirty seconds. Two strips were made for one piece of

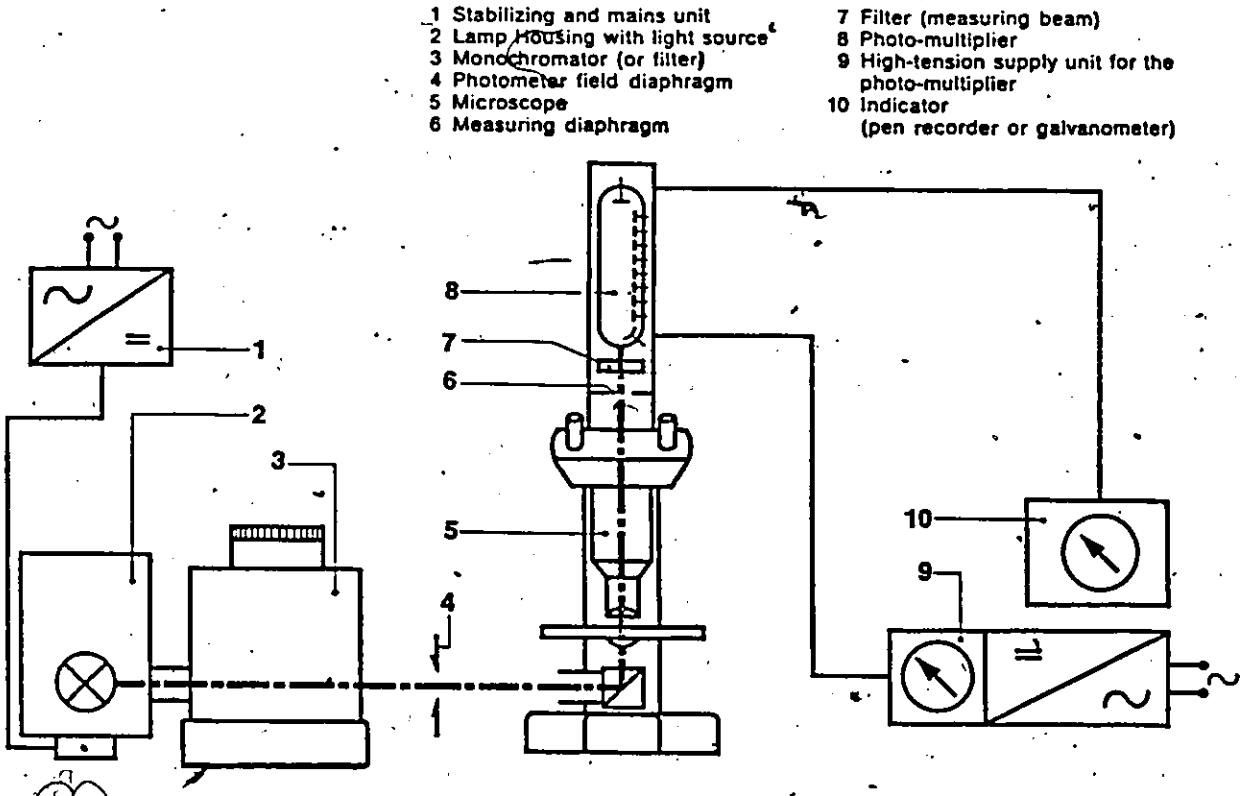

Fig. 6.3: The Leitz Wetzlar travelling stage (scanning) microdensitometer and chart recorder unit.

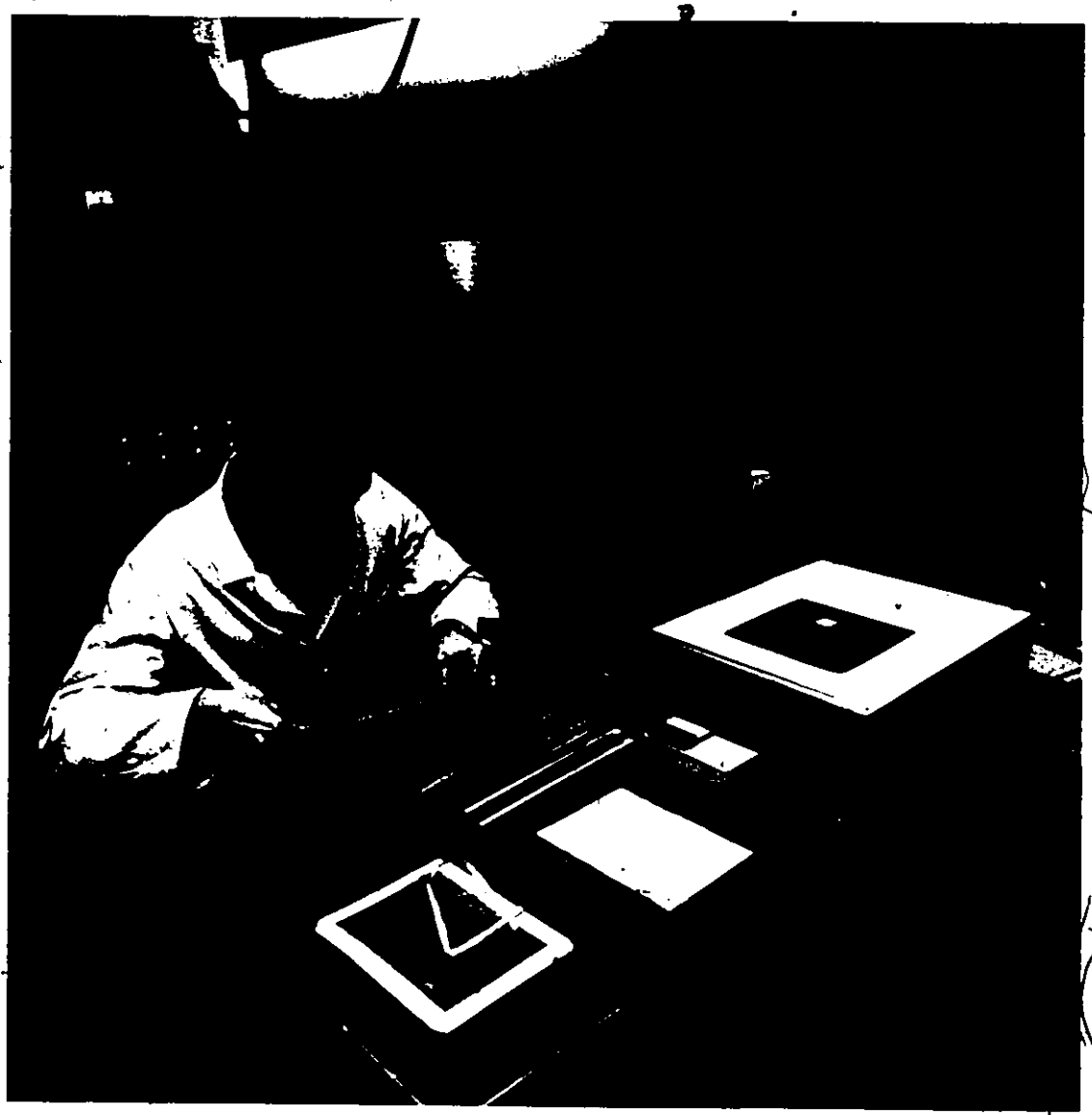

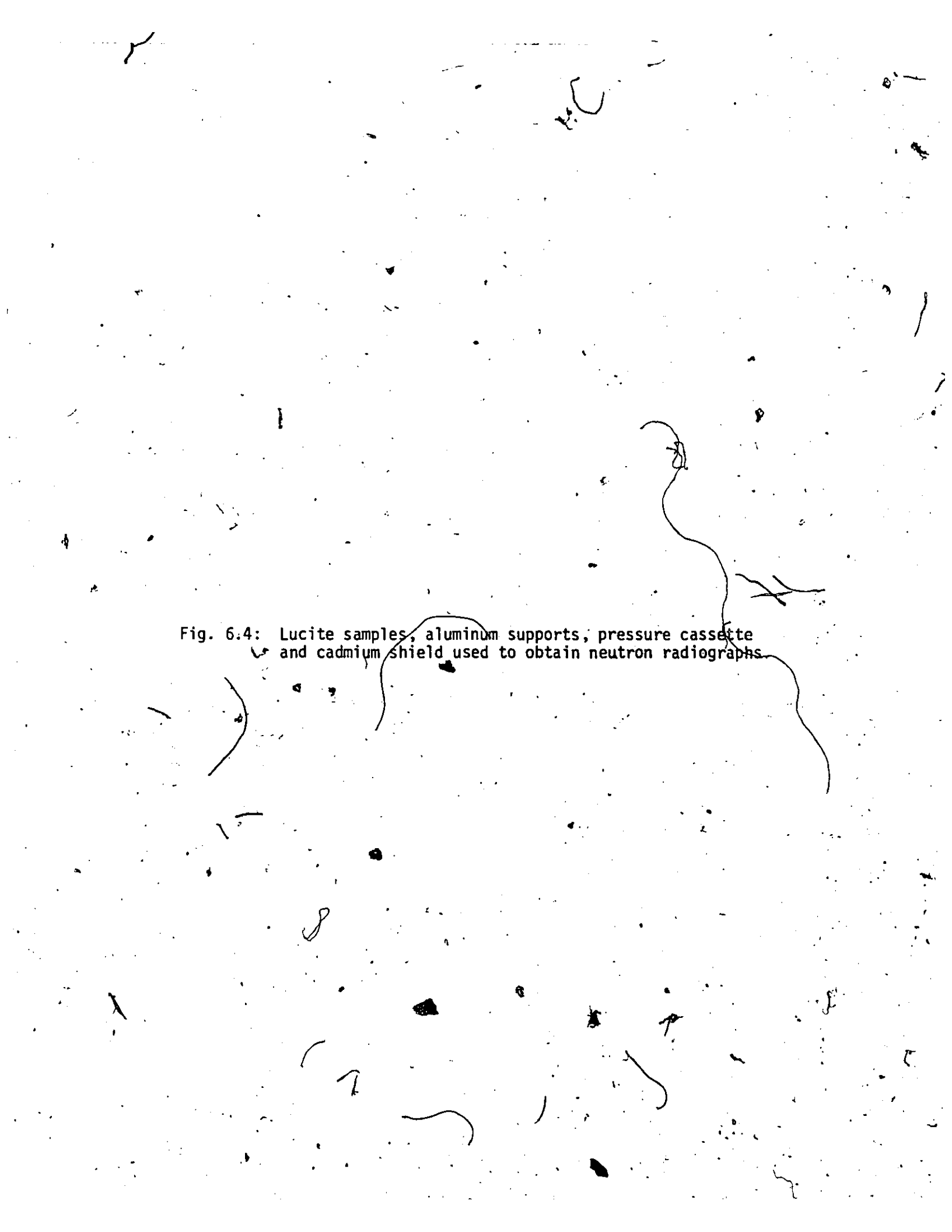

Fig. 6.4: Lucite samples, aluminum supports, pressure cassette and cadmium shield used to obtain neutron radiographs.

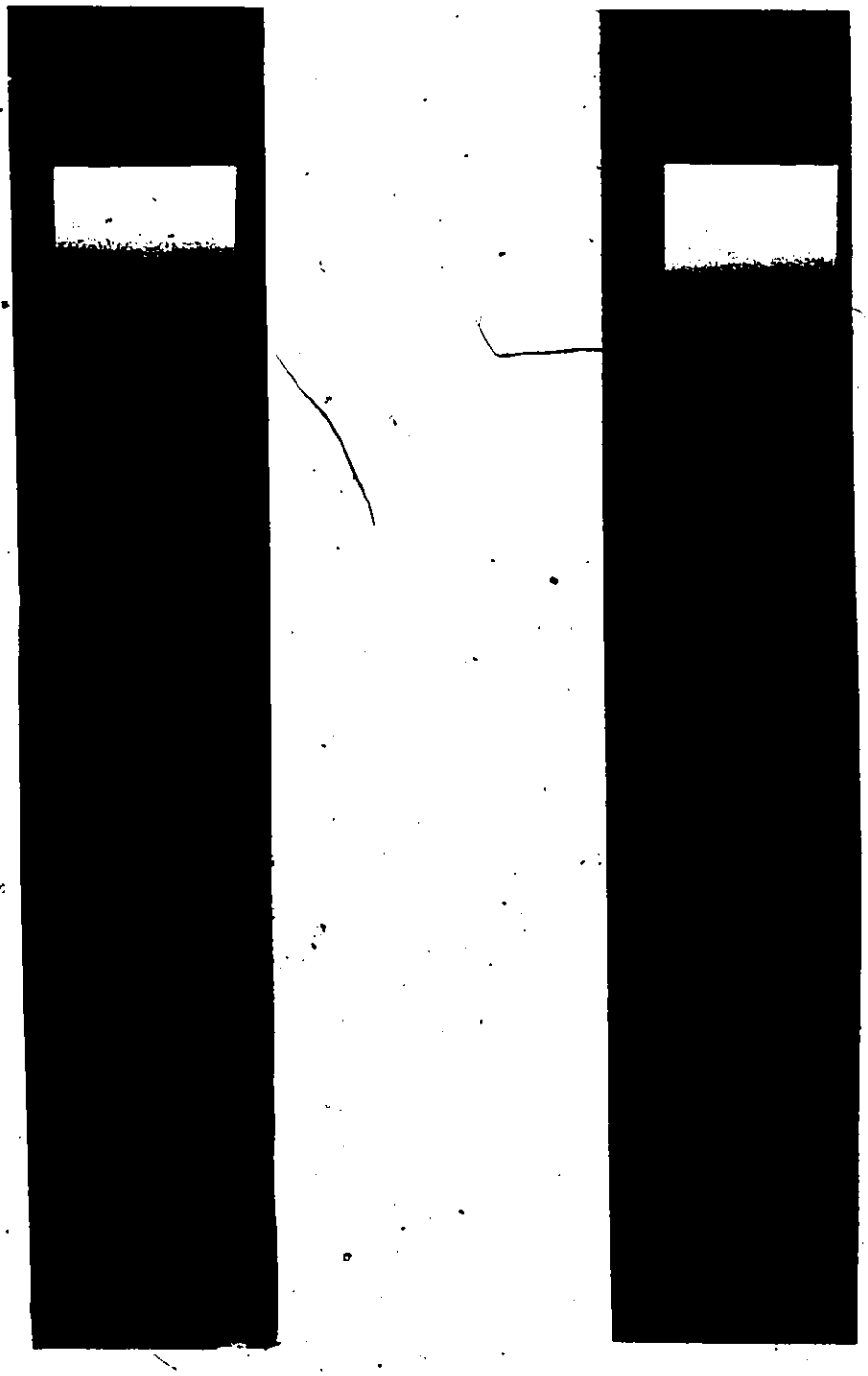

Fig. 6.5: Sensitometric strips for generation of density vs. exposure curve and calibration of scanning microdensitometer.

film, Fig. 6.5, in order to determine the extent of regional variation over an individual radiograph. This was accomplished by initially shielding an otherwise exposed cassette with a cadmium slab and then incrementally raising the slab approximately 1 cm every 30 seconds. The slab consisted of three cadmium sheets of individual thickness (16.0 ± 0.5) * 25.4 μm, so that the emergent fraction of the incident beam was smaller than

$$\frac{I}{I_o} = \exp[-\Sigma_t x]$$

$$= \exp\left[\frac{-114(48.0 \pm 1.5)(2.54)}{1000}\right]$$

$$\approx (9.2 \pm 5.0)10^{-7}, \qquad (6\text{-}1)$$

and hence negligibly small; the macroscopic total cross-section for cadmium used in this equation was taken from reference 75. The resulting density vs. exposure curve is plotted in Fig. 6.6. The value of the background fogging component of subsequent neutron radiographs was estimated by this sensitometric procedure as corresponding to an optical density of 0.49 ± 0.02. Possible errors for each optical density value were estimated as the maximum deviation of six readings from their average, repeated for each strip and then combined. In practice, microdensitometric optical density variations are usually projected back to the object attenuation properties that they image so that background fog is customarily subtracted from readings. This leads to the definition of a "net optical density", given by

$$\text{net optical density} = \text{measured optical density} - \text{background fog}. \qquad (6\text{-}2)$$

For this radiographic facility and film, the linear portion of the density vs. exposure curve appears to lie between exposures of one to three and one-half minutes corresponding to optical densities between 1.0 and 2.2. As will be shown, it is desirable to restrict radiographs to this linear range for these investigations.

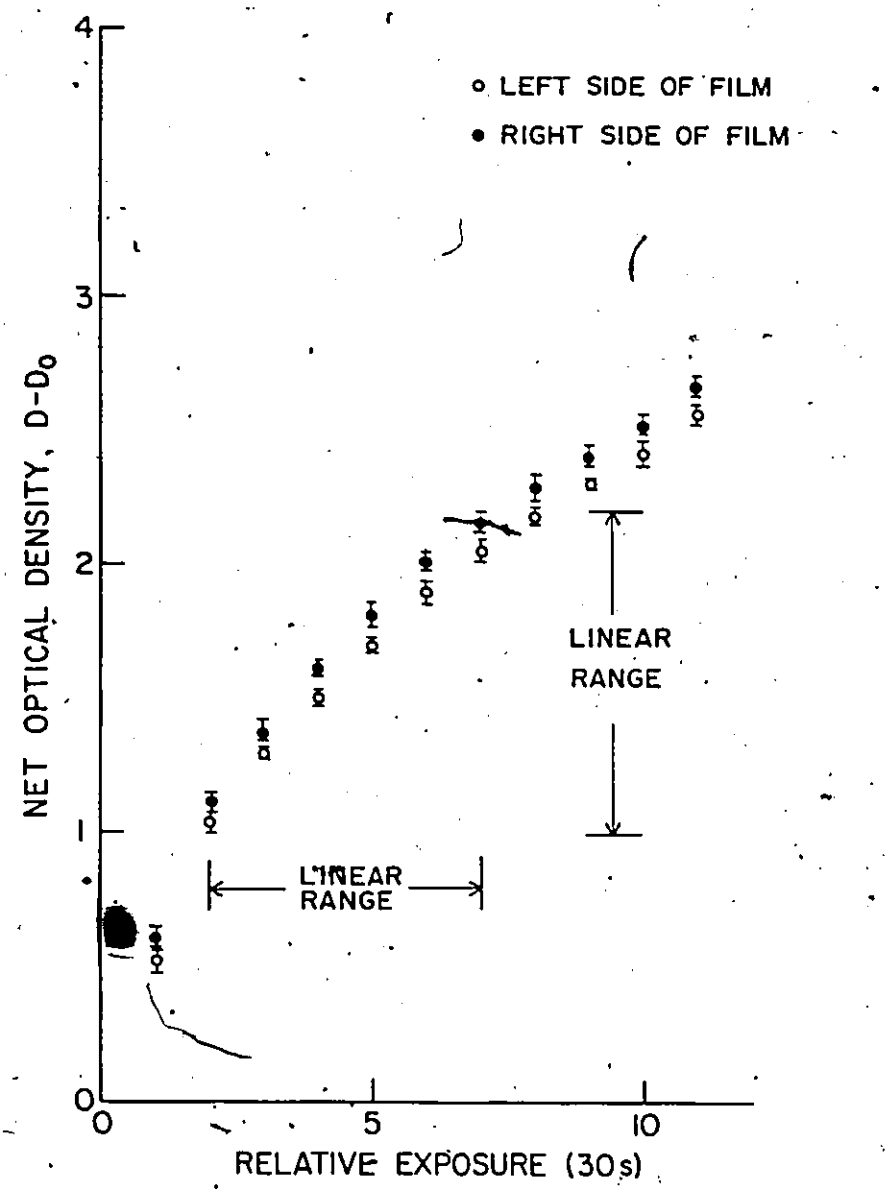

Fig. 6.6: Density vs. exposure curve for direct exposure neutron radiography with a gadolinium convertor and type T X-ray film. Relative exposure maximum error is ±1.5 s.

6.3 Procedure

Since the knife-edged slab sample to be radiographed must have a large Σ_s/Σ_a ratio, the plastic compound lucite (polymethyl methacrylate) was selected as a sample. The chemical composition of lucite is $[CH_2C(CH_3)(CO_2CH_3)-]_n$ so that each unit has 5 carbon, 8 hydrogen and 2 oxygen atoms. Denoting the type "i" microscopic cross-section of the element with atomic symbol "j" by $\sigma_{i,j}$, the cross-sections for lucite are

$$\sigma_{a,L} = 8\,\sigma_{a,H} + 5\,\sigma_{a,C} + 2\,\sigma_{a,O}, \tag{6-3a}$$

$$\sigma_{s,L} = 8\,\sigma_{s,H} + 5\,\sigma_{s,C} + 2\,\sigma_{s,O}. \tag{6-3b}$$

Substituting thermal cross-sections for C, H and O(75), $\sigma_{a,L}$ and $\sigma_{s,L}$ are evaluated to be $\sigma_{a,L}$ = 2.66 b and $\sigma_{s,L}$ = 336.40 b. Now the type "i" macroscopic cross-section is given by

$$\Sigma_{i,L} = \sigma_{i,L}\left(\frac{\rho\, N_A}{A}\right), \tag{6-4}$$

where ρ is the density, N_A is Avogadro's number and A is the atomic weight. Taking A = 100.13 g/mole and ρ = 1.19 g/cm^3 (reference 108), $\Sigma_{a,L}$ and $\Sigma_{s,L}$ are found to be $\Sigma_{a,L}$ = 0.019 cm^{-1} and $\Sigma_{s,L}$ = 2.408 cm^{-1}.

After passage through 1/2 cm of lucite, a fraction

$$\gamma_s = 1 - \exp[-\Sigma_{s,L}/2]$$
$$\approx 0.700 \tag{6-5}$$

of the collimated incident beam will undergo at least one scattering event. This should be sufficient to permit observation of the SBED while not effecting too great a difference in exposures across the slab edge. A readily-obtained square slab lucite sample of thickness 0.592 $\pm$ 0.003 cm and side length 2.54 cm was chosen.

The sample was radiographed by affixing it to the exposed surface of the recording cassette prior to insertion in the neutron beam as shown in Fig. 6.7. The sample to film separation is estimated as the thickness of the cassette wall, measured to be 0.86 $\pm$ 0.03 mm. A photograph of the resulting radiograph is given in Fig. 6.8a.

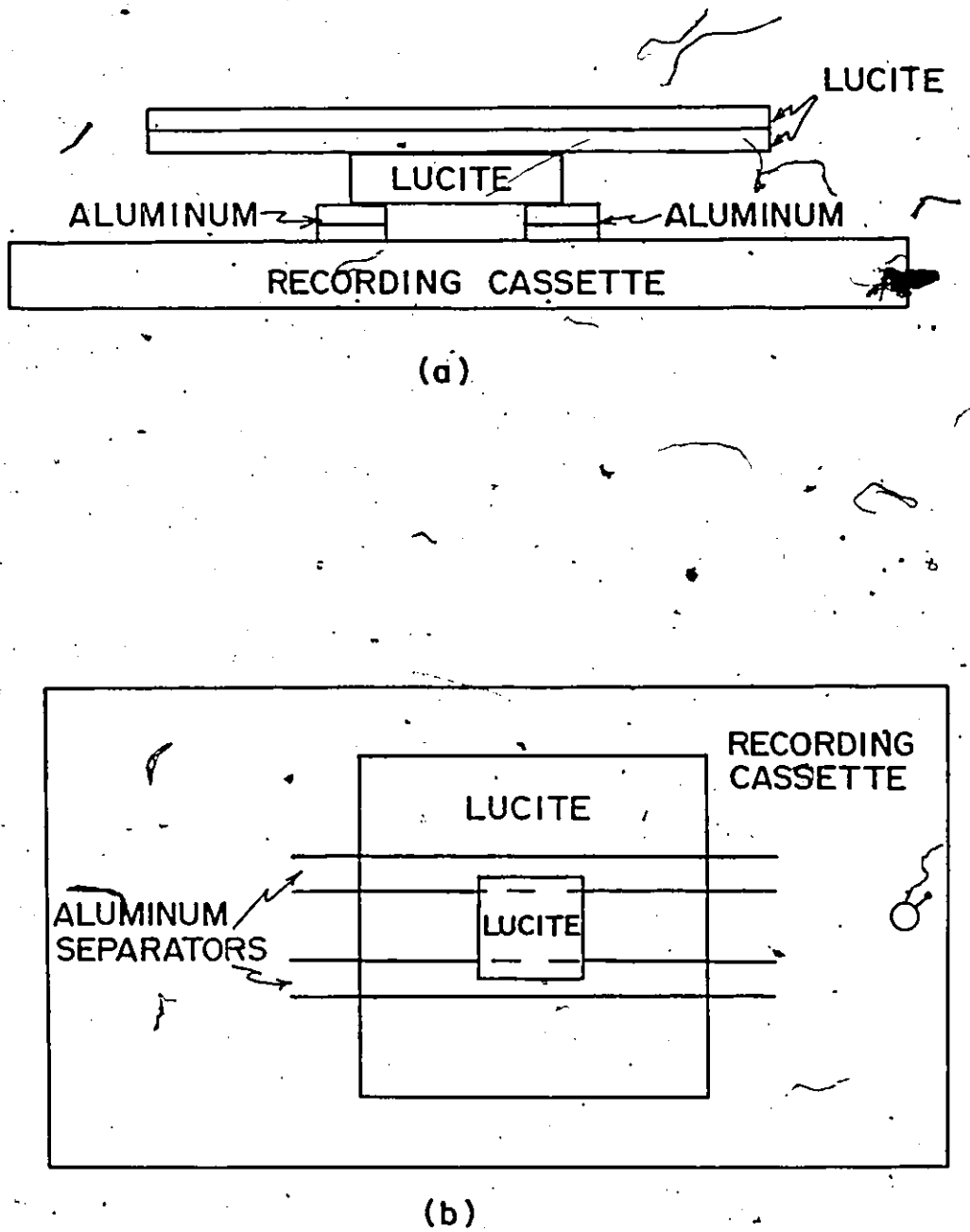

Fig. 6.7: Configuration of radiographed lucite knife-edged slab samples on the pressurized recording cassette (not to scale). (a) Side view. (b) Top view.

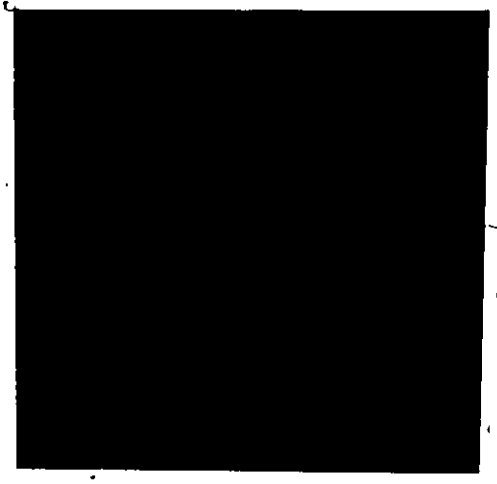

(a)

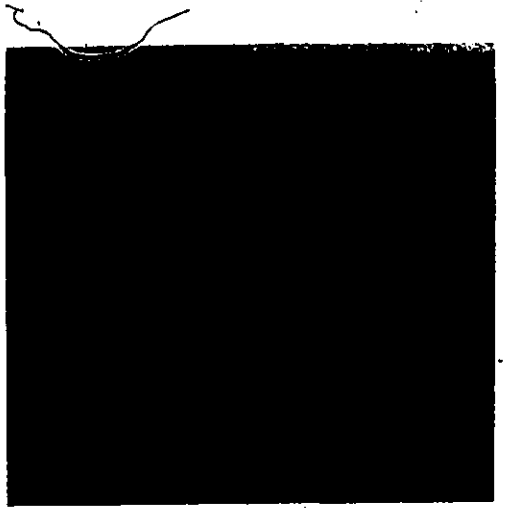

(b)

Fig. 6.8: Neutron radiograph of the 0.592 cm lucite slab with collimated incident neutrons and a slab to film separation of (a) 0.86± 0.03 mm, (b) 1.67± 0.06mm.

In order to determine the magnitude of the effect of the sample to film separation on the resulting SBED in the edge scan, the separation was increased to 1.67 ± 0.06 mm. This was accomplished by inserting aluminum runners of width 0.81 ± 0.03 mm between the sample and the cassette as shown in Fig. 6.7. A photograph of the resulting radiograph is given in Fig. 6.8b. The separation was further increased to 2.48 ± 0.09 mm by inserting two sets of aluminum runners and a radiograph was again taken.

In order to ascertain the plausibility of the SBED as an indicator of object scatter, various degrees of diffuseness of incident radiation were required. This was accomplished by interposing large flat lucite plates between the edge sample and the neutron beam, as shown in Fig. 6.7. The ratio of scattered to total radiation emergent from a single plate with normally incident radiation is, section A.7, for isotropic scattering given by the following intensity ratio:

$$R_s = I_{scattered,exit}/I_{exit}$$
$$\approx \left[1 + 2\left(\frac{\Sigma_t}{\Sigma_s}\right)\left(\frac{1}{\exp[\Sigma_t \Delta x] - 1}\right)\right]^{-1}. \qquad (6\text{-}6)$$

In the derivation of Eq. (6-6), the plate thickness Δx is assumed to be sufficiently small that secondary interactions are negligible. Since the thickness of each lucite plate was 1.95 ± 0.01 mm, the R_s values for small numbers of plates are, in decreasing order of accuracy, approximated using Eq. (6-6) to be

$$R_{s,1} \approx 0.23$$
$$R_{s,2} \approx 0.44$$
$$R_{s,3} \approx 0.61 \qquad (6\text{-}7)$$
$$R_{s,4} \approx 0.74 .$$

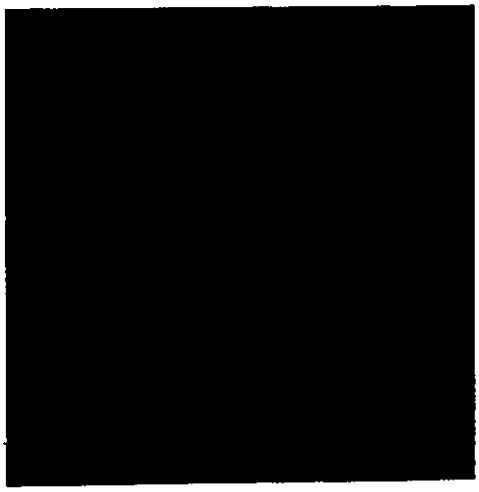

(a)

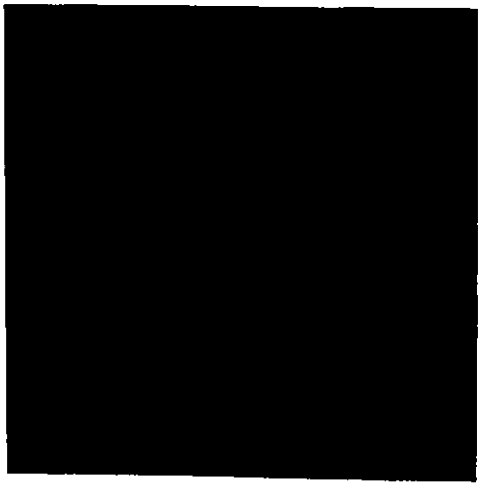

(b)

Fig. 6.9: Neutron radiograph of the 0.592 cm lucite slab with fractionally diffuse (R_s) incident neutrons. (a) R_s = 0.23 and BUF = 1.30, (b) R_s = 0.44 and BUF = 1.78

Here, $R_{s,n}$ denotes R_s for an insertion of n adjacent plates. The build-up factors corresponding to the R_s values in Eq. (6-7) can be calculated using

$$BUF = \frac{1}{1 - R_s}. \tag{6-8}$$

Thus, for one inserted scattering plate, approximately 23% of the neutrons incident on the knife edge sample are obliquely incident and 77% are collimated. Photographs of radiographs taken with up to two interposed plates are shown in Fig. 6.9. For thicker plates, the $R_{s,n}$ values should be calculated more accurately than is accorded by Eq. (6-6). While the model of section 2.2 would function well in this capacity, it was found, section 6.4, that the SBED's were almost completely flattened after the insertion of three or more plates. Such calculations are therefore unnecessary.

6.4 Results and Discussion

The SBED phenomenon is macroscopically observable, as seen in Fig. 6.8, being manifested as a light halo around the inner edge of the square slab image. The expansion of the halo width near the image of the slab corners is expected as a two-dimensional effect.

Notice, however, that there appears to be no corresponding darkened shadow around the outer edge image. The most likely explanation for this apparent removal of the positive SBED is saturation of the film emulsion. Indeed, all completely exposed areas on the radiographs were extremely dark, so that the hump-shaped exposure variation would be suppressed upon film development. Furthermore, nonlinearity of the human eye as a light receptor and also of the scanning system for high optical densities additionally suppresses the darkened shadow and corresponding positive SBED.

We add that the halos in Fig. 6.8 are fundamentally different from those resulting from the reflection and refraction of light passing through ice crystals. These latter halos are

wave based phenomena and are the subject of recent interest (109-111). The thermal energies ($\approx$ 0.025 eV) of neutrons in the transport analyses constituting this dissertation suppress the neutron wave properties; the halos in Fig. 6.8 are strictly a nuclear scattering outward transport phenomenon. For example, negligible refraction of thermal neutrons occurs upon transport across media boundaries.

The magnitude of this negative SBED for the bare knife-edged lucite sample with no lucite plate insertions or increased separation is significant, as apparent in Fig. 6.10. This encouraging initial result suggests the viability of the SBED height as a diagnostic tool in the previously discussed capacity. As indicated by visual inspection of Fig 6.8, the SBED phenomenon exists up to a centimetre away from the edge. This partially explains the relatively infrequent observation of SBED's by researchers conducting scans across edges of scattering materials. Often, such scans span less than a millimetre around either side of the edge so that the SBED could easily remain unnoticed.

In order to deduce much quantitative information from edge scans such as that in Fig. 6.10, linearity of the recording system is essential. Since, in the prospective diagnostic application, radiographs being analyzed will have varying optical density ranges, it will be necessary to have a scanning system that is linear over a wide optical density range. In this case, a useful SBED height indicator would have to be exposure independent, given validity over some range of exposures. For example, suppose the valid exposure range is linear so that optical density (D) and exposure (E) are related as follows:

$$D = \gamma E + D_0 \tag{6-9}$$

for some parameters γ, D_0. Let the exposure E_H generate the optical density D_H corresponding to the SBED peak, and E_B generate D_B corresponding to the base, or level value of the hump. Then the actual relative SBED height, given by

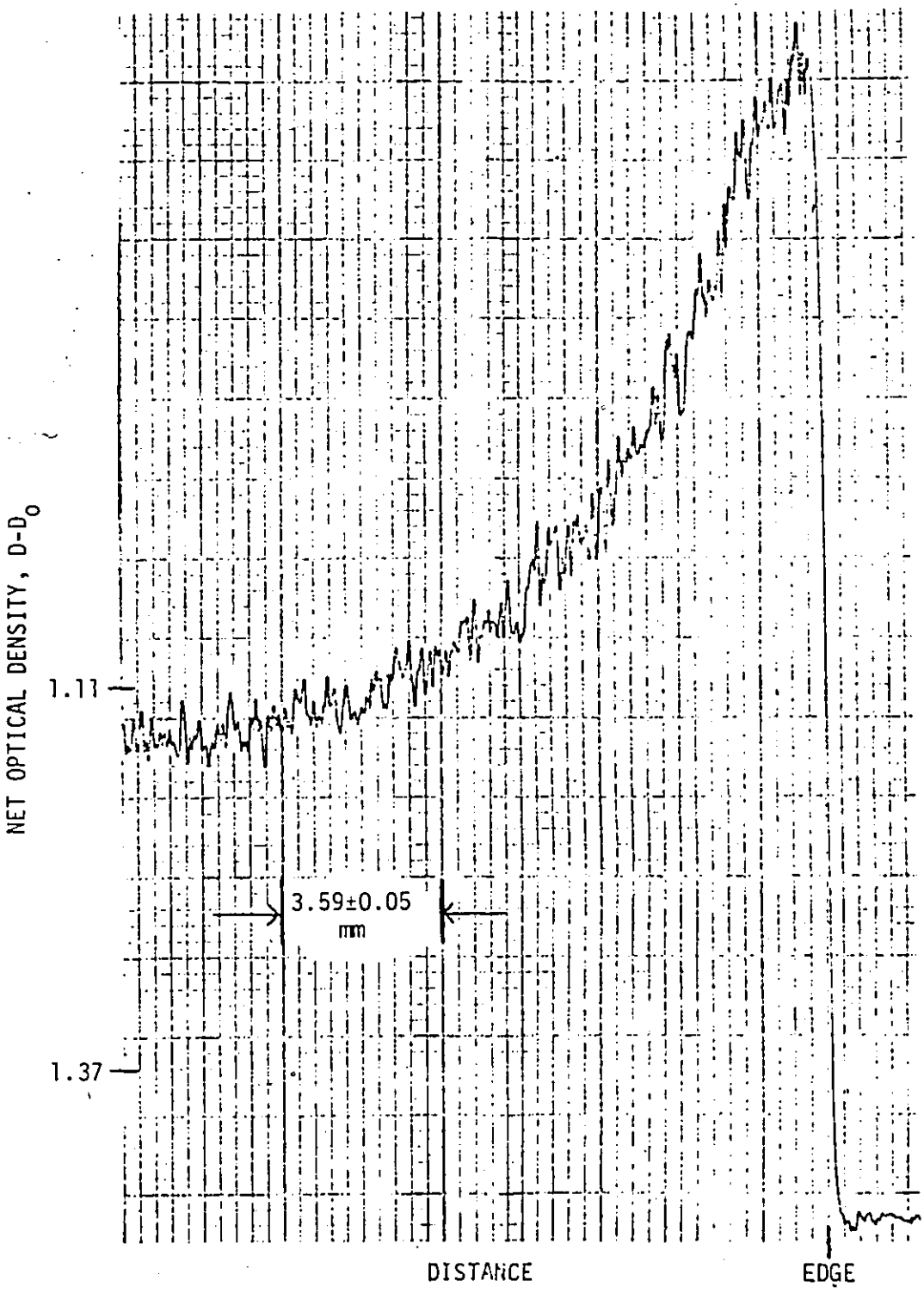

Fig. 6.10: SBED for the 0.592 cm lucite slab with collimated incident neutrons and a slab-to-film separation of 0.86±0.03 mm.

$$\Delta_{SBED} = D_H - D_B$$
$$= \gamma (E_H - E_B), \tag{6-10}$$

is a poor diagnostic indicator since it is exposure dependent. Rather, the indicator

$$w_{SBED} = \frac{D_H - D_o}{D_B - D_o} \tag{6-11}$$

is preferred. To understand this, substitute Eq. (6-9) into Eq. (6-11) to obtain

$$w_{SBED} = \frac{E_H}{E_B}. \tag{6-12}$$

For a given angular distribution of neutrons incident on the lucite slab this ratio is constant, independent of the general incident neutron intensity, and hence also of the resulting exposures. That is, w_{SBED} is a function only of the geometric and material characteristics of the sample being inspected. Now suppose the incident neutron integrated intensity, commonly referred to as the "fluence", is increased from an initial value of F to F + ΔF, thereby increasing exposures from E to E′ = E + ΔE. Optical densities would then increase from D to D′ = D + ΔD. From Eq. (6-9), these differences are related by

$$\Delta D = \gamma \Delta E. \tag{6-13}$$

The new SBED height indicator, from Eq. (6-11), is therefore

$$w'_{SBED} = \frac{D_H + \Delta D_H - D_o}{D_B + \Delta D_B - D_o}$$

$$= \frac{E_H + \Delta E_H}{E_B + \Delta E_B}$$

$$= \frac{E'_H}{E'_B}$$

$$= \frac{E_H}{E_B}$$

$$= w_{SBED}, \tag{6-14}$$

since the exposure ratio is constant. The indicator w_{SBED} is therefore independent of the fluence and thus the exposure of the film.

For the general case in which the film's density vs. exposure curve is, in the range of interest, approximated by a continuous and monotonic function

$$D = f(E), \tag{6-15}$$

a useful and exposure independent SBED height indicator is

$$w_{SBED} = \frac{f^{-1}(D_H)}{f^{-1}(D_B)}. \tag{6-16}$$

Equation (6-16) suggests the transformation of optical densities through the inverse f function. For example, many film emulsions have a log-linear density vs. exposure characteristic, given by

$$D = \gamma \log(E) + D_o. \tag{6-17}$$

In this case, Eq. (6-16) suggests as an indicator

$$w_{SBED} = \exp\left[\frac{D_H - D_B}{\gamma}\right]. \tag{6-18}$$

This w_{SBED} value is certainly as easy to calculate as that in Eq. (6-11), corresponding to a linear film. The chief difference in these two indicators is the different film characteristic parameter that they require (slope vs. intercept) for evaluation.

Figure 6.11 presents an edge scan of the radiographic negative shown in Fig. 6.8b and also of the radiograph of the lucite knife-edged slab with a film to sample separation of 2.48 ± 0.09 mm. It appears, as expected, that increasing this separation corresponds to elongating and flattening the SBED. Qualitatively, the obvious elongation of the SBED in Fig 6.11b relative to that in Fig. 6.11a implies a corresponding decrease in relative SBED height, due to conservation of SBED area. This conservation principle is valid here because the integrated SBED area represents the integrated distribution of neutrons that have

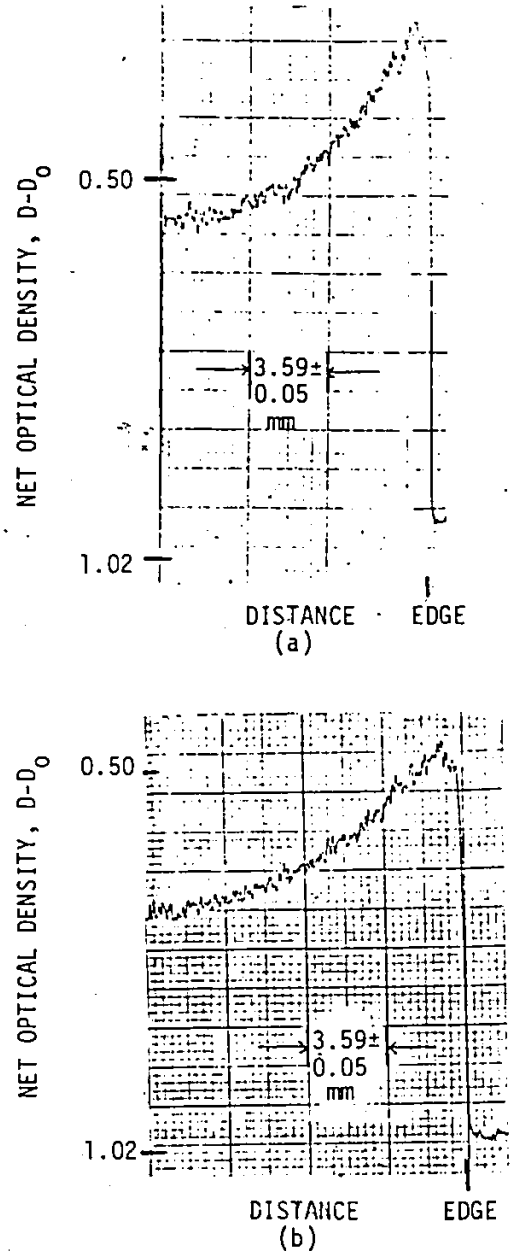

Fig. 6.11: Variation of SBED with slab-to-film separation, for the 0.592 cm lucite slab.
(a) Separation = 1.67±0.06 mm.
(b) Separation = 2.48±0.09 mm.

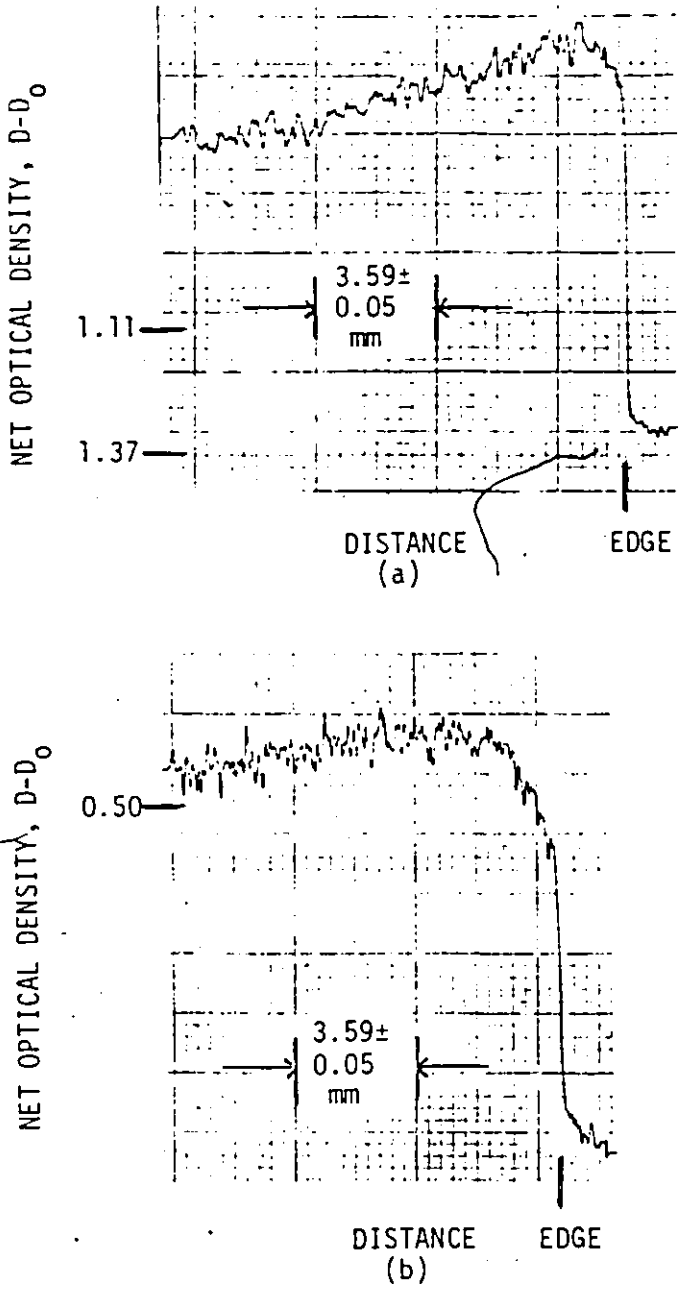

Fig. 6.12: Variation of SBED with degree of diffuseness of incident neutrons, for the 0.592 cm lucite slab.
(a) One interposed lucite sheet ($R_s \approx 0.18$, BUF ≈ 1.22).
(b) Two interposed lucite sheets ($R_s \approx 0.36$, BUF ≈ 1.56).

scattered from the solid portion of the slab ($y < 0$) into the empty ($y > 0$) region. This integrated distribution is clearly independent of the slab to film separation.

One important implication of Fig. 6.11 is that typical slab to film separations admit substantially large SBED's, so that this separation parameter should pose no obstacle to the application of the SBED as a BUF diagnostic indicator. On the other hand, such boundary scattering phenomena can in practice be removed by using separations greater than a centimetre. However, the existence of scattering impacts on edge location optical densities irrespective of this separation.

Figure 6.12 presents edge scans taken on the radiographic negatives shown in Fig. 6.9. Clearly, the SBED in Fig. 6.12a is less elongated than that in Fig. 6.10 so that the apparent significant difference in relative peak heights must also be valid. A significant difference in SBED geometry therefore exists over R_s values of 0.0 and 0.23, confirming qualitatively the applicability of the SBED height as an indicator of the BUF in neutron radiation emergent from a radiographed object.

In Fig. 6.12b, the SBED has almost disappeared for $R_s = 0.44$, corresponding to a BUF of approximately 1.78. This suggests that any diagnostic determinations will be achievable only when the radiographed object scatters less than roughly 40% of the incident collimated neutrons, consistent with the prediction of applicability for BUF values smaller than 1.4 from section 5.7.

To quantify the two-dimensional nature of the SBED's, as apparent in Fig. 6.8, edge scans of the radiograph in Fig. 6.8a were taken orthogonally across one edge and hence parallel to another edge, at a separation of "d_{edge}" from this other edge. The results are presented in Fig. 6.13. It is clear that as the scans progress towards the slab image centre, that is as d_{edge} increases, the SBED peaks decrease in absolute height and increase in relative height. Correspondingly, the SBED bases decrease with d_{edge}. Indeed, for scans taken

in the centre of the slab image, the absolute SBED height should correspond to the SBED base value for a scan taken at the edge (d_{edge} = 0.0 cm). Figure 6.13 appears consistent with this observation; note that for this particular slab sample, diagnostic edge scans should be taken at least 1 cm away from the edge. Qualitatively, the scans in Fig. 6.13 confirm the visual observation that the radiographic image halo is brighter and more expansive at corners than along edges.

A quantitative analysis of the two-dimensional outscattering phenomenon is undertaken in section 7.3.

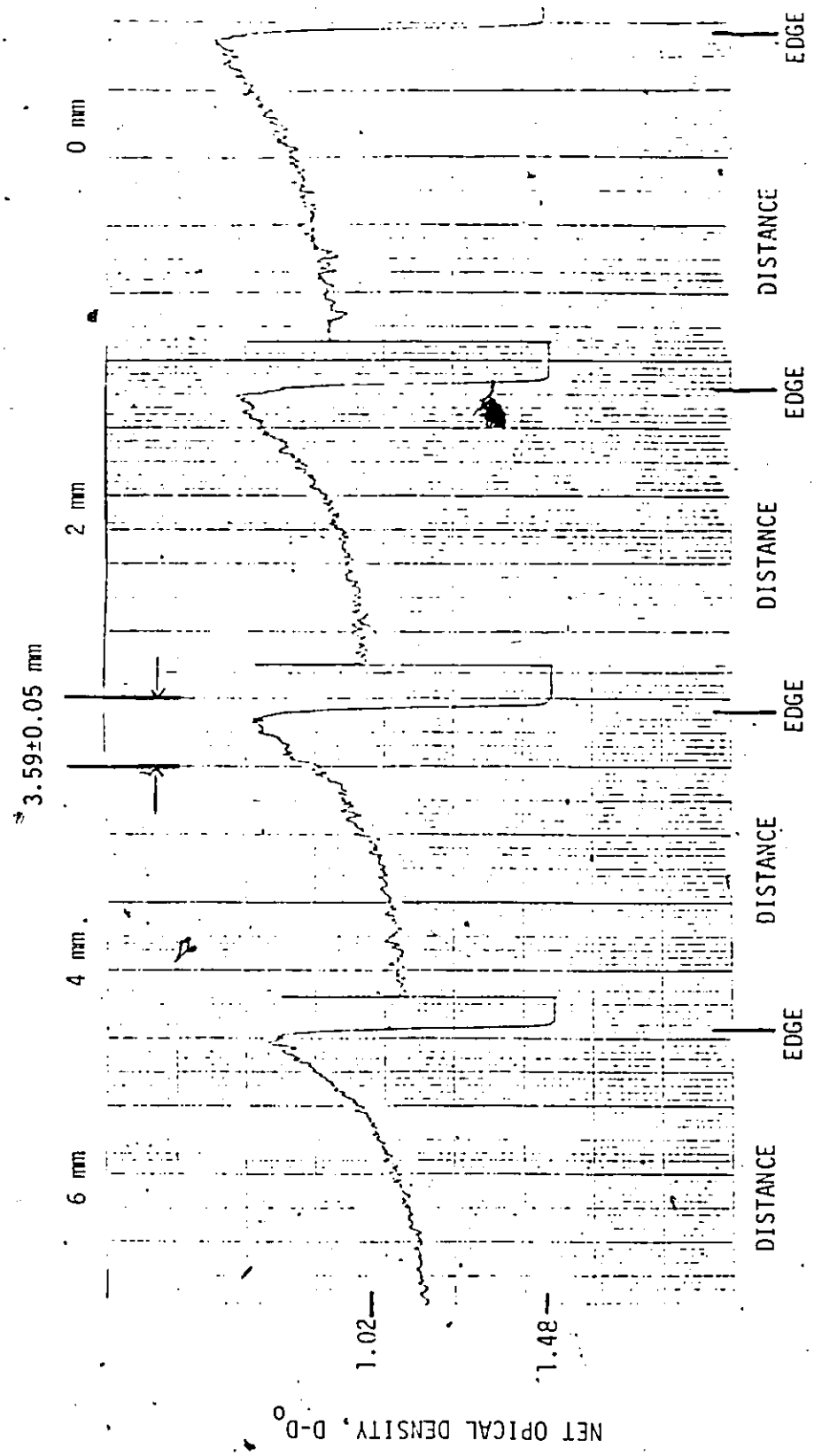

Fig. 6.13: Variation of SBED with normal distance "d_{edge}" from an edge of a rectangular corner, illustrating two-dimensional properties of the scattering phenomenon, all for the 0.592 cm lucite slab.

CHAPTER 7

EXTENSIONS AND GENERALIZATIONS

7.1 Extensions to X-ray and γ-ray Radiography

The neutron radiographic transport analysis developed in this dissertation is based on the assumption of a collimated thermalized neutron beam incident on an object being inspected. The collimation assumption effectively removes geometrical unsharpness considerations from the analysis and is an accurate approximation for high resolution neutron radiographic facilities using nuclear reactor neutron sources.

In medical and industrial radiography, however, the radiation source is usually either the focal spot of an x-ray tube or a radioactive source (3). The areas of these sources are small, but finite, so that the imaging rays diverge from their point of origin to the object. This results in geometric unsharpness as illustrated in Fig. 1.2. In most such instances, the assumption of collimated incident radiation is therefore inappropriate.

This suggests the logical extension of this research to include a divergent probing radiation source. Indeed, such an approach was adopted in the Monte Carlo analysis of section 5.7, in which a specifiable degree of incident neutron obliquity was introduced in the calculations.

Aside from the important geometrical difference between reactor beam neutron radiography and x-ray, γ-ray radiography, the actual transport of these neutral particles through a medium is treated almost identically. Unlike neutron scattering, the incoherent and coherent scattering of photons occurs by interaction with free and bound electrons as opposed to the nucleus. However, differential scattering cross-sections can still be calculated. Similarly, the photon interaction processes of pair production and photoelectric ejection, while not relevant for neutrons, affect the photon population simply as removal processes and

can thus be characterized by an absorption cross-section. An excellent treatise on the subject of electromagnetic radiation transport, including the development of cross- section formulae, has been developed by Pomraning (82).

In neutron transport, one works with neutron densities, fluxes or currents as formally defined in Chapter 3. In photon transport, it is conventional to introduce the "specific intensity" of radiation in the phase space element dr dv dΩ, by

$$I(r, \nu, \Omega, t) = ch\nu n(r, \nu, \Omega, t). \tag{7-1}$$

Here, c is the speed of light, h is Planck's constant, ν is the photon frequency and n is the photon population density, completely analogous to the neutron density defined in Eq. (1-6). The direction (Ω), spatial (r) and time (t) variables are used as defined for neutron transport in section 1.3. The frequency dependence in photon transport corresponds to the energy dependence in neutron transport.

The physical interpretation of I is contained in the relationship

$$dE = I(r, \nu, \Omega, t) \cos(\theta)\, dv\, d\Omega\, dt\, dS. \tag{7-2}$$

Here, dE is the amount of radiant energy with direction dΩ about Ω and frequency dv about ν that crosses a surface dS in time dt such that the normal to dS makes an angle θ with Ω.

The specific intensity I and the radiant energy E thus correspond to the neutron flux and current, respectively, in neutron transport.

The neutron transport equation is frequently referred to as the "linearized Boltzmann transport equation". In photon transport, the corresponding Eulerian- derived integro-differential equation is often called "the equation of radiative transfer". It typically appears in the form (82)

$$\frac{1}{c}\frac{\partial I}{\partial t} + \Omega \cdot \nabla I + \sigma(r,\nu) I(r, \nu, \Omega, t) = S(r, \nu, \Omega, t)$$

$$+ \int_{4\pi} \int_0^{\infty} \frac{\nu}{\nu'} \sigma_s(\nu' \rightarrow \nu, \Omega' \rightarrow \Omega)\, I(\nu', \Omega')\, d\nu'\, d\Omega' , \qquad (7\text{-}3)$$

where σ and σ_s are the total and scattering macroscopic cross-sections, and S is a general source term. The equivalence of Eq. (7-3) and the neutron transport equation, Eq. (1-5), is obvious. The chief difference in the two transport calculations arises in the calculation of the cross-sections.

Another feature distinguishing neutron and photon transport lies in the accounting of polarization. Four parameters are required to specify the state of polarization of a beam of light, necessitating the inclusion of four coupled transfer equations (82). The above transfer equation, Eq. (7-3), is actually an average over these four equations and is therefore inexact. Chandrasekhar(124) first formulated radiative (photon) transfer with a proper accounting of polarization. While polarization effects on neutron transport have been formulated (125,126), they are usually negligible and are very rarely necessary in neutron transport calculations.

Polarization effects and geometrical beam divergence aside, the integro-differential equation based analysis of Chapter 3 should therefore be applicable to x-ray and γ-ray transport in radiography. Likewise, the integral transport equation of Chapter 2 will also be approximately correct in radiographic photon transport, although the collimation assumption becomes most restrictive here. It should be noted that the general integral transport equations for photon and neutron transport are also isomorphic when averaged over states of polarization.

Given the calculation of cross-sections and scattering kernels, it follows that the STF framework of Chapter 4 and analog Monte Carlo calculations such as those in Chapter 5 are also applicable to photon transport in x-ray and γ-ray radiography. As before, modifications to account for the divergence of incident radiation will be necessary.

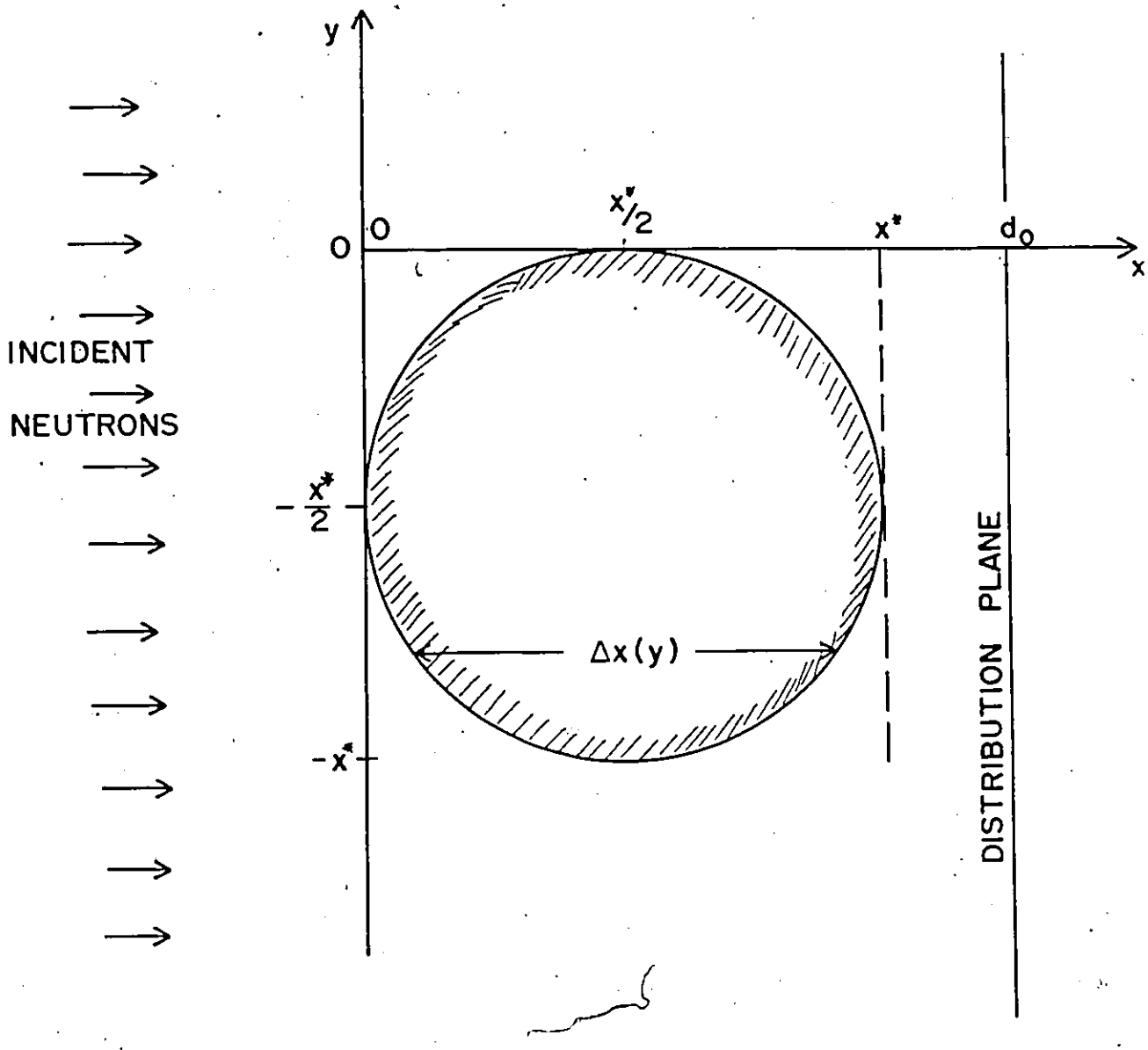

Fig. 7.1: Neutron radiography of a uniformly scattering and absorbing cylindrical object.

In summary then, a common body of existing transport formulations and solution techniques binds neutron and photon transport, although the specific names of each method may vary between the two fields. For example, the diffusion and one-group approximations of neutron transport are also referred to as the "Eddington" and "gray" approximations in photon transport.

7.2 Scattering Edge Function for Cylindrical Objects

The important result in section 4.3 was the analytical derivation of scattering based edge distortions (SBED's) in the neutron radiographic response to an infinite knife-edged object of constant depth. Many studies have focussed on the edge response for cylindrical objects (52,96, 100-102) since an important application of neutron radiography lies in the inspection of cylindrical nuclear fuel assemblies. None of these studies, however, has quantitatively accounted for the edge outscattering phenomenon that can be manifested as hump-shaped distortions in the cylindrical edge response. This suggests the logical extension of the analysis in Chapter 4 to cylindrical objects.

It should be noted that the SBED's qualitatively presented by Matfield (96) are inverted relative to those obtainable in such an analysis. This is because the scattering source in Matfield's study is the convertor in the recording device. As derived in section A.1, this secondary radiation source can be analyzed in a manner identical to object scattering under the assumption of at most single scattering. For high resolution neutron radiography, however, it was shown in section 4.5 that screen-film unsharpness effects – including the humps discussed by Matfield – typically occur on a much smaller scale than the SBED's. These effects tend to smooth the SBED's.

Proceeding with the determination of the SEF response to the uniform cylindrical object of radiographically "infinite" extent shown in Fig. 7.1, the input function, consistent

with the definition used throughout Chapter 4, is the neutron intensity distribution at the plane $x = d_o$ under the assumption of no scattering. It is therefore given by

$$\text{INPUT}(y) = \begin{cases} I_o, \; y \geq 0 \\ I_o \exp[-\Sigma_a \Delta x(y)], \; y \in [-x^*, 0], \\ I_o, \; y \leq -x^* \end{cases} \tag{7-4}$$

where I_o is the incident neutron intensity, and the cylinder "optical depth" is the function

$$\Delta x(y) = 2\sqrt{-y(x^* + y)}, \;\; y \in [-x^*, 0]. \tag{7-5}$$

The macroscopic scattering, absorption and total cross-sections are denoted by Σ_s, Σ_a and Σ_t, respectively. As in Chapter 4, "intensity" denotes the forward partial neutron current.

For a unit intensity line source of neutrons normally incident at $y = y_o$, the resulting intensity distribution at the plane $x = d_o$ is the sum of uncollided and scattered distributions and is given by

$$I_{x^*}(y, y_o) = I_{1,x^*}(y, y_o) + I_{2,x^*}(y; y_o). \tag{7-6}$$

The constituent distributions in Eq. (7-6) are firstly the uncollided neutron distribution, given by

$$I_{1,x^*}(y, y_o) = \begin{cases} \delta_D(y - y_o), \; y_o \geq 0 \\ \exp[-\Sigma_t \Delta x(y_o)]\, \delta_D(y - y_o), \; y_o \in [-x^*, 0], \\ \delta_D(y - y_o), \; y_o \leq -x^* \end{cases} \tag{7-7}$$

and secondly the once-scattered neutron distribution, given by

$$I_{2,x^*}(y, y_o) = \begin{cases} 0, \; y_o \geq 0 \\ \dfrac{\Sigma_s}{2\pi} \displaystyle\int_{\left(\frac{x^* - \Delta x(y_o)}{2}\right)}^{\left(\frac{x^* + \Delta x(y_o)}{2}\right)} f(x, y, y_o)\, dx, \; y_o \in [-x^*, 0], \\ 0, \; y_o \leq -x^* \end{cases} \tag{7-8}$$

where

$$f(x,y,y_o) = \frac{\exp[-\Sigma_t x]}{(d_o - x)} \left[1 + \left(\frac{y - y_o}{d_o - x} \right)^2 \right]^{-1} . \tag{7-9}$$

The once-scattered distribution is derived identically to Eq. (A-23), with the integration limits arising from the cylindrical geometry.

Normalizing $I_{x^*}(y,y_o)$ to a unit input in each of the three y_o ranges, the following scattering line function (SLF) is obtained:

$$SLF(y,y_o) = \begin{cases} I_{x^*}(y,y_o), & y_o \geq 0 \\ \exp[\Sigma_a \Delta x(y_o)]\, I_{x^*}(y,y_o), & y_o \in [-x^*, 0] \\ I_{x^*}(y,y_o), & y_o \leq -x^* . \end{cases} \tag{7-10}$$

The scattering edge function (SEF), giving the total intensity distribution at any line y in the plane $x = d_o$, spans the two cylindrical edges at $y = 0, -x^*$ and is the convolution of the input, Eq. (7-4), with the above SLF. Mathematically, the SEF is given by

$$\begin{aligned} SEF(y) &= \int_{-\infty}^{\infty} INPUT(y_o)\, SLF(y,y_o)\, dy_o \\ &= I_o \{ H(-y-x^*) + H(y) + \exp[-\Sigma_t \Delta x(y)] \{ H(-y) - H(-y-x^*) \} \\ &\quad + \frac{\Sigma_s}{2\pi} \int_{-x^*}^{0} \int_{\left(\frac{x^* - \Delta x(y_o)}{2} \right)}^{\left(\frac{x^* + \Delta x(y_o)}{2} \right)} f(x,y,y_o)\, dx\, dy_o \}, \end{aligned} \tag{7-11}$$

where H(y) is the Heaviside step function (83). Evaluation of the double integral in Eq. (7-11) is facilitated if $f(x,y,y_o)$ is first expanded into the following Taylor series, centred at $x = x^*/2$:

$$f(x,y,y_o) = \sum_{n=0}^{\infty} f^{(n)}\left(\frac{x^*}{2}, y, y_o \right) \frac{\left(x - \frac{x^*}{2} \right)^n}{n!} . \tag{7-12}$$

Upon substitution of Eq. (7-12) into Eq. (7-11) and subsequent evaluation, every second term of the series vanishes so that the n^{th} order approximation is as good as the $(n+1)^{th}$ order approximation. The resulting SEF is

$$SEF(y) = I_o \{ H(-y-x^*) + H(y) + \exp[-\Sigma_t \Delta x(y)] \{ H(-y) - H(-y-x^*) \}$$

$$+ \frac{\Sigma_s}{\pi} \sum_{n=0}^{\infty} \frac{1}{(2n+1)!} \int_{-x^*}^{0} f^{(2n)}\left(\frac{x^*}{2}, y, v \right) \left(\frac{\Delta x(v)}{2} \right)^{2n+1} dv \}. \qquad (7\text{-}13)$$

As for the knife-edged slab in Chapter 4, the relative magnitude of any SBED's in SEF should be greatest when $\Sigma_a = 0.0\,cm^{-1}$. The SEF in Eq. (7-13) has been calculated using the FORTRAN program CYLSEF, listed in Appendix D, for a uniform cylinder with diameter $x^* = 1.0\,cm$. Only the first term of the Taylor series expansion for $f(x,y,y_o)$, Eq. (7-12), was used in this expository calculation. This corresponds to a replacement of the integrand in Eq. (7-11) by its midpoint value, an approximation procedure used in sections 4.4 and A.4. We note that the accuracy of those approximations can be increased if more terms of the Taylor series approximation to the integrand are used in each case. The results are presented in Fig. 7.2.

As expected, SBED's of non-negligible magnitude appear near the cylinder edge locations. Unlike the knife-edged slab SEF in Figs. 4.3 to 4.5, there are positive but no negative SBED's. Indeed the outscattering loss of neutrons near the internal cylinder edges serves to further diminish a decreasing function; that is, the negative SBED is absorbed into the decreasing SEF.

Since nuclear fuel pins often take the geometry of a cylindrical fuel pellet encased in a layer of cladding, imaging analysis has been undertaken to assess the neutron radiographic response to an object consisting of concentric cylinders, each of roughly uniform composition. The study by Osuwa (52) focussed on the determination of the edge location in the image of such an object, assuming the object to be absorbing but not scattering. For nuclear fuel pins consisting of uranium compounds, however, the thermal neutron scattering cross-section is of the same order of magnitude as the absorption cross-section. For these and more general cases, the object scattering of neutrons is non-negligible. Furthermore, the results of section 4.5 suggest that the image optical density corresponding to edge locations

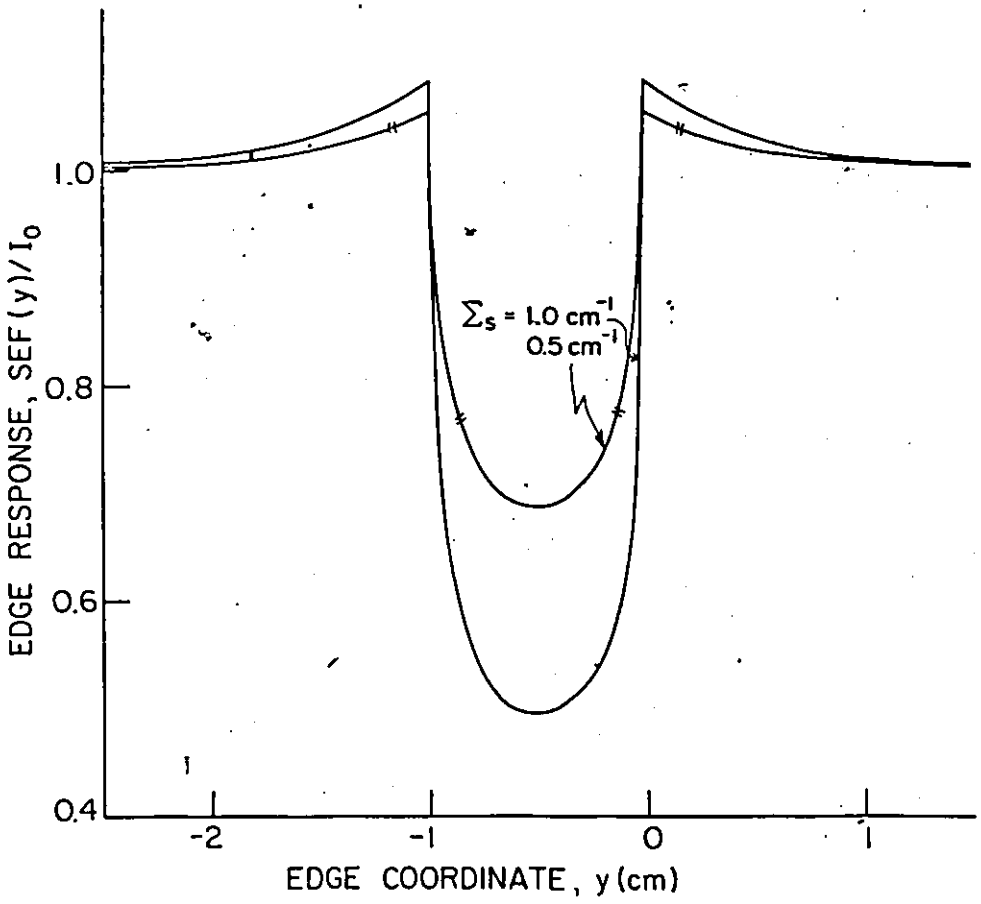

Fig. 7.2: Normalized SEF for a homogeneous cylindrical scattering object with diameter $x^* = 1.0$ cm and negligible absorption cross-section. The distribution plane is at $x = d_o = x^*$.

depends on the scattering cross-section in such cases. The inclusion of object scattering effects in the SEF for concentric cylindered objects is therefore of practical importance and is now briefly considered.

The concentric cylindered object to be analyzed is assumed to be radiographically of "infinite" extent and is shown in Fig. 7.3. Each of the N concentric regions is uniform with distinct scattering, absorption and total cross- sections Σ_{sn}, Σ_{an} and Σ_{tn}, respectively. By tracing the paths of collimated neutrons through the various regions and assuming at most single scattering of neutrons, the following generalization of Eq. (7-11) is obtained:

$$SEF(y) = I_o\left\{ H(-y-x^*) + H(y) + \exp\left[-\sum_{n=0}^{N} \Sigma_{sn}\,\Delta x_n(y)\right]\left\{ H(-y) - H(-y-x^*)\right\}\right.$$

$$\left. + \frac{1}{2\pi}\int_{-x^*}^{0}\sum_{n=0}^{N}\Sigma_{sn}(y_o)\,g_n(y,y_o)\,dy_o\right\}, \tag{7-14}$$

where the effective optical depth of the n^{th} cylindrical region is defined recursively by

$$\Delta x_n(y) = \begin{cases} 0, & y \le -x^*/2 - r_n \\ 0, & y \ge -x^*/2 + r_n \\ \Delta x^*_n(y), & y \in [-x^*/2 - r_n, -x^*/2 - r_{n-1}] \\ \Delta x^*_n(y), & y \in [-x^*/2 + r_{n-1}, -x^*/2 + r_n] \\ \Delta x^*_n(y) - \sum_{i=0}^{n-1}\Delta x_i(y), & y \in [-x^*/2 - r_{n-1}, -x^*/2 + r_{n-1}], \end{cases} \tag{7-15}$$

and the recursion is initiated by

$$\Delta x_o(y) = \begin{cases} \Delta x^*_o(y), & y \in [-x^*/2 - r_o, -x^*/2 + r_o] \\ 0, & \text{otherwise}, \end{cases} \tag{7-16}$$

Here, $\Delta x_n^*(y)$ is the optical depth of the n^{th} cylindrical region in the absence of interior concentric regions and is given by

$$\Delta x_n^*(y) = 2\sqrt{r_n^2 - \left(y + \frac{x^*}{2}\right)^2}. \tag{7-17}$$

The following additional functions are implicitly defined in Eq. (7-14):

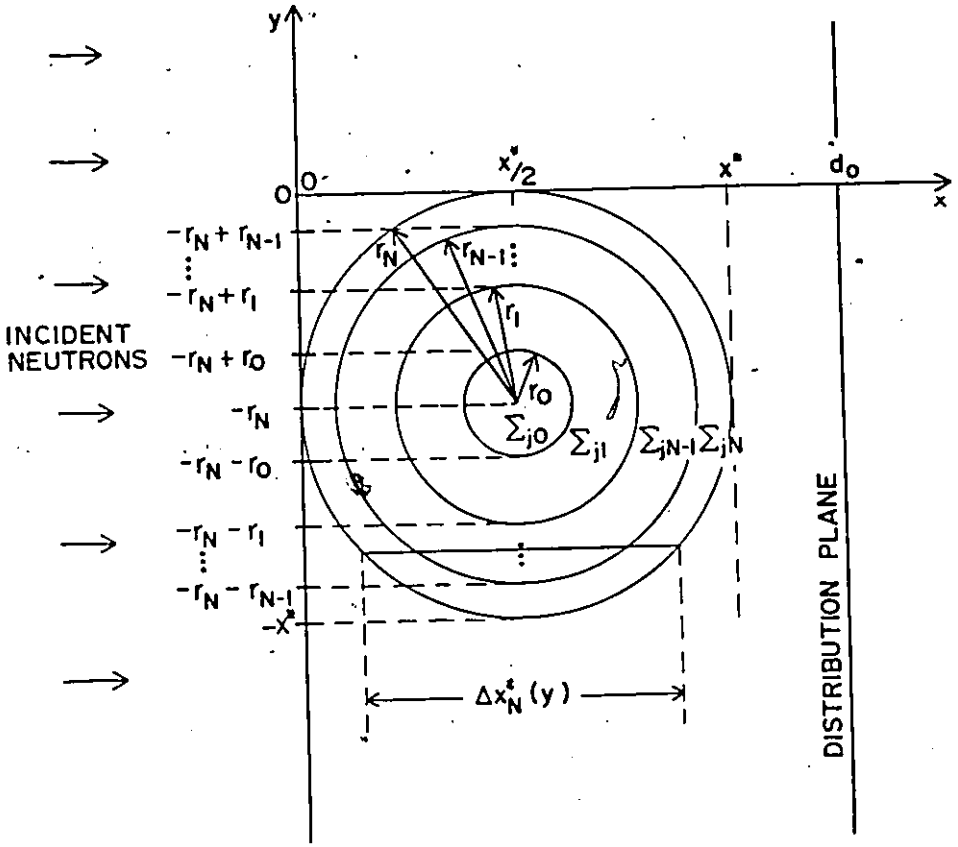

Fig. 7.3: Neutron radiography of concentric cylinders with distinct uniform scattering (j = s), absorption (j = a) and total (j = t) cross-sections, Σ_{ji}.

$$\Sigma_{sn}(y) = \begin{cases} \Sigma_{sn}, y \in [-x^*/2 - r_n, -x^*/2 + r_n] \\ 0, \text{otherwise}, \end{cases} \tag{7-18}$$

$$g_n(y, y_o) = \begin{cases} \int_{x_{\ell,0}(y_o)}^{x_{u,o}(y_o)} f_o(x,y,y_o)\,dx, & n = 0 \\ \int_{x_{\ell,n}(y_o)}^{x_{\ell,n-1}(y_o)} f_n(x,y,y_o)\,dx + \int_{x_{u,n-1}(y_o)}^{x_{u,n}(y_o)} f_n(x,y,y_o)\,dx, & n > 0. \end{cases} \tag{7-19}$$

$$f_n(x,y,y_o) = \frac{\exp[\Sigma_{tn} x]}{(d_o - x)} \left[1 + \left(\frac{y - y_o}{d_o - x} \right)^2 \right]^{-1}, \tag{7-20}$$

$$x_{\ell,n}(y) = \begin{cases} \dfrac{x^* - \Delta x^*_n(y)}{2}, y \in [-x^*/2 - r_n, -x^*/2 + r_n] \\ \dfrac{x^*}{2}, \text{otherwise}. \end{cases} \tag{7-21}$$

$$x_{u,n}(y) = \begin{cases} \dfrac{x^* + \Delta x^*_n(y)}{2}, y \in [-x^*/2 - r_n, -x^*/2 + r_n] \\ \dfrac{x^*}{2}, \text{otherwise}. \end{cases} \tag{7-22}$$

When $N = 1$, $\Delta x_o(y)$ and $\Delta x_o^*(y)$ reduces to $\Delta x(y)$ in Eq. (7-5), $f_o(x,y,y_o)$ reduces to $f(x,y,y_o)$ in Eq. (7-9) and the SEF in Eq. (7-14) reduces to that in Eq. (7-11). Equation (7-14) has thus already been evaluated for $N = 1$.

The logical extension of this work is therefore the expansion of the program CYLSEF to evaluate Eq. (7-14) for values of N larger than unity. We note here that the recursive definition of the $\Delta x_n(y)$ facilitates computation. While not performed here, the expected results for a two-region cylinder are qualitatively presented in Fig. 7.4. The existence of SBED's at the image of an internal boundary should depend primarily on the ratio of the scattering cross-sections on either side of the boundary. The SBED can be expected to occur on either side of the boundary, depending on whether or not this ratio is greater or

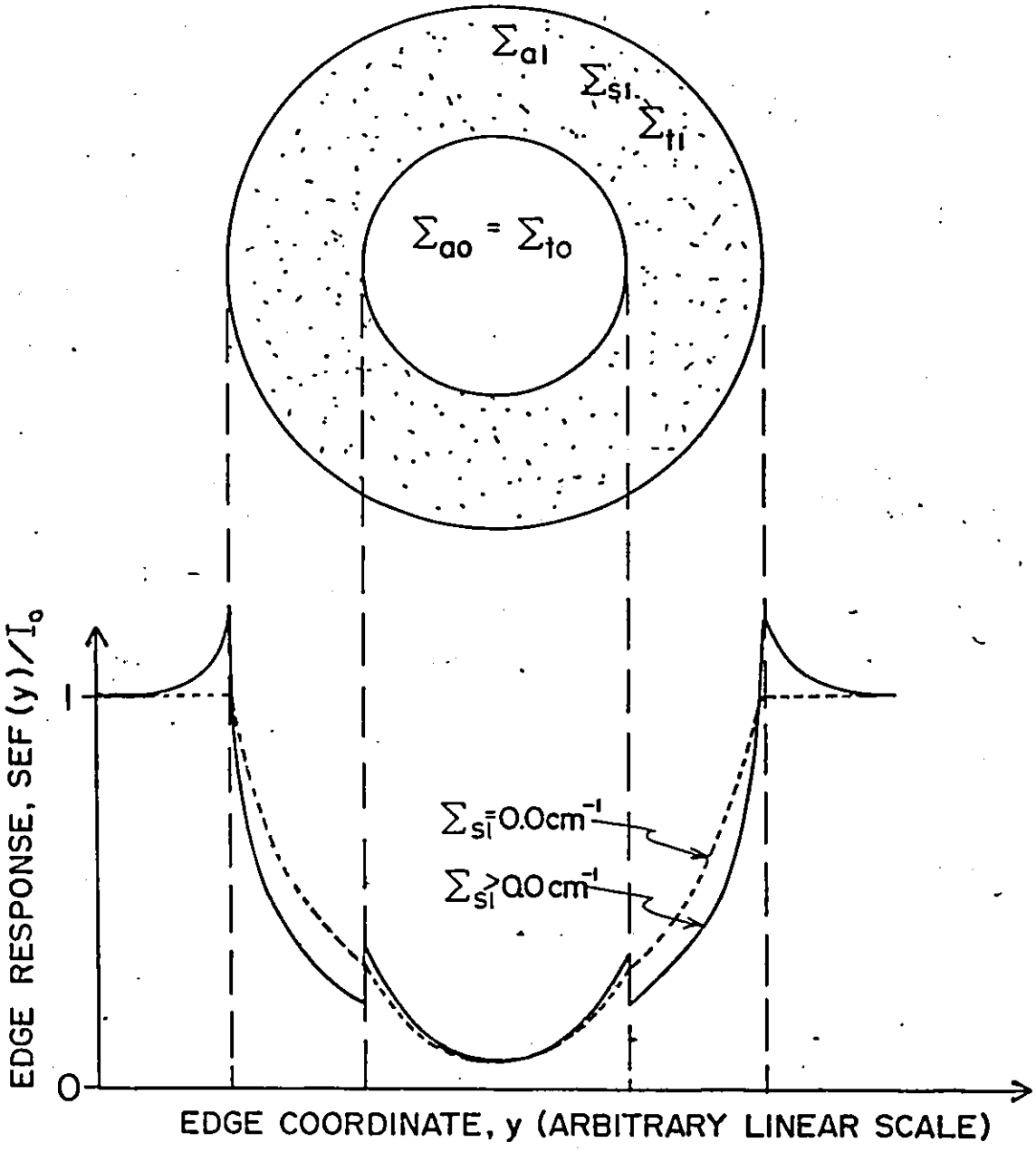

Fig. 7.4: Sketch of SEF response to two concentric cylinders with distinct uniform cross-sections, illustrating SBED's at interfaces. Here, Σ_{so} = 0.0 cm^{-1} and $\Sigma_{ao} > \Sigma_{al}$.

lesser than unity. For the object in Fig. 7.4, the regions are such that the internal boundary has an internal SBED.

In the same manner that the work in Chapter 6 verified the existence and magnitude of these SBED's for a knife-edged slab, it is suggested that experimental confirmation be undertaken to verify the SBED characteristics for the cylindrical objects of Figs. 7.1 and 7.3.

7.3 Two-Dimensional Outscattering: The Scattering Corner Function (SCF)

The spatial variation of the SBED in the edge response near two-dimensional corners is illustrated in Fig. 6.12 and was qualitatively analyzed in section 6.4. Basically, for the corner formed when the object occupies a single Cartesian quadrant, the negative SBED in the edge response was seen to expand and intensify with proximity of the edge scan to the corner. This variation can be quantified using the "ϕ-wedge" geometry and notation of Fig. C.1.

Consistent with the definition used throughout Chapter 4 and in section 7.2, the input here is the neutron intensity distribution at a plane $x = d_o$ under the assumption of no scattering. This plane is parallel to and at a distance d_o behind the front face of the ϕ-wedge which is located at the plane $x = 0$. The input is therefore

$$\text{INPUT}(r',\theta') = \begin{cases} I_o, \theta' \in (\phi_1, \phi_2) \\ I_o \exp[-\Sigma_a x^*], \theta' \in (\phi_2, 2\pi + \phi_1) \end{cases} \qquad (7\text{-}23)$$

where the incident neutron beam has intensity I_o and the ϕ-wedge is of constant depth x^* with macroscopic absorption, scattering and total cross-sections Σ_a, Σ_s and Σ_t respectively.

The spatially variant PSF, based on the scattering point function (SPF) derived in section 4.2, denotes the response at (r,θ) in the plane $x = d_o$ to a point source of neutrons normally incident on the ϕ-wedge at (r',θ') and normalized in intensity to yield an input; Eq.

(7-23), of unity at all points. It is given by

$$SPF(r,\theta,r',\theta') = \begin{cases} \delta_D(r-r')\,\delta_D(\theta-\theta'), & \theta' \in (\phi_1, \phi_2) \\ \exp[-\Sigma_s x^*]\,\delta_D(r-r')\,\delta_D(\theta-\theta') + \dfrac{\Sigma_s}{4\pi}\exp[\Sigma_a x^*]\displaystyle\int_0^{x^*} h(x,r,r',\theta,\theta')\,dx, & \theta' \in (\phi_2, 2\pi+\phi_1) \end{cases} \tag{7-24}$$

where

$$h(x,r,r',\theta,\theta') = \frac{1}{(d_o-x)^2}\left[1+\frac{r^2+r'^2-2rr'\cos(\theta-\theta')}{(d_o-x)^2}\right]^{-3/2}\exp[-\Sigma_t x]\,. \tag{7-25}$$

Given the SPF and INPUT functions, the resulting response function is the convolution of SPF with INPUT and is here named the "scattering corner function" (SCF). Mathematically, the SCF is given by

$$SCF(r,\theta) = \int_0^{2\pi}\int_0^{\infty} INPUT(r',\theta')\,SPF(r,\theta,r',\theta')\,r'\,dr'\,d\theta'$$

$$= \int_{\phi_1}^{\phi_2}\int_0^{\infty} I_o\,\delta_D(r-r')\,\delta_D(\theta-\theta')\,r'\,dr'\,d\theta'$$

$$+ \int_{\phi_2}^{2\pi+\phi_1}\int_0^{\infty} I_o\{\exp[-\Sigma_t x^*]\,\delta_D(r-r')\,\delta_D(\theta-\theta') + \frac{\Sigma_s}{4\pi}\int_0^{x^*} h(x,r,r',\theta,\theta')dx\}\,r'\,dr'\,d\theta'. \tag{7-26}$$

Define an angular step function in analogy with the Heaviside step function as follows

$$H_\theta(\phi_\ell, \phi_u) = \begin{cases} 1, \theta \in (\phi_\ell, \phi_u) \\ 0, \theta \in (\phi_u, 2\pi+\phi_\ell) \end{cases} \tag{7-27}$$

The SCF in Eq. (7-26) then reduces to

$$\frac{SCF(r,\theta)}{I_o} = H_\theta(\phi_1,\phi_2) + \exp[-\Sigma_t x^*]\,H_\theta(\phi_2, 2\pi+\phi_1)$$

$$+ \frac{\Sigma_s}{4\pi}\int_{\phi_2}^{2\pi+\phi_1}\int_0^{\infty}\int_0^{x^*} h(x,r,r',\theta,\theta')\,dx\,r'\,dr'\,d\theta'. \tag{7-28}$$

In order to facilitate the evaluation of Eq. (7-28), the integrand $h(x,r,r',\theta,\theta')$ was approximated by its midpoint value throughout the inner range of integration. As discussed

in section 7.2, this approximation is equivalent to selecting the first term of a Taylor series expansion for $h(x,r,r',\theta,\theta')$. The resulting double integral was evaluated through an analytical solution of the inner integral followed by a numerical evaluation of the outer integral. These calculations were performed using the FORTRAN program CALCUL, in conjunction with the calculations of Appendix C. A listing of CALCUL is included in Appendix D.

While much development of the two-dimensional formulation is possible, only a single evaluation of Eq. (7-28) will be given here. The ϕ-wedge for which the calculation was performed was a "3/4-corner", with the solid sector occupying the first, second and fourth Cartesian quadrants, having depth $x^* = 1.0$ cm and cross-sections $\Sigma_a = 0.0\ cm^{-1}$, $\Sigma_s = 1.0\ cm^{-1}$. For this case of no absorption, the SBED's should be of maximal relative magnitude, as discussed in section 4.3. The results are displayed as SCF radial profiles in Fig. 7.5.

As expected, positive and negative SBED's occur in the directions leading from the corner location into the open and solid sectors of the wedge corner, respectively. A discontinuity in the SCF occurs at the corner and along edge locations due to the discontinuity in the wedge geometry and also the SPF at those boundaries. Note that a shift invariant PSF, such as that representing screen-film unsharpness, will in practice smoothen these discontinuities, enabling a precise and unique assessment of the corner response such as was obtained in Appendix C.

The positive SBED's decrease the fastest for $\theta = 5\pi/4$, being that direction leading into the center of the open sector, and increase the fastest for $\theta = \pi/4$, being that direction leading into the center of the solid sector. It should be noted that the anomalous positive SBED for $\theta = \pi$, $3\pi^+/2$ is only a mathematical curiosity existing for that single, isolated

profile along the discontinuous edge locations. All other lower profiles approach the single indicated asymptote.

For this particular ϕ-wedge, the positive SBED's are evidently larger than their negative counterparts. Qualitatively, this is expected since each positive SBED represents outscattered neutrons collected from three quadrants. Quantitatively, for the range $\theta\epsilon(\phi_1,\phi_2)$, the SCF response corresponding to the wedge corner is given, using Eq. (7-28), as follows:

$$\frac{SCF_c^+}{I_o} = \lim_{r\to 0} \frac{SCF(r,\theta)}{I_o}$$

$$= 1 + \frac{\Sigma_s}{4\pi}\int_0^{x^*}\int_{\phi_2}^{2\pi+\phi_1} \exp[-\Sigma_t x]\, R(x)\, d\theta'\, dx\,, \tag{7-29}$$

where

$$R(x) = \int_0^{\infty}\left[1+\left(\frac{r'}{d_o-x}\right)^2\right]^{-3/2} + \frac{r'}{(d_o-x)^2}\, dr'\,. \tag{7-30}$$

Now R(x) is immediately evaluated to be unity, so that the separable double integral in Eq. (7-29) results in

$$\frac{SCF_c^+}{I_o} = 1+\left(\frac{\Sigma_s}{2\Sigma_t}\right)\left(1-\frac{\phi}{2\pi}\right)\left(1-\exp[-\Sigma_t x^*]\right). \tag{7-31}$$

For the case of a knife-edged slab, Eq. (7-31) reduces to

$$\frac{SCF_c^+}{I_o} = 1+\left(\frac{\Sigma_s}{4\Sigma_t}\right)\left(1-\exp[-\Sigma_t x^*]\right). \tag{7-32}$$

Similarly, for the range $\theta\,\epsilon(\phi_2, 2\pi+\phi_1)$, the corner response is found, using Eq. (7-28), to be

$$\frac{SCF_c^-}{I_o} = \exp[-\Sigma_t x^*]+\left(\frac{\Sigma_s}{2\Sigma_t}\right)\left(1-\frac{\phi}{2\pi}\right)\left(1-\exp[-\Sigma_t x^*]\right), \tag{7-33}$$

reducing to

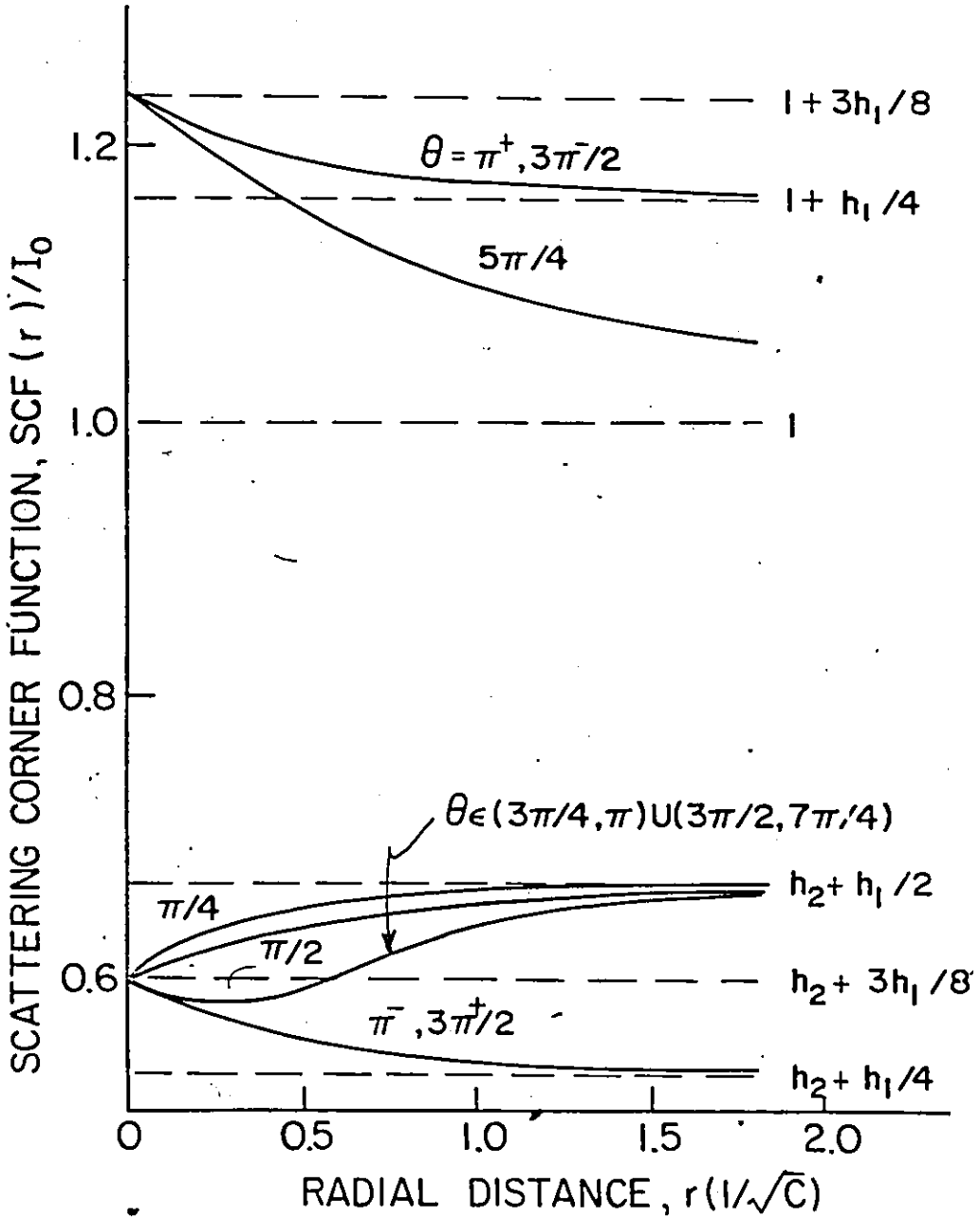

Fig. 7.5: Normalized SEF radial profiles for a ϕ-wedge in which $\phi_1 = \pi$, $\phi_2 = 3\pi/2$, $\Sigma_s = 1.0$ cm^{-1} and $\Sigma_a = 0.0$ cm^{-1}, illustrating two-dimensional SBED's. The constants h_1 and h_2 are

(a) $h_1 = (\frac{\Sigma_s}{\Sigma_t})(1-\exp[-\Sigma_t x^*])$,

(b) $h_2 = \exp[-\Sigma_t x^*]$.

The profiles are taken at the plane $d_o = x^* = 1.0$ cm.

$$\frac{SCF_c^-}{I_o} = \exp[-\Sigma_t x^*] + \left(\frac{\Sigma_s}{4\Sigma_t}\right)\left(1-\exp[-\Sigma_t x^*]\right) \tag{7-34}$$

for the case of a knife-edged slab. Note that Eqs. (7-32) and (7-34) identify with the edge location responses calculated in section 4.3 and shown in Fig. 4.3, under the assumption of a "zeroth order" model, corresponding to the first two terms in the Taylor series for $\exp[-\Sigma_t x^*]$.

An important result from Eq. (7-31), (7-33) is that the corner and edge responses are functions of the object itself and possess strong dependence on the scattering cross-section. In similarity to the problem of locating an edge in a radiographic image, any subsequently developed corner location methodology should account for this dependence.

For the range $\theta \in (\phi_1, \phi_2)$ the infinity response is

$$\frac{SCF_\infty^+}{I_o} = \lim_{r\to 0} \frac{SCF(r,\theta)}{I_o}$$

$$= 1. \tag{7-35}$$

Similarly, for the range $\theta \in (\phi_2, 2\pi + \phi_1)$ the infinity response is

$$\frac{SCF_\infty^-}{I_o} = \lim_{r\to 0} \frac{SCF(r,\theta)}{I_o}$$

$$= \frac{SCF_c^-}{I_o}, \tag{7-36}$$

evaluated for a ϕ-wedge with an angle of $\phi = 0$. Substitution of Eq. (7-33) with $\phi = 0$ for Eq. (7-36) results in

$$\frac{SCF_\infty^-}{I_o} = \exp[-\Sigma_t x^*] + \left(\frac{\Sigma_s}{2\Sigma_t}\right)\left(1-\exp[-\Sigma_t x^*]\right). \tag{7-37}$$

The physical interpretation of each term in Eq. (7-37) is obvious, and has been previously discussed in section 4.7.

From Eq. (7-31) and Eq. (7-35), the positive SBED height is

$$HH^{+} = \left(\frac{\Sigma_s}{2\Sigma_t}\right)\left(1 - \frac{\Phi}{2\pi}\right)\left(1 - \exp[-\Sigma_t x^{*}]\right).$$

Likewise, from Eq. (7-33) and Eq. (7-37), the negative SBED height is

$$HH^{-} = \frac{SCF_c^{-}}{I_o} - \frac{SCF_\infty^{-}}{I_o}$$

$$= \left(\frac{\Sigma_s}{2\Sigma_t}\right)\left(\frac{\Phi}{2\pi}\right)\left(1 - \exp[-\Sigma_t x^{*}]\right). \tag{7-38}$$

The total SCF amplitude, defined as the difference between the "positive" and "negative" infinity responses in Eq. (7-35) and Eq. (7-37), is

$$\Delta\left(\frac{SCF}{I_o}\right) = \left(1 - \frac{\Sigma_s}{2\Sigma_t}\right)\left(1 - \exp[-\Sigma_t x^{*}]\right). \tag{7-39}$$

The ratio of the total SBED height to the SCF amplitude is therefore

$$\frac{HH}{\Delta\left(\frac{SCF}{I_o}\right)} \overset{df}{=} \frac{HH^{+} + HH^{-}}{\Delta\left(\frac{SCF}{I_o}\right)}$$

$$= \frac{\Sigma_s}{\Sigma_s + 2\Sigma_a}. \tag{7-40}$$

This relative total SBED height is precisely that given in Eq. (4-17) for a knife-edged object. The significant result here is that the relative total SBED height is independent of the actual wedge angle. Rather, the wedge angle determines the distribution of this total SBED height to the component positive and negative SBED's. This distribution is clearly linear in ϕ. That is, for the ϕ-wedge, the positive and negative SBED heights assume the following portions of the total SBED height:

$$\frac{HH^{+}}{HH} = 1 - \frac{\Phi}{2\pi}, \tag{7-41}$$

$$\frac{HH^-}{HH} = \frac{\phi}{2\pi} . \tag{7-42}$$

Thus, the positive SBED height is three times the negative SBED height in Fig. 7.5.

The most interesting profile in Fig. 7.5 is certainly that with a local minimum, representing a continuum of such profiles. This peculiar deviation from monotonicity is also found for a class of profiles in Fig. C.3 and was explained in a screen-film unsharpness context in section C.3. To explain this phenomenon in the context of scattering based image degradation, consider the radial profile gradient at the origin, $\partial(SCF)/\partial r|_{r=0}$. While SCF_c is discontinuous, its first derivative is not. From Eq. (7-25) and Eq. (7-28), using Leibnitz' rule of differentiation across integral signs:

$$\left.\frac{\partial(SCF(r,\theta))}{\partial r}\right|_{r=0} = \frac{I_o\Sigma_s}{4\pi}\int_{\phi_2}^{2\pi+\phi_1}\int_0^{\infty}\int_0^{x^*}\frac{\exp[-\Sigma_t x]}{(d_o-x)^2}\left.\frac{\partial}{\partial r}(R_{pt}(x,r,r',\theta,\theta'))\right|_{r=0} dx\, r'\, dr'\, d\theta', \tag{7-43}$$

where

$$R_{pt}(x,r,r',\theta,\theta') = \left[1+\frac{r^2+r'^2-2rr'\cos(\theta-\theta')}{(d_o-x)^2}\right]^{-3/2} \tag{7-44}$$

From Eq. (7-44)

$$\left.\frac{\partial R_{pt}(x,r,r',\theta,\theta')}{\partial r}\right|_{r=0} = \frac{3r'\cos(\theta-\theta')}{(d_o-x)^2}\left[1+\left(\frac{r'}{d_o-x}\right)^2\right]^{-5/2}$$

$$= r'\cos(\theta-\theta')\,\beta^2(r',x), \tag{7-45}$$

implicitly defining the positive function $\beta^2(r',x)$. Equation (7-43) can thus be rewritten as

$$\left.\frac{\partial(SCF(r,\theta))}{\partial r}\right|_{r=0} = \frac{I_o\Sigma_s}{4\pi}\int_0^{x^*}\frac{\exp[-\Sigma_t x]}{(d_o-x)^2}\left\{\int_0^{\infty}\beta^2(r',x)\,r'^2\,dr'\right\}\left\{\int_{\phi_2}^{2\pi+\phi_1}\cos(\theta-\theta')d\theta'\right\}dx$$

$$= \frac{I_o\Sigma_s\gamma^2}{4\pi}\left\{\sin(\theta-\phi_2)-\sin(\theta-\phi_1)\right\}, \tag{7-46}$$

for the implicitly defined positive constant γ^2. It is shown in Appendix C that Eq. (7-46) is also valid, with an appropriate γ^2, for any isotropic and realistic point spread function, R_{PT}

From Eq. (7-46), $\partial(SCF)/\partial r|_{r=0}$ vanishes for radial axes with directions along the particular angles specified by the general formula

$$\theta_p = (2n-1)\frac{\pi}{2} + \left(\frac{\Phi_1 + \Phi_2}{2}\right), \; n \in Z. \tag{7-47}$$

As a result, $\partial(SCF)/\partial r|_{r=0}$ is negative for all radial axes leading into the solid sector of the wedge with directions between an angle θ_p and a wedge arm. Such axes will exist only for ϕ-wedges with $\phi < \pi$. For the $\pi/2$-wedge used to generate Fig. 7.5, the two θ_p angles are $\theta_p = 3\pi/4, 7\pi/4$. Since each profile along these axes must eventually approach the single indicated asymptote, each profile therefore contains a local minimum.

Qualitatively, these minima are explained as follows. Upon leaving the origin at $r = 0$, an initial decrease in response occurs due to a diminished fraction of outscattered neutrons from a sub-sector of the solid sector of the ϕ-wedge reaching the point of concern. This sub-sector is identifiable as that part of the solid sector that is "greater than π" and lies adjacent to the wedge arm furthest from the point of concern. As the profile leads on into the solid sector of the wedge, this loss is overtaken by the gain from locally scattered neutrons, explaining the shape of the profile.

Note that for a ϕ-wedge with $\phi < \pi$, there is correspondingly a set of positive SBED radial profiles with local maxima.

The exact corner responses in Eq. (7-31) and Eq. (7-33) provide a useful check on the validity of the midpoint value approximation used to evaluate Eq. (7- 28). The actual positive and negative corner responses are 1.237 and 0.605, respectively. The corresponding calculated values were 1.227 and 0.596, representing errors of approximately 1% and 2%, respectively. These errors are small relative to the actual SBED heights.

Finaly, the extension of the analysis in this section to include the effects of multiple scattering and also convolution with a screen-film unsharpness PSF – as performed for the

knife-edged slab in section 4.5 – can be identified as worthwhile endeavors. Experimental confirmation of the above properties has been initiated in Chapter 6.

7.4 Generalized Formal Imaging Equation

As discussed in section 1.4 and depicted in Fig. 1.4, radiation diagnostic systems can be classified according to the constancy (C) or variability (V) of their source (S), object (O) and recorder (R) components. While the transport analysis constituting the main body of this dissertation has been undertaken for an (S_C,O_C,R_C) neutron radiographic imaging system, it can logically be extended to the several other categories of radiation diagnostic systems. Such extensions are both meaningful and of practical importance since most of these systems are based on the same transport principles analyzed in this research; specifically, object scattered radiation degrades the ideal ray image consisting of emergent uncollided probing radiation.

It is possible to formally characterize the most general radiation diagnostic system, categorized as (S_V,O_V,R_V), by a generalized formal imaging equation. In practice, diagnostics are usually conducted for at least one of S, O or R constant. In such cases, the general imaging equation appropriately reduces to a more manageable form. This general equation is now developed for a diagnostic system in which the probing radiation is well approximated as being collimated.

Each of the source, object and recording device will move inside some spatial volume throughout the duration of diagnosis existing from initial time t_o to final time $t_o + \tau$. Each of these three volumes are described relative to some three-dimensional Cartesian coordinate system R', which remains fixed throughout the duration interval τ and, for convenience, has its origin in the initial object plane. The object plane is at any time t defined as that plane adjacent to the object, lying between the source and object and orthogonal to the direction of incident radiation. Also, the recording device is assumed to contain an image

plane -- such as a radiographic film emulsion -- upon which the information-carrying emergent radiation registers a latent image. Since the image plane here is not an abstraction, it will generally be nonparallel to the source and object planes at time t.

Since all three planes are, in the general case, in motion, it is necessary to describe them each by planar Cartesian coordinate systems that remain fixed relative to their respective planes and thus are in motion relative to the R′ coordinate system. Denote these planar coordinates systems by $\mathbf{r} = (r_1, r_2)$, $\mathbf{r}' = (r'_1, r'_2)$ and $\mathbf{r}'' = (r_1'', r_2'')$ for the image, object and source planes, respectively. Since the source and object planes are always parallel to each other, it is useful to define the r′ and r″ systems such that the coordinate axes in one plane are always parallel to those in the other. Denote also the normals to the r, r′ and r″ planes at any time t by $\mathbf{n}(t)$, $\mathbf{n}'(t)$ and $\mathbf{n}''(t)$, where each normal is a three component vector defined relative to the R′ system. Then at any time t, the angle between the r and r′ plane is given by

$$\theta(t) = \cos^{-1}[|\mathbf{n}(t) \cdot \mathbf{n}'(t)|], \tag{7-48}$$

lying between 0 and $\pi/2$.

The "input" for the system, consistent with the definition used throughout this research, is the uncollided ideal ray image intensity in the object plane, given at any time t by

$$\text{INPUT}(\mathbf{r}',t) = I'(\mathbf{r}',t) \exp\left[- \int_{r'_n(\mathbf{r}',t)} \Sigma_t(\mathbf{R}'(r'_n(\mathbf{r}',t),\mathbf{r}'),t)\, dr'_n(\mathbf{r}',t) \right]. \tag{7-49}$$

Here, Σ_t is the linear absorption parameter permitting imaging. Since the object is in motion, Σ_t exhibits both spatial and temporal dependence. The single coordinate $r'_n(\mathbf{r}',t)$ runs normally to the object plane through the implied particular planar coordinate r′. In essence, $r'_n(\mathbf{r}',t)$ accounts for the spatial motion of the source relative to the object. Also in Eq. (7-49), $I'(\mathbf{r}',t)$ is the intensity of radiation incident on the object and normal to the source plane. Because r′ and r″ are aligned systems, it follows that

$$I'(\mathbf{r}',t) = I''(\mathbf{r}',t) \tag{7-50}$$

where I^{e} denotes the source radiation intensity in the source plane. In this context, the temporal dependence of I^{e} results from a possible stochastic variability of the source intensity (127) and not from motion, since the source plane has been modelled as moving with the source itself. Note that Eq. (7-49) assumes that object motion speeds are small relative to the speed of the probing radiation particles. This is always an excellent approximation.

It is understood that in most diagnostic situations, the initial spatial distribution -- or some integration thereof -- of the absorption parameter, $\Sigma_t(\mathbf{R}',t_o)$ is the desired imaging output. However, Eq. (7-49) involves $\Sigma_t(\mathbf{R}',t)$ for all t in the duration interval. Given the object's velocity $\mathbf{V}'(t)$ in the $\mathbf{R}'$ system at any time t, the above quantities are related by

$$\Sigma_t(\mathbf{R}',t) = \Sigma_t\left(\mathbf{R}' - \int_{t_o}^{t_o+t} \mathbf{V}'(t)\,dt,\, t_o\right). \tag{7-51}$$

The instantaneous image plane response at any time t is the convolution of the INPUT function, Eq. (7-49), with an overall system PSF and is given by

$$S_{inst}(\mathbf{r},t) = \int_{\mathbf{r}'} \mathrm{INPUT}(\mathbf{r}',t)\,\mathrm{PSF}(\mathbf{r}',\mathbf{r},t,\theta(t))\,d\mathbf{r}'. \tag{7-52}$$

Here, PSF describes the fraction of the object plane radiation intensity at $\mathbf{r}'$ that reaches $\mathbf{r}$. Of course, PSF depends strongly on $\theta(t)$ because, in the general case, the object and image planes are in constant motion.

Over the entire duration interval, the integrated image plane response is given by

$$S(\mathbf{r},\tau) = \int_{t_o}^{t_o+\tau} S_{inst}(\mathbf{r},t)\,dt. \tag{7-53}$$

Substituting Eqs. (7-49) to (7-52) into Eq. (7-53) results in the following integrated image plane response for a general radiation diagnostic system in which all three components are in motion:

$$S(\mathbf{r},\tau) = \int_{t_o}^{t_o+\tau} \int_{\mathbf{r}'} \left\{ I^{e}(\mathbf{r}',t) \exp\left[-\int_{\mathbf{r}'_n(\mathbf{r}',t)} \Sigma_t\left[\mathbf{R}'(\mathbf{r}'_n(\mathbf{r}',t),\mathbf{r}') - \int_{t_o}^{t+\tau} \mathbf{V}'(\mathbf{r}'_n(\mathbf{r}',t),\mathbf{r}',t)dt,\, t_o \right] \right] \right.$$

$$d\,r'_n(r',t)\Big\}\,PSF(r',r,t,\theta))\,dr'\,dt. \tag{7-54}$$

Note that Eq. (7-54) is only of formal significance, requiring extensive and complex modification to account for a divergent radiation source. Eq. (7-54) can also be further extended by developing exact expressions for the function $r'_n(r',t)$, $PSF(r',r,t,\theta(t))$, $\theta(t)$, into which the motion effects of the source and recording device have been formally incorporated.

7.5 Neutron Radiographic Response to an Oscillating Object

As discussed in section 7.4, the general imaging equation, Eq. (7-54), is far too general to be of practical utility. In this section, a particular case involving the reduction of Eq. (7-54) is examined in which the diagnostic imaging system is classified as (S_C,O_V,R_C). This represents an extension of the research presented in the main body of this dissertation, which is classified as (S_C,O_C,R_C).

The diagnostic system to be examined is direct exposure neutron radiography where the object is an infinite slab oscillating sinusoidally, as indicated in Fig. 7.6. At time t, the single line coordinate of the knife edge is given by $y = v(t)$, where

$$v(t) = v_o + v_m \cos(\omega t),\ t \geq 0. \tag{7-55}$$

The slab's knife edge thus oscillates sinusoidally between $v_o - v_m$ and $v_o + v_m$ with period $\tau = 2\pi/\omega$.

The potential application of the following analysis lies in the interpretation of the neutron radiographic image of operational oscillating machine parts. For example, it may be desirable to noninvasively determine the amplitude of the oscillations when the component is encased or otherwise obstructed from view.

For this case, the general imaging equation, Eq. (7-54), reduces to

$$SOF(y,t) = \int_0^t \int_{-\infty}^{\infty} INPUT(y_o,t)\,L(y,y_o,t)\,dy_o\,dt, \tag{7-56}$$

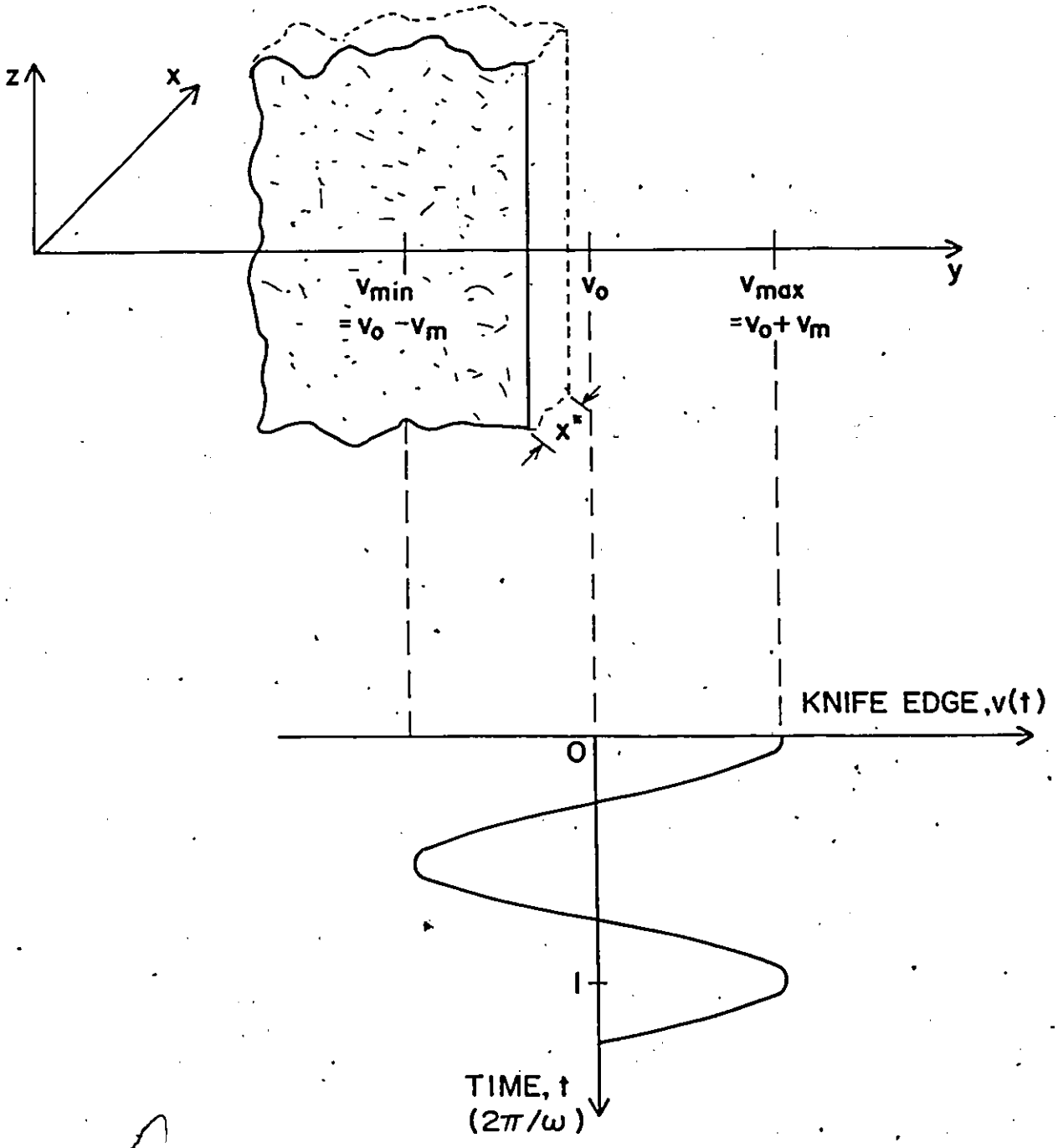

Fig. 7.6: Infinite slab with knife edge oscillating sinusoidally between v_{min} and v_{max}. The neutron beam is normally incident on the page.

where the image plane response is here named the "scattering oscillating function" (SOF). Also, y and y_o are identical coordinate systems in the image and object planes, respectively. L is the overall system line spread function (LSF) which, in its most general form here, is the convolution of the screen-film unsharpness LSF and the scattering subsystem SLF, as outlined in section 4.5. Consistent with previous definitions, the INPUT function is here given by

$$\text{INPUT}(y_o,t)=\begin{cases} I_o \exp[-\Sigma_a x^*], & y_o \in (-\infty, v(t)) \\ I_o, & y_o \in (v(t),\infty) \end{cases}, \tag{7-57}$$

where the slab has macroscopic scattering, absorption and total cross-sections denoted by Σ_s, Σ_a, Σ_t, and is of depth x^*. The incident neutron beam has intensity I_o.

In order to illustrate the neutron radiographic response to the oscillating slab of Fig. 7.6, including the effects of object scattering, it is unnecessary to include screen-film unsharpness in the formulation since this occurs on a much smaller scale than scattering effects, as discussed in section 4.5. The system LSF is then comprised of $SLF^{(1)}(y,y_o)$ from Eq. (4-10) and a separate collimated term, and is given by

$$SLF(y,y_o,t)=\begin{cases} \exp[-\Sigma_s x^*]\,\delta_D(y-y_o)+\dfrac{\Sigma_s}{2\pi}\exp[\Sigma_a x^*]\displaystyle\int_0^{x^*} f(x,y,y_o)\,dx, & y_o \in (-\infty, v(t)) \\ \delta_D(y-y_o), & y_o \in (v(t),\infty) \end{cases}, \tag{7-58}$$

where $f(x,y,y_o)$ is given in Eq. (7-9).

Splitting the inner integral in Eq. (7-56) into the two ranges $(-\infty,v(t))$, $(v(t),\infty)$ and substituting Eqs. (7-57) and (7-58) then yields upon partial evaluation

$$\begin{aligned} \frac{SOF(y,t)}{I_o} &= \int_0^t H(y-v(t))\,dt + \exp[-\Sigma_t x^*]\int_0^t H(-y+v(t))\,dt \\ &\quad + \frac{\Sigma_s}{2\pi}\int_0^t \int_{-\infty}^{v(t)} \int_0^{x^*} f(x,y,y_o)\,dx\,dy_o\,dt \\ &= T1(y,t)+T2(y,t)+T3(y,t), \text{ say,} \end{aligned} \tag{7-59}$$

where H is the Heaviside step function (83).

In practice, the "infinity" response, SOF(y,∞), is likely to be of concern, since presumably the component will oscillate many times over the neutron exposure of several minutes duration, and the selection of a particular time τ during the first few oscillations suggests the necessity of knowing where the knife edge actually is at time τ in order to interpret the radiographic image thereby rendering the imaging procedure superfluous. Actually, it is the distribution of the infinity response that is desired, given by

$$SOF_{\infty}(y) = N \lim_{\tau,n\to\infty}\left(\frac{SOF(y,\tau)}{n}\right) \tag{7-60}$$

where n is the total number of oscillations that have occurred after time τ, and N is an arbitrary normalization constant. Clearly, SOF(y,τ) can be written in the form

$$SOF(y,\tau) = (n + k(y))\,SOF(y, 2\pi/\omega) \tag{7-61}$$

for some function k(y) bounded by k(y) ∈ [0,1]. Substitution of Eq. (7-61) into Eq. (7-60) yields

$$\begin{aligned} SOF_{\infty}(y) &= N \lim_{\tau,n\to\infty} \frac{(n + k(y))}{n} SOF(y, 2\pi/\omega) \\ &= N \cdot SOF(y, 2\pi/\omega). \end{aligned} \tag{7-62}$$

Equation (7-62) also constitutes a proof of the evident recognition that the infinity distribution, $SOF_{\infty}(y)$, is proportional to the SOF response obtained after one complete oscillation. Each of the three terms in Eq. (7-59) will now be evaluated in sequence at time $\tau = 2\pi/\omega$, corresponding to one complete oscillation. The resulting distributions are presented in simplest form when the normalization constant N is chosen as the frequency, $\omega/2\pi$. Firstly, from Eq. (7-55), for the first "downstroke",

$$\underset{(\omega\tau\in(0,\pi))}{T1(y,\tau)} = \begin{cases} 0, & y\in(v_{min}, v(\tau)) \\ \tau - \dfrac{1}{\omega}\cos^{-1}\left(\dfrac{y - v_o}{v_m}\right), & y\in(v(\tau), v_{max}). \end{cases} \tag{7-63a}$$

Building from Eq. (7-63a), it is found that for the first "upstroke",

$$\underset{(\omega\tau\in(\pi,2\pi))}{T1(y,\tau)} = \begin{cases} 2\left[\dfrac{\pi}{\omega} - \dfrac{1}{\omega}\cos^{-1}\left(\dfrac{y - v_o}{v_m}\right)\right], & y\in(v_{min}, v(\tau)) \\ \tau - \dfrac{1}{\omega}\cos^{-1}\left(\dfrac{y - v_o}{v_m}\right), & y\in(v(\tau), v_{max}). \end{cases} \tag{7-63b}$$

Using Eq. (7-63b) and extending to y values outside the oscillation boundaries, one obtains

$$N\cdot T1(s,2\pi/\omega) = \begin{cases} 1, s > 1 \\ 1 - 1/\pi\,(\cos^{-1}(s)), s \in (-1, +1) \\ 0, s < -1, \end{cases} \tag{7-64}$$

where the dimensionless distance s is defined by

$$s = \frac{y + v_o}{v_m}. \tag{7-65}$$

Similarly, it can be shown that

$$N\cdot T2(s,2\pi/\omega) = \begin{cases} 0, s > 1 \\ \dfrac{\exp[-\Sigma_t x^*]}{\pi} \cos^{-1}(s), s \in (-1, +1) \\ \exp[-\Sigma_t x^*], s < -1. \end{cases} \tag{7-66}$$

In order to facilitate the evaluation of $T3(y,2\pi/\omega)$, the midpoint approximation of sections 7.2, 7.3 will be utilized. This leads to

$$N\cdot T3(y,2\pi/\omega) = N\frac{\Sigma_s x^*}{2\pi}\int_0^{2\pi/\omega}\int_{-\infty}^{v(t)} f\left(\frac{x^*}{2}, y, y_o\right) dy_o\, dt,$$

$$= \left(\frac{\Sigma_s x^*}{2\pi}\right)\exp\left[\frac{-\Sigma_t x^*}{2}\right]\left\{\frac{\pi}{2} - N\int_0^{2\pi/\omega}\tan^{-1}\left[\frac{y - v(t)}{\left(d_o - \frac{x^*}{2}\right)}\right] dt\right\}, \tag{7-67}$$

where $f(x,y,y_o)$ has been substituted from Eq. (7-9) prior to evaluation. Using the FORTRAN program OSCIL, listed in Appendix D, Eq. (7-67) has been evaluated in the following dimensionless form, substituting u for ωt,

$$N\cdot T3(s,2\pi/\omega) = \left(\frac{\Sigma_s x^*}{2\pi}\right)\exp\left[\frac{-\Sigma_t x^*}{2}\right]\left\{\frac{\pi}{2} - \frac{1}{2\pi}\int_0^{2\pi}\tan^{-1}\left[\frac{v_m(s - \cos(u))}{\left(d_o - \frac{x^*}{2}\right)}\right] du\right\}, \tag{7-68}$$

$$s \in (-\infty, \infty).$$

From Eqs. (7-59) to (7-62), the resultant infinity distribution is given as the following sum of Eqs. (7-64), (7-66) and (7-67):

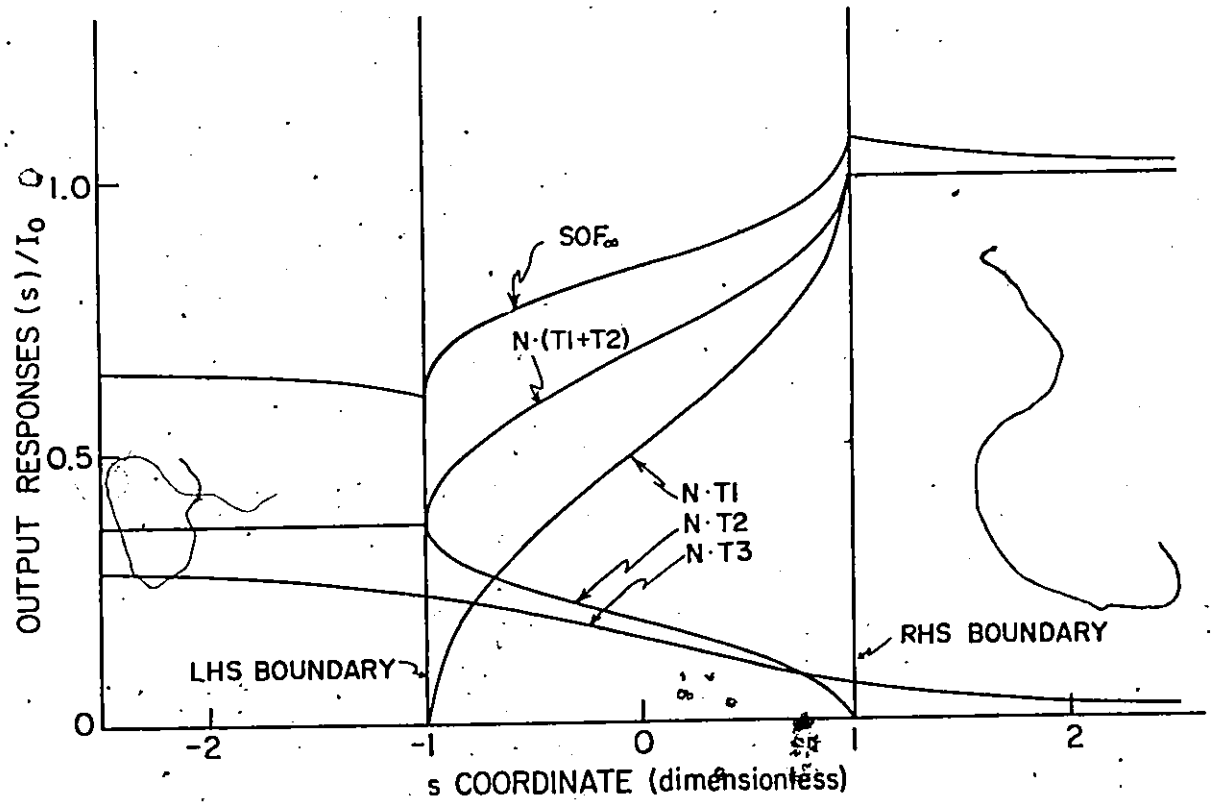

Fig. 7.7: SOF and component responses for a knife-edged infinite slab oscillating sinusoidally with the edge between s = -1 and s = +1, corresponding here to an amplitude of x_m = 1.0 cm. The slab has cross-sections Σ_s = 1.0 cm^{-1} and Σ_a = 0.0 cm^{-1} with depth $x^* = d_o$ = 1.0 cm.

$$\frac{SOF_{\infty}(s)}{I_o} = N\{T1(s,2\pi/\omega) + T2(s,2\pi/\omega) + T3(s,2\pi/\omega)\}. \quad (7\text{-}69)$$

The infinity and component distributions have been plotted in Fig. 7.7 for a non-absorbing slab of depth $x^* = 1.0$ cm and with $\Sigma_s = 1.0\ cm^{-1}$. As discussed in section 4.3, the scattering effects on the output response distribution are greatest when $\Sigma_a = 0.0\ cm^{-1}$. Note, as expected, that the infinity distribution is completely independent of the angular frequency ω. In the absence of object scattering, the infinity distribution in Eq. (7-69) reduces to

$$\left.\frac{SOF_{\infty}(s)}{I_o}\right|_{\Sigma_s = 0} = N\{T1(s,2\pi/\omega) + T2(s,2\pi/\omega)\}. \quad (7\text{-}70)$$

and has also been plotted in Fig. 7.7. The scattering contribution, represented by $N \cdot T3(s,2\pi/\omega)$, is significantly large relative to the uncollided terms, and thus is seen to appreciably increase the ideal infinity response given by Eq. (7-70). Specifically, the ideal infinity response is modified by scattered neutrons to include positive and negative SBED's at $s = 1.0$ and -1.0, corresponding to the oscillation boundaries at $y = v_{max}$ and v_{min}.

As was shown to be the case for each of the stationary knife-edged slab, the concentric cylindered object and the two-dimensional ϕ-wedge, application oriented boundary location methodologies are indicated here to require the explicit incorporation of object scattering effects.

7.6 Transport Based STF Analysis for General Geometries

The system transfer function (STF) and transport calculations performed throughout this research have involved simplified object geometries, usually consisting of one or two rectangular dimensions, with the exception of section 7.2. The analytical formulations accorded by these geometries have in most cases necessitated numerical solutions or

evaluations. The extension of these analyses to more general goemetries would, in the absence of approximations, render the formulations unwieldy.

Such approximations seem appropriate, however, given the approximations already inherent in several of the formulations — single scattering, isotropic scattering, one-group cross-sections, collimated uniform beam. While solutions have been explicitly calculated in all instances, the purpose of these approximate solutions has usually been to estimate the magnitude of object scattering effects on some neutron radiographic output response function. This estimation objective is most prominent in Chapter 3, where the spreading of a band of neutrons within the incident beam is examined, to the exclusion of the remainder of the beam as the band traverses a two-dimensional rectangular object. The resulting "band spreading function", increasing in accuracy with the band width, represents a departure from conventional STF analysis with considerable potential for general application.

Specifically, wide objects of variable depth can be approximately partitioned into these bands, as illustrated in Fig. 7.8, for purposes of object scattering estimation and response function approximation calculations. The infinite and semi-infinite slab models of Chapters 2, 4 and 5 correspond to the approximation in Fig. 7.8a. Of course, a sensitivity analysis describing the potential error incurred by these approximations should accompany the calculations. Calculational methods based on these macroscopic decompositions should be superior to those involving precise calculation of point spread functions, such as the SPF, at many points in the object plane, since these latter calculations would in general be expensive and would still combine to give only an approximate result. In summary, calculations based on these decompositions appear to be a practically oriented extension of the research embodied in this dissertation.

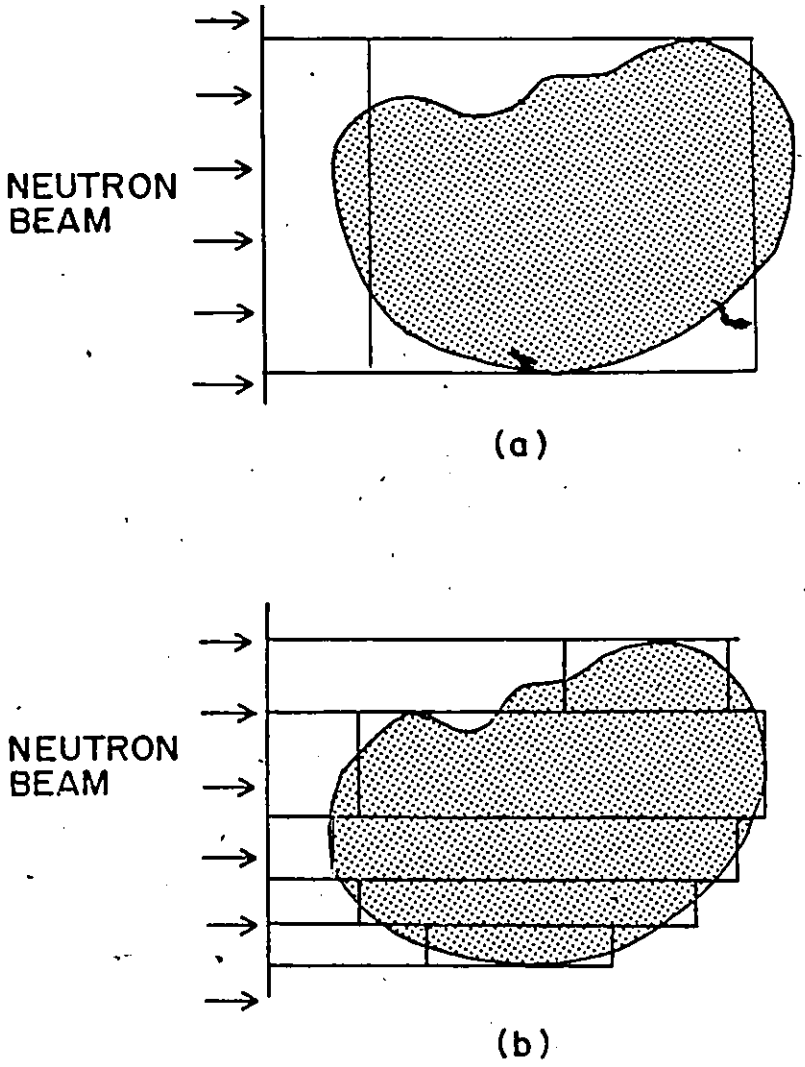

Fig. 7.8: Cross-sectional depiction of partitioning of an object into rectangular infinite slab regions for purposes of scattering estimation and response function approximation calculations. For one region ((a) above), the calculations of Chapters 2, 3, 4 and 5 apply. For multiple regions ((b) above), the calculations of Chapter 3 apply.

7.7 Miscellaneous Extensions of the Transport Analysis

The following extensions of the transport analysis presented in this dissertation can be identified, most of these involving the relaxation of assumptions and approximations adopted for purposes of computational expediency and analytical tractability.

Firstly, the assumption of isotropic neutron scattering is usually valid in the centre-of-mass frame (56), and is valid in the laboratory frame for all but the lightest elements. For example, the average cosine of the scattering angle in the laboratory frame, $\bar{\mu}_0$, decreases from 0.6614 for hydrogen to 0.0953 for lithium to 0.0417 for oxygen (56) and decreases further with increasing atomic mass, A ($\bar{\mu}_0 \approx 2/(3A)$). Radiographic transport analysis for objects containing hydrogenous compounds should therefore include some consideration of anisotropic scattering. Indeed, an arbitrary degree of anisotropic scattering is incorporated into the neutron transport formulation of Chapter 3 through the Legendre eigenfunction expansion in Eq. (3-29). The resulting calculation was actually performed assuming linearly anisotropic scattering, corresponding to the first two terms in Eq. (3-29), for which the coefficients can be shown to be related by

$$\begin{aligned} \Sigma_{s1}(x,y) &= \bar{\mu}_0 \, \Sigma_{s0}(x,y) \\ &= \bar{\mu}_0 \, \Sigma_s(x,y). \end{aligned} \tag{7-71}$$

The extension of the other transport analyses in this dissertation to include anisotropic scattering can be identified as worthwhile endeavors.

An arbitrary order of scattering was incorporated into the formulations of Chapters 2, 3 and 5. While the explicit accounting of multiple scattering would grossly encumber the analytical STF formulations in Chapters 4 and 7, it is suggested that multiple scattering might be introduced as a broadening factor in the several SLF and SPF derivations presented in Appendix A. Further research is thus indicated.

With the exception of the Monte Carlo calculations in Chapter 5, all transport analyses in this dissertation have assumed a uniform and collimated incident neutron beam. While this assumption is usually valid for reactor based neutron radiographic facilities, it might be worthwhile to incorporate a finite maximum beam divergence into these transport calculations.

For radiography with epithermal neutrons, the neutron-nuclear interaction cross-sections will be different from the one-group thermal cross-sections used parametrically in this research. Furthermore, energy dependence will need to be included in the scattering term calculations.

Finally, this research has focussed on the transport of neutrons through the object and onto a generalized image plane. With the exception of a general derivation in section A.1, no assumptions regarding the conversion of neutrons into an ionizing radiation at or near the image plane have been made. This radiation conversion process represents a source of image degradation that can be modelled by a general screen-film unsharpness STF, such as that given in Eq. (A-18). The analyses presented in this dissertation should therefore also be applicable to neutron radiography in which the "transfer technique" of imaging is employed, section 1.2.

CHAPTER 8

SUMMARY AND CONCLUSIONS

The goal of the research presented in this dissertation has been to investigate the transport of neutrons through an object being radiographed and onto the plane at which image formation occurs. The significance of this research is that it establishes a mathematical/physical basis for the quantitative evaluation of scattering based image degradation. As suggested in the Introduction, such transport analyses are logically divided into two domains.

Firstly, the spatial and directional distribution of neutrons emergent from the object is a function of the material and geometrical characteristics of the object, and also of the incident neutron source distribution. This distribution constitutes the information carrying ray image in the object plane.

The other domain of radiographic transport analysis involves the determination of the final image plane radiation distribution resulting from a given object plane neutron distribution. Since the scattered neutrons reaching the object plane have some nontrivial angular distribution, the object-to-film separation is of great importance in assessing the impact of scattered neutrons on image degradation as is evidenced by the prominence of this parameter in this research. The rationale for the division of radiographic transport analyses into two domains is thus clear; the object plane spatial and angular neutron distribution logically serves as an input to the particular neutron imaging system at hand. This decoupling has been generally maintained throughout the various chapters for consistency.

Neutron imaging calculations found in the literature often assume simple exponential attenuation with the object scattering of neutrons assumed negligible or simply

ignored. The calculations in this research suggest, however, that for objects of even nearly trivial geometry such as the finite or knife-edged slab, the imaging effects of object scattered neutrons can be considerable, and more profound than the often cited general decrease in contrast (2).

The chapters constituting this dissertation will now be briefly and sequentially summarized. For each chapter, the significant results will be outlined and the important original contributions to knowledge identified. Where appropriate, conclusions will be drawn.

In Chapter 1 a brief historical outline and technical overview of neutron radiography was presented. The need for transport based characterizations of scattering based image degradation was identified. Subsequently, an introduction to neutron transport and imaging analysis was presented.

In Chapter 2 the object scattering of neutrons was presented as a nonlinearity in the transfer characteristics of the imaging system. This nonlinearity arises because, in the presence of scattering, the system point spread function (PSF) is spatially variant. Specifically, the PSF, like the input distribution with which it is convolved, exhibits dependence on the material and geometrical characteristics of the object being inspected. One of the very few situations in which this nonlinearity is naturally removed occurs for an infinite slab object.

An integral equation based on the point source diffusion kernel was therefore developed to describe the transport of collimated incident thermal neutrons through such a slab. This transport equation, in its general form, is well known and found in several modelling domains. However, for the relevant particular component functions of the general equation, in the context of an infinite slab with a collimated thermal neutron source, the developed Neumann series solution is original involving both analytical and computational

evaluation. This series solution, by nature, allows for an arbitrary degree of multiple scattering. Specifically, each mode represents a different order of scattering. The solution form permits the ready calculation of the exact build-up factor (BUF) at any point. Several important properties of the neutron intensity and BUF were deduced and then analytically proven.

In Chapter 3, the transport of neutrons through the object was analyzed from a neutron transport equation perspective. Specifically, the one-group, time-independent, two-dimensional neutron transport equation was solved for an object of rectangular slab geometry in a radiographic context. The purpose of these calculations was to estimate the maximum extent of spreading that could occur in a band of a collimated neutron beam incident on a section of the rectangular slab face. The approximations made at various stages of the equation development reflect this purpose.

The solution procedure developed for the governing neutron transport equation is best classified as an original extension to the existing "double spherical harmonics" (DP_L) procedure first introduced by Yvon(90) for the corresponding one-dimensional equation. It should be noted that the analytical framework represented by this extension is flexible with respect to possible enhancement.

One interesting and significant result of this neutron band transport analysis is that for collimated neutrons incident on the assumed homogeneous band, all neutrons emergent and impingent on the image plane within the extrapolated band boundaries are assumed to contribute to the imaging of the band, regardless of how many scatterings they may have undergone. Thus, for inspected objects containing regions that can be approximated by a homogeneous rectangular band, the imaging quality will be superior to that predicted by traditional object scattering analyses in which all scattered neutrons contribute to the BUF and are therefore considered to be non-image forming.

In Chapter 4 the object scattering of thermal neutrons was incorporated into a system transfer function (STF) framework. This involved the development of original line and point spread functions that were applied in the quantitative assessment of scattering based image degradation. A significant obtained result is the elucidation of hump-shaped distortions occurring in the neutron radiographic response to a knife-edged slab object. While these scattering based edge distortions (SBED's) have previously been predicted and qualitatively observed (96,97), their quantitative description in Chapter 4 is original.

The result that the SBED's magnitude decreases with increased diffuse obliquity of neutrons incident on the knife edge led to the suggestion that the relative magnitude of these SBED's could serve as an indicator of the BUF in the neutron beam emergent from a radiographed object. The assessment of the feasibility of such an application was seen to require either Monte Carlo calculations or experimental confirmation, the subject of Chapters 5 and 6.

An interesting property of the total edge output response, that is, involving both scattering degradation and screen-film unsharpness, is that the edge location response exhibits dependence on the macroscopic scattering cross-section, Σ_s, but not on the screen-film unsharpness parameter. This result is of significance in dimensioning analyses such as those designed to calculate the image location of a nuclear fuel pin edge on a blurred radiograph. Previous studies involving this edge location determination have failed to quantitatively include Σ_s in the resulting edge location prescription (52,100-102).

Finally, modulation transfer functions corresponding to the important STF's developed were calculated for purposes of completion. A quantitative criterion was developed to describe the particular screen-film unsharpness and scattering degradation parameter values at which superiority of fidelity switches from one degradation subsystem to the other. It was recognized that the convolution of two Lorentzian functions is also Lorentzian in form.

This latter result is of potential significance in imaging analyses for the following reason. If each degradation subsystem (scattering and screen-film unsharpness were analyzed here) were modelled, to some degree of approximation, by a Lorentzian LSF, then the total system LSF would also be Lorentzian with a degradation parameter equal to the sum of the component degradation parameters. In this context degradation sources could thus be treated as possessing additivity. The usefulness of such a framework is obvious.

In order to assess the feasibility of the edge scattering output response as an indicator of the BUF in the neutron beam emergent from a radiographed object, it is necessary to admit an arbitrary degree of diffuseness in the neutrons incident on the knife-edged slab. It was therefore decided to perform a Monte Carlo calculation of the SEF response, Chapter 5, admitting both an arbitrary order of multiple scattering and an arbitrarily, but uniformly, diffuse incident neutron distribution. Substantial variance reduction was achieved through application of the familiar importance sampling techniques that are "splitting" and "Russian roulette".

Initially a collimated neutron source was assumed in order to verify the existence and approximate magnitude of the SBED's. A significant result was a confirmation of the expectation that the relative SBED height should increase with the ratio Σ_s/Σ_t of macroscopic neutron cross-sections. For application of these SBED's as a diagnostic indicator the knife-edged slab should possess a large Σ_s, both absolutely and relative to Σ_a.

It was subsequently found that increasing the degree of incident diffuseness served to decrease the relative SBED height in the edge response. These calculations suggest that the relative SBED height might be an effective indicator of the BUF for BUF values smaller than approximately 1.4.

The significance of the Monte Carlo calculations of Chapter 5 is thus a confirmation of the existence, magnitude and suggested application of the SBED's as a diagnostic image

quality indicator (IQI). It is stressed that no implication of superiority of this potential IQI over existing IQI's(2,16) is intended. Further research is required for an assessment of the practical utility of this IQI.

The calculations described in Chapter 5 are superior to those performed by Butler (97) since they allow for multiple scattering and oblique neutron incidence. The quantitative assessment of the SBED's performed in Chapter 5 is original.

Direct exposure neutron radiographs of an "infinite" lucite knife-edged square slab were obtained at beamport 2 of the McMaster Nuclear Reactor, using a well thermalized, well collimated neutron beam.

The results of experimental work designed to confirm the existence and magnitude of these SBED's are reported in Chapter 6. The existence of the SBED phenomena can be visually confirmed by noting the light halo superimposed on the square slab radiographic image. This nuclear scattering based halo is fundamentally different from halos resulting from light reflection and refraction in ice crystals. Only the negative SBED was reproduced on the corresponding optical density scans. This is explained primarily by the saturation characteristic of the film emulsion at large exposures.

In order to assess the extent to which the BUF in the incident neutron beam degrades the SBED's, various thicknesses of lucite slabs were interposed between the collimated neutron beam and the lucite knife-edged slab. As predicted by the Monte Carlo calculations, the negative SBED height diminishes appreciably with increasing BUF suggesting viability of the relative SBED height as a BUF indicator, valid for BUF values smaller than approximately 1.4.

The two-dimensional nature of the SBED's in the square slab image was analyzed by taking edge scans at various distances from the corner image. Consistent with the visual observation of a brighter and expanded halo near corners, the SBED's obtained on edge scans

became elongated and negatively shifted in optical density with decreasing separation from the corner.

Radiographs being analyzed using this prospective diagnostic tool would have varying optical density ranges. An exposure independent SBED height indicator would be necessary since the BUF in a neutron beam is independent of a particular film emulsion's density vs. exposure characteristic. The transformation that should thus be applied to the SBED peak and base optical density values was derived.

Several extensions and generalizations of the analyses presented in Chapters 2 through 6 are initiated and discussed in Chapter 7. These include extensions to x-ray and γ-ray radiography, an analysis of scattering degradation in the neutron radiographic response to cylindered, wedge-shaped and oscillating objects, the extension of this work to generalized imaging systems and finally to objects of general geometries.

In Appendix B, the degradation of an edge optical density trace induced by a microdensitometer scanning window of finite area was quantitatively assessed. This degradation occurs because information is integrated over a region the size of the window at each point of the scan, effecting a smoothing of the actual variation that is similar in nature to convolution. An original quantitative criterion, formulated in terms of a dimensionless parameter, was derived to permit the specification of an upper bound on the window width.

In Appendix C several interesting imaging properties of isotropic systems, possessing rotationally symmetric PSF's, are analyzed. The significance of these properties lies in their applicability to general imaging systems. While originally developed for screen-film unsharpness analysis, the results in Appendix C apply to any imaging system or subsystem characterized by an isotropic PSF. In the context of this work, the following results are original extensions to the PSF application in neutron radiography.

For neutron radiographic systems with a locally isotropic and isoplanatic PSF the optical density at a point in the blurred radiographic image of an object is completely independent of the system PSF if the object's attenuation properties are radially constant in all directions leading from that point. This independence is valid for both scattering and nonscattering objects. One particularly useful result is that the location of two- dimensional wedge corners on blurred radiographs is determinable from a description of the original wedge-shaped object and the film emulsion's density vs. exposure characteristic; no other knowledge of the system PSF is required, removing the need for image enhancement.

Additionally, a useful result is the general analytical resolution of the question of which optical density corresponds to an infinite knife edge on a blurred radiograph of an absorbing knife-edged object, for a locally isotropic and isoplanatic system.

APPENDIX A

MATHEMATICAL DERIVATIONS

A.1 Derivation of Lorentzian Distribution for Isotropic Secondary Radiation

As suggested in Fig. A.1, the problem is to determine the distribution of "secondary" radiation impingent on some receiving plane posed parallel to an infinite and attenuating slab which is subjected to normally and uniformly incident primary radiation. Within this context, secondary radiation can be taken as either

(i) radiation emitted upon absorption of the incident primary radiation, such as occurs in the convertor of a neutron radiographic recording cassette, or

(ii) simply the incident radiation once scattered.

For each application, this secondary radiation is taken to be isotropic about the point of emission. For each infinitesimal slab element of thickness Δx, the secondary radiation collectively emanates from a plane. Consider probabilistically the secondary radiation emitted from the first slab element, as indicated in Fig. A.1, and impingent on the upper half ($y \geq y_o$) of the distribution plane at $X = d_o$. The probability that secondary radiation traverses the distribution plane between the Y coordinates of zero and y_o is given by the cumulative distribution function

$$G(y) = Pr(y_o \leq Y \leq y)$$

$$= Pr\left(\tan(\Phi) \leq \frac{y - y_o}{d_o}\right)$$

$$= Pr\left(\Phi \leq \tan^{-1}\left(\frac{y - y_o}{d_o}\right)\right), \qquad \text{(A-1)}$$

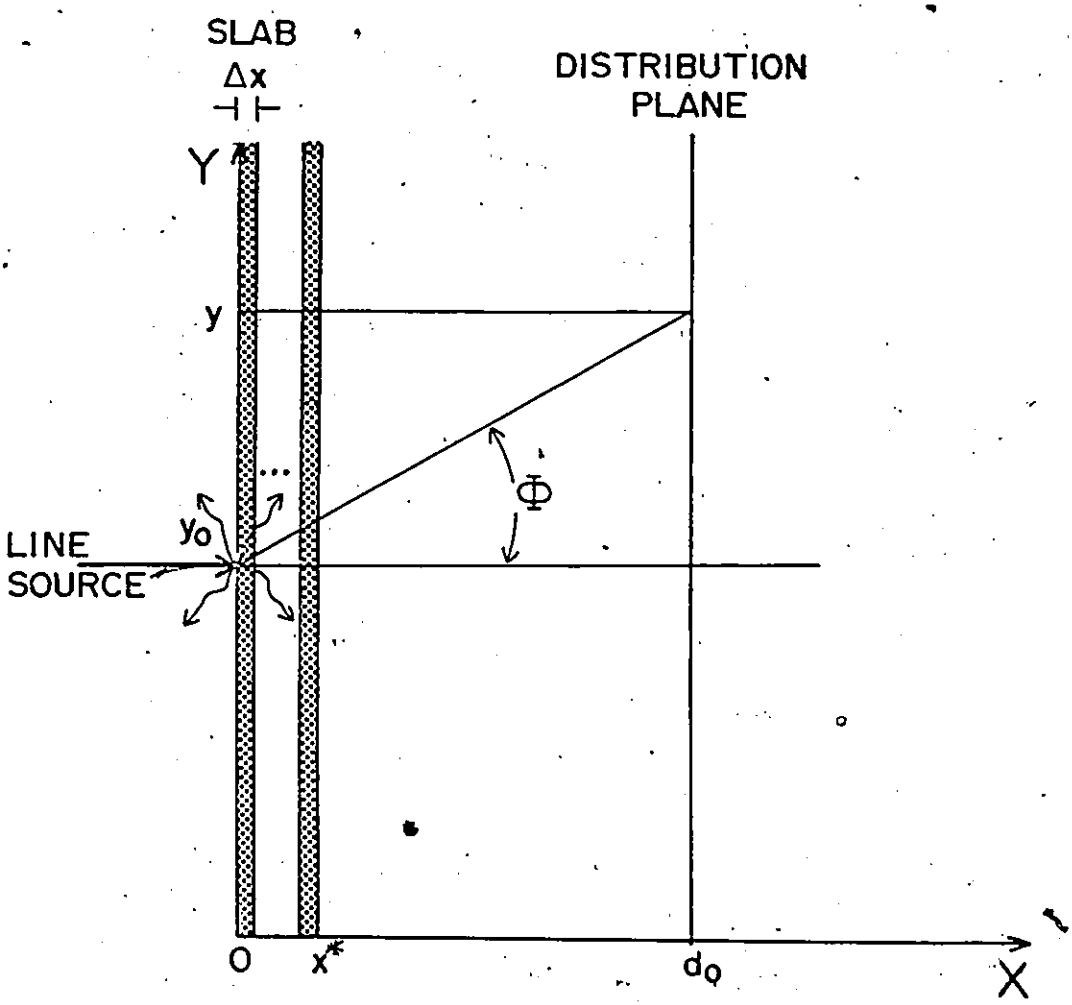

Fig. A.1: Configuration for determination of secondary radiation distribution from a line source at $Y = y_o$ onto the plane at $X = d_o$.

where the final equality is determined by the monotonicity of Φ on $(0, \pi/2)$. For isotropic emission, however,

$$\Pr(\Phi \leq \phi) = \frac{2\phi}{\pi}, \quad \phi \in (0, \pi/2). \tag{A-2}$$

Substitution of Eq. (A-2) into Eq. (A-1) yields

$$G(y) = \frac{2}{\pi} \tan^{-1}\left(\frac{y - y_o}{d_o}\right). \tag{A-3}$$

Since the probability density function associated with G(y) is

$$g(y) = \frac{d}{dy} G(y), \tag{A-4}$$

the distribution of secondary radiation at $X = d_o$ is

$$g(y) = \frac{2}{\pi d_o}\left[1 + \left(\frac{y - y_o}{d_o}\right)^2\right]^{-1}. \tag{A-5}$$

Extending to the lower half plane, and normalizing to unit area, the resulting distribution of secondary radiation at $X = d_o$, known as a "Lorentzian" distribution, is then

$$f(y) = \frac{1}{\pi d_o}\left[1 + \left(\frac{y - y_o}{d_o}\right)^2\right]^{-1}. \tag{A-6}$$

For the case of neutron conversion in a neutron radiographic recorder, this distribution is the line spread function (LSF), since it describes the system spreading of an incident line source of neutrons. The extent of spreading is indicated by the Lorentzian spreading coefficient, d_o.

If the convertor has a finite width x^*, each infinitesimal plane contributes a characteristic Lorentzian distribution, so that the overall distribution is

$$L(y) = \int_0^{x^*} \frac{\exp[-\Sigma_t x]}{\pi(d_o - x)}\left[1 + \left(\frac{y - y_o}{d_o - x}\right)^2\right]^{-1} dx, \tag{A-7}$$

where Σ_t is the total macroscopic cross-section for the convertor. The exponential factor in Eq. (A-7) accounts for attenuation of the incident neutron beam as it traverses the slab and can be approximated over the range $[0, x^*]$ by the constant value

$$\exp[-\Sigma_t x] \approx 1 - \Sigma_t x$$

$$\approx 1 - \frac{\Sigma_t x^*}{2}, \quad x \in [0, x^*]. \tag{A-8}$$

To evaluate Eq. (A-7) using the constancy approximation of Eq. (A-8), substitute for x the variable

$$t = x - d_o. \tag{A-9}$$

Up to a constant of proportionality, Eq. (A-7) becomes

$$L(y) \propto \int_{-d_o}^{x^* - d_o} \frac{t}{t^2 + (y - y_o)^2}\, dt$$

$$\propto \ell n \left| \frac{(x^* - d_o)^2 + (y - y_o)^2}{d_o^2 + (y - y_o)^2} \right|$$

$$= \ell n \left| 1 + \frac{x^*(x^* - 2d_o)}{d_o^2 + (y - y_o)^2} \right|. \tag{A-10}$$

Now x^* is always smaller than d_o, so that the above logarithmic argument always lies between zero and one. This validifies usage of the following logarithmic expansion (117):

$$\ell n(a + x) = \ell n(a) + 2\left[\left(\frac{x}{2a + x} \right) + \frac{1}{3}\left(\frac{x}{2a + x} \right)^3 + \frac{1}{5}\left(\frac{x}{2a + x} \right)^5 + \ldots \right]. \tag{A-11}$$

Applying this expansion to Eq. (A-10) results, upon retention of the zeroth and first order terms, in

$$L(y) \propto \left[1 + \frac{(y - y_o)^2}{d_o^2 + x^*(x^* - 2d_o)/2} \right]^{-1} \tag{A-12}$$

reducing to the simple Lorentzian form of Eq. (A-6), as $x^* \to 0$. Thus, the effect of expanding the convertor from infinitesimal width Δx to finite width x^* is roughly to transform the Lorentzian spreading coefficient from d_o^2 to

$$d_1^2 = d_o^2 + \frac{x^*(x^* - 2d_o)}{2}. \tag{A-13}$$

Other image degradation effects, such as the spatially differential absorption of secondary radiation in the film emulsion, result in a screen-film LSF which deviates from, but can be well approximated by a Lorentzian LSF in high resolution neutron radiography. It is therefore unsurprising that experimental corroboration exists for the Lorentzian LSF (105).

The Lorentzian LSF has been shown to arise from the geometric combination of isotropic emission and parallel planes. Another familiar angular emission distribution is the Lambertian cosine distribution for diffuse emission, with the angular distribution function

$$h(\phi) = \cos(\phi). \tag{A-14}$$

In this case,

$$\Pr(\Phi \leq \phi) = \int_0^{\phi} \cos(\Phi)\, d\Phi$$

$$= \sin(\phi), \quad \phi \in [0, \pi/2], \tag{A-15}$$

so that

$$G(y) = \sin\left[\tan^{-1}\left(\frac{y - y_o}{d_o} \right) \right]$$

$$= \frac{(y - y_o)}{\sqrt{d_o^2 + (y - y_o)^2}}. \tag{A-16}$$

The resulting distribution at the plane $X = d_o$ is then

$$g(y) = \frac{1}{d_o}\left[1 + \left(\frac{y - y_o}{d_o} \right)^2 \right]^{-3/2} \tag{A-17}$$

This distribution is similar to the Lorentzian, with the distinguishing feature of a $-3/2$ exponent.

Clearly, different angular distributions yield different LSF's. In light of the similarity of Eq. (A-5) and Eq. (A-17), it has been proposed (116) that the following general two-parameter family of LSF's should cover most cases of interest:

$$LSF(y, y_o) = k_p^C [1 + C(y - y_o)^2]^{-(p-1)/2}; \; C \in \mathbb{R}; \; p = 3,4,5,\ldots . \tag{A-18}$$

Here, k^C_p is a normalization constant; the parameters p and C characterize the line spreading nature.

For the case in which the "emitted" secondary radiation is simply once-scattered incident radiation, consider the line source of radiation normally incident on the first slab element to have unit intensity. Then, the fraction $\Sigma_s \Delta x$ of that radiation will scatter in the slab element, half of it forward and half of it in reverse for isotropic scatter. The Lorentzian distribution of once-scattered radiation at the plane $X = d_o$ must therefore have an area of $\Sigma_s \Delta x/2$ and is thus

$$L(y) = \left(\frac{\Sigma_s \Delta x}{2}\right)\left(\frac{1}{\pi d_o}\right)\left[1 + \left(\frac{y - y_o}{d_o}\right)^2\right]^{-1} \tag{A-19}$$

For a slab of finite width x^*, each infinitesimal slab element contributes a characteristic Lorentzian distribution, so that the overall distribution is

$$L(y) = \frac{\Sigma_s}{2\pi}\int_0^{x^*} \frac{\exp[-\Sigma_t x]}{(d_o - x)}\left[1 + \left(\frac{y - y_o}{d_o - x}\right)^2\right]^{-1} dx. \tag{A-20}$$

As for the convertor emission case, Eq. (A-20) can also be approximated by a Lorentzian distribution.

A.2 Derivation of $SLF^{(1)}$

Referring to section 4.1; for a slab of finite width x^*, the uncollided emergent beam corresponding to an incident unit neutron line source at $y = y_o$ has intensity

$$I_{1,x^*}(y,y_o) = \exp[-\Sigma_t x^*]\,\delta_D(y-y_o) \tag{A-21}$$

This compares to

$$I_{1,\Delta x}(y,y_o) = [1-\Sigma_t \Delta x]\,\delta_D(y-y_o) \tag{A-22}$$

for passage through an infinitesimal slab element of width Δx.

Likewise, the emergent once-scattered neutron intensity distribution at the plane $x = d_o$, section A.1, is

$$I_{2,x^*}(y,y_o) = \frac{\Sigma_s}{2\pi}\int_0^{x^*} \frac{\exp[-\Sigma_t x]}{(d_o-x)}\left[1+\left(\frac{y-y_o}{d_o-x}\right)^2\right]^{-1} dx, \tag{A-23}$$

so that the total emergent intensity distribution at $x = d_o$ is

$$I_{x^*}(y,y_o) = I_{1,x^*}(y,y_o) + I_{2,x^*}(y,y_o). \tag{A-24}$$

Consistent with the definition in section 4.1, the "input" here is the idealized emergent beam intensity for a nonscattering finite slab, and is thus

$$I^{\circ}_{x^*}(y,y_o) = \exp[-\Sigma_a x^*]\,\delta_D(y-y_o) \tag{A-25}$$

Normalizing $I_{x^*}(y,y_o)$ in Eq. (A-24) to correspond to a unit integrated "input" then yields the geometrically first order scattering line function $SLF^{(1)}$, given by

$$SLF^{(1)}(y,y_o) = \exp[-\Sigma_s x^*]\,\delta_D(y-y_o)$$

$$+ \frac{\Sigma_s}{2\pi}\exp[\Sigma_a x^*]\int_0^{x^*} \frac{\exp[-\Sigma_t x]}{(d_o-x)}\left[1+\left(\frac{y-y_o}{d_o-x}\right)^2\right]^{-1} dx. \tag{A-26}$$

A.3 Derivation of $SPF^{(0)}$, $SPF^{(1)}$

The isotropic point spread function (PSF) corresponding to the Lorentzian LSF, Eq. (A-6), can be shown to be (116)

$$PSF(R) = \frac{1}{2\pi d_o^2}\left[1+\left(\frac{R}{d_o}\right)^2\right]^{-3/2}, \tag{A-27}$$

where R represents distance from the emission origin point. Using the notation of section 4.2, denote the ray from the origin of the (y, z) Cartesian coordinate system to the emission origin point by $\mathbf{r}_1$, and to a point (y, z) of interest by $\mathbf{r}_2$. Then, using the triangle cosine law,

$$R^2 = |\mathbf{r}_1|^2 + |\mathbf{r}_2|^2 - 2|\mathbf{r}_1|\cdot|\mathbf{r}_2|\cos(\theta_1-\theta_2), \tag{A-28}$$

where θ_1 and θ_2 are the elevation angles of $\mathbf{r}_1$ and $\mathbf{r}_2$. As in section A.1, the situation consists of a unit point source of neutrons normally incident on a slab element of width Δx. A fraction $\Sigma_s \Delta x/2$ of these will isotropically scatter forward so that the scattering component of the emergent distribution at the plane $x = d_o$ has intensity

$$I_{2,\Delta x}(R) = \frac{\Sigma_s \Delta x}{4\pi d_o^2}\left[1+\left(\frac{R}{d_o}\right)^2\right]^{-3/2}. \tag{A-29}$$

The uncollided beam component has intensity

$$I_{1,\Delta x}(R) = (1-\Sigma_t \Delta x)\ \delta_D(R), \tag{A-30}$$

where $\delta_D(R)$ denotes the product $\delta_D(|\mathbf{r}_1|-|\mathbf{r}_2|)\ \delta_D(0_1-\theta_2)$. The total emergent intensity distribution at $x = d_o$ is

$$I_{\Delta x}(R) = I_{1,\Delta x}(R) + I_{2,\Delta x}(R). \tag{A-31}$$

Consistent with the definition in section 4.1, the "input" here is the idealized emergent beam intensity for a nonscattering finite slab element and is thus

$$I^*_{\Delta x}(R) = (1-\Sigma_a \Delta x)\ \delta_D(R). \tag{A-32}$$

Normalizing $I_{\Delta x}(R)$ in Eq. (A-31) to correspond to a unit integrated input then yields the geometrically zeroth order scattering point function (SPF) given by

$$SPF^{(0)}(R) = \frac{1}{(1-\Sigma_a \Delta x)}\left\{(1-\Sigma_t \Delta x)\delta_D(R) + \frac{\Sigma_s \Delta x}{4\pi d_o^2}\left[1+\left(\frac{R}{d_o}\right)^2\right]^{-3/2}\right\}. \tag{A-33}$$

For a finite slab of width x^*, the first order SPF is obtained from $SPF^{(0)}$ in the same manner that $SLF^{(1)}$ is obtained from $SLF^{(0)}$, section A.2, and is

$$SPF^{(1)}(R) = \exp[-\Sigma_s x^*]\,\delta_D(R)$$

$$+ \frac{\Sigma_s}{4\pi} \exp[\Sigma_a x^*] \int_0^{x^*} \frac{\exp[-\Sigma_t x]}{(d_o - x)^2} \left[1 + \left(\frac{R}{d_o - x} \right)^2 \right]^{-3/2} dx. \tag{A-34}$$

A.4 Derivation of $SEF^{(n)}$ and the Infinite Slab Response

A.4.1 $SEF^{(n)}$

The geometrically n^{th} order scattering edge function, $SEF^{(n)}$, is obtained as the convolution of the scattering line function $SLF^{(n)}$ with the system input which, for the knife-edged object of Fig. 4.2, is the idealized nonscattering emergent beam intensity given by

$$\text{INPUT}(y) = \begin{cases} I_o(1 - \Sigma_a \Delta x); & n = 0; y < 0 \\ I_o \exp[-\Sigma_a \Delta x]; & n = 1; y < 0 \\ I_o; & n = 0, 1; y > 0 \end{cases} \tag{A-35}$$

Mathematically, the convolution is

$$SEF^{(n)}(y) \stackrel{df}{=} \text{INPUT}(y) * SLF^{(n)}(y)$$

$$= \int_{-\infty}^{0} \text{INPUT}(v) SLF^{(n)}(y - v) dv + \int_{0}^{\infty} \text{INPUT}(v) SLF^{(n)}(y - v) dv. \tag{A-36}$$

The above integration is split at $v = 0$, since $SLF^{(n)}$ is discontinuous at $v = 0$ due to the material discontinuity that is the knife edge.

For the zeroth order model ($n = 0$),

$$SEF^{(0)}(y) = I_o \int_{-\infty}^{0} (1 - \Sigma_t \Delta x) \delta_D(y - v) + \left(\frac{\Sigma_s \Delta x}{2\pi d_o} \right) \left[1 + \left(\frac{y - v}{d_o} \right)^2 \right]^{-1} dv$$

$$+ I_o \int_{0}^{\infty} \delta_D(y - v) dv$$

$$= I_o(1 - \Sigma_t \Delta x) H(-y) - I_o \left(\frac{\Sigma_s \Delta x}{2\pi} \right) \tan^{-1} \left(\frac{y - v}{d_o} \right) \Bigg|_{-\infty}^{0} + I_o H(y)$$

$$= I_o\left\{ H(y) + (1-\Sigma_t\Delta x)H(-y) + \left(\frac{\Sigma_s\Delta x}{2}\right)\text{ftan}\left(\frac{y}{d_o}\right)\right\} \tag{A-37}$$

where H(y) is the Heaviside step function (83), and

$$\text{ftan}(y) = \frac{1}{2} - \frac{1}{\pi}\tan^{-1}(y). \tag{A-38}$$

For the first order model (n = 1), Δx now represents the finite slab width, corresponding to x^* of sections A.1, A.2 and A.3, consistent with the notation used in section 4.3 and the SEF is

$$SEF^{(1)}(y) = I_o\int_{-\infty}^{0} \exp[-\Sigma_t\Delta x]\,\delta_D(y-v) + \left(\frac{\Sigma_s}{2\pi}\right) I(y-v;d_o)\,dv$$

$$+ I_o\int_0^{\infty} \delta_D(y-v)\,dv \tag{A-39}$$

where

$$I(y-v;d_o) = \int_0^{\Delta x} \frac{\exp[-\Sigma_t x]}{(d_o-x)}\left[1+\left(\frac{y-v}{d_o-x}\right)^2\right]^{-1} dx. \tag{A-40}$$

The knife edge of section 4.4 is characterized by the attenuation product $\Sigma_t\,\Delta x = 0.05 << 1$. To an excellent approximation, the integrand in Eq. (A-40) can be replaced by its midpoint value, giving

$$I(y-v;d_o) \approx \left(\frac{\Delta x}{d_o - \frac{\Delta x}{2}}\right)\exp\left[\frac{-\Sigma_t\Delta x}{2}\right]\cdot\left[1+\left(\frac{y-v}{d_o-\frac{\Delta x}{2}}\right)^2\right]^{-1}. \tag{A-41}$$

As discussed in section 7.2, this approximation is equivalent to selecting the first term in the Taylor series expansion for the integrand in Eq. (A-40), centred on the midpoint of the integration range.

Substitution of Eq. (A-41) into Eq. (A-39) and subsequent evaluation results in

$$SEF^{(1)}(y) = I_o\left\{ H(y) + \exp[-\Sigma_t \Delta x]\, H(-y) + \left(\frac{\Sigma_s \Delta x}{2}\right)\right.$$

$$\left. \exp\left[\frac{-\Sigma_t \Delta x}{2}\right] \text{ftan}\left(\frac{y}{d_o - \frac{\Delta x}{2}}\right)\right\}. \qquad \text{(A-42)}$$

A.4.2 Infinite Slab Response

For traversal of the incident neutron beam through an infinite slab, as opposed to the knife edge of section A.4.1, the system input is

$$\text{INPUT}(y) = \begin{cases} I_o(1 - \Sigma_a \Delta x); & n = 0 \\ I_o \exp[-\Sigma_a \Delta x]; & n = 1 \end{cases} \qquad \text{(A-43)}$$

Proceeding directly to the first-order model ($n = 1$), the output response is here named the "scattering slab function" (SSF) and is given by the following reduction of Eq. (A-39):

$$SSF^{(1)}(y) = I_o \int_{-\infty}^{\infty} \left\{ \exp[-\Sigma_t \Delta x]\, \delta_D(y - v) + \left(\frac{\Sigma_s}{2\pi}\right) I(y - v) \right\} dv. \qquad \text{(A-44)}$$

Reversing the integration order over the integrand of I(y - v) enables a direct evaluation of the second term in Eq. (A-44). The result is

$$SSF^{(1)}(y) = I_o \left\{ \exp[-\Sigma_t \Delta x] + \left(\frac{\Sigma_s}{2\Sigma_t}\right)(1 - \exp[-\Sigma_t \Delta x]) \right\}$$

$$= \text{constant.} \qquad \text{(A-45)}$$

Here, the integration over the entire v range in Eq. (A-44) implies an SSF given by Eq. (A-45), regardless of the distribution model used for SLF, providing the SLF has a fixed total area. The physical interpretation of Eq. (A-45) is suggested in section 4.7.

A.5 Multiple Convolution in the Calculation of System Transfer Functions

The calculation of $TSLF_+^{(n)}(y, v)$, as defined in Eq. (4-31), and using the notation of section 4.5, is

$$TSLF_+^{(n)}(y,v) = SLF_+^{(n)}(y,v) * LSF(y)$$

$$= \int_{-\infty}^{\infty} \delta_D(u-v)\, LSF(y-u)\, du$$

$$= LSF(y-v). \qquad \text{(A-46)}$$

Equation (A-46) states that in the absence of object scattering, the total system transfer function is simply the screen-film LSF.

For neutrons incident on the solid portion of the slab,

$$TSLF_-^{(n)}(y,v) = SLF_-^{(n)}(y,v) * LSF(y), \qquad \text{(A-47)}$$

so that

$$TSLF_-^{(0)}(y,v) = \int_{-\infty}^{\infty} \left\{ (1-\Sigma_t\Delta x)\,\delta_D(u-v) + \left(\frac{\Sigma_s\Delta x}{2\pi d}\right)\left[1+\left(\frac{u-v}{d}\right)^2\right]^{-1} \right\} *$$

$$\left\{ \frac{LSF(y-u)}{(1-\Sigma_a\Delta x)} \right\} du \qquad \text{(A-48)}$$

and

$$TSLF_-^{(1)}(y,v) = \int_{-\infty}^{\infty} \left\{ \exp[-\Sigma_s\Delta x]\,\delta_D(u-v) + \frac{\Sigma_s \exp[\Sigma_n\Delta x]}{2\pi} I(u-v;d) \right\} *$$

$$\{LSF(y-u)\}du, \qquad \text{(A-49)}$$

where $I(u-v; d)$ is defined by Eq. (A-40).

As in section A.4, $I(u-v; d)$ is approximated using midpoint values, valid when $\Sigma_t\Delta x << 1$. The resulting facilitated integration enables Eqs. (A-48) and (A-49) to be written collectively as follows:

$$TSLF_-^{(n)}(y,v) = A^{(n)}(\Sigma_a\Delta x)\left\{ K^{(n)}(\Sigma_t\Delta x)\, LSF(y-v) + \left(\frac{s_n\Sigma_s\Delta x}{2\pi d_n}\right) F_-^{(n)}(y-v) \right\}. \qquad \text{(A-50)}$$

Here, the following additional functions and parameters have been defined:

$$A^{(n)}(\Sigma_a \Delta x) = \begin{cases} (1-\Sigma_a \Delta x)^{-1}; & n=0 \\ \exp[\Sigma_a \Delta x]; & n=1 \end{cases}, \tag{A-51}$$

$$K^{(n)}(\Sigma_t \Delta x) = \begin{cases} 1-\Sigma_t \Delta x; & n=0 \\ \exp[-\Sigma_t \Delta x]; & n=1 \end{cases}, \tag{A-52}$$

$$d_n = \begin{cases} d; & n=0 \\ d-\Delta x/2; & n=1 \end{cases}, \tag{A-53}$$

$$s_n = \exp[-n\Sigma_t \Delta x/2], \tag{A-54}$$

$$F^{(n)}(y-v) = f(y-v) * LSF(y), \tag{A-55}$$

$$f(y-v) = \left[1+\left(\frac{y-v}{d_n}\right)^2\right]^{-1}, \tag{A-56}$$

$$LSF(y) = \left(\frac{1}{n\,d_f}\right)\left[1+\left(\frac{y}{d_f}\right)^2\right]^{-1}. \tag{A-57}$$

The simplest way to evaluate $F^{(n)}(y - v)$ is to use Fourier transforms. Define the Fourier Transform of a function a(y) in the usual manner (70) by

$$F\{a(y)\} \Rightarrow \int_{-\infty}^{\infty} \exp[-2\pi i v_y y]\, a(y)\, dy$$

$$\stackrel{df}{=} \bar{a}(v_y). \tag{A-58}$$

Then

$$\bar{f}(v_y) = \int_{-\infty}^{\infty} \exp[-2\pi i v_y y]\left[1+\left(\frac{y}{d_n}\right)^2\right]^{-1} dy$$

$$= \pi d_n \exp[-2\pi i v_y d_n], \tag{A-59}$$

using integral tables (reference 118, #1.2.11). Similarly,

$$\overline{LSF}(v_y) = \exp[-2\pi v_y \bar{d}_f]. \tag{A-60}$$

Now

$$\overline{F_-^{(n)}}(v_y) = F\{f(y) * LSF(y)\}$$

$$= \bar{f}(v_y)\,\overline{LSF}(v_y) \tag{A-61}$$

by the Convolution Theorem (70). Combining Eqs. (A-59) to (A-61),

$$\overline{F_-^{(n)}}(v_y) = \pi d_n \exp[-2\pi v_y(d_n + \bar{d}_f)]. \tag{A-62}$$

This equation inverts immediately to

$$F_-^{(n)}(y-v) = \left(\frac{1}{\beta_n}\right)\left[1+\left(\frac{y-v}{d_n\beta_n}\right)^2\right]^{-1} \tag{A-63}$$

where β_n is the following dimensionless constant:

$$\beta_n = 1 + \bar{d}_f/d_n. \tag{A-64}$$

An interesting result here is that the convolution of two Lorentzian functions is itself a Lorentzian function.

The final function to be evaluated is TSEF(y), given in Eq. (4-34) as

$$TSEF^{(n)}(y) = I_-^{(n)}(y) * TSLF_-^{(n)}(y) + I_+^{(n)}(y) * TSLF_+^{(n)}(y) \tag{A-65}$$

where

$$I^{(n)}(y) = \begin{cases} I_o(1 - \Sigma_a \Delta x); & n = 0; y < 0 \\ I_o \exp[-\Sigma_a \Delta x]; & n = 1; y < 0 \\ I_o; & n = 0; \ y > 0 \end{cases} \tag{A-66}$$

Substitution of Eqs. (A-50) and (A-66) into Eq. (A-65) yields

$$TSEF^{(n)}(y) = I_o\left\{K^{(n)}(\Sigma_t \Delta x)\int_{-\infty}^{0} LSF(y-v)\,dv + \left(\frac{s_n \Sigma_s \Delta x}{2\pi d_n}\right)\int_{-\infty}^{0} F_-^{(n)}(y-v)\,dv\right.$$

$$\left. + \int_0^{\infty} LSF(y-v)\,dv\right\}, \tag{A-67}$$

which evaluates to

$$TSEF^{(n)}(y) = I_o\left\{ \frac{G_+^{(n)}(\Sigma_t \Delta x)}{2} + \frac{G_-^{(n)}(\Sigma_t \Delta x)}{\pi} \tan^{-1}(y/\bar{d}_f) \right.$$

$$\left. + \left(\frac{s_n \Sigma_s \Delta x}{2}\right) \text{ftan}\left(\frac{y}{d_n \beta_n}\right) \right\}. \qquad \text{(A-68)}$$

Several properties of the STF's developed in this section are now briefly discussed.

Firstly, and regarding the normalization of $TSLF_-^{(n)}$, the area under the curve is

$$AREA = \int_{-\infty}^{\infty} TSLF_-^{(n)}(y - v)\, dy$$

$$= A^{(n)}\left\{ K^{(n)} \int_{-\infty}^{\infty} LSF(y - v)\, dy + \left(\frac{s_n \Sigma_s \Delta x}{2\pi d_n}\right) \int_{-\infty}^{\infty} F_-^{(n)}(y - v)\, dy \right\}$$

$$= A^{(n)}\left\{ K^{(n)} + \frac{s_n \Sigma_s \Delta x}{2} \right\}, \qquad \text{(A-69)}$$

reducing to unity when $\Sigma_s = 0.0\ cm^{-1}$.

Secondly, the TSEF response corresponding to the knife edge is, from Eq. (A-68),

$$TSEF^{(n)}(0) = I_o\left\{ \frac{G_+^{(n)}}{2} + \left(\frac{s_n \Sigma_s \Delta x}{4}\right) \right\}. \qquad \text{(A-70)}$$

Evaluating the infinity TSEF responses, from Eq. (A-68),

$$TSEF^{(n)}(+\infty) = I_o, \qquad \text{(A-71)}$$

$$TSEF^{(n)}(-\infty) = I_o\left\{ K^{(n)} + \left(\frac{s_n \Sigma_s \Delta x}{2}\right) \right\}. \qquad \text{(A-72)}$$

A.6 Modulation Transfer Functions

As explained in section 4.6, the modulation transfer function (MTF) corresponding to each STF developed in sections 4.2 and 4.5 will simply be the optical transfer function (OTF), which is the Fourier Transform of that STF. This results from isotropy of the imaging system.

Corresponding to LSF (and thus $TSLF_+^{(n)}$) in Eq. (4-30) is the MTF

$$MTF(v_y) = \overline{LSF}(v_y)$$

$$= \exp[-2\pi v_y \bar{d}_f], \tag{A-73}$$

as given by Eq. (A-60).

For $SLF_-^{(n)}$, defined in Eq. (4-29), the corresponding MTF is

$$MTF^{(n)}(v_y) = A^{(n)} \int_{-\infty}^{\infty} K^{(n)} \delta_D(y-v) \exp[-2\pi i v_y (y-v)]\, d(y-v)$$

$$+ A^{(n)} \left(\frac{s_n \Sigma_s \Delta x}{2} \right) \left(\frac{1}{\pi d_n} \right) \int_{-\infty}^{\infty} \exp[-2\pi i v_y (y-v)] \left[1 + \left(\frac{y-v}{d_n} \right)^2 \right]^{-1} d(y-v)$$

$$= A^{(n)} \left[K^{(n)} + \left(\frac{s_n \Sigma_s \Delta x}{2} \right) \exp[-2\pi v_y d_n] \right] \tag{A-74}$$

using integral tables (reference 118, #1.2.11).

For $SPF^{(n)}$, defined in Eqs. (4-11) and (4-12), the corresponding MTF is

$$MTF^{(n)}(v_r) = 2\pi \int_0^{\infty} SPF^{(n)}(r)\, J_0(2\pi v_r r)\, r\, dr \tag{A-75}$$

where J_0 is the zeroth order Bessel function (117). Using integral tables (reference 118, #8.2.7), Eq. (A-75) evaluates as follows:

$$MTF(v_r) = 2\pi A^{(n)} \int_0^{\infty} K^{(n)} \frac{\delta_D(r)}{2\pi} J_0(2\pi v_r r)\, r\, dr$$

$$+ \frac{A^{(n)}}{\sqrt{2\pi v_r}} \left(\frac{s_n \Sigma_s \Delta x}{2} \right) d_n \int_0^{\infty} \sqrt{r} [d_n^2 + r^2]^{-3/2} J_0(2\pi v_r r) \sqrt{2\pi v_r r}\, dr$$

$$= A^{(n)}\left\{ K^{(n)} + \left(\frac{s_n \Sigma_s \Delta x}{2} \right) \exp[-2\pi v_r r d_n] \right\}. \quad \text{(A-76)}$$

For $TSLF_-^{(n)}$, note that

$$TSLF_-^{(n)}(y,v) = SLF_-^{(n)}(y,v) * LSF(y), \quad \text{(A-77)}$$

implying, by the Convolution Theorem, that

$$\overline{TSLF_-^{(n)}}(v_y) = \overline{SLF_-^{(n)}}(v_y) \cdot \overline{LSF}(v_y). \quad \text{(A-78)}$$

Thus, the MTF for $TSLF_-^{(n)}$ is simply the product of the MTF's for $SLF_-^{(n)}$ and LSF, given in Eqs. (A-73) and (A-74).

A.7 Emergent Scattered Ratio Estimate

Define the ratio of scattered to total neutron radiation emergent from a single slab plate with normally incident radiation of intensity I_o as

$$R_s = I_{scat,exit}/I_{tot,exit}$$

$$= I_{scat,exit}/(I_{scat,exit} + I_{coll,exit}). \quad \text{(A-79)}$$

Here, the subscripts "scat", "exit", "tot" and "coll" denote "scattered", "exiting", "total" and "collimated", and I is intensity. For a narrow plate of thickness Δx, secondary interactions – scattering or absorption of once-scattered neutrons – are negligible. Under this condition, and when the scattering is isotropic, precisely half of all scattered neutrons are emergent from each face of the plate. Thus,

$$I_{scat,exit} = I_{scat}/2, \quad \text{(A-80)}$$

where I_{scat} is the total scattered neutron intensity, given by

$$I_{scat} = \left(\frac{\Sigma_s}{\nu \Sigma_t} \right) (\text{total number of interactions})$$

$$= \left(\frac{\Sigma_s}{\Sigma_t} \right) (I_o - I_{coll,exit}), \quad \text{(A-81)}$$

and

$$I_{coll,exit} = I_0 \exp[-\Sigma_t \Delta x]. \tag{A-82}$$

Substituting Eqs. (A-80) to (A-82) into Eq. (A-79) and simplifying leads to

$$R_c = \left| 1 + 2 \left(\frac{\Sigma_t}{\Sigma_s} \right) \left(\frac{1}{\exp[\Sigma_t \Delta x] - 1} \right) \right|^{-1} \tag{A-83}$$

A.8 Coordinate Transformation of Integral Transport Equation

In rectangular coordinates, the integral transport equation of section 2.2, obtained by substituting Eqs. (2-15), (2-20) into Eq. (2-19) is

$$I(w) = I^*(w) + \Sigma_s \int_0^{w^*} \int_{-\infty}^{\infty} \int_{-\infty}^{\infty} \frac{I(t) \exp[-\Sigma_t [(r-u)^2 + (s-v)^2 + (t-w)^2]^{1/2}]}{4\pi [(r-u)^2 + (s-v)^2 + (t-w)^2]} \, d(r-u)\, d(s-v)\, dt, \tag{A-84}$$

valid for $w \in [0, w^*]$.

Substitution of the spherical polar coordinates defined implicitly in Eq. (2-21) and illustrated in Fig. 2.1 into Eq. (A-84) results in

$$I(w) = I^*(w) + \frac{\Sigma_s}{4\pi} \int_0^{2\pi} \int_0^{\pi} \int_0^{\text{Boundary}(\theta)} \frac{I(w + \rho \cos(\theta)) \exp[-\Sigma_t \rho]}{\rho^2} \rho^2 \sin(\theta) \, d\rho \, d\theta \, d\phi, \tag{A-85}$$

where the upper limit boundary function is found from a geometrical construction to be

$$\text{Boundary}(\theta) = \begin{cases} (w^* - w)/\cos(\theta), & \theta \in (0, \pi/2) \\ -w/\cos(\theta), & \theta \in (\pi/2, \pi) \end{cases} \tag{A-86}$$

Defining $\mu = \cos(\theta)$ and substituting Eq. (A-86) into Eq. (A-85) yields, after evaluation of the outer integral,

$$I(w) = I^*(w) + \left(\frac{\Sigma_s}{2} \right) \int_0^{2\pi} \int_0^{1} \int_0^{(w^* - w)/\mu} I(w + \rho\mu) \exp[-\Sigma_t \rho] \, d\rho \, d\mu$$

$$+\int_{-1}^{0}\int_{0}^{-w/\mu} I(w+\rho\mu)\exp[-\Sigma_t\rho]\,d\rho\,d\mu\Bigg]. \qquad \text{(A-87)}$$

Substitution for $I^*(w)$ from Eq. (2-14), and subscripting $I(w)$ to $I_{in}(w)$ to denote evaluation at a point inside the slab, then reduces Eq. (A-87) to Eq. (2-22), completing the transformation.

For points outside the slab, $w > w^*$, the upper and lower boundaries for integration over ρ become $-w/\mu$ and $(w^* - w)/\mu$ respectively. Also, the transport kernel given in Eq. (2-15) becomes, in rectangular coordinates,

$$K(r-u, s-v, t, w) = \frac{\exp\left[-\Sigma_t[(r-u)^2+(s-v)^2+(t-w)^2]^{1/2}\left(\frac{w^*-t}{w-t}\right)\right]}{4\pi[(r-u)^2+(s-v)^2+(t-w)^2]}. \qquad \text{(A-88)}$$

Conversion to spherical polar coordinates results in

$$K(\rho, \mu, \phi) = \exp\left[\frac{\Sigma_t}{\mu}(w^*-w-\rho\mu)\right]. \qquad \text{(A-89)}$$

This kernel, along with the above integration boundaries, generates Eq. (2-23) in the same manner that Eq. (2-22) was derived.

APPENDIX B

SCANNING MICRODENSITOMETER WINDOW DIMENSIONS

The optical density traces given in Chapter 6 were obtained using a scanning microdensitometer depicted schematically in Fig. 6.3. This measurement system is based on the property that the transmission optical density of an infinitesimal area element, dA, on a radiographic negative is logarithmically inversely proportional to the radiant flux transmitted through that area as expressed in Eq. (1-4). In practice, light transmitted through a window of controllably finite size and geometry provides the measurement. This finite window area effects a smoothing of the desired optical density variation through the integration of the densities for all the elemental areas that constitute the window at any point in time. The accuracy provided by narrowing the beam window is offset by the commensurate increase in the relative magnitude of the noise component, generated primarily by granularity in the radiograph. The task of the analyst is thus to select window dimensions that will generate a sufficiently accurate scan while admitting an acceptably low noise component. In this appendix we examine the effects on the output signal of a finite beam window and attempt to prescribe an upper bound on the window dimensions for scans taken across knife edge images.

For knife edge images, the beam window geometry should clearly be rectangular, as shown in Fig. B.1. The window height, ϵ, should be as large as possible within the assumption that the image possesses no general optical density variation in the y direction. This has the effect of minimizing the noise component while not integrating the signal information. For edge scans in which the image possesses a monotonic y variation, the analyst must reduce the window height accordingly. That problem is not addressed here,

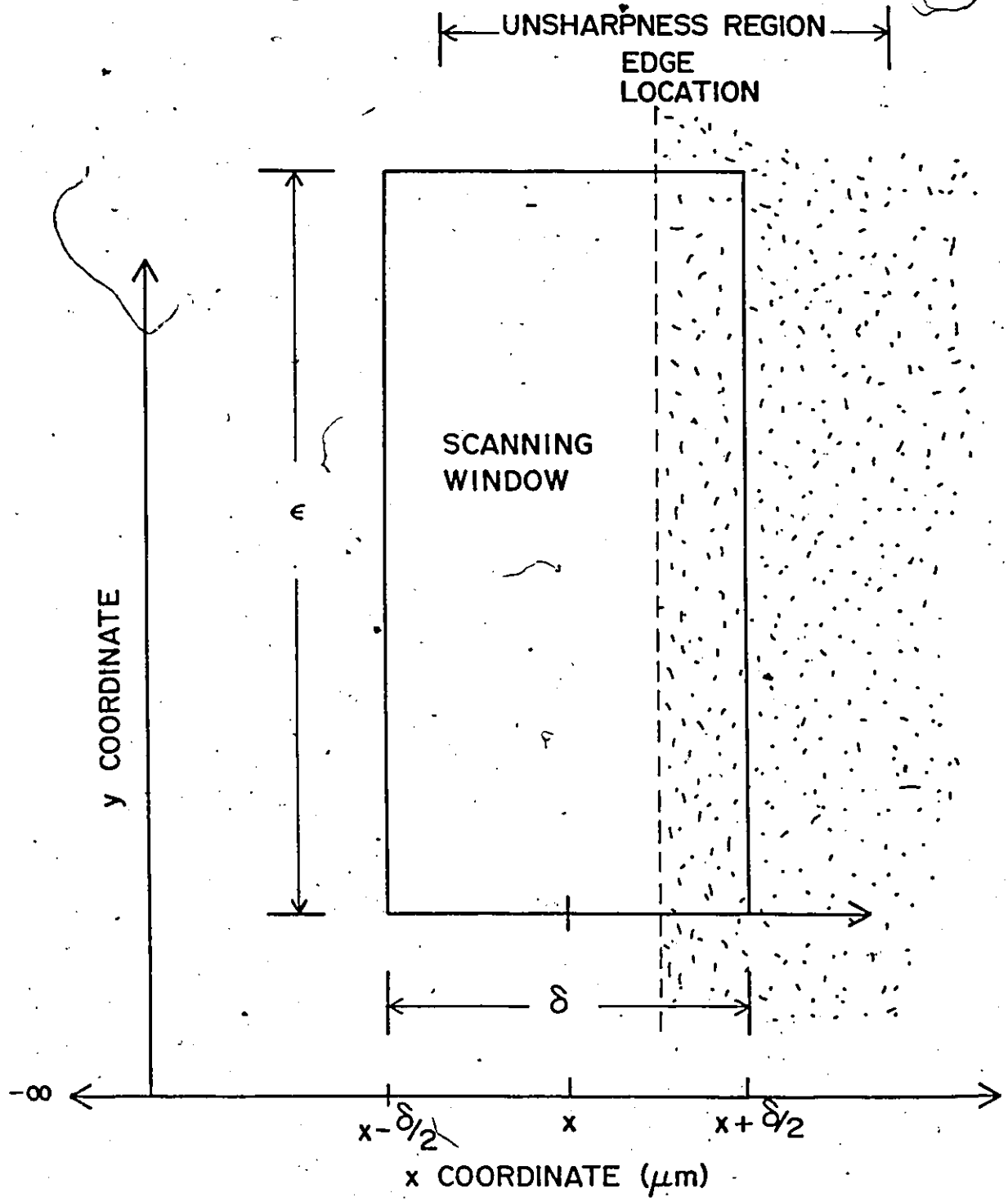

Fig.-B.1: Finite area scanning window moving with speed v across a knife edge image, illustrating notational features.

except to note that it applies, for example, to scans taken across the image of a square slab edge and near a corner image. Such scans are found in Fig. 6.13.

The process of beam width selection has previously been examined (119) with specific reference to scans across neutron radiographic knife edge images. Guidelines in setting the window width were established assuming the sensitivity parameter of interest to be the gradient of the optical density at the knife edge. In this work, the beam window setting is analyzed with respect to the extent of incurred degradation of the actual optical density variation.

The microdensitometer beam window has width δ, as shown in Fig. B.1. It traverses the knife edge image from left to right or, equivalently, from low to high optical density with constant speed v. The actual optical density variation across the edge is represented generally here by the following one-parameter family of "edge spread" functions:

$$D(x;C) = D_{high}\left(\frac{1}{2} + \frac{1}{\pi}\tan^{-1}(x\sqrt{C})\right) + D_{fog} \qquad \text{(B-1)}$$

The shape of D(x;C) is illustrated in Fig. B.2. The background fog density is D_{fog}, upon which rests a density variation between values of zero and D_{high}. This density variation is obtained through convolution of the knife edge step attenuation function with a Lorentzian radiographic system LSF and has been found in good agreement with experiment for non-scattering materials (105). The Lorentzian LSF was derived for screen-film unsharpness in section A.1. It suffices here to say that the parameter C characterizes the extent of image degradation incurred by the recording system.

Note that D(x;C) in Eq. (B-1) is valid for nonscattering materials but fails to represent the scattering based edge distortions (SBED's) discussed in Chapters 4, 5 and 6. However, these SBED's appear on a much larger scale than the region over which the main knife edge variation occurs as shown clearly in Fig. 6.10. If the window width δ is to be set

sufficiently small that this main variation is accurately traced, then errors in the SBED traces should be negligible. This justifies the usage of Eq. (B-1) as an edge spread function (ESF).

The scanning system output response is proportional to the optical density integrated over the patch of film viewed through the beam window. Assuming linearity of the scanning system, this is represented mathematically as follows:

$$O_\delta(x;C) = K \in \int_{x-\delta/2}^{x+\delta/2} D(x';C)\,dx' . \tag{B-2}$$

Here, the proportionality constant K accounts for the scanning system conversion from optical density to an output trace. Among other parameters, K is proportional to the stage speed, v.

In order to compare the various output shapes arising from a single optical density variation, it is necessary to normalize each output to some arbitrarily set, but constant range. This can be accomplished here by subtracting the integrated background fog response from each output and then normalizing the remaining response to a maximum of unity. The resulting output response shape is therefore

$$g_\delta(x;C) = \gamma[O_\delta(x;C) - K \in \delta D_{fog}] \tag{B-3}$$

where the normalization constant γ is chosen so that

$$g_\delta(\infty;C) = 1 . \tag{B-4}$$

Substitution of Eqs. (B-1) and (B-2), (B-3) evaluated at $x = \infty$ into Eq. (B-4) results in

$$\gamma = [K \in \delta D_{high}]^{-1} . \tag{B-5}$$

Substitution of Eqs. (B-1) and (B-2), (B-5), into Eq. (B-3) then results in

$$g_\delta(x;C) = \frac{1}{\delta} \int_{x-\delta/2}^{x+\delta/2} \left| \frac{1}{2} + \frac{1}{\pi} \tan^{-1}(x'\sqrt{C}) \right| . dx' . \tag{B-6}$$

The scanning densitometer output response shape is obtained through the evaluation of Eq. (B-6), and is given in the following comparative dimensionless form:

$$g_d(u) = \frac{1}{2} + \frac{1}{\pi} \tan^{-1}(p_d(u)). \tag{B-7}$$

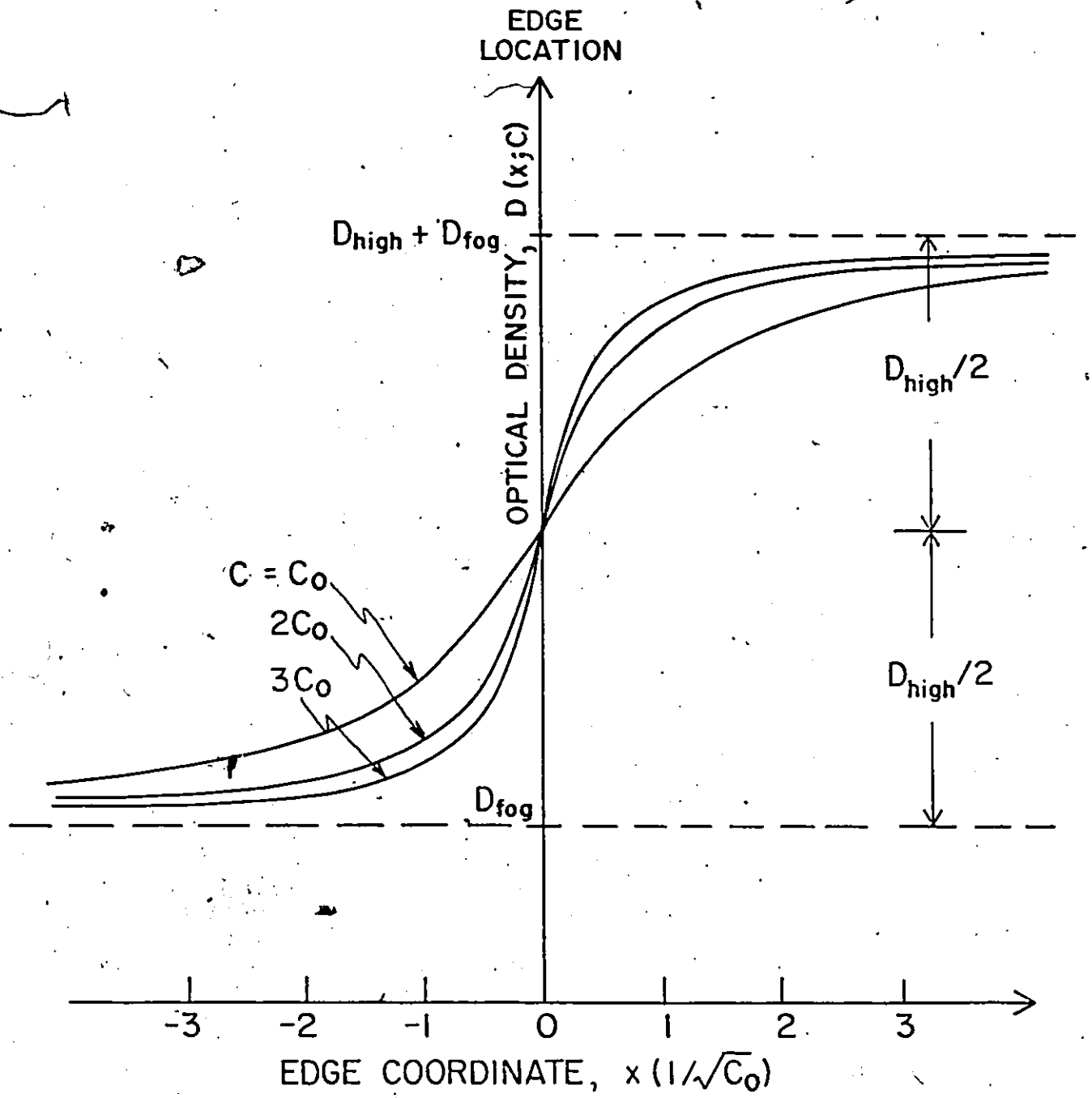

Fig. B.2: Edge spread function used in analysis of integration effect of finite area scanning window. C_0 is some particular value of the Lorentzian degradation parameter and

$$D(x;C) = D_{high}\left(\frac{1}{2} + \frac{1}{\pi}\tan^{-1}(x\sqrt{C})\right) + D_{fog}.$$

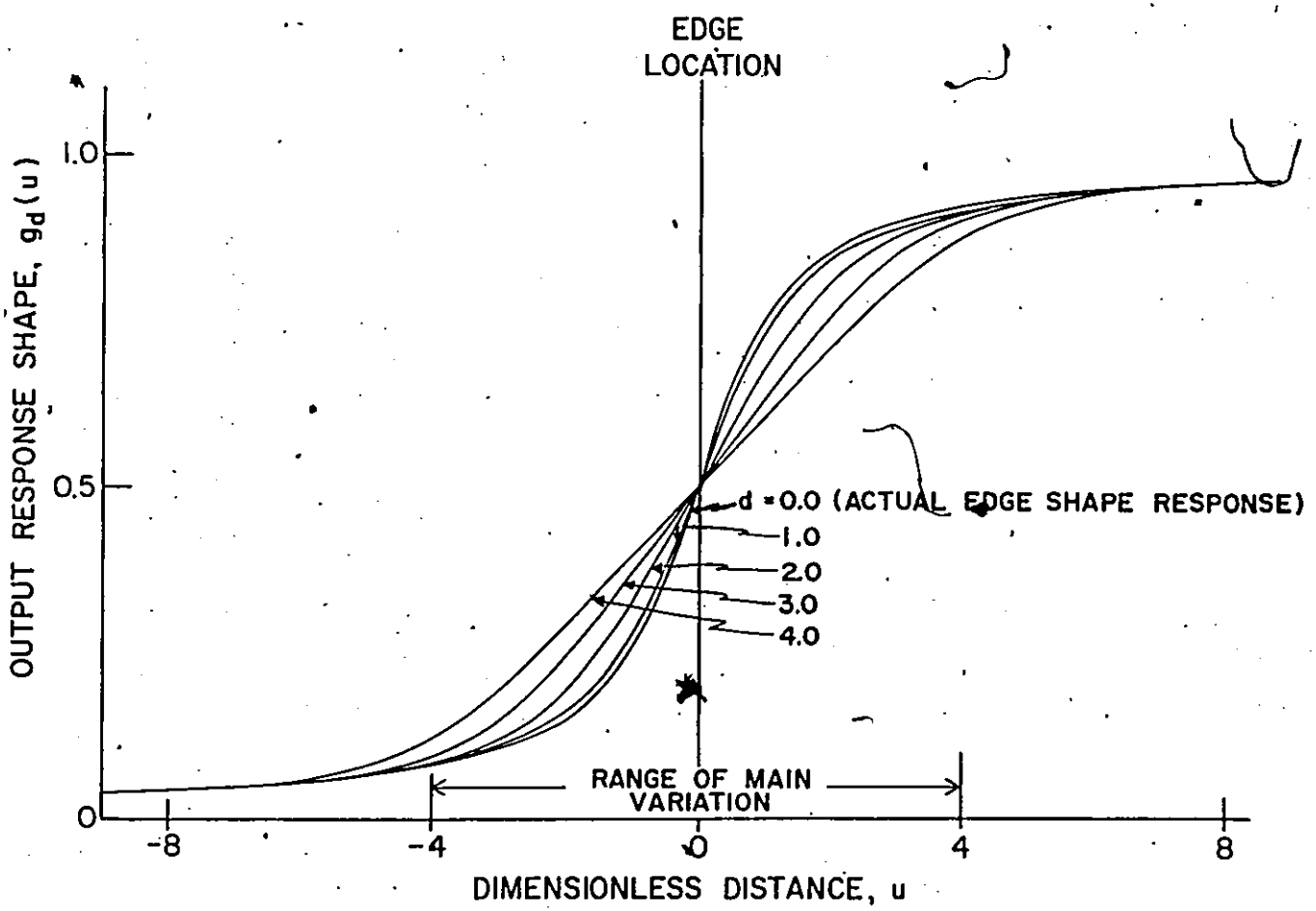

Fig. B.3: Output response shape illustrating potential for miscalculation of actual edge optical density variation.

Here, the dimensionless distance variable is

$$u = x\sqrt{C}, \tag{B-8}$$

the dimensionless window half-width is

$$d = (\delta/2)\sqrt{C}, \tag{B-9}$$

and

$$p_d(u) = \tan\left\{ \frac{(u+d)\tan^{-1}(u+d) - (u-d)\tan^{-1}(u-d) - \frac{1}{2}\log\left[\frac{1+(u+d)^2}{1-(u+d)^2}\right]}{2d} \right\}. \tag{B-10}$$

Figure B.3 depicts $g_d(u)$ over the range of dimensionless beam widths $0.0 \leq d \leq 4.0$. Notice that $g_{0.0}(u)$ possesses the shape of the original ESF in Eq. (B-1). Specifically,

$$g_{0.0}(u) = \frac{1}{2} + \frac{1}{\pi}\tan^{-1}(u). \tag{B-11}$$

As expected, widening the beam window serves to degrade the output response. Figure B.3 also suggests a potential error that can occur in interpretation of the edge scan output. If this response is supposed to represent the actual optical density variation, Eq. (B-1), and the analyst wishes to estimate the imaging system spreading coefficient C from the resulting edge scan, he may greatly underestimate C if the window is too wide. This is because each of the curves in Fig. B.3 can be well approximated by the form

$$g_d(u) = \frac{1}{2} + \frac{1}{\pi}\tan^{-1}(\alpha u) \tag{B-12}$$

for some positive value of α less than unity. As d approaches zero, α approaches unity.

Based on an overall and qualitative visual comparison, the interpretation that $g_d(u)$ accurately represents the shape of the optical density variation, D(x;C), should incur an acceptably small error when the positive dimensionless half-width parameter lies in the range

$$d \leq 1.0. \tag{B-13}$$

For typical neutron radiographic values of $C = 1.0 * 10^{-3}\ \mu m^{-2}$ and $5.0 * 10^{-3}\ \mu m^{-2}$, Eq. (B-13) implies beam window widths of $\delta \leq 63\ \mu m$ and $\delta \leq 28\ \mu m$, respectively. These upper bounds compare favorably with the observation (119) that in practice, window widths of 25 μm generally yield results accurate to better than 10% if the sensitivity parameter of interest is the gradient of the optical density variation at the edge location.

It is useful to calculate an upper bound for δ without first having to calculate the imaging system parameter C. From Fig. B.3, it is evident that the main variation in the edge response will usually occur over a range of the dimensionless distance parameter, u, that is smaller than eight. Denoting this range by u_r, and the corresponding main variation range in the edge scan output by x_r, Eq. (B-8) relates u_r and x_r by

$$u_r = x_r \sqrt{C}. \tag{B-14}$$

Since $u_r \leq 8$, x_r values estimated by the analyst will overestimate the value of C if they are calculated using Eq. (B-14) with $u_r = 8$. This overestimated C value, when substituted into Eqs. (B-9) and (B-10), yields the following underestimated window width:

$$\delta \leq \frac{x_r}{4}. \tag{B-15}$$

Thus, an acceptably small integration error should be incurred in the optical density trace if the beam window width is set to less than one quarter of the range containing the main edge variation. From Fig. B.3, this range is well defined as the distance over which the trace is approximately linear.

For all scans included in Chapter 6, x_r is at least 300 μm. The selected beam window width of $\delta = 30\ \mu m$ easily falls within the range specified by Eq. (B-15).

The possibility of numerically reconstructing the actual optical density variation, D(x), given the output trace, $O_\delta(x)$, the background fog density, D_{fog}, and the window width, δ, is now examined. The only assumption to be made regarding the functional form of D(x) is the obvious boundary condition that $D(-\infty) = D_{fog}$. In this general case, Eq. (B-2) is written as

$$O_\delta(x) = K \epsilon \int_{x-\delta/2}^{x+\delta/2} D(x')\,dx'$$

$$= \frac{O_\delta(-\infty)}{\delta D_{fog}} \int_{x-\delta/2}^{x+\delta/2} D(x')\,dx' . \qquad \text{(B-16)}$$

Differentiating Eq. (B-16) yields, using Leibnitz' Rule,

$$\frac{dO_\delta(x)}{dx} = \frac{O_\delta(-\infty)}{\delta D_{fog}} [D(x+\delta/2) - D(x-\delta/2)]. \qquad \text{(B-17)}$$

Equation (B-17) can be arranged to

$$D(x+\delta/2) = D(x-\delta/2) + \left(\frac{\delta D_{fog}}{O_\delta(-\infty)}\right)\frac{dO_\delta(x)}{dx_{x_o}} . \qquad \text{(B-18)}$$

For a particular value of x_o, Eq. (B-18) describes the calculation procedure for $D(x_o + \delta/2)$ given a previous value for $D(x_o - \delta/2)$ and the local slope of the trace, $(dO_\delta/dx)_{x=x_o}$. The iterative calculational algorithm suggested by Eq. (B-18) is obvious. Starting with the following representation of $D(-\infty)$:

$$D(x_{left}) \approx D(-\infty)$$
$$= D_{fog}, \qquad \text{(B-19)}$$

one proceeds to calculate $D(x_{left} + \delta/2)$, then $D(x_{left} + 3\delta/2)$, and so on.

However, the error incurred by estimation of the slope at a given point has been found to magnify through propagation, even when the optical density trace was artificially smoothened and the slope was accurately estimated. In retrospect, this instability is expected given the finite value of δ. At present, this numerical reconstructive procedure therefore appears to be limited.

It would be desirable to develop some other useful reconstructive procedure for the purpose of checking the similarity of $O_\delta(x)$ and $D(x)$.

APPENDIX C

TWO DIMENSIONAL RADIOGRAPHIC IMAGING ANALYSIS

C.1 Introduction

The application of industrial radiography to the precise location of interface boundaries and "thin" inclusions is limited by image blurring or "unsharpness". While several researchers have analytically addressed this problem (52, 94, 100-102, 120-122) for the precise determination of edges in neutron radiographic applications such as nuclear fuel pin dimensioning, the general question of the optical density which corresponds to an edge in a blurred radiograph remains unresolved.

Qualitatively, the edge optical density is expected to exhibit dependence on (a) the geometrical and material attenuation properties of the object being radiographed, (b) the characteristic curve of the film emulsion describing the optical density generated in the film by a given exposure, and (c) the radiographic system transfer function that is responsible for the observed blurring.

As discussed in section 1.3, the mathematical tools of transfer function imaging analysis are the point spread function, line spread function and modulation transfer functions. In this appendix, it is shown that if the system point spread function (PSF) possesses rotational symmetry and shift invariance, then the optical density corresponding to "infinite" knife edges, and also to the two- dimensional corner formed by the superposition of such edges, is completely independent of the system PSF. This enables the identification of such corners and edges on neutron radiographs without image enhancement techniques. These results are directly applicable specializations of a more general mathematical result. The neutron radiographic analysis constituting this appendix can be found in the literature

(115). It is clear that with minor interpretational changes of several symbols, the results here are also applicable to x-ray radiographic imaging.

If the PSF is rotationally symmetric, the system is said to be "isotropic". In general, isotropy can be expected for screen-film systems (65) and examples of isotropic PSF analysis frequent the literature (38, 39, 68, 123). Further, shift invariance or "isoplanatism" is often not fulfilled in the entire image plane. In such cases, the image plane can be decomposed into isoplanatic "patches" over each of which the isoplanatism assumption is valid (99).

C.2 Image-Forming Response to Objects of Radially Constant Attenuation

Defining (u,v) as a Cartesian coordinate system in the object plane and (x,y) as the same system in the image plane, the exposure distribution, S(x,y), in the image plane is the convolution of the attenuated incident radiation intensity distribution, I(u,v), and the system PSF $R_{PT}(x,y,u,v)$:

$$S(x,y) = N \int_{-\infty}^{+\infty} \int_{-\infty}^{+\infty} I(u,v)\, R_{PT}(x,y,u,v)\, du\, dv . \qquad (C\text{-}1)$$

Here, the positive constant N has been introduced to accommodate the possible intensification or conversion of the information carrying radiation, and the general interpretation of "convolution", described in section 4.5, is understood.

Also, R_{PT} is the overall system PSF which, in the general case of interest, includes screen-film and geometric unsharpness effects. This PSF represents the radiation intensity at (x,y) due to a unit point source of radiation at (u,v) and is normalized to integrate to unity over the x-y plane. The effects of radiographic noise are assumed negligible.

In general, the PSF can be specified to arbitrary accuracy by a series expansion in orthogonal functions (67). Based on the PSF, or its one-dimensional analog, the line spread

function (LSF), a single parameter indicator of total radiographic unsharpness can be defined (48,49).

For an isoplanatic system,

$$R_{PT} = R_{PT}(x-u, y-v). \tag{C-2}$$

If isotropy is also valid, then, as discussed in section 2.1,

$$R_{PT} = R_{PT}((x-u)^2 + (y-v)^2). \tag{C-3}$$

Defining (r,θ) and (r',θ') as the polar coordinates corresponding to (x,y) and (u,v), respectively, an isoplanatic and isotropic system has

$$R_{PT} = R_{PT}(r^2 + r'^2 - 2rr'\cos(\theta-\theta')). \tag{C-4}$$

In this case, Eq. (C-1) can be written in polar coordinates as follows:

$$S(r,\theta) = N\int_0^{2\pi}\int_0^{\infty} I(r',\theta')\,R_{PT}(r^2+r'^2-2rr'\cos(\theta-\theta'))\,r'\,dr'\,d\theta'. \tag{C-5}$$

At the origin, the exposure is

$$S_o = \lim_{r\to 0} S(r,\theta)$$

$$= N\int_0^{2\pi}\int_0^{\infty} I(r',\theta')\,R_{PT}(r'^2)\,r'\,dr'\,d\theta' \tag{C-6}$$

where the latter equality follows from continuity of the integrand.

The differentially attenuated intensity $I(r',\theta')$ is given by

$$I(r',\theta') = I_o \exp\left[-\int_0^{z_w(r',\theta')} \Sigma_t(r',\theta',z)dz\right] \tag{C-7}$$

where z is the direction orthogonal to the object plane, $z_w(r',\theta')$ is the object depth at (r',θ'), $\Sigma_t(r',\theta',z)$ is the spatially variable total macroscopic absorption cross-section and I_o is the incident neutron intensity. Exponential attenuation is the relevant transport process; scattering of neutrons in the object is initially assumed negligible.

For the special case in which the dimensionless attenuation parameter, defined by

$$\alpha(r',\theta') = \int_0^{z_w(r',\theta')} \Sigma_t(r',\theta',z)dz \tag{C-8}$$

is angularly variable but radially constant, $\alpha = \alpha(\theta')$ so that Eq. (C-6) reduces to

$$S_o = N \int_0^{2\pi} I(\theta') \int_0^{\infty} R_{PT}(r'^2)\, r'\, dr'\, d\theta'$$

$$= \left(N \int_0^{2\pi} I(\theta')\, d\theta' \right) \left(\int_0^{\infty} R_{PT}(r^2)\, r dr \right)$$

$$= \frac{N}{2\pi} \int_0^{2\pi} I(\theta')\, d\theta'$$

$$= N\bar{I}. \qquad \text{(C-9)}$$

Here, $\bar{I}$ is the average value of $I(\theta')$. The variable change from r' to r enables evaluation and is justified since r and r' assume mathematically identical roles in R_{PT}.

The condition implied by the radial constancy of α is an idealization since it implies a discontinuity in $I(0,\theta')$ for all but the simplest of cases in which I is everywhere constant. The value of $I(0,\theta')$ must therefore be assigned the average value $\bar{I}$. Note that S_o in Eq. (C-9) is completely independent of the system PSF and is determined strictly by the attenuation properties of the radiographed object. Stated differently, under the above conditions, the imaging system images the origin exactly.

Furthermore, it is clear from Eq. (C-9) that the above imaging property is also valid for any object that scatters neutrons providing the object possesses radially constant attenuation properties and the overall system PSF is isotropic. Since, as discussed in section 4.5, the overall system PSF in high resolution neutron radiography is the convolution of the screen-film unsharpness PSF with the scattering point function (SPF), the isotropy condition reduces to requiring isotropy of both the SPF and the PSF.

C.3 Prospective Applications

While the condition that $\alpha = q(\theta')$ is restrictive, the PSF independence implied by Eq. (C-9) has potential application in the precise location of edge boundaries in blurred radiographs. As previously mentioned, the problem of determining which optical density should correspond to an "infinite" knife edge in a blurred radiograph has received much attention.

This edge location problem is here generalized to the determination of the optical density corresponding to the corner of an absorbing "ϕ-wedge" in a radiograph. The infinite knife-edged slab is considered as a special case. With no loss in generality, the wedge is placed with its corner at the origin of the polar coordinate system defining the object plane, as illustrated in Fig. C.1. In this case,

$$I(r',\theta') = \begin{cases} I_o, \theta' \in (\phi_1, \phi_2) \\ I_o \exp[-\Sigma_{tw} z_w], \theta' \in (\phi_2, 2\pi + \phi_1) \end{cases} \tag{C-10}$$

where Σ_{tw} and z_w are, respectively, the constant absorption cross-section and thickness of the solid portion of the wedge.

Since the condition of radially constant attenuation is met here, the resulting corner exposure follows from Eq. (C-9) and is

$$S_o = NI_o\left[\left(\frac{\Phi_2 - \Phi_1}{2\pi}\right)(1 - \exp[-\alpha_w]) + \exp[-\alpha_w]\right] \tag{C-11}$$

where the dimensionless wedge attenuation parameter is $\alpha_w = \Sigma_{tw} z_w$.

Conversion of this exposure to an optical density is accomplished through the H-D curve (3), taken here to be the characteristic curve in which optical density, D, is plotted against the logarithm of exposure, log (S).

In the general case, the film emulsion gradient

$$\gamma(S) = \frac{dD(S)}{d\log(S)} \tag{C-12}$$

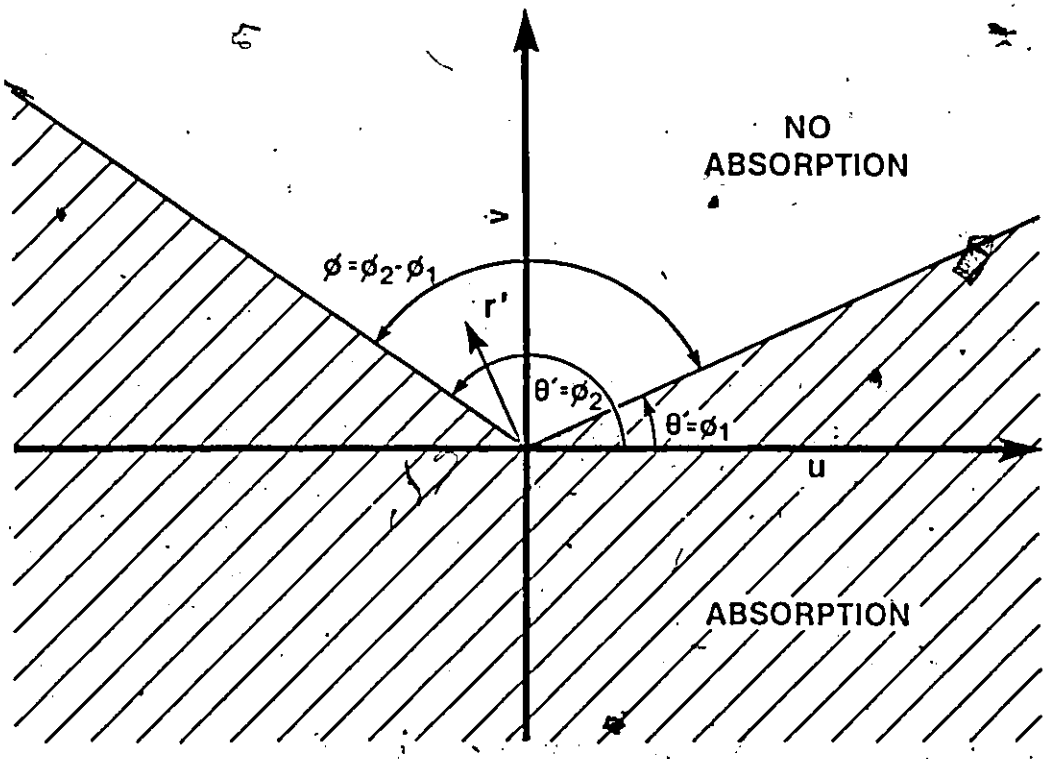

Fig. C.1: Planar view of ϕ-wedge geometry.

Incident neutrons are impingent on the page.

gives the slope of the characteristic curve at any exposure S. For example, if exposures are in the log-linear range of the film, then

$$\Delta D = \gamma\, \Delta(\log S) \tag{C-13}$$

where the proportionality constant γ is referred to as the "gamma". In this case, the optical density at the corner can be written as

$$D_o = D_{max} + \gamma \log\left[\left(\frac{\Phi_2 - \Phi_1}{2\pi}\right)(1 - \exp[-\alpha_w]) + \exp[-\alpha_w]\right]. \tag{C-14}$$

Here, D_{max} is the measured maximum optical density minus the background fog component and corresponds to the fully unattenuated exposure NI_o.

Given a priori knowledge of the material and geometric characteristics of the wedge, the important implication of Eq. (C-14) is that the location of the wedge corner can be determined on a highly blurred radiograph by locating a particular point with optical density D_o. This requires no elevation of the system PSF and no contrast enhancement techniques; the only requirements are local isotropy and isoplanatism.

Note that the location of the wedge corner is facilitated if D_o is an isolated value. Mathematically, isolation occurs if, for any radial axis r extending from the corner along an angle θ, $\partial D/\partial r \neq 0$ at $r = 0$.

Using the chain rule of differentiation we get

$$\frac{\partial D}{\partial r} = \frac{dD}{dS(r,\theta)}\,\frac{\partial S}{\partial r}$$

$$= \frac{\gamma(S)}{S}\,\frac{\partial S}{\partial r} \tag{C-15}$$

where we are also invoking the general definition of $\gamma(S)$, Eq. (C-12). Now $S > 0$ and in the desired absence of solarization (3) $\gamma(S) > 0$. Thus, to show that $\partial D/\partial r|_{r=0} \neq 0$, it suffices to show $\partial S/\partial r|_{r=0} \neq 0$.

From Eq. (C-5) and for the ϕ-wedge,

$$\left.\frac{\partial S}{\partial r}\right|_{r=0} = N\int_{\phi_1}^{\phi_2}\int_0^{\infty} I_o \frac{\partial R_{PT}(r^2+ r'^2- 2rr'\cos(\theta-\theta'))}{\partial r} r'\,dr'\,d\theta'$$

$$+ N\int_{\phi_2}^{2\pi+\phi_1}\int_0^{\infty} I_o \exp[-a_w] \frac{\partial R_{PT}(r^2+ r'^2- 2rr'\cos(\theta-\theta'))}{\partial r} r'\,dr'\,d\theta'$$

$$= T_1 + T_2, \text{ say,} \qquad \text{(C-16)}$$

where Leibnitz' rule of differentiation across integral signs has been applied. Defining $R^2 = r^2 + r'^2 - 2rr'\cos(\theta-\theta')$, T_1 can be evaluated using the chain rule as follows:

$$T_1 = NI_o\int_{\phi_1}^{\phi_2}\int_0^{\infty} \left.\frac{dR_{PT}(R^2)}{d(R^2)}\right|_{r=0} \left.\frac{\partial(R^2)}{\partial r}\right|_{r=0} r'\,dr'\,d\theta'$$

$$= -2NI_o\int_{\phi_1}^{\phi_2}\left(\int_0^{\infty}\frac{dR_{PT}(r'^2)}{d(r'^2)} r'^2\,dr'\right)\cos(\theta-\theta')\,d\theta'$$

$$= 2\beta^2 NI_o(\sin[\theta-\phi_1]- \sin[\theta-\phi_2]) \qquad \text{(C-17)}$$

Here, the positive constant β^2 is defined by

$$\beta^2 = -\int_0^{\infty}\frac{dR_{PT}(r'^2)}{d(r'^2)} r'^2\,dr'$$

$$= -\int_0^{\infty}\frac{dR_{PT}(r^2)}{d(r^2)} r^2 dr \qquad \text{(C-18)}$$

using the same variable substitution as employed in deriving Eq. (C-9), and is positive since for a realistic isotropic PSF, $R_{PT}(r^2)$ is maximum at $r = 0$ and decreases monotonically with r.

Further, T_2 is similarly evaluated so that

$$\left.\frac{\partial S}{\partial r}\right|_{r=0} = 2\beta^2 NI_o(\sin[\theta-\phi_1]- \sin[\theta-\phi_2])(1-\exp[-a_w]). \qquad \text{(C-19)}$$

It can be shown from Eq. (C-19) that for non-identical angles ϕ_1 and ϕ_2, $\partial S/\partial r|_{r=0}$ vanishes for axes with directions along the particular angles specified by the general formula

$$\theta_p = (2n-1)\frac{\pi}{2} + \left(\frac{\phi_1 + \phi_2}{2}\right), \quad n \in Z. \tag{C-20}$$

We define here "acute" and "obtuse" wedges as being characterized by wedge angles of $\phi < \pi$ and $\phi \geq \pi$, respectively.

For acute wedges, the two θ_p axes lead from the corner into the solid sector of the wedge. For axes with directions leading into the solid sector of the wedge and between these two angles, $\partial S/\partial r|_{r=0} < 0$. All other axes, including those with directions leading into the solid sector of the wedge but not between the two θ_p angles, have $\partial S/\partial r|_{r=0} > 0$. Since these latter axes must also have the property that

$$\lim_{r\to\infty} S(r,\theta) = NI_0 \exp[-a_w] < S_0, \tag{C-21}$$

it follows that along each such axis, the corner exposure value S_0 also occurs for some point separated from the corner. The locus of these points defines the contour in which $S = S_0$ so that the value S_0, and hence the corresponding density D_0, are not isolated.

This and other exposure contours are illustrated in Fig. C.2 for a ϕ-wedge in which $\phi = \pi/4$. The contours were calculated using the FORTRAN program CALCUL, listed in Appendix D. The attenuation parameter a_w has been taken as infinity, such as applies, for instance, to the gadolinium absorption of neutrons. From Eq. (C-11), the corner exposure is then $S_0 = NI_0/8$. The PSF

$$R_{PT}(r,\theta,r',\theta') = \{1 + C[r^2 + r'^2 - 2rr'\cos(\theta - \theta')]\}^{-3/2} \tag{C-22}$$

was used to calculate the contours; the dispersion coefficient C determines the magnitude of point spreading. This compact PSF corresponds to the Lorentzian LSF (94) and also to the modulation transfer function (71)

$$MTF(\omega) = \exp[-\omega/\omega_c] \tag{C-23}$$

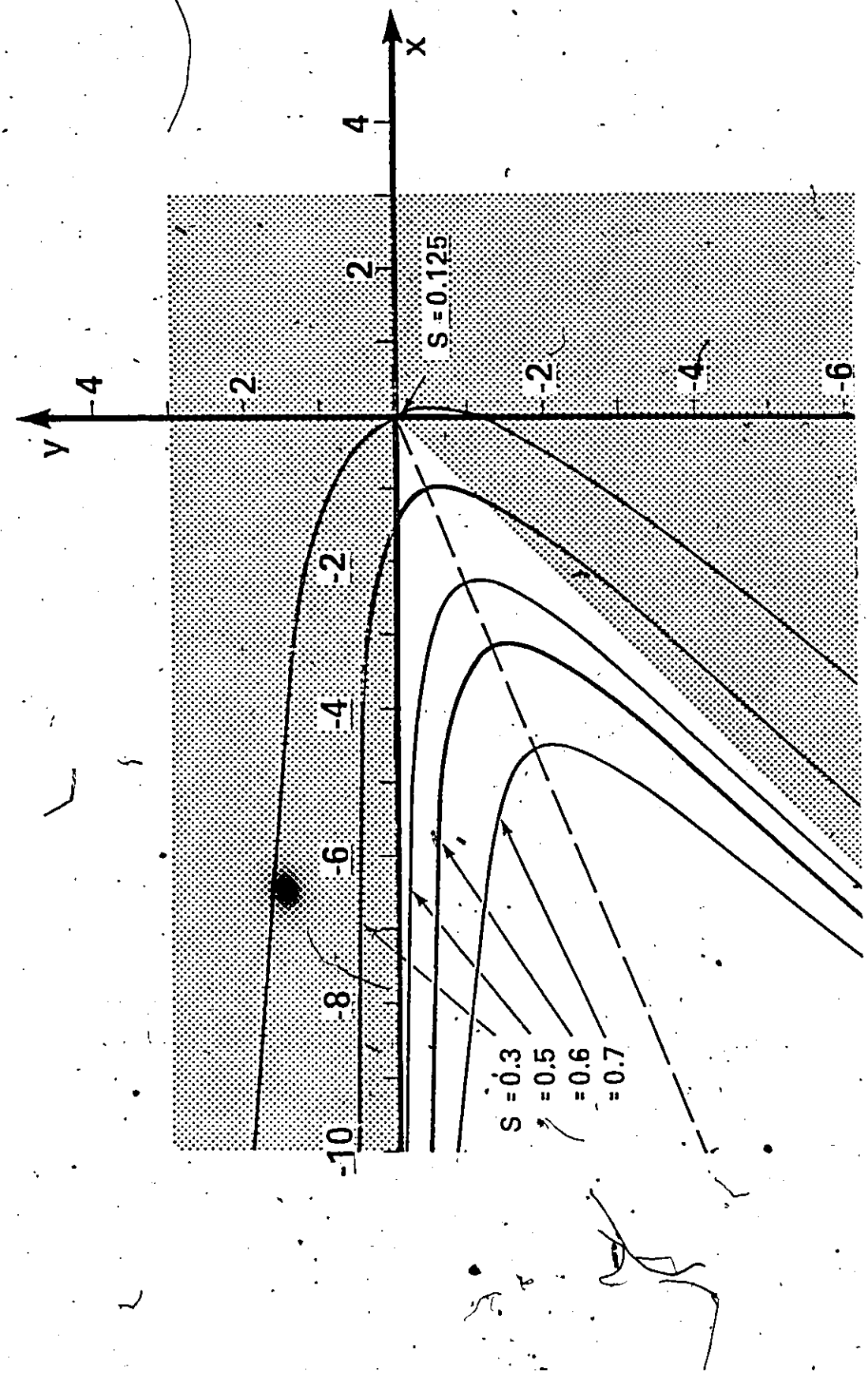

Fig. C.2: Schematic of radiographic image of a π/4-wedge illustrating blurred images of wedge corner and arms, and several exposure contours normalized to a maximum of unity. Coordinates have units of $C^{-1/2}$, where C is the dispersion coefficient.

where ω denotes spatial frequency.

For obtuse wedges, the two θ_p axes lead from the corner into the empty sector of the wedge. Unlike acute wedges, $\partial S/\partial r|_{r=0} > 0$ for axes with directions leading into the empty sector of the obtuse wedge and between the two θ_p angles. All other axes, including those with directions leading into the empty sector of the wedge but not between the two θ_p angles, have $\partial S/\partial r|_{r=0} < 0$. For these latter axes,

$$\lim_{r\to\infty} S(r,\theta) = NI_o > S_o, \tag{C-24}$$

so that exposure values of S_o also occur away from the corner.. In similarity to acute wedges, the corner values S_o and D_o are thus located on contours and are not isolated.

For the degenerate corner – that is a straight edge for which $\phi = \pi$ – the corner contour is along the edge itself.

This lack of complete corner value isolation does not preclude the precise location of wedge corners, however, since the corner is that point at which the wedge arms intersect. The wedge arms are easily identifiable as being those lines formed by points which, far from the two-dimensional corner, have exposure

$$S_{edge} = \frac{NI_o}{2}[1+\exp[-a_w]] \tag{C-25}$$

corresponding to the optical density

$$D_{edge} = D_{max}\,\gamma \log\left[\frac{1+\exp[-a_w]}{2}\right]. \tag{C-26}$$

Furthermore, the corner corresponds to the point about which the corner-valued contour is symmetric. Collectively, the above properties overdetermine the corner, thereby facilitating its location.

In Fig. C.3, the convergence of radial exposure profiles to the corner value of $S_o = NI_o/4$ is demonstrated for an acute ϕ-wedge in which $\phi = \pi/2$, and for which the system RSF is

also given by Eq. (C-22). Included are the radial profiles extending along $\theta_p = 3\pi/4, 7\pi/4$, with the property that $\partial S/\partial r|_{r=0} = 0$. Also, the profiles extending with directions between $3\pi/4$ and π, and between $3\pi/2$ and $7\pi/4$, possess the unique property of a local maximum away from the corner. For obtuse wedges, a corresponding local minimum exists in profiles leading into the empty sector of the wedge and not between the two θ_p angles. The radial profiles were calculated using the FORTRAN program RADPOL, listed in Appendix D.

If exposures do not necessarily lie in the log-linear range, then the general film gradient, Eq. (C-12), describes the relationship between exposure and optical density. For this more general case, the maximum exposure I_o is related to D_{max} through

$$D_{max} = \gamma^* \log(NI_o) + k^* \qquad \text{(C-27)}$$

assuming that the "reciprocity" property holds for the film (15). Here, the parameters γ^* and k^* are obtained simultaneously with NI_o from the characteristic curve at D_{max}.

The corner exposure is then directly determinable from Eq. (C-11) so that the optical density at the wedge corner is

$$D_o = \frac{\gamma^c}{\gamma^*}\{D_{max} + \gamma^* \log\left[\left(\frac{\phi_2 - \phi_1}{2\pi}\right)(1 - \exp[-\alpha_w]) + \exp[-\alpha_w]\right] + \frac{\gamma^*}{\gamma^c}k^c - k^*\} \qquad \text{(C-28)}$$

where γ^c and k^c are the local log linearization parameter for D_o corresponding to γ^* and k^* for D_{max} and similarly obtained. For a constant γ, Eq. (C-28) reduces to Eq. (C-14).

The optical density corresponding to an infinite knife edge in a blurred radiograph has been shown to be $D_{edge} = 0.5\, D_{max}$ (94) for the special case of a perfectly absorbing knife-edged object. Others have suggested and used $D_{edge} = 1/7\, D_{max}$ (101,102). The point of maximum optical density gradient has also been suggested as corresponding to the edge (100, 101).

For the knife edge of an infinite half-plane perfect absorber, the wedge angle is $\phi = \pi$, $\alpha_w \to \infty$ for the solid half-plane; and Eq. (C-28) reduces to

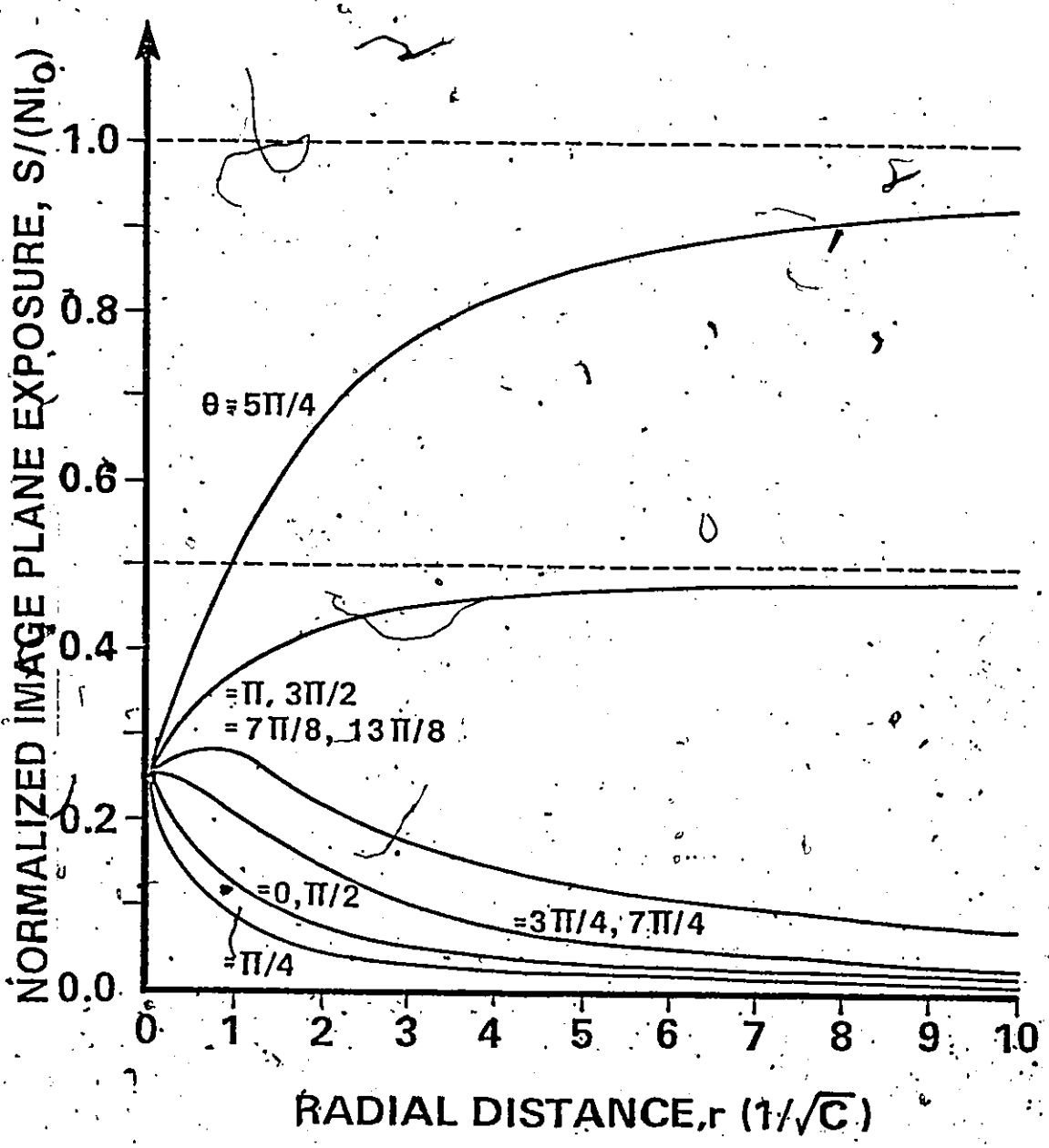

Fig. C.3: Image plane exposure radial profiles for a ϕ-wedge in which $\phi_1 = \pi$, $\phi_2 = 3\pi/2$ and the planar polar coordinates are (r,θ). Exposures are normalized to a maximum of unity.

$$D^{\infty}_{edge} = \frac{\gamma^c}{\gamma^*}\{D_{max} + \gamma^* \log(0.5) + \frac{\gamma^*}{\gamma^c} k^c - k^*\}. \quad \text{(C-29)}$$

If, in the range of exposures under consideration, the characteristic curve has the linear form

$$D(S) = \left(\frac{D_{max}}{NI_o}\right) S \quad \text{(C-30)}$$

then Eq. (C-28) reduces to $D^{\infty}_{edge} = 0.5\ D_{max}$, this result was previously obtained (100) by fitting compact mathematical functions to microdensitometer scans taken orthogonal to the "infinite" knife edge in a radiograph. These functions actually predict a D^{∞}_{edge} value of 0.5 D_{max}. The applicability of Eq. (C-30) depends on such factors as whether or not an intensifying screen or convertor is used and the range of exposures involved (3), accordingly restricting the validity of a 0.5 D_{max} edge optical density. Note that for emulsions characterized by Eq. (C-30), the conventional optical density gradient defined by Eq. (C-12) equals the optical density itself.

As for wedge corners, the correct D^{∞}_{edge} value given by Eq. (C-29) is independent of the isotropic and isoplanatic system PSF.

For the general infinite knife edge with a finite a_w, the edge optical density can be written as

$$D_{edge} = D^{\infty}_{edge} + \gamma^c \log[1 + \exp[-a_w]]$$

$$> D^{\infty}_{edge}, \quad \text{(C-31)}$$

illustrating clearly the combined dependence of D_{edge} on the wedge attenuation properties and the film emulsion characteristics.

APPENDIX D

COMPUTER PROGRAM SOURCE LISTINGS

D.1 Program Listing of Modal Transport Calculations Code.

```
PROGRAM TO EVALUATE THE FIRST THREE MODES IN A
NEUMANN SERIES EXPANSION SOLUTION TO AN INTEGRAL TRANSPORT
EQUATION ARISING IN NEUTRON RADIOGRAPHY.

      PROGRAM CALKERN(INPUT,OUTPUT,TAPE5=INPUT,TAPE6)

      REAL W,W0,WSTAR,SIGTOT,SIGS,COMP
      REAL ANS1,ANS2,ONEMIN,ZERPLUS,EULER
      REAL MODE0(10),MODE1(10),MODE2(10),MODETOT(10),BUF(10)
      REAL F1,G1,FINTGRD,GINTGRD,LAMBDA,FLO,FUP1,FUP2
      REAL GEVAL1,GEVAL2,DCADRE,WRUN

      INTEGER I,J,K,TYPE,FLUX,CURRENT

      COMMON W,SIGTOT,WSTAR,EULER,WRUN

      EXTERNAL F1,G1,FINTGRD,GINTGRD,FLO,FUP1,FUP2,MMDEI
      EXTERNAL GEVAL1,GEVAL2,DCADRE

MODE0(I),MODE1(I),MODE2(I) ARE THE FIRST 3 INTENSITY
MODES CALCULATED AT THE ITH GRID (W) POINT.

MODETOT(I) IS THE SUM OF THE 3 MODES AT THE ITH POINT.

BUF(I) IS THE BUILD-UP FACTOR AT THE ITH POINT.

W IS THE DIMENSION OF VARIATION.

WRUN IS A WORKING DUMMY FOR W.

INITIALIZATIONS

      FLUX = 1
      CURRENT = 2
      TYPE = CURRENT

      COMP = 2.0
      W0 = 0.0001
      WSTAR = 0.5
      SIGTOT = 2.0
      EULER = 0.577215665
      ONEMIN = 1.0 - 0.000001
      ZERPLUS = 0.000001

      WRITE(6,500)

CALCULATE THE MODES FOR VARIOUS SIGTOT, W VALUES.

      DO 20 I=1,1
         SIGS = SIGTOT/2.
         LAMBDA = SIGS/2.
         W = W0
         DO 10 J=1,6
            IF(J.EQ.6) W = WSTAR - W0
            MODE0(J) = EXP(-SIGTOT*W)

            IF(TYPE.EQ.CURRENT) GOTO 5

A SCALAR FLUX CALCULATION

            MODE1(J) = F1(W)*MODE0(J)*LAMBDA
```

```
            CALL D.ITER(ANS1,-ONEMIN,-ZERPLUS,FINTGRD,FLO,FUP1)
            CALL DOITER(ANS2,ZERPLUS,ONEMIN,FINTGRD,FLO,FUP2)
            MODE2(J) = ANS1 + ANS2
            GOTO 7

A FORWARD PARTIAL CURRENT CALCULATION

  5         MODE1(J) = G1(W)*MODE0(J)*LAMBDA

            CALL DRITER(ANS1,-ONEMIN,-ZERPLUS,GINTGRD,FLO,FUP1)
            CALL DOITER(ANS2,ZERPLUS,ONEMIN,GINTGRD,FLO,FUP2)
            MODE2(J) = -ANS1 + ANS2

  7         MODE2(J) = MODE2(J)*MODE0(J)*LAMBDA**2
            MODETOT(J) = MODE0(J) + MODE1(J) + MODE2(J)
            BUF(J) = MODETOT(J)/MODE0(J)

            W = W + 1.0
 10       CONTINUE

          WRITE(6,502) SIGTOT,COMP,(MODE0(J),J=1,6)
          WRITE(6,504) SIGTOT,COMP,(MODE1(J),J=1,6)
          WRITE(6,504) SIGTOT,COMP,(MODE2(J),J=1,6)
          WRITE(6,504) SIGTOT,COMP,(MODETOT(J),J=1,6)
          WRITE(6,504) SIGTOT,COMP,(BUF(J),J=1,6)

          SIGTOT = SIGTOT + 0.5
 20     CONTINUE

500   FORMAT("0","      SIGTOT    COMP          MODES"),
502   FORMAT("0",8F10.4)
504   FORMAT(8F10.4)

      STOP
      END

FUNCTION TO EVALUATE THE INTEGRAND FOR THE SECOND MODE (FLUX)

      REAL FUNCTION FINTGRD(MU,RHO)

      REAL MU,RHO,W,SIGTOT,WSTAR,F1

      COMMON W,SIGTOT,WSTAR

      FINTGRD = EXP(-RHO*SIGTOT*(1.+MU))*F1(W+RHO*MU)

      RETURN
      END

FUNCTION TO EVALUATE THE INTEGRAND FOR THE SECOND MODE (CURRENT)

      REAL FUNCTION GINTGRD(MU,RHO)

      REAL MU,RHO,W,SIGTOT,WSTAR,G1

      COMMON W,SIGTOT,WSTAR

      GINTGRD = EXP(-RHO*SIGTOT*(1.+MU))*G1(W+RHO*MU)*MU

      RETURN
      END
```

```
FUNCTION TO EVALUATE F1(W,SIGTOT,WSTAR)

      REAL FUNCTION F1(W)

      REAL W,DUM,SIGTOT,WSTAR,EULER,T1,T2,T3,T4,ARG1,ARG2
      REAL MMDEI

      INTEGER IOPT,IER
      COMMON DUM,SIGTOT,WSTAR,EULER

      IOPT = 1
      ARG1 = SIGTOT*W
      ARG2 = SIGTOT*(WSTAR - W)

      IF(ABS(ARG1).LT.0.00000001) ARG1 = 0.00000001
      IF(ABS(ARG2).LT.0.00000001) ARG2 = 0.00000001

      T1 = ALOG(2.*ARG1)
      T2 = -MMDEI(IOPT,-2.*ARG2,IER)
      T3 = -EXP(ARG1)*MMDEI(IOPT,-ARG1,IER)
      T4 = EXP(-ARG2)*MMDEI(IOPT,-ARG2,IER)

      F1 = (T1 + T2 + T3 + T4 + EULER)/SIGTOT

      RETURN
      END


FUNCTION TO EVALUATE G1(W,SIGTOT,WSTAR)

      REAL FUNCTION G1(W)

      REAL W,DUM,DUMM,WRUN,SIGTOT,WSTAR,AERR,RERR,ERROR,T1,T2
      REAL DCADRE,GEVAL1,GEVAL2,ONEMIN,ZERPLUS

      INTEGER IER

      COMMON DUM,SIGTOT,WSTAR,DUMM,WRUN

      EXTERNAL GEVAL1,GEVAL2

      ONEMIN = 0.99999
      ZERPLUS = 0.000001
      AERR = 1.0E-5
      RERR = 1.0E-5

      WRUN = W
      T1 = -DCADRE(GEVAL1,-ONEMIN,-ZERPLUS,AERR,RERR,ERROR,IER)
      T2 = DCADRE(GEVAL2,ZERPLUS,ONEMIN,AERR,RERR,ERROR,IER)
      G1 = (T1 + T2)/SIGTOT

      RETURN
      END


FUNCTION TO EVALUATE THE FIRST INTEGRAND USED IN G1

      REAL FUNCTION GEVAL1(U)

      REAL U,DUM,DUMM,WRUN,SIGTOT,WSTAR,PROD,FACTOR
```

```
      COMMON DUM,SIGTOT,WSTAR,DUMM,WRUN

      PROD = SIGTOT*WRUN
      FACTOR = 1. + 1./U
      GEVAL1 = (1. - EXP(PROD*FACTOR))/FACTOR

      RETURN
      END


FUNCTION TO EVALUATE THE SECOND INTEGRAND USED IN G1

      REAL FUNCTION GEVAL2(U)

      REAL U,SIGTOT,DUM,DUMM,WRUN,WSTAR,PROD,FACTOR

      COMMON DUM,SIGTOT,WSTAR,DUMM,WRUN

      PROD = SIGTOT*(WSTAR - WRUN)
      FACTOR = 1. + 1./U
      GEVAL2 = (1. - EXP(-PROD*FACTOR))/FACTOR

      RETURN
      END


FUNCTION TO EVALUATE THE LOWER INNER LIMIT(S).

      REAL FUNCTION FLO(MU)

      REAL MU

      FLO = 0.000001
      RETURN
      END

FUNCTION TO EVALUATE AN INNER UPPER LIMIT.

      REAL FUNCTION FUP1(MU)

      REAL MU,W
      COMMON W

      FUP1 = -W/MU
      RETURN
      END

FUNCTION TO EVALUATE AN INNER UPPER LIMIT.

      REAL FUNCTION FUP2(MU)

      REAL MU,W,DUM,WSTAR
      COMMON W,DUM,WSTAR

      FUP2 = (WSTAR - W)/MU
      RETURN
      END
```

D.2 Program Listing of DP_L Two-Dimensional Transport Code

```
PROGRAM TO CALCULATE THE MAGNITUDE OF SCATTERING
IN A 2-DIMENSIONAL SLAB, WITH NEUTRONS IMPINGENT
UPON A LIMITED SECTION OF THE LEFT FACE

      PROGRAM SCATTER(INPUT,OUTPUT,TAPE6,TAPE7)

      REAL PHIP(82,22),PHIM(82,22),PSIP(82,22),PSIM(82,22)
      REAL PHI(82,22),BI(22),PI,X,V,DELX,DELV,ALPHA,LENGTH
      REAL BIN(82),HEIGHT,DELY,V0
      REAL SIGA,SIGS0,SIGS1,SIGF,NU,NUSIGF,MU0BAR,SIGTOT
      REAL S0,EPS,OLDVAL,NEWVAL,OMEGA1,OMEGA2
      REAL D0,D1,D2,D3,D4,D5,D6,D7,D8,D9,D10,D11
      REAL D12,D13,D14,D15,D16,T1,T2,T3,T4,T5

      INTEGER I,J,J1,J2,J3,K,L,MAXITER,FLAG,TRUE,FALSE,DIRN
      INTEGER DUMI,DUMJ,JCENT,LBDRY,UBDRY,JUMP
      INTEGER VMAX,IMAX,JMAX,YMAX

      COMMON/B/BI,BIN

PHIP IS THE ZEROTH ORDER FORWARD NEUTRON FLUX.
PHIM IS THE ZEROTH ORDER REVERSE NEUTRON FLUX.
PSIP IS THE FIRST ORDER FORWARD NEUTPON FLUX.
PSIM IS THE FIRST ORDER REVERSE NEUTRON FLUX.
PHI IS THE TOTAL NEUTRON SCALAR FLUX.

BIN IS THE INPUT COSINE AMPLITUDE VERTICAL DISTRIBUTION.
BI IS THE VERSION OF BIN, AFTER CONVERSION TO THE
COORDINATES USED IN THIS PROGRAM.

INITIALIZATIONS

      SIGS0 = 3.45
      READ7,SIGS0
      MU0BAR = 0.32
      SIGS1 = MU0BAR*SIGS0
      SIGA = 0.022
      SIGF = 0.00
      NU = 2.5
      NUSIGF = NU*SIGF
      SIGTOT = SIGA + SIGS0

      LENGTH = 5.0
      ALPHA = 0.114732
      PI = 3.14159265358
      S0 = 1.0

      MAXITER = 100
      EPS = 1.0E-4
      TRUE = 1
      FALSE = 2
      DIRN = 1

      READ600,IMAX,JMAX

      DELX = LENGTH/(IMAX-1.)
      DELV = PI/(JMAX-1.)
      OMEGA1 = 1.2
      READ7,OMEGA1
      OMEGA2 = 1. - OMEGA1

      LBDRY = 3
      UBDRY = 19
```

```
      YMAX = UBDRY - LBDRY + 1
      DUMJ = JMAX - 1
      JCENT = DUMJ/2 + 1

C     DUMMY DEFINITION

      D0 = DELX/DELV
      D1 = SIGS1*DELX/4.
      D2 = 3.*SIGS1*DELX/4.
      D3 = DELX*(SIGS0 + 3.*SIGS1/4.)
      D4 = DELX*(SIGS0 - 3.*SIGS1/4.)

      D9 = 1. + DELX*(2.*SIGTOT - NUSIGF) - D3
      D11 = D4 + DELX*NUSIGF
      D12 = 1. + DELX*(2.*SIGTOT - SIGS1/4.)

C     INITIALIZE MATRICES INCLUDING BOUNDARY CONDITIONS

      DO 20 I=1,IMAX
         DO 10 J=1,JMAX
            PHIP(I,J) = 0.0
            PHIM(I,J) = 0.0
            PSIP(I,J) = 0.0
            PSIM(I,J) = 0.0
   10    CONTINUE
   20 CONTINUE

      DO 30 J=LBDRY,JBDRY
         PHIP(1,J) = S0
         PSIP(1,J) = S0
   30 CONTINUE

C     FETCH THE Y-ANGULAR VARIATION VECTOR, B1(J)

      READ(7,522) HEIGHT
      READ(7,522) YMAX
      DELY = HEIGHT/(YMAX - 1.)

C     CHECK THAT HEIGHT VALUES MATCH BEFORE CONVERTING

      T1 = 2.*TAN(PI*(UBDRY-LBDRY)/(2.*(JMAX-1.)))
       IF(ABS(HEIGHT - T1).LT.EPS)GOTO 50
       WRITE(6,524) T1,HEIGHT
       STOP

C     OK TO FETCH THE INPUT VECTOR, BIN(J)

   50 WRITE(6,530)
      WRITE(6,520)
      DO 60 J=1,YMAX
         READ(7,521) BIN(J)
         WRITE(6,532) BIN(J)
   60 CONTINUE
      WRITE(6,520)
      WRITE(6,532)
      WRITE(6,520)

      VO = -PI/2. + (LBDRY-1.)*DELV

      CALL CONVERT(DELV,LBDRY,JBDRY,JMAX,DELY,YMAX,VO)

C     OUTER ITERATIVE LOOP - EACH ITERATION
C     CALCULATES ONCE ACROSS THE ENTIRE GRID

C     FOR A SYMMETRIC SOLUTION, HALVE THE SOLUTION RANGE
```

```
      DUMJ = JCENT

      DO 140 K=1,MAXITER
         FLAG = TRUE
         DIRN = +1
         V =  PI/2. - DELV

SET CENTERLINE REFLECTION BOUNDARY CONDITION

         DO 90 I=1,IMAX
            PHIP(I,JCENT-1)  = PHIP(I,JCENT+1)
            PHIM(I,JCENT-1)  = PHIM(I,JCENT+1)
            PSIP(I,JCENT-1)  = PSIP(I,JCENT+1)
            PSIM(I,JCENT-1)  = PSIM(I,JCENT+1)
             PHIP(I,JMAX)  = PHIP(I,JMAX-1)
             PSIP(I,JMAX)  = PSIP(I,JMAX-1)
             PHIM(I,JMAX)  = PHIM(I,JMAX-1)
             PSIM(I,JMAX)  = PSIM(I,JMAX-1)
 90      CONTINUE

         DO 120 J=1,DUMJ
            J1 = J
            J2 = J - 1
            J3 = J + 1
            IF(DIRN.EQ.1) J3 = JMAX+2 - J
            IF(DIRN.EQ.1) J2 = JMAX - J
            IF(DIRN.EQ.1) J1 = JMAX+1 - J

            D5 = DJ*B1(J1)*(COS(V)**2)
            D6 = DJ*(B1(J1) - B1(J2))*(COS(V)**2)
            D7 = ALPHA*D5
            D8 = ALPHA*D6

            D10 = D9 + PI*(D5+D6)/4.
            D12 = 3.*D7
            D13 = 3.*D8
            D14 = PI*D5/4.
            D16 = D15 + 6.*(D7+D8)

            DO 100 I = 2,IMAX
               L = IMAX+1 - I

               T1 = PHIP(I-1,J1) + PSIP(I-1,J1) - PSIP(I,J1)
               T2 = D11*PHIM(I,J1)  + D2*(PSIP(I,J1)+PSIM(I,J1))
               T3 = D14*PHIP(I,J2)  + D12*(PSIP(I,J1)-PSIP(I,J2))
               T4 = D13*PSIP(I,J1)

               OLDVAL = PHIP(I,J1)
               NEWVAL = (T1 + T2 + T3 + T4)/D10
               PHIP(I,J1) = OMEGA1*NEWVAL + OMEGA2*OLDVAL
               IF(ABS(PHIP(I,J1)-OLDVAL).GT.EPS) FLAG = FALSE


               T1 = PSIP(I-1,J1) + (PHIP(I-1,J1)-PHIP(I,J1))/3.
               T2 = D1*(PHIP(I,J1)  - PHIM(I,J1) + PSIM(I,J1))
               T3 = D7*(PHIP(I,J2)  - PHIP(I,J2) + 6.*PSIP(I,J2))
               T4 = D8*PHIP(I,J1)

               OLDVAL = PSIP(I,J1)
               NEWVAL = (T1 + T2 + T3 + T4)/D16
               PSIP(I,J1) =  OMEGA1*NEWVAL + OMEGA2*OLDVAL
               IF(ABS(PSIP(I,J1)-OLDVAL).GT.EPS) FLAG = FALSE
```

```
                T1 = PHIM(L+1,J1) - PSIM(L+1,J1) + PSIM(L,J1)
                T2 = D11*PHIP(L,J1) - D2*(PSIP(L,J1) + PSIM(L,J1))
                T3 = D14*PHIM(L,J2) - D12*(PSIM(L,J1)-PSIM(L,J2))
                T4 = -D13*PSIM(L,J1)

                OLDVAL = PHIM(L,J1)
                NEWVAL = (T1 + T2 + T3 + T4)/D10
                PHIM(L,J1) = OMEGA1*NEWVAL + OMEGA2*OLDVAL
                IF(ABS(PHIM(L,J1)-OLDVAL).GT.EPS) FLAG = FALSE


                T1 = PSIM(L+1,J1) + (PHIM(L,J1)-PHIM(L+1,J1))/3.
                T2 = D1*(PHIP(L,J1) - PHIM(L,J1) + PSIP(L,J1))
                T3 = D7*(PHIM(L,J2)-PHIM(L,J1)+6.*PSIM(L,J2))
                T4 = -D8*PHIM(L,J1)

                OLDVAL = PSIM(L,J1)
                NEWVAL = (T1 + T2 + T3 + T4)/D16
                PSIM(L,J1) = OMEGA1*NEWVAL + OMEGA2*OLDVAL
                IF(ABS(PSIM(L,J1)-OLDVAL).GT.EPS) FLAG = FALSE

  100       CONTINUE
            V = V - DELV
  120     CONTINUE
          IF(FLAG.EQ.TRUE) GOTO 150
  140   CONTINUE

CALCULATE THE NEUTRON SCALAR FLUX, PHI(I,J)

  150   CONTINUE
        DO 155 J=1,JMAX
           DO 154 I=1,IMAX
              PHI(I,J) = PHIP(I,J) + PHIM(I,J)
  154      CONTINUE
  155   CONTINUE

        WRITE(6,520)
        IF(FLAG.EQ.FALSE) WRITE(6,510)
        WRITE(6,516) IMAX,JMAX
        WRITE(6,508) OMEGA1
        WRITE(6,518) MAXITER
        WRITE(6,512) V
        WRITE(6,520)

        JUMP = (IMAX-1)/10
        WRITE(6,514) ((I-1.)*LENGTH/10.,I=1,11)
        WRITE(6,520)
        WRITE(6,520)

        DO 160 J=1,JDENT
           L = JMAX+1 - J
           WRITE(6,514) (PHIP(1+JUMP*(I-1),L),I=1,11)
  160   CONTINUE

        WRITE(6,520)

        DO 170 J=1,JDENT
           L = JMAX+1 - J
           WRITE(6,514) (PSIP(1+JUMP*(I-1),L),I=1,11)
  170   CONTINUE

        WRITE(6,520)

        DO 180 J=1,JDENT
```

```
      L = JMAX+1-J
      WRITE(6,514) (PHI(1+JJMP*(I-1),L),I=1,11)
150 CONTINUE

  7 FORMAT(1F5.2)
508 FORMAT("0","RELAXATION PARAMETER IS OMEGA = ",F5.3)
510 FORMAT("0","CONVERGENCE FAILED")
512 FORMAT("0","VALUES AFTER ",I3," ITERATIONS ARE : ")
514 FORMAT(11F9.5)
516 FORMAT("0","GRID SIZE IS (I,J) = ",2I4)
518 FORMAT("0","MAXIMUM NUMBER OF ITERATIONS IS ",I4)
520 FORMAT("0")
522 FORMAT(1E14.7)
524 FORMAT("0","WEIGHT VALUES OF ",2F12.5," ARE UNEQUAL")
530 FORMAT("0","INPUT VECTOR, BIN(J), IS ")
532 FORMAT("0","CONVERTED VECTOR, B1(J), IS ")
600 FORMAT(2I3)
610 FORMAT(I3)

    STOP
    END


SUBROUTINE TO CONVERT THE VERTICAL FLUX COSINE COMPONENT
DISTRIBUTION FROM BIN(Y) TO B1(J)  (OR TO B1(V)).

    SUBROUTINE CONVERT(DELV,LBDRY,UBDRY,JMAX,DELY,YMAX,V0)

    REAL V0,V,Y,DELV,DELY,T1,T2
    REAL B1(22),BIN(82),YCOORD(82)

    INTEGER I,J,K,YMAX,JMAX,LBDRY,UBDRY,COUNT1,COUNT2

    COMMON/B/B1,BIN

DETERMINE THE Y GRID POINTS,

    COUNT1 = LBDRY + 1
    COUNT2 = UBDRY - 1
    V = V0
    YCOORD(1) = TAN(V)
    DO 10 I=2,YMAX
       YCOORD(I) = YCOORD(I-1) + DELY
 10 CONTINUE

CALCULATE THE B1(J) BY LINEAR INTERPOLATION BETWEEN
THE APPROPRIATE BIN(J)

    DO 15 J=1,LBDRY
       B1(J) = BIN(1)
       WRITE(6,50) B1(J)
 15 CONTINUE

    DO 40 J=COUNT1,COUNT2
       V = V + DELV
       Y = TAN(V)
       DO 20 K=2,YMAX
          IF(Y.LE.YCOORD(K)) GOTO 30
 20    CONTINUE

 30    CONTINUE
       T1 = (Y - YCOORD(K-1))/DELY
       T2 = (YCOORD(K) - Y)/DELY
```

```
      B1(J) = T1*BIN(K) + T2*BIN(K-1)
      WRITE(6,50) B1(J)
40 CONTINUE

   DO 45 J=JBDRY,JMAX
      B1(J) = BIN(YMAX)
      WRITE(6,50) B1(J)
45 CONTINUE

50 FORMAT(1E14.7)

   RETURN
   END
```

D.3 Program Listing of DP_L One-Dimensional Transport Code

```
PROGRAM TO CALCULATE THE NEUTRON FLUX IN A 1-DIMENSIONAL
SLAB DRIVEN INTERNALLY, USING THE DP-1 TRANSPORT
APPROXIMATION
OUTPUT IS THE NORMALIZED FLUX COSINE COMPONENT, BOUT(J)

      PROGRAM PLANAR(INPUT,OUTPUT,TAPE6,TAPE7)

      REAL PHIP(162,2),PHIM(162,2),PSIP(162,2),PSIM(162,2)
      REAL PHI(162,2),BOUT(162),PI,X,V,DELX,ALPHA,LENGTH
      REAL SIGA,SIGS0,SIGS1,SIGF,NU,NUSIGF,MU0BAR,SIGTOT
      REAL S0,EPS,OLDVAL,NEWVAL,OMEGA1,OMEGA2,FACTOR
      REAL D0,D1,D2,D3,D4,D5,D6,D7,D8,D9
      REAL T1,T2,T3,T4,T5

      INTEGER I,J,K,L,MAXITER,FLAG,TRUE,FALSE,DIRN
      INTEGER DUMI,ICENT,IMAX,LBDRY,UBDRY,JUMP,JMAX

PHIP IS THE ZEROTH ORDER FORWARD NEUTRON FLUX.
PHIM IS THE ZEROTH ORDER REVERSE NEUTRON FLUX.
PSIP IS THE FIRST ORDER FORWARD NEUTRON FLUX.
PSIM IS THE FIRST ORDER REVERSE NEUTRON FLUX.

PHI IS THE TOTAL NEUTRON SCALAR FLUX.

BOUT IS THE OUTPUT COSINE AMPLITUDE VERTICAL DISTRIBUTION.

INITIALIZATIONS

   SET PARAMETERS NECESSARY TO CALCULATE "LENGTH"

      LBDRY = 3
      UBDRY = 19
      JMAX = 21
      SIGS0 = 3.45
      READ7,SIGS0
      MU0BAR = 0.324
      SIGS1 = MU0BAR*SIGS0
      SIGA = 0.022
      SIGF = 0.00
      NU = 2.5
      NUSIGF = NU*SIGF
      SIGTOT = SIGA + SIGS0

      PI = 3.14159265536
      LENGTH = 2.*TAN(PI*(UBDRY-LBDRY)/(2.*(JMAX-1.)))
      ALPHA = 0.237462
      S0 = 1.0

      MAXITER = 200
      EPS = 1.0E-6
      TRUE = 1
      FALSE = 2
      DIRN = 1

      READ600,IMAX

      DELX = LENGTH/(IMAX-1.)
      OMEGA1 = 0.75
      READ7,OMEGA1
    7 FORMAT(1F5.2)
      OMEGA2 = 1. - OMEGA1

      ICENT = IMAX/2 + 1
```

```
DUMMY DEFINITION

      D0 = 1./ALPHA
      D1 = SIGS1*DELX/4.
      D2 = 3.*D1
      D3 = DELX*(SIGS0 + NUSIGF) - D2
      D4 = DELX*(2.*SIGTOT - SIGS0 - NUSIGF) - D2 + 1.
      D5 = D2 - 1.
      D7 = 1. + DELX*(2.*SIGTOT - SIGS1/4.)

INITIALIZE MATRICES INCLUDING BOUNDARY CONDITIONS

      DO 30 J=1,2
         DO 20 I=1,IMAX
            PHIP(I,J) = 1.0
            PHIM(I,J) = 1.0
            PSIP(I,J) = 1.0
            PSIM(I,J) = 1.0

            PHI(I,J) = 0.0
   20    CONTINUE
   30 CONTINUE

      PHIP(1,2) = 1.0
      PSIP(1,2) = 0.0
      PHIM(IMAX,2) = 0.0
      PSIM(IMAX,2) = 0.0

OUTER ITERATIVE LOOP - EACH ITERATION
CALCULATES ONCE ACROSS THE ENTIRE GRID

      DO 140 K=1,MAXITER
         FLAG = TRUE

NORMALIZE SCALAR FLUX TO UNITY AT THE SLAB CENTER
AND RESET FLUX COMPONENT VALUES

         DO 70 I=1,IMAX
            PHIP(I,1) = PHIP(I,2)
            PHIM(I,1) = PHIM(I,2)
            PSIP(I,1) = PSIP(I,2)
            PSIM(I,1) = PSIM(I,2)

            PHI(I,1) = PHIP(I,1) + PHIM(I,1)
   70    CONTINUE

         FACTOR = 1./PHI(ICENT,1)

         DO 80 I=1,IMAX

            PHIP(I,1) = FACTOR*PHIP(I,1)
            PHIM(I,1) = FACTOR*PHIM(I,1)
            PSIP(I,1) = FACTOR*PSIP(I,1)
            PSIM(I,1) = FACTOR*PSIM(I,1)

            NEWVAL = FACTOR*PHI(I,1)
            IF(ABS(NEWVAL-PHI(I,2)).GT.EPS) FLAG=FALSE
            PHI(I,2) = NEWVAL
   80    CONTINUE

         DO 100 I = 2,IMAX
            L = IMAX+1 - I

               T1 = PHIP(I-1,2) + PSIP(I-1,2) + D2*PSIP(I,1)
```

```
      T2 = D3*PHIM(I,1) + D2*PSIM(I,1) - PSIP(I,1)

      OLDVAL = PHIP(I,1)
      NEWVAL = (T1 + T2)/D4
      PHIP(I,2) = OMEGA1*NEWVAL + OMEGA2*OLDVAL


      T1 = PSIP(I-1,2) + (PHIP(I-1,2)+D2*PHIP(I,1))/3.
      T2 = D1*(PSIM(I,1) - PHIM(I,1)) - PHIP(I,1)/3.

      OLDVAL = PSIP(I,1)
      NEWVAL = (T1 + T2)/D7
      PSIP(I,2) = OMEGA1*NEWVAL + OMEGA2*OLDVAL


      T1 = PHIM(L+1,2) - PSIM(L+1,2) - D2*PSIM(L,1)
      T2 = D3*PHIP(L,1) - D2*PSIP(L,1) + PSIM(L,1)

      OLDVAL = PHIM(L,1)
      NEWVAL = (T1 + T2)/D4
      PHIM(L,2) = OMEGA1*NEWVAL + OMEGA2*OLDVAL


      T1 = PSIM(L+1,2) - (PHIM(L+1,2)+D2*PHIM(L,1))/3.
      T2 = D1*(PHIP(L,1) + PSIP(L,1)) + PHIM(L,1)/3.

      OLDVAL = PSIM(L,1)
      NEWVAL = (T1 + T2)/D7
      PSIM(L,2) = OMEGA1*NEWVAL + OMEGA2*OLDVAL

  130 CONTINUE
      IF(FLAG.EQ.TRUE) GOTO 150
  140 CONTINUE

  150 IF(FLAG.EQ.FALSE) WRITE(6,510)
      WRITE(6,516) IMAX
      WRITE(6,508) OMEGA1
      WRITE(6,518) MAXITER
      WRITE(6,512) <
      WRITE(6,520)

      JUMP = (IMAX-1)/10
      WRITE(6,514) ((I-1.)*LENGTH/10.,I=1,11)

      WRITE(6,520)

      WRITE(6,514) (PHIP(1+JUMP*(I-1),1),I=1,11)

      WRITE(6,520)

      WRITE(6,514) (PHIM(1+JUMP*(I-1),1),I=1,11)

      WRITE(6,520)

      WRITE(6,514) (PHI(1+JUMP*(I-1),2),I=1,11)

CALCULATE THE OUTPUT COSINE DISTRIBUTION, BOUT(J)

      WRITE(7,522) LENGTH
      WRITE(7,600) IMAX

      DO 160 I=1,IMAX
         T1 = 2.*(PSIP(I,1) + PSIM(I,1))
         T2 = (PHIP(I,1) + PHIM(I,1))/3.
```

```
      T2 = T2 - (PSIP(I,1) - PSIM(I,1))
      BOUT(I) = T1/T2
      WRITE(7,522) BOUT(I)
160 CONTINUE

503 FORMAT("1","RELAXATION PARAMETER IS OMEGA = ",F5.3)
510 FORMAT("0","CONVERGENCE FAILED")
512 FORMAT("0","VALUES AFTER ",I3," ITERATIONS ARE : ")
514 FORMAT(11F9.5)
516 FORMAT("0","GRID SIZE IS I = ",I4)
518 FORMAT("0","MAXIMUM NUMBER OF ITERATIONS IS ",I4)
520 FORMAT("0")
522 FORMAT(1E14.7)
600 FORMAT(1I3)

    STOP
    END
```

D.4 Program Listing of System Transfer Function Calculations in Object Scattering Analysis

```
PROGRAM TO EVALUATE THE SYSTEM TRANSFER FUNCTIONS
TSLF(N)+/-(Y,V) AND TSEF(N)(Y,V) FOR N = 0,1.

THE MODULATION TRANSFER FUNCTIONS (MTF'S) CORRESPONDING
TO EACH OF THE STF'S ARE ALSO CALCULATED.

THE SOURCE FOR TSLF+/- IS TAKEN AT V = 0+/-.

      PROGRAM STFS(INPUT,OUTPUT,TAPE5,TAPE6)

      REAL TSLF(201,3),TSEF(201,2),F1MINUS(201),F1MINUS(201)
      REAL ZERO,IO,PI,SIGTOT,SIGS,DELTAX,Y,V,S0,S1,D
      REAL DELTAY,YLOWER
      REAL DFBAR,A0,A1,K0,K1,G0PLUS,G0MINUS,G1PLUS,G1MINUS
      REAL LITD(2),BETA(2)
      REAL FTAN,LSF,QUOT,DUM,DJMM
      REAL T1,T2,TT1,TT2
      REAL MTF(201,5),NUY,DELTNUY,NUYMAX

      INTEGER I,J,NUMYPTS,NUMNUY

      COMMON/PARMS/PI,DFBAR

TSLF(I,1) IS TSLF+(N)(Y,V=0) FOR N=0,1 AND VARIOUS Y.
TSLF(I,2) IS TSLF-(0)(Y,V=0) FOR VARIOUS Y.
TSLF(I,3) IS TSLF-(1)(Y,V=0) FOR VARIOUS Y.
TSEF(I,1) IS TSEF(0)(Y) FOR VARIOUS Y.
TSEF(I,2) IS TSEF(1)(Y) FOR VARIOUS Y.
F0MINUS(I) IS F-(0)(Y) FOR VARIOUS Y.
F1MINUS(I) IS F-(1)(Y) FOR VARIOUS Y.

MTF(I,1) IS THE MTF FOR LSF AND TSLF+.
MTF(I,2) IS THE MTF FOR SLF-(0).
MTF(I,3) IS THE MTF FOR SLF-(1).
MTF(I,4) IS THE MTF FOR TSLF-(0).
MTF(I,5) IS THE MTF FOR TSLF-(1).

PRIMARY INITIALIZATIONS

      SIGS = 6.0
      SIGA = 0.0
      SIGTOT = SIGA + SIGS
      DELTAX = 0.05
      PI = 3.14159265
      ZERO = 1.0E-8
      IO = 1.0
      NUMYPTS = 201

      D = 0.1
      DFBAR = 10.0*1.0E-4

SECONDARY INITIALIZATIONS

      LITD(1) = 0
      LITD(2) = D - DELTAX/2.
      S0 = 1.0
      S1 = EXP(-SIGTOT*DELTAX/2.)
      A0 = 1./(1. - SIGA*DELTAX)
      A1 = EXP(SIGA*DELTAX)
      K0 = 1. - SIGTOT*DELTAX
      K1 = EXP(-SIGTOT*DELTAX)
      G0PLUS = 1. + K0
      G0MINUS = 1. - K0
```

```
      GPLUS = 1. + K1
      GMINUS = 1. - K1

      BETA(1) = 1. + DFBAR/LITD(1)
      BETA(2) = 1. + DFBAR/LITD(2)

C     CALCULATE TSLF+(N)(Y,V) FOR A LINE SOURCE AT V = 0.

      YLOWER = -0.01
      DELTAY = -(2.*YLOWER)/(NUMYPTS - 1.)

      Y = YLOWER
      V = ZERO
      WRITE(6,502)
      DO 20 I = 1,NUMYPTS
         TSLF(I,1) = LSF(Y,V)
         WRITE(6,504) Y,TSLF(I,1)

         Y = Y + DELTAY
   20 CONTINUE

C     CALCULATE F0-(Y) AND F1-(Y).

      YLOWER = -0.02
      DELTAY = -(2.*YLOWER)/(NUMYPTS - 1.)
      YLOWER = YLOWER + DELTAY/2.

      Y = YLOWER
      V = -ZERO
      DO 30 I=1,NUMYPTS
         F0MINUS(I) = BETA(1)*(1.+((Y-V)/(LITD(1)*BETA(1)))**2)
         F0MINUS(I) = 1./F0MINUS(I)

         F1MINUS(I) = BETA(2)*(1.+((Y-V)/(LITD(2)*BETA(2)))**2)
         F1MINUS(I) = 1./F1MINUS(I)

         Y = Y + DELTAY
   30 CONTINUE

C     CALCULATE TSLF-(N)(Y,V) FOR A LINE SOURCE AT V = 0-.

      DUM = S0*SIGS*DELTAX/(2.*PI*LITD(1))
      DUMM = S1*SIGS*DELTAX/(2.*PI*LITD(2))

      Y = YLOWER
      V = -ZERO
      WRITE(6,506)
      DO 40 I=1,NUMYPTS
         TSLF(I,2) = A0*(K0*LSF(Y,V) + DUM*F0MINUS(I))
         TSLF(I,3) = A1*(K1*LSF(Y,V) + DUMM*F1MINUS(I))
         WRITE(6,508) Y,TSLF(I,2),TSLF(I,3)

         Y = Y + DELTAY
   40 CONTINUE

C     CALCULATE TSLF(N)(Y)

      YLOWER = -0.10
      DELTAY = -(2.*YLOWER)/(NUMYPTS - 1.)
      YLOWER = YLOWER + DELTAY/2.

      DUM = S0*SIGS*DELTAX/2.
      DUMM = S1*SIGS*DELTAX/2.

      Y = YLOWER
```

```
      WRITE(6,510)
      DO 50 I=1,NUMYPTS
         T1 = G0PLUS/2. + G0MINUS*ATAN(Y/DFBAR)/PI
         T2 = G1PLUS/2. + G1MINUS*ATAN(Y/DFBAR)/PI

         TSEF(I,1) = I0*(T1 + DUM*FTAN(Y/(LITO(1)*BETA(1))))
         TSEF(I,2) = I0*(T2 + DUMM*FTAN(Y/(LITO(2)*BETA(2))))
         WRITE(6,518) Y,TSEF(I,1),TSEF(I,2)

         Y = Y + DELTAY
   50 CONTINUE

C  CALCULATE THE MODULATION TRANSFER FUNCTIONS, NORMALIZED TO
C  UNIT NEUTRON INCIDENCE.

      NUYMAX = 30.0
      WRITE(6,512)

      DUM = S0*SIGS*DELTAX/2.
      DUMM = S1*SIGS*DELTAX/2.
      NUMNUY = 100
      DELTNUY = NUYMAX/NUMNUY

      NUY = 0.0
      DO 60 I=1,NUMNUY
         T2 = 2.*PI*NUY
         MTF(I,1) = EXP(-T2*DFBAR)
         MTF(I,2) = K0 + DUM*EXP(-T2*LITO(1))
         MTF(I,3) = K1 + DUMM*EXP(-T2*LITO(2))
         MTF(I,4) = MTF(I,1)*MTF(I,2)
         MTF(I,5) = MTF(I,1)*MTF(I,3)

         WRITE(6,514) NUY,(MTF(I,J),J=1,5)
         NUY = NUY + DELTNUY
   60 CONTINUE

  502 FORMAT("0","   Y          TSLF+(Y,V=0)")
  504 FORMAT(2F12.6)
  506 FORMAT("0","   Y           TSLF-(0)(Y,V=0)  TSLF-(1)(Y,V=0)")
  508 FORMAT(3F12.6)
  510 FORMAT("0","   Y             TSEF(0)(Y)    TSEF(1)(Y)")
  512 FORMAT("0","    NUY       MODULATION TRANSFER FUNCTIONS")
  514 FORMAT(6F12.6)

      STOP
      END

C  STANDARD USAGE FUNCTION

      REAL FUNCTION FTAN(Y)

      REAL Y,PI
      COMMON/PARMS/PI

      FTAN = 0.5 - ATAN(Y)/PI

      RETURN
      END

C  FUNCTION TO EVALUATE THE SCREEN/FILM LSF

      REAL FUNCTION LSF(Y,V)
```

```
      REAL Y,V,PI,DFBAR
      COMMON/PARMS/PI,DFBAR
      LSF = 1./(PI*DFBAR*(1. + ((Y-V)/DFBAR)**2))
      RETURN
      END
```

D.5 Program Listing of Monte Carlo Code for Edge Scattering Analysis

```
EOR
C PROGRAM TO CALCULATE DISTRIBUTION FUNCTIONS (SPF,SLF,SEF)
C DESCRIBING THE SCATTERING OF AN INCIDENT NEUTRON BEAM AS
C IT TRAVERSES AN OBJECT.  MONTE-CARLO CALCULATION IS
C USED, INCLUDING RUSSIAN ROULETTE AND SPLITTING AS
C VARIANCE REDUCTION TECHNIQUES.  THE RADIATION IS
C ASSUMED TO BE THERMALIZED, SO THAT ONLY ONE ENERGY
C GROUP IS USED, WITH AN ISOTROPIC SCATTERING KERNEL.

      PROGRAM PSFSCAT(INPUT,OUTPUT,TAPE5=INPUT,TAPE6=OUTPUT)

      REAL PTCLS(1500,3),OMEGA(1500,3),LTOT,ATOT,RTOT
      REAL SIGA,SIGS,SIGTOT,RATIO
      REAL XMAX,DELFILM,DELTAX,RMAX,DELTAR,Y0
      REAL YMAX,DELTAY
      REAL YLOWER,YUPPER,ELOWER,EUPPER,DELTAY0,DELTAE,OFFSET
      REAL ROULNUM,DELTA,SCATRAT,THETMAX,MUMIN,PI

      INTEGER MAXPART,MAXCOLL,MOSTCOL
      INTEGER SCATTER,ABSORB,EXITR,EXITL,LIVE,DIE
      INTEGER MODE,POINT,LINE,EDGE
      INTEGER NUMPART,OLDNUM,NUMINIT,NUMREG,SPLIT,EXITWT
      INTEGER NUMTRI,TRIAL
      INTEGER I,J,K,L,COUNT,INDEX
      INTEGER STATE(1500,2),TYPE,CROSSED,ROULETT
      INTEGER DIST(100,5),NUMBINS,RBINS,YBINS,EBINS

      DOUBLE PRECISION DSEED

C THE THREE COLUMNS OF "PTCLS" ARE CARTESIANS X,Y,Z.

C THE THREE COLUMNS OF "OMEGA" ARE MU=COS(THETA), COS(PHI)
C AND SIN(PHI).  NOTE THAT X & MU, Y & SIN(THETA)*COS(PHI) AND
C Z & SIN(THETA)*SIN(PHI).

C THE FIRST COLUMN OF "STATE" DESCRIBES THE PARTICLE'S NATURE
C OF EXISTENCE.  THE SECOND COLUMN IS THE NUMBER OF BOUNDARIES
C THE PARTICLE CROSSED DURING ITS LAST TRAJECTORY.

C "SIGA","SIGS", AND "SIGTOT" ARE MACROSC. 1-GROUP X-SECTIONS.
C "RATIO" IS THE RATIO OF "SIGA" TO "SIGTOT".

C THE SLAB OBJECT LIES BETWEEN 0. AND "XMAX".  THE FILM RECORDER
C LIES AT "DELFILM" + "XMAX".

C "LTOT", "RTOT" AND "ATOT" ARE THE TOTAL AMOUNTS OF LEFT EXITANT,
C RIGHT EXITANT AND ABSORBED WEIGHT, RESPECTIVELY,

C "NUMPART" IS THE CURRENT NUMBER OF PARTICLES GENERATED BY THE
C ORIGINAL INCIDENT PARTICLE.  "OLDNUM" IS A WORKING DUMMY
C FOR "NUMPART".

C THERE ARE "NUMINIT" TOTAL ORIGINAL HISTORIES, DIVIDED INTO 5
C GROUPS OF "NUMTRI" HISTORIES FOR PURPOSES OF ERROR ESTIMATION.
C "TRIAL" IS THE CURRENT GROUP BEING SIMULATED.

C PARTICLES SPLIT INTO, OR ROULETTE FROM, "SPLIT" PARTICLES AT
C EACH CROSSING OF ONE OF THE "NUMREG" IMPORTANCE REGION
C BOUNDARIES.  EACH REGION HAS WIDTH "DELTAX", "ROULNUM"
C DESCRIBES THE PROPER ROULETTE DEATH PROBABILITY.

C ALL EXITANT PARTICLES HAVE WEIGHT 1./"EXITWT".

C "SCATTER", "ABSORB", "EXITL"(EFT), "EXITR"(IGHT), "LIVE" AND
```

```
"MOSTCOL" IS THE MAX. NUMBER OF COLLISIONS THAT HAVE OCCURRED
AT ANY POINT, AND MUST BE SMALLER THAN "MAXCOLL".

"CROSSED" ASSUMES A VALUE OF "STATE(2)".

THE PROGRAM RUNS IN THREE "MODE"S - "POINT", "LINE" OR "EDGE"
TO CALCULATE A SPF, SLF OR SEF, RESPECTIVELY.

"DIST" CARRIES THE OUTPUT SPF, SLF OR SEF DISTRIBUTION IN
"RBINS", "YBINS" OR "EBINS" NUMBER OF HISTOGRAM BINS, RESP.
"NUMBINS" ASSUMES ONE OF THESE BIN VALUES.  THE BINS SPAN
THE RANGE, RESPECTIVELY, FROM 0. TO "RMAX", -"YMAX" TO
+"YMAX", OR "ELOWER" TO "EUPPER", AND ARE OF WIDTH "DELTA" =
"DELTAR", "DELTAY" OR "DELTAE".
ALSO, FOR "EDGE" MODE, PARTICLES ARE INCIDENT FROM "YLOWER"
TO "YUPPER" AT REGULAR CLOSE INTERVALS OF WIDTH "DELTAYO".

AFTER EACH TRIAL "YO" IS MODIFIED BY "OFFSET" TO INCREASE THE
UNIFORMITY OF INCIDENCE.

A FRACTION "SCATRAT" OF ALL INCIDENT PARTICLES HAVE UNIFORMLY
DISTRIBUTED INCIDENT DIRECTIONS WITH THETA BETWEEN 0. AND
"THETMAX", CORRESPONDING TO A MU OF "MUMIN".

"I","J","K","L","COUNT" AND "INDEX" ARE ALL DUMMIES.

"DSEED" IS THE RANDOM NUMBER GENERATOR SEED.

      COMMON/PARTICL/PICLS,STATE
      COMMON/DIRNS/OMEGA
      COMMON/NUMBERS/NUMPART,MAXPART
      COMMON/TOTALS/LTOT,ATOT,RTOT,DIST,TRIAL,NUMBINS
      COMMON/SEEDS/DSEED
      COMMON/TYPES/SCATTER,ABSORB,EXITR,EXITL
      COMMON/EXIST/LIVE,DIE
      COMMON/MODES/EDGE,LINE,POINT,DELTA
      COMMON/DIMNS/YMAX,EUPPER,DELFILM

      EXTERNAL RANDIRN,GGUBS

PRIMARY INITIALIZATIONS - UNITS ARE C.G.S.

      READ(5,512) NUMINIT,MAXCOLL,MODE

      NUMTRI = NUMINIT/5
      MAXPART = 1500
      SPLIT = 2
      RTOT = 0.0
      LTOT = 0.0
      ATOT = 0.0
      MOSTCOL = 0
      DSEED = 123457.00
      PI = 3.141592653

      SIGA = 1.0
      SIGS = 1.0
      SIGTOT = SIGA + SIGS
      RATIO = SIGA/SIGTOT

      YMAX = 2.5
      YBINS = 50
      DELTAY = 2.*YMAX/YBINS

      YUPPER = 5.0
```

```
      YLOWER = - YUPPER
      EUPPER = 3.0
      ELOWER = - EUPPER
      EBINS = 40
      DELTAE = (EUPPER - ELOWER)/EBINS
      DELTAYO = (YUPPER - YLOWER)/(NUMTRI - 1.)
      OFFSET = DELTAYO/5.
      THETMAX = PI/4.
      MUMIN = COS(THETMAX)

      RMAX = 5.0
      RBINS = 50
      DELTAR = RMAX/RBINS

      XMAX = 0.5
      DELFILM = 0.0
      NUMREG = 3
      DELTAX = XMAX/NUMREG
      EXITWT = SPLIT**NUMREG

      POINT = 1
      LINE = 2
      EDGE = 3
      SCATTER = 4
      ABSORB = 5
      EXITL = 6
      EXITR = 7
      LIVE = 8
      DIE = 9

      NUMBINS = RBINS
      DELTA = DELTAR
      IF(MODE.NE.EDGE) READ(5,522) YO
      IF(MODE.EQ.EDGE) READ(5,522) SCATRAT

      IF(MODE.EQ.EDGE) NUMBINS = EBINS
      IF(MODE.EQ.EDGE) DELTA = DELTAE
      IF(MODE.EQ.LINE) NUMBINS = YBINS
      IF(MODE.EQ.LINE) DELTA = DELTAY

ECHO RELEVANT INPUT

      WRITE(6,502)
      WRITE(6,504) NUMINIT,MAXPAFT,MAXCOLL,DELTA
      WRITE(6,506)
      WRITE(6,508) SIGA,SIGS,SIGTOT,RATIO
      WRITE(6,518)
      WRITE(6,520) SPLIT,XMAX,DELTAX,NUMREG,MODE,DELFILM
      IF(MODE.EQ.EDGE) WRITE(6,519)
      IF(MODE.EQ.EDGE) WRITE(6,522) SCATRAT,THETMAX
      IF(MODE.NE.EDGE) WRITE(6,521)
      IF(MODE.NE.EDGE) WRITE(6,522) YO

CLEAR THE DISTRIBUTION FUNCTION BINS

      DO 7 J=1,5
         DO 5 I=1,100
            DIST(I,J) = 0
    5    CONTINUE
    7 CONTINUE

OUTER ITERATIVE LOOPS - INITIATE A PARTICLE

      DO 75 TRIAL = 1,5
```

```
      IF(MODE.EQ.EDGE) Y0 = YLOWER + (TRIAL-3.0001)*OFFSET
      DO 70 I=1,NUMTRI

SECONDARY INITIALIZATIONS

          NUMPART = 1
          CALL INITALL(Y0,SCATRAT,MODE,MUMIN)
          IF(Y0.LT.0.0) GOTO 15

     PERFORM INITIAL COLLISION FOR SPACE-INCIDENT PTCLS.

          CALL INSPACE(Y0,XMAX,DELTAX,SIGTOT,RATIO,TYPE,CROSSED)
          IF(TYPE.EQ.SCATTER) GOTO 12

     SPACE-INCIDENT PTCLE EXITS RIGHT OR IS ABSORBED

          IF(TYPE.EQ.EXITR) CALL STORE(1,EXITWT,YC,MODE)
          NUMPART = 0
          GOTO 15

     SPACE-INCIDENT PTCLE SCATTERS IN SLAB

 12       CALL RANDIRN(1)
          IF(CROSSED.EQ.0) GOTO 15

     THE SCATTER INVOLVES SPLITTING

          CALL NEWPART(1,SPLIT**CROSSED)

INNER LOOP - EACH ITERATION IS ONE COLLISION FOR
EACH OF "NUMPART" PARTICLES

 15       DO 60 J=1,MAXCOLL
             IF(NUMPART.EQ.0) GOTO 65

PERFORM NEXT WAVE OF INTERACTIONS

DETERMINE COLLISION SITES AND TYPES GIVEN INITIAL
POSITIONS AND DIRECTIONS - UPDATE X,Y,Z AND STATE.

             CALL COLLIDE(XMAX,DELTAX,SIGTOT,RATIO,[redacted]T)

PRESCREEN THE COLLISIONS FOR EXITS AND ABSORPTIONS.

             COUNT = 0
             DO 20 K=1,MAXPART
                L = K - COUNT

                IF(L.GT.NUMPART) GOTO 25
                IF(STATE(L,2).EQ.EXITR)
     +          CALL STORE(L,SPLIT**(STATE(L,2)),Y0,MODE)
                IF(STATE(L,1).EQ.SCATTER) GOTO 20

                CALL REDUCE(L,NUMPART)
                COUNT = COUNT + 1

 20          CONTINUE

SPLIT, ROULETTE OR DO NOTHING TO THE SURVIVING PARTICLES,
DEPENDING ON THEIR POSITION.
ALL PARTICLES ARE IN THE "SCATTER" STATE HERE.
```

```
 25         OLDNUM = NUMPART
            COUNT = 0
            DO 50 K=1,MAXPART
               INDEX = K - COUNT
               IF(INDEX.GT.OLDNUM) GOTO 60
               IF(STATE(INDEX,2).LT.0) GOTO 30

SCATTER THE INCIDENT PARTICLE

               CALL RANDIRN(INDEX)
               IF(STATE(INDEX,2).EQ.0) GOTO 50

SPLIT THE INCIDENT PARTICLE.

               CALL NEWPART(INDEX,SPLIT**(STATE(INDEX,2)))
               IF(INDEX.EQ.-1) GOTO 55
               GOTO 50

ROULETTE THE INCIDENT PARTICLE

 30            ROULNUM = SPLIT**FLOAT(STATE(INDEX,2))
               IF(ROULETT(ROULNUM).NE.LIVE)GOTO 40

IF PARTICLE SURVIVES THE ROULETTE

               CALL RANDIRN(INDEX)
               GOTO 50

IF THE ROULETTE KILLS THE PARTICLE

 40            CALL REDUCE(INDEX,OLDNUM)
               CALL REDUCE(OLDNUM+1,NUMPART)
               COUNT = COUNT + 1
 50         CONTINUE

IF TOO MANY PARTICLES ARE FORMED AT ANY STAGE

 55         WRITE(6,514) I,J
            STOP
 60      CONTINUE

 65      IF(J.GE.MOSTCOL) MOSTCOL = J
         IF(J.GE.MAXCOLL) WRITE(6,510)
         IF(J.GE.MAXCOLL) STOP

         IF(MODE.EQ.EDGE) Y0 = Y0 + DELTAY0

 70   CONTINUE
 75   CONTINUE
      WRITE(6,516) MOSTCOL

CALCULATE AND DISPLAY THE SPECIFIED DISTRIBUTION FUNCTION

      CALL OUTCALC(EXITWT)

OUTPUT FORMATS

502 FORMAT("0","  NUMINIT  MAXPART  MAXCOLL DELTA")
504 FORMAT(3I8,F10.3)
506 FORMAT("0","     SIGA      SIGS      SIGTOT     RATIO")
508 FORMAT(4F9.3)
510 FORMAT("0"," TOO MANY COLLISIONS - HISTORIES TERMINATED")
512 FORMAT(3I6)
514 FORMAT("0","TOO MANY PARTICLES AT (I,J) = ",2I6)
516 FORMAT("0","MAXIMUM # OF COLLISIONS WAS ",I6)
```

```
518 FORMAT("0","  SPLIT    XMAX       DELTAX   NUMREG MODE DELFILM")
519 FORMAT("0","    SCATRAT  THETMAX")
520 FORMAT(I6,2F10.3,2I6,F10.3)
521 FORMAT("0","      Y0")
522 FORMAT(2F10.3)

    STOP
    END


ROUTINE TO SIMULATE A COLLISION - RETURNS THE NEW
POSITION (=POSITION OF COLLISION) AND NEW STATE.

    SUBROUTINE COLLIDE(XMAX,DELTAX,SIGTOT,RATIO,SPLIT)

    REAL XMAX,DELTAX,SIGTOT,RATIO,LTOT,ATOT,RTOT
    REAL LENGTH(1500),LEN,NEWX,NEWY,MU,THETSIN,TYPE
    REAL PTCLS(1500,3),OMEGA(1500,3)

    INTEGER I,NUMPART,STATE(1500,2),REG
    INTEGER SCATTER,ABSORB,EXITR,EXITL,SPLIT

    DOUBLE PRECISION DSEED

    COMMON/PARTICL/PTCLS,STATE
    COMMON/DIRNS/OMEGA
    COMMON/NUMBERS/NUMPART
    COMMON/SEEDS/DSEED
    COMMON/TYPES/SCATTER,ABSORB,EXITR,EXITL
    COMMON/TOTALS/LTOT,ATOT,RTOT

    CALL GGUBS(DSEED,NUMPART,LENGTH)

LOOP CALCULATES THE COLLISION POINT FOR EACH PARTICLE

    DO 40 I=1,NUMPART
       LEN = -ALOG(LENGTH(I))/SIGTOT
       MU = OMEGA(I,1)
       THETSIN = SQRT(1. - MU*MU)
       NEWX = PTCLS(I,1) + LEN*MU
       REG = INT(PTCLS(I,1)/DELTAX)
       IF(NEWX.GT.0.0) GOTO 10

PARTICLE EXITS LEFT - TERMINATE THE HISTORY

  5    STATE(I,1) = EXITL
       LTOT = LTOT + 1./SPLIT**REG
       GOTO 40

 10    IF(NEWX.LT.XMAX) GOTO 15

PARTICLE EXITS RIGHT - CALCULATE LEN, THE DISTANCE
TO THE PROJECTED POINT OF EXIT

 12    LEN = (XMAX - PTCLS(I,1))/MU
       STATE(I,1) = EXITR
       RTOT = RTOT + 1./SPLIT**REG
       NEWX = XMAX*1.0000001
       GOTO 30

CHECK IF EXIT BECAUSE DESTINATION IS IN SLAB SPACE

 15    NEWY = PTCLS(I,2) + LEN*THETSIN*OMEGA(I,2)
       IF(NEWY.LT.0.0) GOTO 20
```

```
IF NEWX IN SLAB BUT NEWY IN SPACE, AND THUS EXITS LEFT
      IF(MU.LE.0.0) GOTO 5
IF NEWX IN SLAB BUT NEWY IN SPACE, AND THUS EXITS RIGHT
      GOTO 12
PARTICLE UNDERGOES A NORMAL COLLISION
 20   CALL GGUBS(DSEED,1,TYPE)
      STATE(I,1) = SCATTER
THE COLLISION IS A SCATTER
      IF(TYPE.GT.RATIO) GOTO 30
THE COLLISION IS AN ABSORPTION
      STATE(I,1) = ABSORB
      ATOT = ATOT + 1./SPLIT**REG
      GOTO 40
CALCULATE THE NEW CARTESIAN COORDINATES X,Y,Z.
 30   STATE(I,2) = INT(NEWX/DELTAX) - REG
      PTCLS(I,1) = NEWX
      PTCLS(I,2) = PTCLS(I,2) + LEN*THETSIN*OMEGA(I,2)
      PTCLS(I,3) = PTCLS(I,3) + LEN*THETSIN*OMEGA(I,3)
 40 CONTINUE
    RETURN
    END


SUBROUTINE TO DECREMENT THE EXISTING PARTICLE VECTORS.
    SUBROUTINE REDUCE(INDEX,REPLACE)
    REAL PTCLS(1500,3),OMEGA(1500,3)
    INTEGER J,REPLACE,INDEX,STATE(1500,2)
    COMMON/PARTICL/PTCLS,STATE
    COMMON/DIRNS/OMEGA
    DO 10 J=1,3
       PTCLS(INDEX,J) = PTCLS(REPLACE,J)
       OMEGA(INDEX,J) = OMEGA(REPLACE,J)
 10 CONTINUE
    STATE(INDEX,1) = STATE(REPLACE,1)
    STATE(INDEX,2) = STATE(REPLACE,2)
    REPLACE = REPLACE - 1
    RETURN
    END


SUBROUTINE TO GENERATE NEW PARTICLES WITH THE
POSITION (AND WEIGHT) OF A GIVEN PARTICLE.
```

```
      SUBROUTINE NEWPART(K,L)

      REAL PTCLS(1500,3)

      INTEGER I,J,K,L,DUM,DUMDUM,NUMPART,NEWK
      INTEGER MAXPART,STATE(1500,2)

      COMMON/PARTICL/PTCLS,STATE
      COMMON/NUMBERS/NUMPART,MAXPART

      DUM = L - 1
      DUMDUM = DUM + NUMPART
      IF(DUMDUM.LT.MAXPART) GOTO 5

TOO MANY PARTICLES WILL BE GENERATED

      K = -1
      RETURN

GENERATE L-1 NEW PARTICLES

    5 DO 20 I=1,DUM
         NEWK = NUMPART + I
         STATE(NEWK,1) = STATE(K,1)

         DO 10 J=1,3
            PTCLS(NEWK,J) = PTCLS(K,J)
   10    CONTINUE

         CALL RANDIRN(NEWK)

   20 CONTINUE

      NUMPART = NUMPART + DUM

      RETURN
      END


SUBROUTINE TO STORE THE POSITION OF AN EXITANT PARTICLE.

      SUBROUTINE STORE(K,NUMEXIT,Y0,MODE)

      REAL R,Y0,YMAX,DELTA,LTOT,ATOT,RTOT
      REAL PTCLS(1500,3),OMEGA(1500,3),DELFILM,EUPPER
      REAL Y,Z,MU,LEN,THETSIN

      INTEGER K,BIN,NUMBINS,MODE,POINT,LINE,EDGE
      INTEGER DIST(100,5),NUMEXIT,TRIAL

      COMMON/PARTICL/PTCLS
      COMMON/TOTALS/LTOT,ATOT,RTOT,DIST,TRIAL,NUMBINS
      COMMON/MODES/EDGE,LINE,POINT,DELTA
      COMMON/DIRNS/OMEGA
      COMMON/DIMNS/YMAX,EUPPER,DELFILM

PROJECT POINT OF EXIT TO IMAGE PLANE;
SEPARATION IS "DELFILM"

      MU = OMEGA(K,1)
      LEN = DELFILM/MU
      THETSIN = SQRT(1.-MU*MU)
      Y = PTCLS(K,2) + LEN*THETSIN*OMEGA(K,2)
```

```
      IF(MODE.EQ.LINE) GOTO 100
      IF(MODE.EQ.EDGE) GOTO 200

MODE IS "POINT"
DETERMINE FINAL RADIAL POSITION OF THE PARTICLE(S) AND ADD
IT(THEM) TO THE APPROPRIATE BIN.

      Z = PTCLS(K,3) + LEN*THETSIN*OMEGA(K,3)
      R = SQRT((Y-Y0)**2 + Z**2)
      BIN = 1 + INT(R/DELTA)
      GOTO 300

MODE IS "LINE"
ADD PARTICLE TO THE BIN DETERMINED BY ITS Y COCRDINATE

100   IF(Y - Y0 + YMAX.LT.-DELTA/2.) RETURN
      BIN = 1 + INT((Y - Y0 + YMAX)/DELTA + 0.5)
      GOTO 300

MODE IS "EDGE"
ADD PARTICLE TO THE BIN DETERMINED BY ITS Y COORDINATE

200   IF(Y + EUPPER.LT.0.0) RETURN
      BIN = 1 + INT((Y + EUPPER)/DELTA)

300   IF(BIN.LT.1) RETURN
      IF(BIN.LE.NUMBINS) DIST(BIN,TRIAL) = DIST(BIN,TRIAL)+NUMEXIT

      RETURN
      END


SUBROUTINE TO GENERATE A RANDOM DIRECTION VECTOR

      SUBROUTINE RANDIRN(INDEX)

      REAL R(3),OMEGA(1500,3),X1,X2,X1SQ,X2SQ,SUMSQ

      INTEGER INDEX

      DOUBLE PRECISION DSEED

      COMMON/DIRNS/OMEGA
      COMMON/SEEDS/DSEED

   10 CALL GGUBS(DSEED,3,R)

      X1 = 2.*R(1) - 1.
      X2 = 2.*R(2) - 1.
      X1SQ = X1*X1
      X2SQ = X2*X2
      SUMSQ = X1SQ + X2SQ
      IF(SUMSQ.GT.1.0) GOTO 10

SAMPLE IS RETAINED FOR CALCULATING MU, COS(PHI) AND SIN(PHI)

      OMEGA(INDEX,1) = (X1SQ - X2SQ)/SUMSQ
      OMEGA(INDEX,2) = 2.*X1*X2/SUMSQ
      OMEGA(INDEX,3) = 2.*R(3) - 1.

      RETURN
      END
```

```
FUNCTION TO PROBABILISTICALLY DETERMINE THE CONTINUED
EXISTENCE OF A PARTICLE

      INTEGER FUNCTION ROULETT(ROULNUM)

      REAL R(1),ROULNUM

      INTEGER LIVE,DIE

      DOUBLE PRECISION DSEED

      COMMON/EXIST/LIVE,DIE
      COMMON/SEEDS/DSEED

      CALL GGUBS(DSEED,1,R)
      ROULETT = DIE
      IF(R(1).LE.ROULNUM) ROULETT = LIVE

      RETURN
      END


SUBROUTINE TO GENERATE THE RESULTING SPECIFIED DISTRIBUTION
FUNCTION ON A HISTOGRAM BASIS

      SUBROUTINE OUTCALC(EXITWT)

      REAL DUM,DUMM,ERRDUM,RELERR,TERM,LTOT,ATOT,RTOT

      INTEGER DIST(100,5),TOTSUM,SUM(5),EXITWT
      INTEGER I,J,NUMBINS,FILL

      COMMON/TOTALS/LTOT,ATOT,RTOT,DIST,FILL,NUMBINS

COMPUTE PARTICLE TOTALS FOR EACH OF THE 5 ITERATIONS

      TOTSUM = 0
      DO 20 J=1,5
         SUM(J) = 0
         DO 10 I=1,NUMBINS
            SUM(J) = SUM(J) + DIST(I,J)
   10    CONTINUE
         TOTSUM = TOTSUM + SUM(J)
   20 CONTINUE

COMPUTE AVERAGES AND ERRORS

      WRITE(6,504)
      DO 40 I=1,NUMBINS
         DUM = 0.0
         DUMM = 0.0
         ERRDUM = 0.0
         DO 30 J=1,5
            TERM = 0.0
            IF(SUM(J).GT.0.0) TERM = 100.*DIST(I,J)/SUM(J)
            DUM = DUM + TERM
            DUMM = DUMM + DIST(I,J)
            ERRDUM = ERRDUM + TERM*TERM
   30    CONTINUE
         DUM = DUM/5.

         ERRDUM = (ERRDUM - 5.*DUM*DUM)/4.
```

```
      ERRDUM = SQRT(ERRDUM/5.)
      RELERR = 0.0
      IF(DUM.GT.0.0) RELERR = 100.*ERRDUM/DUM

      WRITE(6,506) I,100.*DUMM/TOTSUM,ERRDUM,RELERR
 40 CONTINUE

    WRITE(6,512) FLOAT(TOTSUM)/EXITWT
    WRITE(6,514) RTOT
    WRITE(6,516) LTOT
    WRITE(6,518) ATOT

504 FORMAT("0","BIN #   % PARTICLES     ABS ERR     REL ERR")
506 FORMAT(I6,3F13.8)
512 FORMAT("0","TOTAL BIN RIGHT EXITANT WEIGHT IS ",F13.5)
514 FORMAT("0","TOTAL RIGHT EXITANT WEIGHT IS ",F13.5)
516 FORMAT("0","TOTAL LEFT EXITANT WEIGHT IS ",F13.5)
518 FORMAT("0","TOTAL ABSORBED WEIGHT IS ",F13.5)
    RETURN
    END


ROUTINE TO PERFORM INITIAL COLLISIONS FOR SPACE-INCIDENT
PARTICLES . - RETURNS "TYPE" AND "CROSSED" WHERE NECESSARY.

    SUBROUTINE INSPACE(Y0,XMAX,DELTAX,SIGTOT,RATIO,TYPE,CROSSED)

    REAL Y0,MU,THETSIN,PTCLS(1500,3),OMEGA(1500,3)
    REAL LENGTH(2),XMAX,DELTAX,SIGTOT,RATIO,L1,L2,DUM
    REAL LEN,NEWX,LTOT,ATOT,RTOT

    INTEGER EXITR,SCATTER,ABSORB,TYPE,CROSSED

    DOUBLE PRECISION DSEED

    COMMON/PARTICL/PTCLS
    COMMON/DIRNS/OMEGA
    COMMON/TYPES/SCATTER,ABSORB,EXITR
    COMMON/TOTALS/LTOT,ATOT,RTOT
    COMMON/SEEDS/DSEED

    IF(Y0.GT.0.0) GOTO 10

Y0 IS 0.0 - A DISCONTINUITY

    WRITE(6,102)
    STOP

 10 MU = OMEGA(1,1)
    THETSIN = SQRT(1. - MU*MU)
    LEN = XMAX/MU
    IF(Y0 + LEN*OMEGA(1,2)*THETSIN.LE.0.0) GOTO 20

PARTICLE EXITS RIGHT

 15 TYPE = EXITR
    LEN = XMAX/MU
    RTOT = RTOT + 1.0
    NEWX = XMAX*1.0000001
    GOTO 40

PARTICLE ENTERS SOLID PORTION OF SLAB

 20 L1 = -Y0/(THETSIN*OMEGA(1,2))
```

```
      L2 = XMAX/MU - L1
      CALL GGUBS(DSEED,1,LENGTH)
      LEN = -ALOG(LENGTH(1))/SIGTOT
IF PARTICLE PASSES THROUGH SLAB
      IF(LEN.GE.L2) GOTO 15
IF PARTICLE COLLIDES IN SLAB
      LEN = LEN + L1
      NEWX = LEN*MU
      CALL GGUBS(DSEED,1,DUM)
      IF (DUM.GT.RATIO) GOTO 30
COLLISION IS AN ABSORPTION
      TYPE = ABSORB
      ATOT = ATOT + 1.0
      RETURN
COLLISION IS A SCATTER
   30 TYPE = SCATTER
      CROSSED = INT(NEWX/DELTAX)
CALCULATE THE NEW COORDINATES
   40 PTCLS(1,1) = NEWX
      PTCLS(1,2) = Y0 + LEN*THETSIN*OMEGA(1,2)
      PTCLS(1,3) = LEN*THETSIN*OMEGA(1,3)
  102 FORMAT("0"," Y0 IS 0.0 - A DISCONTINUITY")
      RETURN
      END


ROUTINE TO INITIALIZE INCIDENT NEUTRONS
      SUBROUTINE INITALL(Y0,SCATRAT,MODE,MUMIN)
      REAL Y0,SCATRAT,MUMIN,DUM(3),X1,X2,X1SQ,X2SQ,SUMSQ
      REAL PTCLS(1500,3),OMEGA(1500,3)
      INTEGER MODE,EDGE,SCATTER,STATE(1500,2)
      DOUBLE PRECISION DSEED
      COMMON/SEEDS/DSEED
      COMMON/PARTICL/PTCLS,STATE
      COMMON/DIRNS/OMEGA
      COMMON/TYPES/SCATTER
      COMMON/MODES/EDGE
INITIALIZE POSITION AND STATE OF INCIDENT PARTICLE
      PTCLS(1,1) = 0.0
      PTCLS(1,2) = Y0
      PTCLS(1,3) = 0.0
      STATE(1,1) = SCATTER
      STATE(1,2) = 0
```

```
INITIALIZE DIRECTIONS ACCORDING TO "MODE" AND "SCATRAT"

      IF(MODE.EQ.EDGE) GOTO 20

MODE IS "POINT" OR "LINE", OR "SCATRAT" IS 0.0 - NORMALITY.

 10   OMEGA(1,1) = 1.0
      OMEGA(1,2) = 1.0
      OMEGA(1,3) = 0.0
      RETURN

MODE IS "EDGE" - "SCATRAT" OF THE INCIDENT DIRNS ARE RANDOM.

 20   IF(SCATRAT.EQ.0.0) GOTO 10
      CALL GGUBS(DSEED,1,DUM)
      IF(DUM(1).GE.SCATRAT) GOTO 10

RANDOM INCIDENT DIRECTION WITH MU BETWEEN -MUMIN AND + MUMIN

 30   CALL GGUBS(DSEED,3,DUM)
      X1 = 2.*DUM(1) - 1.
      X2 = 2.*DUM(2) - 1.
      X1SQ = X1*X1
      X2SQ = X2*X2
      SUMSQ = X1SQ + X2SQ
      IF(SUMSQ.GT.1.0) GOTO 30

SAMPLE IS RETAINED FOR CALCULATING MU, COS(PHI) AND SIN(PHI)

      OMEGA(1,2) = (X1SQ - X2SQ)/SUMSQ
      OMEGA(1,3) = 2.*X1*X2/SUMSQ
      OMEGA(1,1) = MUMIN + DUM(3)*(1.-MUMIN)

      RETURN
      END
EQ000     40      3
     0.0
    -0.01
EOF
```

D.6 Program Listing of Cylindrical Geometry Edge Scattering Code

```
PROGRAM TO CALCULATE THE SCATTERING EDGE FUNCTION
FOR THE NEUTRON RADIOGRAPHY OF AN INFINITE CYLINDER,
ASSUMING AT MOST SINGLE SCATTERING OF THERMAL NEUTRONS.

      PROGRAM CYLSEF(INPUT,OUTPUT,TAPE5=INPUT,TAPE6)

      REAL SEF,F1FACT,F2FACT,F3FACT
      REAL PI,SIGS,SIGA,SIGTOT,DD,XSTAR
      REAL YINIT,YSPAN,DELTAY,AERR,RERR,ERROR
      REAL COLLIM,SCATTER,TERM,SMALL,XL,XU
      REAL H,DELTAX,FMIDPT,INTGRD,DCADRE

      INTEGER I,NUMPTS,IER

      COMMON/MAIN/DD,XSTAR,F2FACT,F3FACT
      COMMON/VBLE/Y

      EXTERNAL DELTAX,FMIDPT,INTGRD

XSTAR IS THE CYLINDER DIAMETER.

SEF IS THE RESULTING SCATTERING EDGE FUNCTION.


INITIALIZATIONS

      SIGS = 1.0
      SIGA = 0.0
      SIGTOT = SIGS + SIGA
      DD = 1.0
      XSTAR = 1.0
      PI = 3.14159265358

      YINIT = -3.*XSTAR
      YSPAN = 5.*XSTAR
      NUMPTS = 101
      DELTAY = YSPAN/(NUMPTS - 1.)

      SMALL = 0.000001
      XL = -XSTAR + SMALL
      XU = -SMALL
      AERR = 1.0E-5
      RERR = 1.0E-5

      F1FACT = EXP(-SIGTOT*XSTAR/2.)
      F2FACT = DD - XSTAR/2.
      F3FACT = F1FACT/F2FACT

      WRITE(6,502)

CALCULATE THE SEF AS A SUM OF COLLIMATED AND
SCATTERING TERMS.

      Y = YINIT
      DO 10 I=1,NUMPTS

CALCULATE THE COLLIMATED NEUTRON CONTRIBUTION

         COLLIM = H(-Y-XSTAR) + H(Y)
         TERM = 0.0
         IF(-XSTAR.LE.Y.AND.Y.LE.0.0) TERM = EXP(-SIGTOT*DELTAX(Y))
         COLLIM = COLLIM + TERM
```

```
C     CALCULATE THE SCATTERED NEUTRON CONTRIBUTION
            SCATTER = DCADRE(INTGRD,XL,XU,AERR,RERR,ERROR,IER)
            SCATTER = SCATTER*SIGS/PI

            SEF = COLLIM + SCATTER
            WRITE(6,504) Y,SEF

            Y = Y + DELTAY
      10 CONTINUE

      502 FORMAT("0","      Y          SEF(Y)")
      504 FORMAT(2F14.7)

          STOP
          END


C     THE HEAVISIDE STEP FUNCTION
          REAL FUNCTION H(Y)

          REAL Y

          H = 0.0
          IF(Y.GT.0.0) H = 1.0

          RETURN
          END


C     FUNCTION TO EVALUATE THE CYLINDER DEPTH
          REAL FUNCTION DELTAX(Y)

          REAL Y,XSTAR,DUM

          COMMON/MAIN/DUM,XSTAR

          DELTAX = 2.*SQRT(-Y*(XSTAR + Y))

          RETURN
          END


C     FUNCTION TO CALCULATE THE DISTRIBUTION OF ONCE-SCATTERED NEUTRONS
          REAL FUNCTION FMIOPT(V)

          REAL V,DO,XSTAR,Y,F2FACT,F3FACT,DUM

          COMMON/MAIN/DO,XSTAR,F2FACT,F3FACT
          COMMON/VBLE/Y

          DUM = (Y-V)/F2FACT
          FMIOPT = F3FACT/(1. + DUM*DUM)

          RETURN
          END
```

```
INTEGRAND FUNCTION FOR ONCE-SCATTERED NEUTRON INTENSITY
      REAL FUNCTION INTGRD(V)
      REAL V,FMIDPT,DELTAX
      INTGRD = FMIDPT(V)*DELTAX(V)/2.
      RETURN
      END
```

D.7 Program Listing of Two-Dimensional Radial Response Profile Calculations Code

```
PROGRAM TO EVALUATE A CONVERTOR RESPONSE TO A WEDGE INPUT
FOR VARIOUS POINT SPREAD FUNCTIONS AND A SCATTERING POINT FUNCTIO

      PROGRAM CALCUL(INPUT,OUTPUT,TAPE4,TAPE6)

      REAL S,ERROR,RERR,AERR,DELC,DELR
      REAL SCF,D0,XSTAR,SIGA,SIGS,SIGTOT,T1,T2,T3,MID
      REAL C,R,THP,THET,PHIL,PHIU,PI

      INTEGER IER,I,P,DOSCF,YES

      COMMON THET,R,C
      EXTERNAL F3,F4,F5

THE WEDGE ANGLE PHI LIES BETWEEN PHIL AND PHIU.

RADIAL PROFILE CONVERTOR RESPONSES (S) ARE CALCULATED AT
THE ANGLE THET ALONG THE RADIAL ARM R.

RADIAL PROFILE SCATTERING CORNER FUNCTION RESPONSES (SCF)
ARE CALCULATED AT THE ANGLE THET ALONG THE RADIAL ARM R.

THE SYSTEM PSF IS DESCRIBED BY THE PARAMETERS P AND C.

C HAS UNITS OF MICRONS**(-2) FOR THE S CALCULATION.
C HAS UNITS OF C**(-2) FOR THE SCF CALCULATION.

INITIALIZATIONS

      PI = 3.14159265535
      AERR = 1.0E-5
      RERR = 1.0E-5
      PHIL = PI
      PHIU = 3.*PI/2.
      DELR = 100.

      YES = 1
      SIGS = 1.0
      SIGA = 0.0
      SIGTOT = SIGS + SIGA
      XSTAR = 1.0
      D0 = 1.0

FETCH DESIRED P,C,DELC, AND THET VALUES

      READ(4,506) P,C,DELC,THET

CHECK IF AN SCF CALCULATION IS TO BE PERFORMED.

      READ(4,508) DOSCF
      IF(DOSCF.EQ.YES) GOTO 30

      DO 20 J=1,11
         WRITE(6,510) P,THET,C
         WRITE(6,512)

 LOOP TO CALCULATE CONVERTOR RESPONSES

         R = 0.0
         DO 10 I=1,10
            IF(P.EQ.3) S = DCADRE(F3,PHIL,PHIU,AERR,RERR,ERPOR,IER)
```

```
            IF(P.EQ.4) S = DCADRE(F4,PHIL,PHIU,AERR,RERR,ERROR,IER)
            IF(P.EQ.5) S = DCADRE(F5,PHIL,PHIU,AERR,RERR,ERROR,IER)
            S = (S + (PHIU-PHIL)/(1.+C*R*R)**((P-2.)/2.))/(2.*PI)

            WRITE(6,504) R,S
            R = R + DELR
 10     CONTINUE
        C = C + DELC
 20  CONTINUE
     GOTO 100

CALCULATE THE SCF

 30  WRITE(6,510)
     DELR = 0.2
     T1 = 0.0
     T2 = 0.0

     IF(PHIL.LE.THET.AND.THET.LE.PHIU) T2 = 1.0
     IF(PHIL.GT.THET.OR.THET.GT.PHIU) T1 = EXP(-SIGTOT*XSTAR)
     MID = EXP(-SIGTOT*XSTAR/2.)*SIGS*XSTAR/(4.*PI)
     C = 1./((D0 - XSTAR/2.)**2)

     R = 0.0
     DO 40 I = 1,10
        T3 = (2.*PI + PHIL - PHIU)/SQRT(1. + C*R*R)
        SCF = DCADRE(F3,PHIU,2.*PI+PHIL,AERR,RERR,ERROR,IER)
        SCF = MID*(SCF + T3) + T1 + T2
        WRITE(6,504) R,SCF
        R = R + DELR
 40  CONTINUE

500  FORMAT("0","SP(R,THETA) FOR P=",I1,", THET=",F6.2,", C=",E10.
502  FORMAT("0","    R          S3(R)")
504  FORMAT("0",2E14.7)
506  FORMAT(I2,2F10.6,F12.8)
508  FORMAT(I2)
510  FORMAT("0","    R          SCF(R)")

100  STOP
     END

FUNCTION TO EVALJATE THE INTEGRAND FOR P = 3

     FUNCTION F3(THP)

     REAL THET,R,THP,C,DISCRM,TERM,PROD,ANGL,COSANGL
     COMMON THET,R,C

     PROD = R*SQRT(C)
     ANGL = THET - THP
     COSANGL = COS(ANGL)
     DISCRM = 1. + (PROD*SIN(ANGL))**2
     TERM = 1. + PROD*COSANGL/SQRT(1.+PROD*PROD)
     F3 = TERM*PROD*COSANGL/DISCRM

     RETURN
     END

FUNCTION TO EVALJATE THE INTEGRAND FOR P=4

     FUNCTION F4(THP)

     REAL THET,R,THP,C,DISCRM,T1,T2,PROD,ANGL,COSANGL,PI
```

```
      COMMON THET,R,C

      PI = 3.14159E6535
      PROD = R*SQRT(C)
      ANGL = THET - THP
      COSANGL = COS(ANGL)
      DISCRM = 1. + (PROD*SIN(ANGL))**2
      T1 = PROD*COSANGL/SQRT(DISCRM)
      T2 = PI/2. + ATAN(T1) + T1*DISCRM/(1.+PROD*PROD)
      F4 = T2*T1/DISCRM

      RETURN
      END
```

FUNCTION TO EVALUATE THE INTEGRAND FOR P=5

```
      FUNCTION F5(THP)

      REAL THET,R,THP,C,DISCRM,T1,T2,PROD,ANGL,COSANGL

      COMMON THET,R,C

      PROD = R*SQRT(C)
      ANGL = THET - THP
      COSANGL = COS(ANGL)
      DISCRM = 1. + (PROD*SIN(ANGL))**2
      T1 = 2.*(1. + PROD*COSANGL/SQRT(1.+PROD*PROD))/DISCRM
      T2 = PROD*COSANGL/((1.+PROD*PROD)**1.5)
      F5 = (T1 + T2)*PROD*COSANGL/DISCRM

      RETURN
      END
```

D.8 Program Listing of Oscillating Slab Response Calculations Code

```
PROGRAM TO CALCULATE THE "SCATTERING OSCILLATING FUNCTION"
(SOF), BEING THE ONE-DIMENSIONAL NEUTRON RADIOGRAPHIC RESPONSE
TO AN OSCILLATING SEMI-INFINITE SLAB.

      PROGRAM OSCIL(INPUT,OUTPUT,TAPE5,TAPE6)

      REAL SOF,PI,SIGS,SIGA,SIGTOT,XSTAR,DD,CONST
      REAL T1,T2,T3,DUM1,DUM2,S,VM,DELS,SMAX,SMIN
      REAL FT1,FT2,FINTGRD,DCADRE
      REAL AERR,RERR,ERROR

      INTEGER I,NUMPTS,IER

      COMMON/ONE/S,VM,CONST
      COMMON/TWO/PI,DUM2

      EXTERNAL FINTGRD

SOF IS THE SCATTERING OSCILLATING FUNCTION EVALUATED FOR
NUMPTS DIFFERENT S VALUES.


INITIALIZATIONS

      SIGS = 1.0
      SIGA = 0.0
      SIGTOT = SIGA + SIGS
      XSTAR = 1.0
      DD = 1.0
      VM = 1.0

      SMAX = 3.0
      SMIN = -3.0
      NUMPTS = 121
      DELS = (SMAX - SMIN)/(NUMPTS - 1.)

      AERR = 1.0E-5
      RERR = 1.0E-5

      PI = 3.14159265358
      CONST = DD - XSTAR/2.
      DUM1 = SIGS*XSTAR/(2.*PI)*EXP(-SIGTOT*XSTAR/2.)
      DUM2 = EXP(-SIGTOT*XSTAR)/PI

CALCULATE THE SOF

      S = SMIN
      WRITE(6,502)
      DO 20 I=1,NUMPTS
         T1 = FT1(S)
         T2 = FT2(S)
         T3 = DCADRE(FINTGRD,0.0,2.*PI,AERR,RERR,ERROR,IER)
         T3 = DUM1*(PI/2. - T3/(2.*PI))

         SOF = T1 + T2 + T3
         WRITE(6,504) S,T1,T2,T3,SOF,T1+T2

         S = S + DELS
   20 CONTINUE

  502 FORMAT("0","S          T1(S),T2(S),T3(S),SOF(S),T1(S)+T2(S)")
  504 FORMAT(6F12.5)
```

```
      STOP
      END

FUNCTION TO EVALJATE THE FIRST NON-SCATTERING TERM.
      REAL FUNCTION FT1(S)
      REAL S,PI
      COMMON/TWO/PI
      FT1 = 1.0
      IF(S.GT.1.0) RETURN
      IF(S.LT.-1.0) FT1 = 0.0
      IF(S.GT.-1.0) FT1 = 1. - ACOS(S)/PI
      RETURN
      END

FUNCTION TO EVALJATE THE SECOND NONSCATTERING TERM.
      REAL FUNCTION FT2(S)
      REAL S,PI,DUM2
      COMMON/TWO/PI,DUM2
      FT2 = 0.0
      IF(S.GT.1.0) RETURN
      IF(S.LT.-1.0) FT2 = PI*DUM2
      IF(S.GT.-1.0) FT2 = DUM2*ACOS(S)
      RETURN
      END

FUNCTION TO EVALJATE THE SINGLE SCATTERING TERM.
      REAL FUNCTION FINTGRD(U)
      REAL U,S,VM,CONST,ARG
      COMMON/ONE/S,VM,CONST
      ARG = VM*(S - COS(U))/CONST
      FINTGRD = ATAN(ARG)
      RETURN
      END
```

D.9 Program Listing of Two-Dimensional Convertor Response Calculations Code

```
C PROGRAM TO INTEGRATE THE POINT-SPREAD FUNCTION OVER A SPECIFIED
C RANGE, TO GENERATE A 2-DIMENSIONAL EDGE-SPREAD FUNCTION
C THE INTEGRATION IS OVER A WEDGE CROSS-SECTION

      PROGRAM RADPOL(INPUT,OUTPUT,TAPE5,TAPE6)

      REAL DBLINT,CART,POLAR
      REAL DELX,DELY,THPL,THPU
      REAL XCO,YCO,RCO,THCO,CR(101,101)
      REAL C,NORM,PI,AERR,ERROR

      INTEGER NUMX,NUMY,I,J,K,L,NUMOUT,XL,XU,YL,YU,DUMX,DUMY
      INTEGER XCENT(10),YCENT(10),STEPX(10),STEPY(10)

      COMMON /CURRENT/ XCO,YCO,RCO,THCO
      COMMON /CONSTS/C

      EXTERNAL DOUBINT

C THE WEDGE ANGLE IS BETWEEN THETAPRIME = THPL, THPU.

C THE EXPOSURE (CONVERTOR) RESPONSE IS STORED IN (X,Y) FORMAT
C IN MATRIX CR(NUMX,NUMY).

C OUTPUT IS SELECTED VALUES OF THE CR MATRIX, GIVEN IN 11*11
C FORM. THE OUTPUT VALUES ARE CENTRED ON THE (XCENT,YCENT)TH
C MATRIX ELEMENT, AND ARE SEPARATED BY (STEPX,STEPY) MATRIX
C POSITIONS.

C DELX AND DELY ARE THE CALCULATIONAL GRID SPACINGS, IN UNITS
C OF 1./SQRT(C).

C THERE ARE NUMOUT SUCH OUTPUT MATRICES.

      PI = 3.14159265
      AERR = 1.0E-3

      READ(5,510) C
      NORM = SQRT(C)/PI

C GET (X,Y) GRID SIZE AND SPACING

      READ(5,512) DELX,DELY,NUMX,NUMY
      WRITE(6,500)
      WRITE(6,512) DELX,DELY,NUMX,NUMY

C GET INTEGRATION LIMITS

      READ(5,514) THPL,THPU
      WRITE(6,502)
      WRITE(6,514) THPL,THPU

C GET OUTPUT FORMAT

      NUMOUT = 0
      DO 10 I=1,10
         NUMOUT = NUMOUT + 1
         READ(5,512) XCENT(I),YCENT(I),STEPX(I),STEPY(I)
         IF(XCENT(I).EQ.0) GOTO 20
   10 CONTINUE
   20 NUMOUT = NUMOUT - 1

C EVALUATE THE DOUBLE INTEGRAL (OVER A (U,V)
```

```
REGION) FOR EACH OF THE POINTS IN THE (X,Y)
REGION

      XCO = -((NUMX - 1)/2)*DELX

POLAR INTEGRATION

      DO 120 I=1,NUMX
         YCO = -((NUMY - 1)/2)*DELY
         DO 110 J=1,NUMY
            RCO = SQRT(XCO*XCO + YCO*YCO)

            IF(XCO.EQ.0.0.AND.YCO.GT.0.0) THCO = PI/2.
            IF(XCO.EQ.0.0.AND.YCO.LT.0.0) THCO = -PI/2.
            IF(RCO.EQ.0.0) THCO = 0.0
            IF(XCO.NE.0.0) THCO = ATAN2(YCO,XCO)

            CR(I,J) = NORM*DOUBINT(RCO,THCO,THPL,THPU)
            YCO = YCO + DELY
  110    CONTINUE
         XCO = XCO + DELX
  120 CONTINUE

OUTPUT SELECT VALUES OF MATRIX CR

      DO 220 L=1,NUMOUT
         DUMX = STEPX(L)
         DUMY = STEPY(L)

         XL = XCENT(L) - 5*DUMX
         YL = YCENT(L) - 5*DUMY
         XU = XL + 10*DUMX
         YU = YL + 10*DUMY

         DO 210 J=1,11,DUMY
            K = YU - J + 1
            WRITE(6,518)(CR(I,K),I=XL,XU,DUMX)
  210    CONTINUE
         WRITE(6,520)
  220 CONTINUE


  500 FORMAT("0","DELX    DELY   NUMX NUMY")
  502 FORMAT("0","THPL          THPU")
  510 FORMAT(F10.5)
  512 FORMAT(F6.3,X,F6.3,X,2I3)
  514 FORMAT(2F10.7)
  516 FORMAT(4I3)
  518 FORMAT(11F7.4)
  520 FORMAT("1")

      STOP
      END

FUNCTION TO EVALUATE THE POLAR DOUBLE INTEGRAL

      FUNCTION DOUBINT(R,TH,THPL,THPU)

      REAL R,TH,THPL,THPU,DTHU,DTHL,C,PI
      REAL T1,T2,T3,T4,UNIT1,UNIT2

      COMMON /CONSTS/C

      PI = 3.14159265358
      UNIT1 = 1.0
```

```
      UNIT2 = 1.0
      DTHU = THPU - TH
      DTHL = THPL - TH

      IF(ABS(DTHU).GT.PI) UNIT1 = -1.
      IF(ABS(DTHL).GT.PI) UNIT2 = -1.

      T1 = C*R*R
      T2 = SQRT(T1) + SQRT(1.+T1)
      T3 = T2*TAN(DTHU/2.)
      T4 = T2*TAN(DTHL/2.)

      IF(ABS(DTHU).GT.PI) T3 = -T3
      IF(ABS(DTHL).GT.PI) T4 = -T4

      T1 = ATAN2(T3,UNIT1)
      T2 = ATAN2(T4,UNIT2)

      IF(DTHU.GT.2.*PI) T1 = 2.*PI + T1
      IF(DTHL.GT.2.*PI) T2 = 2.*PI + T2

      DOUBINT = (T1 - T2)/SQRT(C)

      RETURN
      END
```

REFERENCES

1. W.C. Roentgen, "On a New Kind of Rays", Nature, 53, 274 (1896).

2. R. Halmshaw, Physics of Industrial Radiology, American Elsevier, New York (1966).

3. R.H. Herz, The Photographic Action of Ionizing Radiations, Wiley-Interscience, New York (1969).

4. R. Gordon and G.T. Herman, "Three-Dimensional Reconstruction from Projections: A Review of Algorithms", Int. Rev. Cytology, 38, 111 (1974).

5. I.L. Pykett, "NMR Imaging in Medicine", Scientific American, 246(5), 54 (1982).

6. G.B. Devey and P.N.T. Wells, "Ultrasound in Medical Diagnosis", Scientific American, 238(5), 98 (1978).

7. J.P. Barton, "Feasibility of Neutron Radiography for Large Bundles of Fast Reactor Fuel", IRT 6247-004, Argonne National Laboratory, U.S.A. (1978).

8. T.F. Budinger and G.T. Gullberg, "Three-Dimensional Reconstruction in Nuclear Medicine Emission Imaging", IEEE Transactions on Nuclear Science, Vol. NS-21 (1974).

9. R.A. Brooks and G. DiChiro, "Principles of Computer-Assisted Tomography in Radiographic and Radioisotopic Imaging", Phys. Med. Biol., 21, 689 (1976).

10. M.M. Ter-Pogossian, M.E. Raichle and B.E. Sobel, "Positron Emission Tomography", Scientific American, 243(4), 170 (1980).

11. T.D. Beynon and A.G. Pink, "Neutron Holography Using Fresnel Zone Plate Encoding", Nature, 283, 749 (1980).

12. H. Berger, Neutron Radiography and Gaging, ASTM, Philadelphia, PA (1975).

13. J.P. Barton, "Neutron Radiography - An Overview", Chapter 1 in reference 12.

14. D.C. Cutforth, "Neutron Sources for Radiography and Gaging", Chapter 1 in reference 12.

15. H. Berger, "Detection Systems for Neutron Radiography", Chapter 1 in reference 12.

16. P. von der Hardt and H. Röttgen, Eds., Neutron Radiography Handbook, Joint Research Centre, Petten Establishment, D. Reidel, Holland (1981).

17. H. Kallman, "Neutron Radiography", Research, 1, 254 (1948).

18. O.Z. Peter, "Neutronen-Durchleuchtung", Naturforsch, 1, 557 (1946).

19. J. Thewlis, "Neutron Radiography", British Journal of Applied Physics, 7, 345 (1950).

20. J.P. Neissel, "Neutron Radiography: Discussion and Preliminary Experiments", Report 59 GL281, General Electric Company, Schenectady, N.Y. (1958).

21. E.L. Criscuolo and D. Polansky in Proceedings, Missiles and Rockets Symposium, U.S. Naval Ammunition Depot, Concord, California, p. 112 (1961).

22. H.V. Watts, "Research Study on Neutron Interactions in Matter as Related to Image Formation", A.R.F. 1164-6, Armour Research Foundation, Chicago, Illinois (1960).

23. H. Berger and W.N. Beck, "Neutron Radiographic Inspection of Radioactive Irradiated Reactor Fuel Specimens", Nucl. Sci. Eng., 15, 441 (1963).

24. W.A. Carbiener, "Nondestructive Examination of Radioactive Material using Neutron Radiography", Nuclear Applications, 2, 468 (1966).

25. D.C. Cutforth and V.G. Aquino, "Neutron Radiography in the EBR-II Fuel Cycle Facility using an Isotopic Neutron Source", Trans. Am. Nucl. Soc., 10, 442 (1967).

26. J.J. Haskins, J.F. Jaklevick and C.D. Wilkinson in Proceedings, 16th Conference on Remote Systems Technology, American Nuclear Society, p. 218 (1969).

27. O.R. Hellig in Proceedings, National Symposium in Irradiation Testing Technology, AEC-NASA Conf. 690910, Lewis Research Centre, Cleveland, Ohio (1969).

28. C.D. Wilkinson and G.F. Hoffman, " Neutron Radiography - Sees Things that X-rays Miss", Precision Metal, Feb. 1969, 39.

29. R.L. Tomlinson and P.E. Underhill, "Production Neutron Radiography Facility for the Routine NDT Inspection of Special Aerospace Components", Report AGN-TP-29, Aerospace General Corporation, San Ramon, California, March, 1969.

30. A. Settipani, "Supplement au Bulletin D'Information", Association Technique pour L'Energie Nucleaire, No. 90, 10 (1971).

31. R.W. Parish, "Neutron Radiography", Engineering, 211 (33) (1971).

32. S.C. Aiken, "Californium-252", Progress Report No. 17, USAEC, p. 40 (1974).

33. J.P. Barton and P. Von der Hardt, Eds., Neutron Radiography, Proceedings of the First World Conference, San Diego, California, Dec. 7-10, 1981, D. Reidel, Holland (1982).

34. Atomic Energy Review, 15, (2), 121-368 (1977).

35. D.C. Cutforth, "Dimensioning Reactor Fuel Specimens from Thermal- Neutron Radiographs", Nucl. Tech. 18, 67 (1973).

36. R.W. Gurney and N.F. Mott, "The Theory of the Photolysis of Silver Bromide and the Photographic Latent Image", Proc. Roy. Soc. (London), Ser. A, 164A, 151 (1938).

37. K. Rossman, "Detail Visibility in Radiographs: An Experimental and Theoretical Study of Geometric and Absorption Unsharpness", Am. J. Roentg., 87, 387 (1962).

38. G. Lubberts, "Random Noise Produced by X-ray Fluorescent Screens", J. Opt. Soc. Am., 58, 1475 (1968).

39. U.V. Gopala Rao and P. Fatouros, "The Relationship between Resolution and Speed of X-ray Intensifying Screens", Med. Phys. 5(3), 205 (1978).

40. A.A. Harms and B.K. Garside, "An Analytical Model of the Recording Process in Neutron Radiography", Trans. Am. Nucl. Soc., 13, 542 (1970).

41. B.K. Garside and A.A. Harms, "Detection Process in Neutron Radiography", J. Appl. Phys., 42(12), 5161 (1971).

42. A.A. Harms, "Physical Processes and Mathematical Methods in Neutron Radiography", Atomic Energy Review, 15(2), 143 (1977).

43. A.A. Harms and G.R. Norman, "The Role of Internal Conversion Electrons in Gadolinium-Exposure Neutron Imaging", J. Appl. Phys., 43, 3209 (1972).

44. G.S. Okawara and A.A. Harms, "Neutron Radiography of Fast Transient Processes", Nucl. Tech., 31, 250 (1976).

45. A. Bouwers and W.J. Oosterkamp, "Die Unschärfe einer Rontgenaufnahme", Fortschr. Geb. Röntgstrahl, 54, 87 (1936).

46. R.R. Newell, "Sharpness of Shadows in Radiography of the Lungs", Radiology, 30, 493 (1938).

47. M.A. Klasens, "The Blurring of X-ray Images", Philips Tech. Rev., 9, 364 (1947).

48. P. Spiegler and A. Norman, "The Total Unsharpness in Radiography", Phys. Med. Biol., 18, 884 (1973).

49. M.J. Day, "Specification and Additivity of Unsharpness in Diagnostic Radiology", Phys. Med. Biol., 21, 399 (1976).

50. A.A. Harms and A. Zeilinger, "A New Formulation of Total Unsharpness in Radiography", Phys. Med. Biol., 22, 70 (1977).

51. M.P. Butler, "Neutron Radiographic Imaging Analysis", Master's Project, McMaster University, Hamilton, Canada (1980).

52. J.C. Osuwa, "Neutron Radiographic Unsharpness and Dimensional Analysis", Ph.D. Thesis, McMaster University, Hamilton, Canada (1982).

53. Y. Segal, A. Gutman, A. Fishman and A. Notea, "Point Spread Functions due to Neutron Scattering in Thermal Neutron Radiography of Aluminum, Iron, Zircaloy and Polyethelene Objects", Nucl. Instr. Meth., 197, 557 (1982).

54. Y. Segal, A. Gutman and A. Notea, "Scattering Point Spread Functions in Neutron Radiography", p. 929, reference 33.

55. A. Gutman, "Analysis and Computation of Point Spread Function in Neutron Radiography due to Scattering in Object", Master's Thesis, Technion-Israel Institute of Technology, Haifa, Israel (1978) (in Hebrew).

56. J.J. Duderstadt and L.J. Hamilton, Nuclear Reactor Analysis, John Wiley and Sons, New York (1976).

57. D.R. Wyman and A.A. Harms, "Kinetics of Driven Multiplying Media", Nucl. Sci. Eng., 83, 483 (1983).

58. K. Doi, "Measurement for Optical Transfer Functions of X-ray Intensifying Screens", Oyo Buturi, 33, 50 (1964).

59. K. Doi, "Optical Transfer Functions of the Focal Spot of X-ray Tubes", Am. J. Roentg., 94, 712 (1965).

60. R.H. Morgan, L.M. Bates, U.V. Gopala Rao and A. Marino, "The Frequency Response Characteristics of X-ray Films and Screens", Am. J. Roentg., 92, 426 (1964).

61. K. Rossmann, "Spatial Fluctuations of X-ray Quanta and the Recording of Radiographic Mottle", Am. J. Roentg., 90, 863 (1963).

62. K. Rossmann, "Measurement of the Modulation Transfer Function of Radiographic Systems Containing Fluorescent Screens", Phys. Med. Biol. 9, 551 (1964).

63. K. Rossmann, in Diagnostic Radiologic Instrumentation, Eds. R.D. Moseley, Jr. and J.H. Rust (Springfield, Illinois: Charles C. Thomas) (1965).

64. M. Höfert, "Messung der Kontrastüber tragungsfunktion von Röntgenverstärkerfolien", Acta Radiol. (Diag.), 1, 1111 (1963).

65. K. Rossmann, "Point Spread-Function, Line Spread-Function, and Modulation Transfer Function", Radiology, 93, 257 (1969).

66. C.E. Metz and K. Doi, "Transfer Function Analysis of Radiographic Imaging Systems", Phys. Med. Biol. 24, 1079 (1979).

67. R.C. Kintner, "Calculating the Encircled Energy in the Point-Spread Function", Optica Acta, 24, 1075 (1977).

68. E.W. Marchand, "Derivation of the Point Spread Function from the Line Spread Function", J. Opt. Soc. Am., 54, 915 (1964).

69. E.W. Marchand, "From Line to Point Spread Function: The General Case", J. Opt. Soc. Am., 55, 352 (1965).

70. R.N. Bracewell, The Fourier Transform and Its Applications, McGraw-Hill, New York (1965).

71. C.B. Johnson, "Edge-Response Functions, Line-Spread Functions, and Point-Spread Functions Corresponding to Electro-Optical Modulation Transfer Functions of the Form EXP-$(f/f_c)^n$, presented at Developments in Electronic Imaging Techniques Conference, San Francisco, California (1972).

72. A.E. Burgess, "An Empirical Equation for Screen MTFs", Med. Phys., 5(3), 199 (1978).

73. E.C. Kintner and R.M. Sillitto, "A New Analytic Method for Computing the Optical Transfer Function", Optica Acta, 23, 607 (1976).

74. C.B. Johnson, "Review and Classification of Electro-Optical Device Modulation Transfer Functions", presented at the Fifth Symposium on Photoelectronic Imaging Devices at Imperial College, London, England (1971).

75. Reactor Physics Constants, ANL-5800, USAEC Division of Technical Information, Washington (1963).

76. R.G. Jaeger, Ed., Engineering Compendium on Radiation-Shielding, Springer-Verlag, New York (1968).

77. N.M. Schaeffer, Ed., Reactor Shielding for Nuclear Engineers, John Wiley and Sons, New York (1977).

78. J.A. Rau and W.L. Parker, "Measurement of Antiscatter Grid Effectiveness in Thermal-Neutron Radiography of Hydrogenous Materials", Trans. Am. Nucl. Soc., 14, 533 (1971).

79. J.P. Barton, "Contrast Sensitivity in Neutron Radiography", Applied Materials Research, April, 1965, 90.

80. U. Fano, "Penetration of X- and Gamma Rays to Extremely Great Depths", J. Research NBS, 51(2), 95 (1953).

81. H. Greenspan, C.N. Kelber and D. Okrent, Computing Methods in Reactor Physics, Argonne National Laboratory, Gordon and Breach, New York (1968).

82. G.C. Pomraning, Radiation Hydrodynamics, Pergamon Press, New York (1973).

83. G.B. Arfken, Mathematical Methods for Physicists, Academic Press, New York (1970).

84. J. Spanier and E.M. Gelbard, Monte Carlo Principles and Neutron Transport Problems, Addison-Wesley, Reading, Massachusetts (1969).

85. I.M. Ryszhik and I.S. Gradshtein, Tables of Integrals, Series and Products, Academic Press, New York (1965).

86. G.I. Bell and S. Glasstone, Nuclear Reactor Theory, Van Nostrand Reinhold, New York (1970).

87. K.D. Lathrop and N.S. DeMuth, "Biothogonal Angular Polynomial Expansions of the Two-Dimensional Transport Equation", Trans. Am. Nucl. Soc., 10, 206 (1957).

88. A.A. Harms and S.A. Kushneriuk, "On a Multidirectional Modal Representation for Neutron Transport Analysis", Nucl. Sci. Eng., 51, 76 (1973).

89. E.A. Attia and A.A. Harms, "A New Expansion for Highly Anisotropic Neutron-Nucleus Scattering", Nucl. Sci. Eng., 59, 319 (1976).

90. J.J. Yvon, "La Diffusion Macroscopique des Neutrons: Une Méthode d'Approximation", J. Nucl. Energy, 1, 305 (1957).

91. S. Ziering and D. Schiff, "Yvon's Method for Slabs", Nucl. Sci. Eng., 3, 635 (1958).

92. H.N. Knickle and P.B. Daitch, "Time Dependent Neutron Transport Theory for Fast Pulsed Assemblies", Nucl. Sci. Eng., 41, 404 (1970).

93. G.D. Zakaib, A.A. Harms and J. Vlachopoulos, "Two Dimensional Void Reconstruction by Neutron Transmission", Nucl. Sci. Eng., 65, 145 (1978).

94. A.A. Harms, M. Heindler and D.M. Lowe, "The Physical Basis for Accurate Dimensional Measurements in Neutron Radiography", Mater. Eval., 36(5), 49 (1978).

95. R. Wideroe, "Recent Theories about Technical Radiography", Brit. J. Non-destr. Test., 1, 23 (1960).

96. R. Matfield, "On the Underlying Causes for the Shape of the Density Trace [redacted] Round Object", p. 817, reference 33.

97. M.P. Butler and A.A. Harms, "Neutron Image Simulation by Monte Carlo Methods", p. 937, reference 33.

98. R. Matfield, "On the Problems Relating to the Accuracy of the Measurement of Fuel Pin Diameters by Neutron Radiography", p. 843, reference 33.

99. E.H. Linfoot, Fourier Methods in Optical Image Evaluation, Focal Press, New York (1964).

100. J.C. Osuwa and A.A. Harms, "The Extremum-Slope Criterion for Precise Dimensional Measurements in Neutron Radiography", p. 859, reference 33.

101. A. Vary and K.J. Bowles, "Application of an Electronic Image Analyzer to Dimensional Measurements from Neutron Radiographs", Mater. Eval., 32(1), 7 (1974).

102. S.J. Basham, D.R. Grieser and J.W. Ray, "Dimensional Measurements of Cylindrical Specimens using Neutron Radiography", Mater. Eval., 26(6), 140 (1970).

103. H.C. Andrews and B.P. Hunt, Digital Image Restoration, Prentice Hall, Englewood Cliffs, New Jersey (1977).

104. L.L. Carter and E.D. Cashwell, Particle Transport Simulation with the Monte Carlo Method, USERDA Technical Information Center, Oak Ridge, Tennessee (1975).

105. A.A. Harms, B.K. Garside and P.S.W. Chan, "Edge-spread Function in Neutron Radiography", J. Appl. Phys., 43(9), 3863 (1972).

106. Private communication from M.P. Butler (1983).

107. K. Mees, Theory of Photographic Process, McMillan and Co., New York (1959).

108. R.C. Weast and M.J. Astle, Eds., CRC Handbook of Chemistry and Physics, 61st Edition, CRC Press, Boca Raton, Florida (1980).

109. W. Tape, "Folds, Pleats and Halos", American Scientist, 70(5), 467 (1982).

110. R. Greenler, Rainbows, Halos and Glories, Cambridge University Press, Cambridge (1980).

111. W. Tape, "Analytic Foundations of Halo Theory", J. Opt. Soc. Am., 70, 1175 (1980).

112. A. Vary, "Investigation of an Electronic Image Enhancer for Radiographs", Mater. Eval. 30(12), 259 (1972).

113. H. Berger and W.N. Beck, "A Thermal-Neutron Television System for Postirradiation Annealing Studies", Trans. Am. Nucl. Soc., 8, 73 (1965).

114. R.I. Brown, "Television System for Neutron Radiography using Small Sources", Trans. Am. Nucl. Soc., 12, 467 (1969).

115. D.R. Wyman and A.A. Harms, "Two-dimensional Radiographic Imaging Analysis", Journal of Nondestructive Evaluation (in press).

116. D.R. Wyman, "Two-dimensional Edge-Spread Analysis in Neutron Radiography", presented at 1982 CNA Student Conference, Ecole Polytechnique, Montreal, Canada.

117. W.H. Beyer, Ed., CRC Standard Mathematical Tab[redacted] Edition, CRC Press, Boca Raton, Florida (1978).

118. A. Erdélyi, Ed., Tables of Integral Transforms, Vol. I, II, McGraw-Hill, New York (1954).

119. A.A. Harms and T.G. Blake, "Densitometer-Beam Effects in High-Resolution Neutron Radiography", Trans. Am. Nucl. Soc., 15, 710 (1972).

120. J.C. Domanus, "Accuracy of Dimension Measurements from Neutron Radiographs of Nuclear Fuel Pins", Proc. Eighth World Conf. Nondestructive Testing, Cannes, France (1976).

121. T.J.M. Robertson, "Neutron Radiography in the Precision Measurement of Irradiated Materials", Proceedings BNES Conf. on Radiography with Neutrons, University of Birmingham, U.K. (1973).

122. L.A. Thaler, "Measurement of Capsule Heat Transfer Gaps using Neutron Radiography", Mater. Eval., 32(3), 57 (1974).

123. D.R. Wyman and A.A. Harms, "Neutron Image Blurring in Two Dimensions", Trans. Am. Nucl. Soc., 44, 206 (1983).

124. S. Chandrasekhar, Radiative Transfer, Dover, New York (1960).

125. E.P. Wigner, "Problems of Nuclear Reactor Theory", Proc. Sympos. Appl. Math. XI, Amer. Math. Soc., Providence, Rhode Island (1961).

126. G.I. Bell and W.B. Goad, "Polarization Effects on Neutron Transport", Nucl. Sci. Eng., 23, 380 (1965).

127. D.R. Wyman and A.A. Harms, "Statistical Uncertainty in the Radiation Diagnosis of Two-Phase Flows", Nucl. Eng. Design (in press).

128. R.S. Barrows and R.N. Wolfe, "A Review of Adjacency Effects in Silver Photographic Images", Photogr. Sci. Eng., 15, 472 (1971).